

Functionalization of nanocarriers with antibodies and their ability of targeting dendritic cells *in vitro* and *in vivo*

Dissertation

Zur Erlangung des Grades
Doktor der Naturwissenschaften

Am Fachbereich Biologie
Der Johannes Gutenberg-Universität Mainz

Maximilian Bernhard Brückner

geb. am 17.04.1992 in Mainz

Mainz, März 2022

Dekan: Prof. Dr. Eckhard Thines

1. Berichterstatter: Prof. Dr. Volker Mailänder
2. Berichterstatter: Prof. Dr. Harald Paulsen

Tag der mündlichen Prüfung:

The scientific studies for the presented work were conducted from December 1st, 2018 until December 15th, 2021 at the Max-Planck-Institute for Polymer Research in Mainz in the department of Prof. Dr. Katharina Landfester under the supervision of Prof. Dr. Volker Mailänder. Some parts of this work were carried out at the Dermatology Clinic, University Medical Center of the Johannes Gutenberg-University in Mainz.

I, Maximilian Brückner, hereby declare that I wrote the dissertation submitted without any unauthorized external assistance and used only sources acknowledged in this work. All textual passages which are appropriate verbatim or paraphrased from published and unpublished texts, as well as all information obtained from oral sources, are duly indicated and listed in accordance with bibliographical rules. In carrying out this research, I complied with the rules of standard scientific practice as formulated in the statutes of Johannes Gutenberg-University Mainz to insure standard scientific practice.

.....

Maximilian Bernhard Brückner

Mainz, March, 2022



Table of contents

Abstract	VII
Zusammenfassung	IX
Publication list	XI
Introduction	1
Chapter A – Nanotechnology in immunotherapy and the influence of the biomolecular corona	3
1. Theoretical background	4
1.1 Advanced cancer treatment by immunotherapy	4
1.2 Nanotechnology in cancer immunotherapy	5
1.3 The biomolecular corona on nanocarriers	6
1.4 Preparation and characterization of the biomolecular corona	8
2. Preparation of the Protein Corona: how Washing Shapes the Proteome and Influences Cellular Uptake of Nanocarriers	11
2.1 Abstract	12
2.2 Introduction	13
2.3 Material and Methods	15
2.4 Results and Discussion	21
2.5 Supporting Information	30
Chapter B – Surface-modification of nanocarriers with antibodies for a precise targeting of dendritic cells	37
3. Theoretical background	38
3.1 Dendritic cells in cancer immunotherapy	38
3.2 Targeting of dendritic cells with antibody-modified nanocarriers	41
3.4 A site-directed strategy for the immobilization of whole antibodies onto the nanocarrier surface	43
4. The conjugation strategy affects antibody orientation and targeting properties of nanocarriers	46
4.1 Abstract	47
4.2 Introduction	48
4.3 Material and Methods	49
4.4 Results and Discussion	57
4.5 Supporting Information	69
5. Achieving dendritic cell subset-specific targeting <i>in vivo</i> by site-directed conjugation of targeting antibodies to nanocarriers	77
5.1 Abstract	78
5.2 Introduction	79
5.3 Material and Methods	81
5.4 Results and Discussion	86

5.5 Supporting Information	96
6. PEG spacer length substantially affects antibody-based nanocarrier targeting of dendritic cell subsets	99
6.1 Abstract	100
6.2 Introduction	101
6.4 Results and Discussion.....	109
6.5 Supporting Information	120
Chapter C – Decoration of nanocarriers with antibody fragments to avoid an undesired F_c-mediated uptake	126
7.1 Abstract	127
7.2 Introduction	128
7.3 Material and Methods	132
7.4 Results and Discussion.....	138
Conclusion and outlook.....	161
References	164
Curriculum Vitae	178
Acknowledgements	179

Abstract

Antibody-functionalized nanocarriers applied as transport vehicles have the potential to significantly enhance the performance of cancer immunotherapy by actively delivering immunomodulatory agents to dendritic cells (DCs). Nevertheless, ongoing misconceptions in the areas of the nano-bio interface, the controlled bioconjugation of targeting moieties onto the nanocarrier surface, and selective drug delivery to DCs, have prevented a successful translation of antibody-functionalized nanocarriers into application and the market.

Therefore, this work firstly aimed to investigate the nano-bio interface of different nanocarrier systems incubated in human blood plasma and serum concerning the influence of the washing media on the composition of the biomolecular corona. Applying sodium dodecyl sulfate polyacrylamide gel electrophoresis (SDS-PAGE) and liquid chromatography coupled to mass spectrometry (LC-MS), it was shown that the washing media altered the composition of adsorbed proteins, and when washed with water, impaired the protein stability, as shown by nanoscale differential scanning fluorimetry (nanoDSF). In addition, differently washed nanocarriers incubated with cancer (HeLa) and macrophage (RAW264.7) cells were observed to deviate in their uptake behavior. Accordingly, the gained knowledge emphasizes the influence of the washing media for the downstream detection of protein compositions and the deliberate tuning of the protein corona to enrich certain proteins for a guided delivery of the nanocarrier system.

The second part of this work focused on the generation of antibody-functionalized nanocarriers precisely targeting DCs *in vitro*. DCs represent a promising target in immunotherapy, *e.g.*, to improve vaccine effectiveness because they orchestrate immune responses as a central player. For this reason, the targeting of the CD11c receptor on DCs (DC2.4) demonstrated important differences between conventional and advanced conjugation strategies. In comparison, a site-directed modification of antibodies at their glycosylation site resulted in an oriented nanocarrier-immobilization (site click chemistry), whereas lysine-modified antibodies resulted in a random surface-immobilization (thiol-maleimide chemistry). This surface-modification directly influenced targeting of DCs either specific via the F_{ab} regions of the antibody, or unspecific via the F_c region analyzed by blocking experiments (flow cytometry). Furthermore, the pre-incubation in mouse plasma was not preventing the binding-ability of site click generated antibody-functionalized nanocarriers highlighting their great targeting effectiveness under physiological conditions. Putting a deeper emphasis onto the physiological environment, experiments in mice represent an essential preclinical procedure to see how patients might respond to treatment. Consequently, the follow-up study investigated the DC subset-specific targeting effectiveness of the antibody-modified nanocarriers *in vivo*. In the

mouse study, it was shown that CLEC9A antibody-functionalized nanocarriers demonstrate a robust DC subset-specific targeting system enabling a selective binding towards conventional DCs type 1 (cDC1) and plasmacytoid DCs. These DCs represent effective subsets in anti-tumor responses. Furthermore, the imitation of the biomolecular corona in our *ex vivo* approach was observed to better mimic the realistic *in vivo* corona than the commonly used *in vitro* formation. Thereby, the murine experiments additionally validated the great potential of our versatile antibody-functionalized nanocarrier system for enhancing DC-based vaccination in cancer immunotherapy. In addition, investigations on the polyethylene glycol (PEG) linker length have shown that a certain distance between the antibody and nanocarrier-surface is necessary to enhance the F_{ab} -mediated targeting of DC subsets with lower influence of the F_c region.

However, the F_c region of whole antibodies prevents their full potential in a precise targeting leading to a possible accumulation in off-target compartments and therefore could increase unwanted side effects for the patient. Consequently, in our third and final aim, it was shown how to modify whole rat antibodies into distinct $F_{(ab)_2}$ and F_{ab}' fragments by enzymatic pepsin digestion and mild reduction by cysteamine, although the purification from undesired remnants and the surface-decoration onto the nanocarrier, hence targeting, remain to be investigated. Furthermore, the nanobody examination has demonstrated the importance of the parameters used for the conjugation affecting the biological binding activity. Also, it was shown that the quantity of nanobodies, hence the surface-coverage, used for the immobilization highly determines the targeting effectiveness of the nanocarrier conjugates in primary cells.

Overall, the findings encourage to transfer the gained knowledge onto a biocompatible nanocapsule platform to validate a targeted immunomodulatory transport to DCs via an antibody derivative.

Zusammenfassung

Antikörper-funktionalisierte Nanoträger, die als Transportmittel eingesetzt werden, haben das Potenzial, die Leistung der Krebsimmuntherapie deutlich zu verbessern in dem sie immunmodulatorische Wirkstoffe an dendritische Zellen adressieren. Dennoch verhindern Missverständnisse in den Bereichen der Nano-Bio-Grenzfläche, der kontrollierten Biokonjugation von Bindeproteinen auf der Nanoträgeroberfläche und der selektiven Wirkstoffabgabe an dendritische Zellen eine erfolgreiche Umsetzung von antikörperfunktionalisierten Nanoträgern für eine direkte Anwendung und kommerziellen Nutzen.

Daher wurde in dieser Arbeit zunächst die Nano-Bio-Grenzfläche verschiedener Nanoträgersysteme untersucht, die in menschlichem Blutplasma und Serum inkubiert wurden, um den Einfluss der Waschmedien auf die Zusammensetzung der biomolekularen Korona zu ermitteln. Mit Hilfe der Natriumdodecylsulfat-Polyacrylamid-Gelelektrophorese (SDS-PAGE) und der Flüssigchromatographie gekoppelt mit Massenspektrometrie (LC-MS) wurde gezeigt, dass die Waschmedien die adsorbierten Proteinzusammensetzungen veränderten und beim Waschen mit Wasser die Proteinstabilität beeinträchtigten, wie die Differential-Scanning-Fluorimetrie im Nanomaßstab (nanoDSF) zeigte. Darüber hinaus wurde beobachtet, dass unterschiedlich gewaschene Nanoträger, die mit Krebs- (HeLa) und Makrophagen-Zellen (RAW264.7) inkubiert wurden, ein abweichendes Aufnahmeverhalten zeigten. Die gewonnenen Erkenntnisse unterstreichen somit den Einfluss des Waschmediums für den Nachweis von Proteinzusammensetzungen und die gezielte Abstimmung der Proteinkorona zur Anreicherung bestimmter Proteine für eine gezielte Aufnahme des Nanoträgersystems.

Der zweite Schwerpunkt dieser Arbeit lag auf der Herstellung von antikörperfunktionalisierten Nanoträgern, die *in vitro* an dendritische Zellen binden. Dendritische Zellen stellen ein vielversprechendes Ziel in der Immuntherapie dar, zum Beispiel zur Verbesserung der Wirksamkeit von Impfstoffen, da sie bestimmte Immunreaktionen steuern können. Aus diesem Grund zeigte die Bindung an CD11c-Rezeptoren auf dendritischen Zellen (DC2.4) wichtige Unterschiede zwischen konventionellen und weiterentwickelten Konjugationsstrategien. Demnach führte eine gezielte Modifizierung von Antikörpern an ihrer Glykosylierungsstelle zu einer ausgerichteten Nanoträgerimmobilisierung (Site-Click Chemie), während Lysin modifizierte Antikörper eine zufällige Oberflächenimmobilisierung (Thiol-Maleimid Chemie) aufwiesen. Diese Oberflächenmodifizierung beeinflusste die Bindung an dendritische Zellen, entweder spezifisch über die F_{ab} Regionen des Antikörpers oder unspezifisch über die F_c Region, was anhand von Blockierungsexperimenten (Durchflusszytometrie) analysiert wurde. Darüber hinaus verhinderte die Vorinkubation in Mausplasma nicht die Bindungsfähigkeit der

mit Site-Click erzeugten antikörperfunktionalisierten Nanoträger, was ihre große Zielgenauigkeit unter physiologischen Bedingungen unterstreicht. Mit Blick auf die physiologische Umgebung stellen Versuche an Mäusen ein wesentliches präklinisches Verfahren dar, um zu sehen, wie Patienten auf die Behandlung reagieren könnten. Daher wurde in der Folgestudie die dendritische populationsspezifische Zielwirksamkeit der antikörpermodifizierten Nanoträger *in vivo* untersucht. In der Mausstudie konnte gezeigt werden, dass CLEC9A antikörperfunktionalisierte Nanoträger ein robust dendritisch und populationsspezifisches Zielsystem darstellen, welches eine selektive Bindung an konventionelle dendritische Zellen vom Typ 1 (cDC1) und plasmazytoide dendritische Zellen ermöglicht. Diese dendritischen Zellen stellen wirksame Populationen in der Behandlung von Krebs wieder. Darüber hinaus wurde festgestellt, dass die Nachahmung der biomolekularen Korona in unserem *ex vivo* Ansatz die realistische *in vivo* Korona besser widerspiegelt als die üblicherweise verwendete *in vitro* Korona. Insgesamt haben die Experimente an Mäusen das große Potenzial unseres vielseitigen, mit Antikörpern funktionalisierten Nanoträgersystems für die Verbesserung der dendritischen zellbasierten Impfung in der Krebsimmuntherapie zusätzlich bestätigt. Weiterhin haben Untersuchungen zur Länge des Polyethylenglycol-Adapters gezeigt, dass ein gewisser Abstand zwischen dem Antikörper und der Nanoträgeroberfläche notwendig ist, um die F_{ab} vermittelte Bindung von dendritischen Zellpopulationen mit geringerem Einfluss der F_c Region zu verbessern.

Die F_c Region ganzer Antikörper verhindert jedoch das volle Potenzial ihrer präzisen Bindung, was zu einer möglichen Anhäufung in unerwünschten Körperregionen und einer Schädigung des Patienten führen kann. Deshalb wurde in unserem dritten und letzten Teil der Arbeit gezeigt, wie Rattenantikörper durch enzymatischen Pepsinverdau und milde Reduktion durch Cysteamin in verschiedene $F_{(ab)2}$ - und F_{ab} -Fragmente umgewandelt werden können. Dennoch steht die Reinigung von unerwünschten Resten und die Oberflächenfunktionalisierung auf dem Nanoträger und damit die Untersuchung der Bindungsfähigkeit noch aus. Experimente mit *Nanobodies* haben außerdem gezeigt, wie wichtig die für die Konjugation verwendeten Parameter sind, die die biologische Bindungsaktivität beeinflussen. Außerdem wurde gezeigt, dass die Menge an *Nanobodies* und damit die Oberflächenbedeckung, die für die Immobilisierung verwendet wird, in hohem Maße die Bindungswirksamkeit der Nanoträgerkonjugate in Primärzellen bestimmt.

Insgesamt regen die Ergebnisse dazu an, die gewonnenen Kenntnisse auf eine biokompatible Nanokapselplattform zu übertragen, um einen gezielten immunmodulatorischen Transport zu dendritischen Zellen über ein Antikörperderivat zu validieren.

Publication list

[1] **Maximilian Brückner***, Johanna Simon*, Shuai Jiang, Katharina Landfester, Volker Mailänder. Preparation of the protein corona: How washing shapes the proteome and influences cellular uptake of nanocarriers. *Acta Biomaterialia*, **2020**, 114, 333-342.

[2] **Maximilian Brückner***, Johanna Simon*, Katharina Landfester, Volker Mailänder. The conjugation strategy affects antibody orientation and targeting properties of nanocarriers. *Nanoscale*, **2021**, 13, 9816-9824.

[3] Johanna Simon*, Michael Fichter*, Gabor Kuhn*, **Maximilian Brückner**, Cinja Kappel, Jenny Schunke, Tanja Klaus, Stephan Grabbe, Katharina Landfester, Volker Mailänder. Achieving dendritic cell subset-specific targeting *in vivo* by site-directed conjugation of targeting antibodies to nanocarriers. *Nano Today*, **2022**, 43, 101375.

[4] **Maximilian Brückner***, Michael Fichter*, Richard da Costa Marques, Katharina Landfester, Volker Mailänder. PEG spacer length substantially affects antibody-based nanocarrier targeting of dendritic cell subsets (preliminary title). To be submitted.

[5] Marie-Luise Frey*, Johanna Simon, **Maximilian Brückner**, Volker Mailänder, Svenja Morsbach and Katharina Landfester. Bio-orthogonal triazolinedione (TAD) crosslinked protein nanocapsules affect protein adsorption and cell interaction. *Polymer Chemistry*, **2020**, 11, 3821-3830.

[6] Leona V. Lingstedt*, Matteo Ghittorelli, **Maximilian Brückner**, Jonas Reinholz, N. Irina Crăciun, Fabrizio Torricelli, Volker Mailänder, Paschalis Gkoupidenis, Paul W. M. Blom. Monitoring of Cell Layer Integrity with a Current-Driven Organic Electrochemical Transistor. *Advanced healthcare materials*, **2019**, 8, 1900128.

[7] Katharina Lieberth*, **Maximilian Brückner**, Fabrizio Torricelli, Volker Mailänder, Paschalis Gkoupidenis, Paul W. M. Blom. Monitoring Reversible Tight Junction Modulation with a Current-Driven Organic Electrochemical Transistor. *Advanced Materials Technologies*, **2021**, 6, 2000940.

[8] Katharina Lieberth, Paolo Romele, Fabrizio Torricelli, Dimitrios A. Koutsouras, **Maximilian Brückner**, Volker Mailänder, Paschalis Gkoupidenis, Paul W. M. Blom. Current-Driven Organic Electrochemical Transistors for Monitoring Cell Layer Integrity with Enhanced Sensitivity. *Advanced Healthcare Materials*, **2021**, 10, 2100845.

[9] Philip Maximilian Knaff*, Christian Kersten*, Lukas Wettstein*, Patrick Müller, Tatjana Weil, Carina Conzelmann, Janis Müller, **Maximilian Brückner**, Stefan Pöhlmann, Markus Hoffmann, Tanja Schirmeister, Jan Münch, Volker Mailänder. Development of Potent Peptidomimetic Inhibitors for the Serine Protease TMPRSS2. Nature Communications. **2021** (Submitted).

[10] Meiyu Gai, **Maximilian Brückner**, Ana Mateos Maroto, Volker Mailänder, Svenja Morsbach, Katharina Landfester. ApoA1-functionalization of Liposomes (preliminary title). To be submitted.

[11] Meiyu Gai, **Maximilian Brückner**, Ana Mateos Maroto, Richard da Costa Marques, Volker Mailänder, Svenja Morsbach, Katharina Landfester. Liposome membrane fluidity determines cell interactions (preliminary title). To be submitted.

Introduction

The functionalization of a particular material with another compound requires the presence of specific and chemically compatible functional groups on both reaction partners, forming a strong, covalent linkage. The resulting derivatization product captivates newly acquired properties created by the combination of both reactants. Consequently, novel strategies in the field of chemical modification and bioconjugation have the potential to generate outstanding materials in numerous application areas¹. Especially, the connection of nanotechnology with biological agents offers promising approaches to revolutionize the treatment of life-threatening diseases. Viewed individually, nanotechnology, in the form of nanoparticles or nanocarriers, possess the intrinsic nature of being manufactured at will. Accordingly, nanotechnology crafts tunable, functionalizable, and biocompatible transport vehicles that enable an enhanced drug delivery compared to traditional methods². Likewise, antibodies represent one of the most important biological agents with applications ranging from life science research, diagnostics, and therapeutics. For example, the development of antibodies directly targeting specific cell surface-receptors has made them perfect candidates for a targeted therapy³.

However, both nanotechnology and antibodies on their own face limitations in their ability to actively and efficiently deliver the cargo to the organ or cells of interest without affecting healthy tissue⁴. Therefore, conjugating antibodies onto the nanocarrier surface enables the generation of a derivative with the advantage of a safer and more selective drug delivery. Especially, cancer immunotherapy benefits from this conjugation. Thus, antibody-functionalized nanocarriers can address a simultaneous delivery of immunomodulatory agents to the same antigen-presenting cells, e.g. dendritic cells, which mediate immune responses resulting in the activation of certain lymphocytes⁵. Thereby, antibody-functionalized nanocarriers trigger anti-tumor immune responses to boost the immune system in fighting against cancer. However, despite the promising advantages of antibody-functionalized nanocarriers, development is still in its early stages and faces obstacles which need to be overcome before finally reaching the market.

Consequently, this dissertation aims to investigate the obstacles that prevent the successful clinical translation of antibody-nanocarrier conjugates in three major chapters. Briefly, **Chapter A** puts a focus on the nano-bio interface, including the impact of the biomolecular corona, which dictates the fate of the nanocarrier in a biological environment. Here, the first study highlights the impact of the washing media used for the biomolecular corona preparation influencing protein stability and cellular uptake behavior of different nanocarrier systems.

In the following **Chapter B**, the overall subject deals with the surface-modification of

nanocarriers with whole antibodies generating a sufficient conjugation chemistry to immobilize antibodies in an oriented manner to efficiently target dendritic cells. Thereby, the second study compares two different conjugation strategies demonstrating the importance of correct antibody immobilization leading to a desired dendritic cell targeting *in vitro*. Furthermore, the third follow-up study analyzes the performance of the established antibody-functionalized nanocarriers *in vivo*, which validates the targeting ability in a living system. In addition, the fourth study points out the influence of the linker molecule length, which distances the immobilized antibody from the nanocarrier surface. This spatial separation shows to be particularly relevant for antibody-based nanocarrier targeting of a specific dendritic cell-subset.

The final **Chapter C** emphasizes the advantage of antibody fragments and derivatives in contrast to intact antibodies applied as targeting ligands. Here, a special focus is put on antibody candidates that lack the F_c region, such as the antibody F_{(ab)₂} and F_{ab} fragments, as well as nanobodies. This work intends to precisely disassemble intact antibodies into distinct fragments for their covalent attachment onto the nanocarrier surface. Furthermore, the examination of the detection of the nanobody binding ability and a first evaluation on nanobody-functionalized nanocarriers demonstrate important aspects to consider when applying nanobodies as targeting ligands.

Chapter A – Nanotechnology in immunotherapy and the influence of the biomolecular corona

The first chapter (A) of this dissertation divides into two subchapters. In the first subchapter, a general introduction into the overall subject of the presented work is given. The second subchapter introduces the first study [1], which demonstrates how the preparation of the biomolecular corona, namely the washing procedure, influences the composition of adsorbed proteins and the nanocarriers' interaction with immune cells. All results from the published paper and the written text represent an almost exclusive reproduction of the peer-reviewed and published paper.

[1] **Maximilian Brückner***, Johanna Simon*, Shuai Jiang, Katharina Landfester, Volker Mailänder. Preparation of the protein corona: How washing shapes the proteome and influences cellular uptake of nanocarriers. *Acta Biomaterialia*, **2020**, 114, 333-342.

1. Theoretical background

1.1 Advanced cancer treatment by immunotherapy

Modulating the patients' immune system to enhance the treatment of different types of diseases is a promising strategy in modern medicine. This enhancement by immunotherapy acts through either the suppression or activation of the patient's immune responses⁶. Suppressing the immune system by a down-regulation of certain immune responses assists in the immunosuppressive therapy of different autoimmune diseases such as type one diabetes, rheumatoid arthritis, obesity, and atherosclerosis. Contrary, activating immune responses in an immunostimulatory therapy help in treating cancer and other infectious diseases⁷. Today also, the treatment of checkpoint inhibitors are successful strategies in die field of tumor therapy⁸. This last aspect is not covered in this thesis, but should be mentioned due to its effectiveness. Especially, cancer represents the second leading cause of death worldwide with 17.5 million cancer cases and 8.7 million fatalities in 2015, with an increasing tendency⁹.

Compared to traditional cancer therapies like chemotherapy, radiotherapy, and surgery, the advantage of the stimulation of the patient's immune system by immunotherapy are the milder side effects, its selectivity, and improved overall survival and tolerance^{5, 10}. Cancer immunotherapy is so promising because it intervenes where the patient's own immune system is no longer capable of fighting against the cancer cells. In a healthy body, the immune system distinguishes between cancer cells and normal cells through the recognition of two types of tumor antigens, tumor-specific antigens (TSAs) or tumor-associated antigens (TAAs). While TSAs represent to the body unknown, exclusively cancer produced proteins, TAAs characterize by their expression of both cancerous and healthy cells, with TAAs being overexpressed in cancer cells¹¹. For most of the known tumor antigens, the major histocompatibility complex (MHC) class I on the cancer cell surface presents a small peptide of the processed tumor antigen for a subsequent recognition by CD8⁺ T cells^{12, 13}. The reason for the expression of these tumor antigens is the accumulation of a variable number of genetic alterations and the loss of normal cellular regulatory processes that associate with cancer¹⁴. In addition, the cancer complexity increases when a malignant tumor grows and spreads to other parts of the body. In the tumor microenvironment (TME), the conglomerations of transformed cells, blood vessels, fibroblasts, and immune cells, all excrete cytokines to facilitate tumor cell growth and impede anti-tumor immune activation. This immunosuppressive nature of the TME restrains the body's immune system to function optimally against the tumor cells on its own¹⁵. Therefore, various approaches aim to activate the patient's immune system under these conditions. For example, several cancer vaccines, monoclonal antibodies, immune checkpoint inhibitors, and cell-based therapies prove their efficacy in many patients¹⁶.

Where traditional cancer treatments fail, the efficacy of cancer immunotherapy exceeds the induction of strong anti-tumor immune responses by further controlling metastasis and hindering cancer recurrence^{17, 18}. Nevertheless, current cancer immunotherapy faces its limitations due to, for example, induction of destructive auto-immunity¹⁹, the immunosuppressive TME²⁰, and a sufficient delivery of cancer antigens to immune cells²¹. This is where nanotechnology offers several advantages to overcome these limitations.

1.2 Nanotechnology in cancer immunotherapy

Nanotechnology, defined as the investigation and utilization of structures between 1 and 100 nm in size²², has long entered the medical field, where its applications function as diagnosis, treatment, or prevention of diseases at tissue and cellular level²³. In the biological context, larger nanoparticles (200 – 2000 nm) are also utilized and show, e.g., a greater uptake in phagocytes²⁴. In the field of nanomedicine, diagnostics and therapy benefit from the nanomaterial's physicochemical properties and biological interactions. Accordingly, a variety of nanomaterials such as polymeric, organic, and inorganic nanoparticles or nanocarriers improve drug delivery by the possibility of surface modification, an enhanced drug stability *in vitro* and *in vivo*, as well as an increased therapeutic efficacy²⁵. Furthermore, the precise design of engineered nanocarriers potentially enable a controlled drug release to the target site with minimal interference of other cells and an early nanocarrier degradation (Figure 1.1)²⁶.

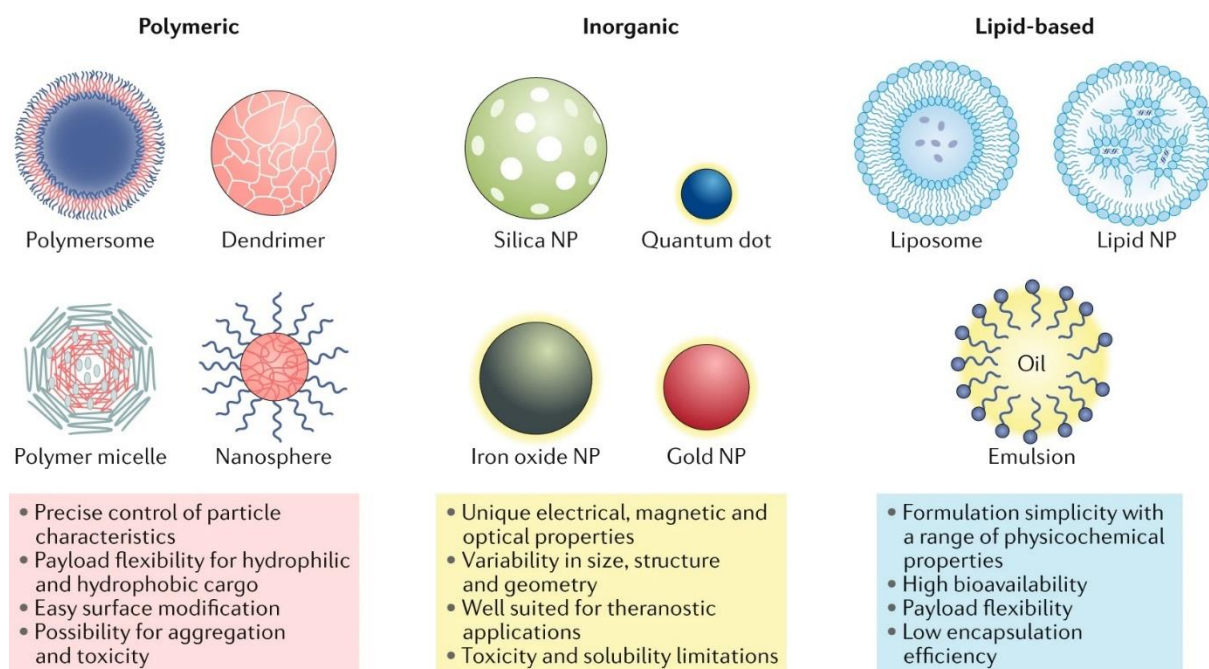


Figure 1.1: Frequently applied nanocarrier systems and their advantages and disadvantages regarding cargo, delivery, and patient response. Reprinted with permission from Mitchell *et al.*²⁶. Copyright © 2022, Springer Nature.

For example, medicinal applications include, the use of nanosystem-based contrast agents in molecular imaging for diagnostics, the thermal eradication of tumors applied in hyperthermia therapy, and the use of nanoparticles or nanocarriers for a cargo delivery of otherwise ineffectively soluble medications²⁷.

In the field of cancer treatment, nanocarriers are especially of interest due to the tumors' leaky vasculature enabling a passive entering and accumulation of the nanocarriers at the tumor tissue while avoiding healthy tissues²⁸. This phenomenon, namely the enhanced permeation and retention (EPR) effect, however, failed in clinical trials due to the inconsistency among different tumor types highlighted in the translation from animal tumor models to humans²⁹. Overall, the effectiveness of tumor targeting nanocarrier systems from pre-clinical studies over the past 10 years only shows a tumor accumulation of a median of 0.7% of the injected dose³⁰. Accordingly, many nanomedicines fail in the clinical trial³¹, with only a few exceptions, including an albumin-stabilized paclitaxel nanoparticle (ABRAXANE), or liposomal formulations of either doxorubicin (DOXIL) or irinotecan (ONIVYDE)³². Currently, many nanoformulations in clinical trials apply tumor-targeting ligands for a cell-selective drug delivery. As a result, the success of these targeted therapies must overcome the challenges of their failed precursors, which will enable their translation into the medical market. One of these great challenges, namely the influence of the nano-bio interface, including the role of the biomolecular corona on targeting³³ and drug release³⁴, must be addressed to understand the parameters for a successful clinical translation of nanotechnologies³².

1.3 The biomolecular corona on nanocarriers

Once introduced to the body, or any other biological system or fluid, nanocarriers alter their physicochemical properties (synthetic or chemical identity) via the rapid adsorption of biomolecules on their surface resulting in a distinct biological identity³⁵. Various factors influence this biological identity, which dictates the nanocarriers' interaction in the biological milieu with certain cell-types and the immune system³⁶. As a result, the biomolecular corona composed of proteins, lipids, sugars, and nucleic acids³⁷, changes the general pharmacological and toxicological profile of the nanocarrier and hence alters its diagnostic or therapeutic purpose³⁸. For example, transferrin-conjugated silica nanoparticles completely lose their targeting specificity when being incubated in serum (55% fetal bovine serum and human serum)³³. In addition, Dai *et al.* further emphasize the importance of the protein corona composition on the targeting ability of their polymer-coated silica nanoparticles decorated with antibody-mimetic ligands. In contrast to their pristine nanoparticles, the incubation with different human serum concentrations (10%, 50%, and 100%) dramatically decreased a

specific cancer targeting, whereas an artificial corona composed of only human serum albumin supported the targeting of the cancer cells³⁹.

Biomolecules interact with the nanocarrier surface spontaneously via attractive intermolecular forces, including Van der Waals, hydrogen bonding, electrostatic forces, and hydrophobic forces⁴⁰. In addition, these interactions dynamically alter over time with protein-to-surface binding and exchanging described by the Vroman effect⁴¹. In detail, the Vroman effect highlights the time-dependency of the adsorption process of blood components onto a surface. While small proteins with high diffusion rates and higher concentrations firstly encounter the surface, proteins with higher affinity to the nanocarrier surface gradually replace these initially bound proteins⁴² (Figure 1.2).

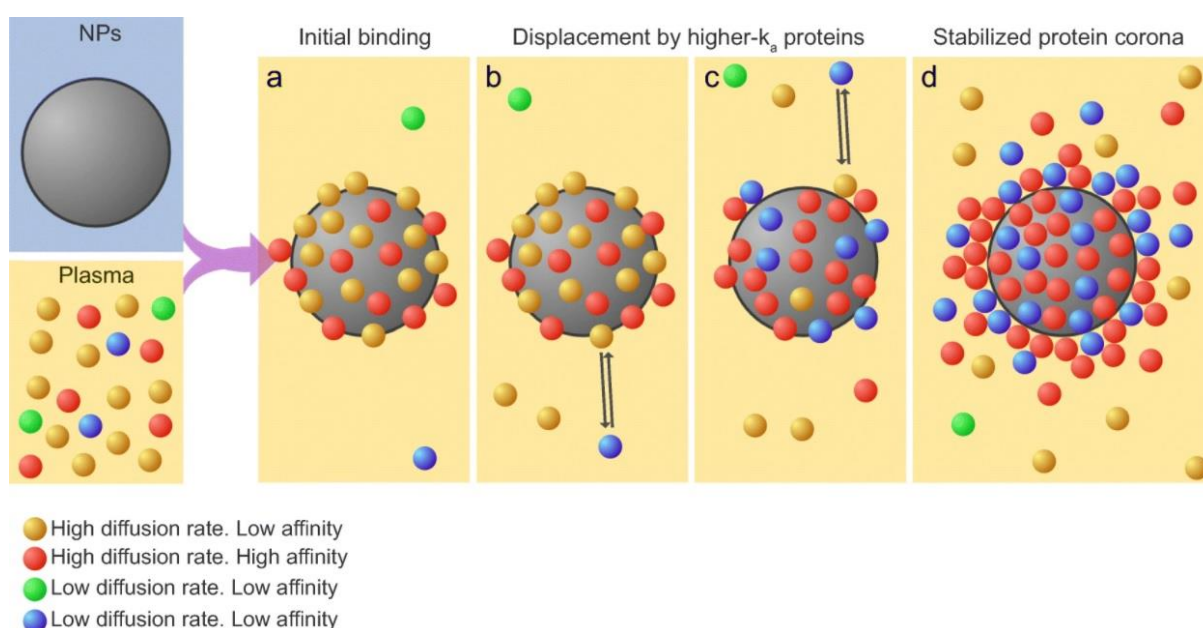


Figure 1.2: Mechanism of the protein corona formation. Proteins with high diffusion rates firstly adsorb onto the nanoparticle (NP) surface within a biological fluid like plasma (a). The exchange between firstly adsorbed proteins and the proteins with a higher affinity constant (k_a) occurs immediately (b). Thereby, the protein corona transforms (c) until reaching its equilibrium state (d). Reprinted with permission from Berrecoso *et al.*⁴⁰. Copyright © 2022, Springer Nature.

Consequently, the biomolecular corona represents an interchanging and complex network of rather loose proteins, referred to as the soft corona, and tightly bound proteins, namely the hard corona³⁵. Despite the versatile amount of different proteins in the human plasma (> 3700), biomolecules selectively form the corona. These mixtures are composed of around 100 – 300 proteins with 10 of them being abundantly detected⁴³. The time of a stable corona formation-process depends on the physicochemical characteristics of the nanocarrier system ranging from a few minutes⁴⁴ to more than hours⁴⁵. Once formed, the biomolecular corona remains intact for hours to days⁴⁶.

In the field of nanomedicine, especially in immunotherapy, the biomolecular corona dictates possible interactions with the immune system triggering certain immune responses. In particular, serum proteins acting as opsonins within the nanomaterials' corona can cause clearance and toxicity by interactions with phagocytes from the mononuclear phagocytic system (MPS) resulting in the recruitment of several immune responses. These immune responses include the secretion of interferons, interleukins, and tumor necrosis factors leading to inflammation or tissue damage⁴⁷. For example, the binding of fibrinogen from human plasma on poly(acrylic acid)-coated gold nanoparticles triggered conformational changes in the fibrinogen structure causing the misfolded protein to interact with the integrin receptor MAC-1, resulting in the activation of the inflammatory nuclear factor- κ B signaling pathway⁴⁸. Furthermore, in a comparison of 108 publications, the major nanomaterial-induced inflammatory mechanisms consist of interactions with toll-like receptors, the generation of oxidative stress, and inflammatory pathways⁴⁹. These outcomes directly correlate with the composition of the protein corona because macrophages from the MPS recognize the layer of specific opsonins and not the pristine nanomaterial⁵⁰. In fact, complement components and immunoglobulins, both representing opsonins that facilitate phagocytic recognition, belong to the most abundantly detected corona components⁵¹. Consequently, the biomolecular corona influences the nanocarriers' medical purpose by clearance through the MPS, a possible loss of the targeting ability through coverage of the targeting ligands, and adsorption of misfolded proteins triggering immune responses⁵².

1.4 Preparation and characterization of the biomolecular corona

As highlighted above, nanomedicine fails to reach the market in most cases because the *in vivo* corona unpredictably determines the fate of the nanocarriers. For this reason, the development of predictable systems to better assess the influence of the biomolecular corona and to improve the accuracy between *in vitro* and *in vivo* data is fundamentally important.

The current methodology of the biomolecular corona preparation and characterization divides into four sections. Those sections include the incubation with a biological media (step 1), the isolation of the corona from the nanocarrier (step 2), the detachment of the corona proteins from the nanosurface (step 3), and the analysis of the proteins (step 4) (Figure 1.3)⁴⁰. Each section needs precise considerations to reflect an unbiased imitation of the *in vivo* biomolecular corona to increase the clinical translation from *in vitro* to *in vivo* nanomedicines in humans.

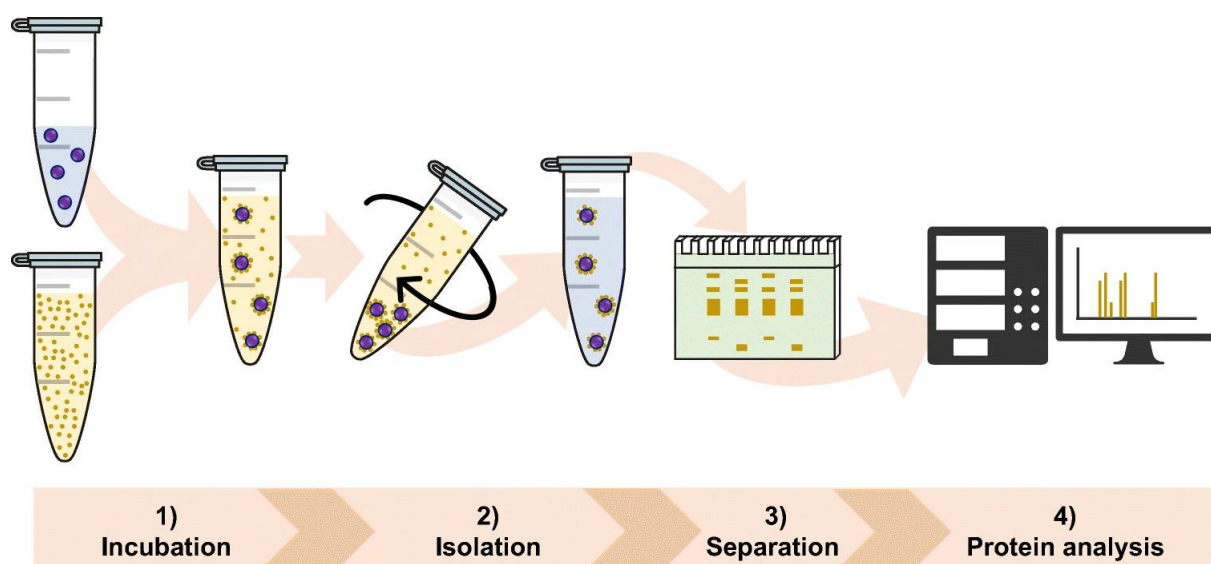


Figure 1.3: The preparation and characterization process of the *in vitro* protein corona divides into four steps. Reprinted with permission from Berrecoso *et al.*⁴⁰. Copyright © 2022, Springer Nature.

Selecting a proper biological media in the first step highly affects the composition of the protein corona. In particular, Müller *et al.* demonstrate that the adsorbed corona differs between the animal plasma sources used for the incubation⁵³. Their comparison further indicates that in studies on the influence of the corona, the plasma source should match the origin of cells and, when used in humans, include human plasma. In general, blood plasma represents a suitable choice of incubation source because serum and fetal bovine serum (FBS) lack coagulation proteins and the latter one causes interspecies differences³². Concerning blood plasma, the choice of an anticoagulant further dictates the corona formation process. Anticoagulants prevent blood clotting by intervening in different coagulation pathways altering the protein adsorption pattern on the surface. For example, the incubation of polystyrene nanoparticles in heparin-treated human plasma influences a discrimination in the uptake between macrophages and HeLa cells⁵⁴. A closer mimicking of the *in vivo* situation includes the use of agitation to imitate blood flow and shear stress on the nanoparticles⁴⁰.

In the second step, the isolation process of the nanocarrier-protein construct from unbound and free proteins commonly applies centrifugation or magnetic force as separation methods. During the isolation process, repeated washing and centrifugation or magnetic separations must ensure a total removal of excess proteins without interfering with the protein corona. For this isolation purpose, Kokkinopoulou *et al.* demonstrate that three washing steps are sufficient to separate the fractions from each other⁵⁵. Nevertheless, the parameters for the isolation procedure depend on the properties of the nanocarrier system. Therefore, further isolation techniques include asymmetric flow field-flow fractionation (AF4), size-exclusion chromatography (SEC), and capillary electrophoresis (CE)⁵⁶.

The third step deals with the separation of the protein corona from the nanocarrier surface via desorption or direct digestion. The desorption procedure commonly involves the use of a desorption buffer that contains sodium dodecyl sulfate (SDS) because of its strong protein solubilizing properties. Furthermore, acting as an anionic and denaturing surfactant, SDS detaches the biomolecular corona from the surface when being incubated for different time points (5 min – 2h), temperatures (50 – 95 °C), and SDS concentrations (2 – 20%)⁴⁰. Contrary, the less common direct digestion approach utilizes an enzymatic digestion, for example with immobilized trypsin⁵⁷, for the separation of the corona proteins.

Following both detachment procedures, the mixture of corona proteins and nanocarriers needs separation (usually centrifugation or magnetic force) for the subsequent identification and quantification of the protein corona. For this purpose, semi-quantitative methods like the polyacrylamide gel electrophoresis (PAGE) and a quantitative characterization by mass spectrometry analyze the composition of the protein corona in the fourth and final step. While the SDS-PAGE gives a first qualitative and visual analysis of the protein corona pattern based on the molecular weight, mass spectrometry quantitatively analyzes the corona. For instance, mass spectrometry analyzes the corona proteome effectively, even for low protein amounts, based on its broad range of molecular weights and isoelectric points^{40, 58}. In general, proteomics usually apply the bottom-up analysis where trypsin enzymatically cleaves the proteins into peptides, followed by their separation due to their chemical or physical characteristics measured by, for example, liquid chromatography mass spectrometry (LC-MS)⁵⁸. The output of the LC-MS data, namely the peptide spectra, require a proteomic software and a protein database, such as MASCOT, MS-FIT, and Swiss-Prot, to assign the peptides back to the initial protein⁵⁹.

2. Preparation of the Protein Corona: how Washing Shapes the Proteome and Influences Cellular Uptake of Nanocarriers

Copyright:

Being published in a peer-reviewed journal [1], this subchapter 2 represents an almost exclusive reproduction of the published text. Therefore, the presented results are reprinted with permission from Acta BioMaterialia. Copyright © 2022, Acta Materialia, Inc. Published by Elsevier Ltd. All rights reserved.

[1] **Maximilian Brückner***, Johanna Simon*, Shuai Jiang, Katharina Landfester, Volker Mailänder. Preparation of the protein corona: How washing shapes the proteome and influences cellular uptake of nanocarriers. Acta Biomaterialia, **2020**, 114, 333-342.

Aim:

A limited understanding of the nanocarriers' behavior in a complex biological environment currently hampers the successful application of nanocarriers as drug delivery vehicles. Once the nanocarrier comes into contact with blood plasma or serum, biomolecules rapidly adsorb onto their surface, covering the nanocarriers and forming a protein corona, which then dictates their biological identity. Analyzing the composition of this dynamic network of bound molecules, has already been shown to be influenced by various factors. However, the impact of the washing media used for the protein corona preparation has so far been neglected. In the present study, we demonstrate a quantitative influence of the washing media on the composition of the hard corona of different nanocarrier systems, which additionally affects protein stability and cellular uptake behavior.

Contribution:

I, Maximilian Brückner, performed the steps of the protein corona preparation on different nanocarrier systems with the eight washing media (Pierce Assay, SDS-PAGE) and all cell uptake experiments (cell culture and flow cytometry). In addition, I investigated the protein stability in the eight media by nanoDSF and measured the DLS. Dr. Johanna Simon analyzed the desorbed corona proteins by LC-MS. Katja Klein and Dr. Shuai Jiang synthesized the polystyrene and silica nanocarriers, respectively. Dr. Johanna Simon, Prof. Dr. Volker Mailänder, and Prof. Dr. Katharina Landfester supervised the project.

2.1 Abstract

A protein coat, termed the protein corona, assembles around the nanocarriers' surface once it gets in contact with a biological environment. We show that the media used for the washing of the protein corona can be crucial, especially for the downstream analysis as well as for the pre-coating used in *in vitro* or *in vivo*. However, this influence has been widely overlooked so far. In this paper, we focus on eight different washing media and analyze how they influence the composition of the hard protein corona of several nanocarriers incubated with human blood plasma and serum. SDS-PAGE and LC-MS analysis showed major differences in protein corona profiles when using diverse washing media. While plasma and serum proteins already have different complexities, each washing media changes the composition of proteins detected by downstream methods with different key proteins bound to the nanocarriers' surface. Furthermore, the protein structure of the most abundant blood proteins incubated in the different media was analyzed with nanoDSF. This analysis also emphasized the importance of the washing media, which had a significant influence on the protein adsorption stability. Lastly, cell uptake experiments for HeLa and RAW 264.7 macrophages also indicated an influence of the washing media. In conclusion, picking a specific washing media is on the one hand an important factor for downstream detection of protein compositions and may on the other hand be used to deliberately tune the protein corona for pre-adsorbed proteins from complex protein compositions. This media selection might further support a guided delivery of the nanocarrier to a desired location within a physiological environment.

2.2 Introduction

Even though nanocarriers have promising features as multifunctional therapeutic candidates for biomedical application, up to now the number of nanocarriers, which have reached clinical practice, is still very low. This is mainly based on the fact that there is a limited understanding and control of the nanocarriers' interactions with biological systems⁶⁰⁻⁶². Ultimately, after a nanocarrier has entered a physiological environment, proteins and other biomolecules rapidly interact with its surface, forming the so-called *biomolecular corona*⁶³. This alters the size and interfacial composition of a nanomaterial, providing it with a biological identity that is different from its synthetic identity⁶⁴. Therefore, it is the nanocarriers' protein corona, which will directly interact with cells and tissue, hereby influencing uptake, toxicity, and body distribution⁶⁵. Due to this confounding effect, precoating has also been used deliberately to tune the uptake into different cell types. Various factors have been shown to influence the composition of the protein corona. Those include, the physiochemical properties of a nanocarrier⁶² such as size, charge, hydrophobicity, and surface targeting and also the protein source in which the nanocarrier is incubated⁶⁶, the structure of the proteins⁶⁷, and the dispersion media⁶⁸, to name a few. All of these studies aim to understand the protein corona formation in order to predict the nanocarriers' behavior in a living organism and to finally enable their successfully clinical translation.

In many protein corona studies, a nanocarrier is introduced to a protein source, incubated for a defined time, and subsequently recovered via centrifugation, magnetic force or chromatographic techniques. Afterwards, several washing steps are performed in order to remove unbound proteins. In this case, the nanocarrier is coated with tightly bound proteins known as *hard corona*. In contrast to this, if the nanocarriers' behavior is analyzed directly within the protein source, its surface is additionally covered with a protein layer referred to as *soft corona* consisting of loosely bound proteins. However, the role of the soft corona is still under debate as it is highly dynamic and might be influenced by other factors such as shear force in a living organism⁶⁹. On the contrary, it is widely accepted that hard corona proteins dictate the physiological behavior of a nanocarrier⁷⁰.

Based on the importance of the hard corona in our studies, we specifically focused on its preparation procedure. After comparing literature reports from different research groups, we noticed that especially the washing media, which was used in the study, is either not specified or differs for each protocol. For example, Lundqvist *et al.* used polystyrene and silica nanocarriers for the formation of the protein hard corona in plasma (containing EDTA) and then cytosolic fluid to investigate the evolution of the protein corona from one biological fluid to another⁷¹. In their washing procedure, an EDTA buffer (10 mM phosphate, pH 7.5, 0.15 M

2. Preparation of the Protein Corona: how Washing Shapes the Proteome and Influences Cellular Uptake of Nanocarriers

NaCl, 1 mM EDTA) was applied. It was shown that through the transfer of nanocarriers from one into another biological fluid the final corona contains a “fingerprint” of its biomolecular history. Furthermore, in another report from Lundquist *et al.* a comparable washing buffer with a slightly lower pH of 7.4 was used to demonstrate the differences between protein sources applied for the corona generation and the influence of nanocarrier size in this process⁷². In contrast to this, Caracciolo *et al.* used a TRIS buffer (Tris-HCl, pH 7.4, 10 mmol/L; NaCl, 150 mmol/L; EDTA, 1 mmol/L) to investigate the protein corona formed around lipid and silica nanocarriers⁷³. Their proteomic approach identified immunoglobulins, complement factors, and coagulation proteins to be enriched in the protein corona. Additionally, by investigating the difference between *in vitro* and *in vivo* mouse protein corona formed around liposomes, Hadjidemetriou *et al.* integrated a HEPES based buffer (20 mM HEPES, 150 mM NaCl, pH 7.4) into the washing procedure⁷⁴. In the majority of corona studies, Dulbecco’s phosphate-buffered saline (PBS) is applied, although the composition of the PBS is not always mentioned, *i.e.*, with or without CaCl₂ and MgCl₂⁷⁵⁻⁸⁰. Besides PBS, other washing media are utilized. Those include water or diverse washing buffers containing different salts, chelating, and buffer agents⁷¹⁻⁷⁴.

Based on the diversity of protein corona protocols, it was our goal to determine the influence of different washing solutions on the corona composition and the further cell uptake behavior. Therefore, we chose eight washing conditions which are most commonly used in the current literature. Those include commercially available reagents like PBS with (++) and without (-) CaCl₂ and MgCl₂, water, Dulbecco’s modified eagle medium (DMEM) as well as buffers like Tris-buffered saline (TBS), HEPES-buffered saline (HBS), phosphate-buffered saline (P), and P with EDTA (P+E), all adjusted to a pH of 7.4 (see Figure 2.S1 for detailed information). In our study, we analyzed a variety of different nanocarriers including inorganic, silica, and polymer-based materials. Here, we show that the choice of the washing media has a major impact on the final hard corona composition. Furthermore, we prove that those differences influence the cellular uptake behavior towards immune and cancer cells. Overall, this underlines the urgent need for standardized protocols to get meaningful and comparable protein corona data.

2.3 Material and Methods

Nanocarrier systems. Magnetic nanocarriers (BNF-Starch-redF, plain) with a solid content of 10 mg mL⁻¹ and a size of 100 nm were purchased from micromod Partikeltechnologie GmbH Germany. The three polystyrene nanocarrier systems (20 mg mL⁻¹, ranging around 122 – 124 nm) were stabilized with the surfactant Lutensol-AT50 (BASF) and synthesized according to an established standard protocol using free-radical miniemulsion polymerization^{55, 81}. For cell uptake targeting, BODIPY (523 nm/536 nm) was internalized into the polystyrene nanocarriers⁸². Silica nanocapsules, consisting of an oil core and having a diameter of roughly 200 nm, were synthesized by using a modified protocol from our previous study⁸³. Cationic surfactant CTAC was used to stabilize the miniemulsion droplets as well as a templating agent to confine the silica deposition at the oil/water surface. The nanocapsules were PEGylated by exchanging the templating surfactant CTAC with the nonionic surfactant Lutensol-AT50.

Dynamic light scattering. Dynamic light scattering analysis was performed on a Zetasizer Nano S90 DLS system equipped with a 4mW 632.8nm red laser. Results represent the average of three consecutive measurements. The laser power settings and the number and duration of the acquisitions for each measurement were set automatically by the software (Zetasizer Software 7.12). The nanocarriers (mgHES, PS-COOH) were measured in the respective media (see Figure 2.S1) at 25 °C with scattered light detected at a 90° angle. Magnetic nanocarriers (mgHES) were measured in a concentration of 0.1 mg mL⁻¹ and polystyrene nanocarriers (PS-COOH) in a concentration of 0.2 mg mL⁻¹. The data was collected and processed using the same Zetasizer Software. Average particle sizes are reported based on the weighted intensity of the scattered light.

Human blood plasma and serum. Human blood was obtained from seemingly healthy donors in accordance with the Declaration of Helsinki by plasmapheresis from the Department of Transfusion Medicine Mainz. For the plasma probes, citrate was added as an anticoagulant. The serum was generated by overnight blood clotting according to the standard protocol to generate human serum. A plasma pool from ten volunteers and a serum pool from seven volunteers was used and stored at -80 °C (long-term storage).

Protein corona preparation. The protein source of either human citrate plasma or serum (kept at -80 °C for long-term storage and transferred to -20 °C prior to the experiments) was centrifuged at 20.000 g for 30 min at 4 °C and then the supernatant was used for the experiments. For the protein adsorption, 0.05 m² of nanocarriers (polystyrene nanocarriers and silica nanocapsules) or 1 mg of magnetic nanocarriers were mixed in a total volume of 300 µL H₂O, and 1 mL of either citrate plasma or serum was added into protein low binding tubes (Eppendorf, Germany). After an incubation period of 1 h, while shaking at a temperature of

2. Preparation of the Protein Corona: how Washing Shapes the Proteome and Influences Cellular Uptake of Nanocarriers

37 °C, the protein source was removed using centrifugation (always 20.000 g, for 1 h at 4 °C) or magnetic force (strong neodymium magnet, Germany). The subsequent washing step (with one of the eight media) was repeated three times with 1 mL respective media (again using either centrifugation or magnetic force). For protein corona analysis, the protein corona containing nanocarriers were separated by centrifugation/magnetic force from the respective media and resuspended in 100 µL desorption buffer (2% (w/v) SDS + 62.5 mM Tris-HCl in 3 mL Ampuwa[®] injection water). After incubating for a period of 5 min, while shaking at a temperature of 95 °C, the protein corona was separated from the nanocarriers by centrifugation (20.000 g, 1 h, 4 °C) or magnetic force.

Protein quantification. The protein quantification of desorbed hard corona proteins was quantified with Pierce 660 nm Assay (Thermo Scientific, Germany) according to the manufacturer's instructions. Bovine serum albumin (BSA) was used as a standard (Serva, Germany). The absorption was measured at 660 nm with a Tecan infinite M1000 plate reader.

IgG quantification. The IgG from human serum (Sigma-Aldrich, Germany) was dissolved at a concentration of 10.5 mg mL⁻¹ in Ampuwa[®] injection water containing 150 mM NaCl. For the IgG adsorption, 200 µg of nanocarriers (PS-COOH and mgHES) were mixed in a total volume of 60 µL in Ampuwa[®] injection water, and 0.2 mL of IgG solution were added into protein low binding tubes (Eppendorf, Germany). After an incubation for a period of 1 h, while shaking at a temperature of 37 °C, the IgG solution was removed involving the use of centrifugation (20.000 g, for 1 h at 4 °C) or magnetic force (strong neodymium magnet, Germany). The subsequent washing step with either LC-MS H₂O or PBS⁻ was repeated three times with 0.2 mL of respective media (again using either centrifugation or magnetic force). For protein corona analysis, the protein corona containing nanocarriers were separated by centrifugation/magnetic force from the respective media and resuspended in 50 µL desorption buffer (2% (w/v) SDS + 62.5 mM Tris-HCl in 3 mL Ampuwa[®] injection water). After incubating for a period of 5 min, while shaking at a temperature of 95 °C, the protein corona was separated from the nanocarriers by centrifugation (20.000 g, 1 h, 4 °C) or magnetic force. The total IgG amount was quantified with Pierce 660 nm Assay (Thermo Scientific, Germany) according to the manufacturer's instructions. IgG from human serum was used as a standard. The absorption was measured at 660 nm with a Tecan infinite M1000 plate reader.

Nanocarrier quantification. To determine the amount of nanocarriers after the protein corona formation (3x washing), a fluorescence calibration of the nanocarrier was conducted. The untreated nanocarriers were utilized as a standard to determine the concentration of the nanocarriers containing a hard corona. All probes, including the standard, were prepared in deionized water. The fluorescence was measured by the Infinite M1000 plate reader (Tecan) with an excitation wavelength of 552 nm and emission of 580 nm for the magnetic nanocarriers

2. Preparation of the Protein Corona: how Washing Shapes the Proteome and Influences Cellular Uptake of Nanocarriers

(BNF-Starch-redF, plain) and an excitation wavelength of 523 nm and emission of 535 nm for the polystyrene nanocarriers (BODIPY).

SDS-PAGE. The protein sample (2 μg in 26 μL total volume) was mixed with 4 μL of NuPage Reducing Agent and 10 μL of NuPage LDS Sample Buffer, loaded on a 10% Bis-Tris-Protein Gels using NuPAGE MES SDS Running Buffer (all Novex, Thermo Fisher Scientific) and run as usual for 1.5 h using SeeBlue Plus2 PreStained (Invitrogen) as a molecular marker. The marker consists of myosin (198 kDa), phosphorylase (98 kDa), BSA (62 kDa), glutamic dehydrogenase (49 kDa), alcohol dehydrogenase (38 kDa), carbonic anhydrase (28 kDa), myoglobin red (17 kDa), lysozyme (14 kDa), aprotinin (6 kDa), and insulin B chain (3 kDa). Silver staining (Thermo Scientific, Germany) was used to visualize protein band migration on the gels according to the manufacturer's instructions.

Nano differential scanning fluorimetry (nanoDSF). Proteins (human serum albumin from human plasma and IgG from human serum, all Sigma, 1 mg mL^{-1} in respective buffer) were transferred into nanoDSF High Sensitivity capillaries (NanoTemper Technologies) and inserted into a Prometheus NT-48 instrument. A linear thermal ramp program starting at 20 $^{\circ}\text{C}$ to 95 $^{\circ}\text{C}$ (1 $^{\circ}\text{C min}^{-1}$) was set and the tryptophan fluorescence was measured at 330 and 350 nm. The thermal unfolding curves of the first derivative of the fluorescence ratio (350 nm/330 nm) were plotted against the temperature. The melting temperature T_m was determined from the minimum of the first derivative.

In solution digestion. For LC-MS analysis, all investigated washing conditions were handled as technical triplicates. This means, for example, that from one incubation (nanocarrier plus human plasma or serum, followed by the three washing steps, and the final protein desorption) three LC-MS sample injections were used. From these protein solutions, the SDS was removed by applying Pierce detergent removal columns (Thermo Fisher, Germany). The digestion was based on previously established protocols^{84, 85}. In summary, the proteins were precipitated overnight using the ProteoExtract protein precipitation kit (CalBioChem, Germany) according to the manufacturer's instructions. The protein isolation was performed by centrifugation (14.000 g, 10 min), followed by several washing steps and resuspension in RapiGest SF (Waters Cooperation, Germany) dissolved in ammonium bicarbonate (50 Mm) buffer. The samples were incubated at 80 $^{\circ}\text{C}$ for 15 min. Dithiothreitol (Sigma, Germany) was used at a final concentration of 5 mM to reduce protein disulfide bonds. The reaction was executed for 45 min at 56 $^{\circ}\text{C}$. The alkylation of proteins with iodoacetamide (final concentration 15 mM, Sigma, Germany) was carried out in the dark for 1 h. A protein-to-trypsin ratio of 50:1 was chosen for the digestion, and the reaction was performed for a period of 14 h at 37 $^{\circ}\text{C}$. The reaction was quenched by adding 2 μL hydrochloric acid (Sigma, Germany). Finally, the

2. Preparation of the Protein Corona: how Washing Shapes the Proteome and Influences Cellular Uptake of Nanocarriers

degradation products of RapiGest SF were removed by centrifugation of the peptide samples at 14.000 g for 15 min (4 °C).

Liquid chromatography-electrospray ionization mass spectrometry (LC-MS). For sample preparation, all specimen were diluted with 0.1% formic acid and spiked with 50 fmol μl^{-1} Hi3 *E. coli* standard (Waters Cooperation) for absolute protein quantification⁸⁶. The tryptic peptides were transferred to a C18 analytical reversed phase column (1.7 μm , 75 μm x 150 mm) and a C18 nanoACQUITY trap column (5 μm , 180 μm x 20 mm) in a nanoACQUITY UPLC system. For the separation, two mobile phases with (A) consisting of 0.1% (v/v) formic acid in water and 0.1% (v/v) formic acid with acetonitrile and a gradient of 2% to 37% of mobile phase (B) were applied for a time period of 70 min. A Synapt G2-Si mass spectrometer was connected to the nanoACQUITY UPLC system and the electrospray ionization (ESI) was performed in positive ion mode using a NanoLockSpray source. A sample flow rate of 0.3 $\mu\text{l min}^{-1}$ was selected and Glu-Fibrinopeptide, as a reference component, was infused with 150 fmol μl^{-1} at a flow rate of 0.5 $\mu\text{l min}^{-1}$. Resolution mode was chosen for operating the Synapt G2-Si and data-independent acquisition (MSE) experiments were conducted. The data was acquired for a time of 90 min with a mass to charge range of 50 – 2000 Da, a scan time of 1 s and ramped trap collision energy from 20 to 40 V. The data acquisition and the processing were performed using the MassLynx 4.1.

Protein identification. The continuum data was corrected post lock mass and further processed by Progenesis QI, (2.0) applying a reviewed human data base (Uniprot) for the identification of peptide and protein. For the noise reduction thresholds, several processing parameters for low energy, high energy, and peptide intensity were set to 120, 25, and 750 counts. The Hi3 *E. coli* standard sequence information was added to the human data base for absolute quantification. The identification of protein and peptide was based on the following criteria: one missed cleavage, maximum protein mass 600 kDa, fixed carbamidomethyl modification for cysteine, variable oxidation for methionine, and protein false discovery rate of 4%. For the identification of protein, at least two assigned peptides and five assigned fragments are required. The identification of peptide relies on three assigned fragments. Identified peptides, which showed a score parameter below 4, were discharged. The amount of each protein in fmol was provided based on the TOP3/Hi3 approach⁸⁷.

Processing of LC-MS data into figures. For the processing of LC-MS data into figures, all detected proteins were first sorted. For this selection, the proteins with a unique peptide value of 1 or less were sorted out. Furthermore, contaminations like keratins, from the user, and trypsin, used for sample preparation, were also removed⁸⁸. On the mgHES nanocarrier, the initially 191 proteins detected were sorted in this way to 109 proteins (82 proteins were sorted out). For the PS-COOH nanocarrier, the 240 proteins detected were sorted out to 142 proteins

2. Preparation of the Protein Corona: how Washing Shapes the Proteome and Influences Cellular Uptake of Nanocarriers

(98 proteins were sorted out). Based on the amount in femtomole, the sum of each individual condition was determined and then each value was converted into a percentage (femtomole value divided by the sum of all detected proteins times 100). Then, the mean value of the three percentages determined for each condition was calculated. UniProt was used to divide the individual proteins into different groups depending on their biological function (Figure 2.2B and 2.2D, Figure 2.S10). If no annotation for a protein was noted, the protein was assigned to the other plasma component group. For the generation of plasma or serum heat maps, the data was size sorted to the top 20 proteins in a descending order for each of the eight washing media. Accordingly, this resulted in the generation of eight top 20 protein lists (160 proteins in total). These lists were then processed by sorting out all redundantly appearing proteins. Afterwards, the resulting list of most abundant proteins for each condition was sorted alphabetically. The mgHES list of plasma proteins was sorted from 160 to 45 proteins and the list of serum proteins from 160 to 36 proteins (see Figure 2.3). The PS-COOH nanocarrier list of plasma proteins was sorted from 160 to 29 proteins and the list of serum proteins from 160 to 29 (see Figure 2.4). For the visualization of each list of most abundant proteins, heat maps were generated by using GraphPad Prism 8 conditional formatting 3-color scale formula selecting a minimum, midpoint, and maximum.

Cell uptake experiments by flow cytometry and data analysis. Human HeLa cells were cultured in Eagle's Minimum Essential Medium (EMEM) supplemented with 10% FBS, 100 U mL⁻¹ penicillin, 100 mg mL⁻¹ streptomycin, and 2 mM glutamine (all Invitrogen, Germany). The murine macrophage RAW 264.7 cells were maintained in Dulbecco's modified eagle medium (DMEM/Thermo, USA), supplemented with 10% FBS, 100 U mL⁻¹ penicillin, 100 mg mL⁻¹ streptomycin, and 2 mM glutamine. For the cell uptake experiments, cells (each condition in triplicates) were seeded at a density of 150.000 cells per well in 24 well plates and grown overnight in an incubator C200 (Labotect, Germany) at 37 °C and 5% CO₂ humidity. The next day, the cells were incubated in fresh serum-free medium for 2 h, before the nanocarrier dispersions were added at a concentration of 75 µg mL⁻¹ to the cells. Hard protein corona coated nanocarriers were prepared as described above (Protein corona preparation). Therefore, the nanocarriers were first incubated with human plasma or serum, centrifuged (20.000 g, 1 h, 4 °C), and washed three times with 1 mL of the respective media to remove unbound proteins. Protein coated nanocarriers were resuspended in serum free medium (final concentration: 75 µg mL⁻¹) and incubated with the HeLa cells for 4 h and for 2 h with the RAW 264.7 cells. For the flow cytometry experiments, the treated cells were washed with PBS⁻ (Sigma, Germany) and detached from the well with Trypsin-EDTA (Thermo, Germany). Measurements were performed on an Attune™ NxT cytometer (Thermo, Germany) with a 561 nm laser for excitation of mgHES (redF) and a 585/16 nm band pass filter for emission detection. The data analysis was conducted using the Attune™ NxT software (ThermoFisher

2. Preparation of the Protein Corona: how Washing Shapes the Proteome and Influences Cellular Uptake of Nanocarriers

Software, USA), selecting the cells with a FSC/SSC plot, thereby excluding cell debris. The gated cell events were analyzed by the fluorescent signal (YL1) expressed as the median fluorescence intensity (MFI). The mean MFI of the cell auto-fluorescence ($n = 3$) was subtracted from each value. Then, the mean value of the MFI of each sample ($n = 3$) was correlated with the mean value of the MFI of the control without a protein corona ($n = 3$) to generate a relative MFI value. For this purpose, the mean of the MFI of each sample was divided by the mean of the control minus one. The control itself was accordingly divided by itself minus one which generates it to zero. Positive values indicate an uptake while negative values represent less uptake by cells in regard to the control.

Statistical Analysis. For the cell uptake experiments, using GraphPad Prism 5, one-way analysis of variance (ANOVA) was performed with a Tukey's multiple comparison test, choosing a confidence interval of 99.9% ($P < 0.001^{***}$) significance. For the quantification of total IgG, using the GraphPad Prism 8, an unpaired t test was conducted, choosing a confidence interval of 99.9% ($P > 0.001^{***}$) significance.

2.4 Results and Discussion

Our general protocol for the protein corona analysis was as follows (Figure 2.1): nanocarriers were incubated in human citrate plasma or serum, followed by washing with one of the eight washing media for three times. Depending on the nanocarrier system, the separation of protein hard corona of the different nanocarriers was investigated qualitatively using the SDS-PAGE and quantitatively using the LC-MS. Cellular uptake experiments with human HeLa cells and murine RAW 264.7 macrophages were conducted to investigate the biological influence of the hard corona. In order to present a clearer image, a special focus was set on nanoferrite nanocarriers, which have a surface of cross-linked starch (mgHES) without any functional groups as they can be prepared by centrifugation and magnetic separation. Results for additionally tested nanocarrier systems can be found in the supporting information (Figure 2.S2 – 2.S11, and Table 2.S1 and 2.S2).

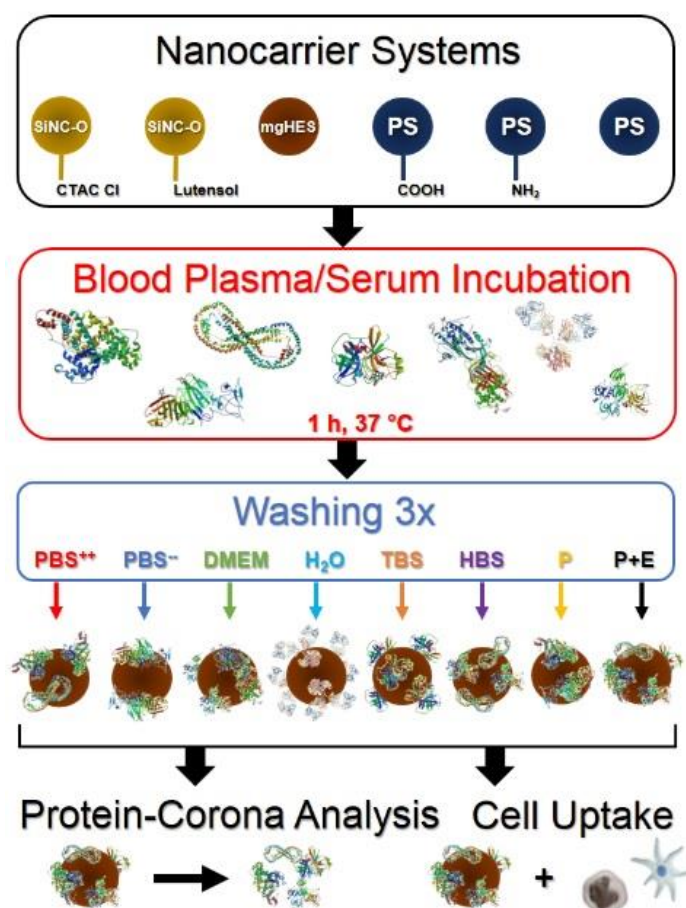


Figure 2.1: Workflow of Protein Corona Analysis. Different nanocarrier systems were incubated in human citrate plasma or serum followed by three successive washing steps with eight commonly used washing media. Afterwards, the samples underwent a protein corona analysis via Pierce 660 nm assay, SDS-PAGE, silver staining, and LC-MS, as well as cellular uptake experiments towards human HeLa and RAW 246.7 macrophage cells. Protein crystal structures were taken from the RCSB Protein Data Bank. Images are not for scaling.

Analysis of Corona Proteins

Overall, the composition of corona proteins was qualitatively visualized using the SDS-PAGE and quantitatively analyzed using the LC-MS. In Figure 2.2, results are exemplary shown for mgHES nanocarriers. Using the SDS-PAGE, the major impact of the chosen washing media becomes quite clear (Figure 2.2 A, C).

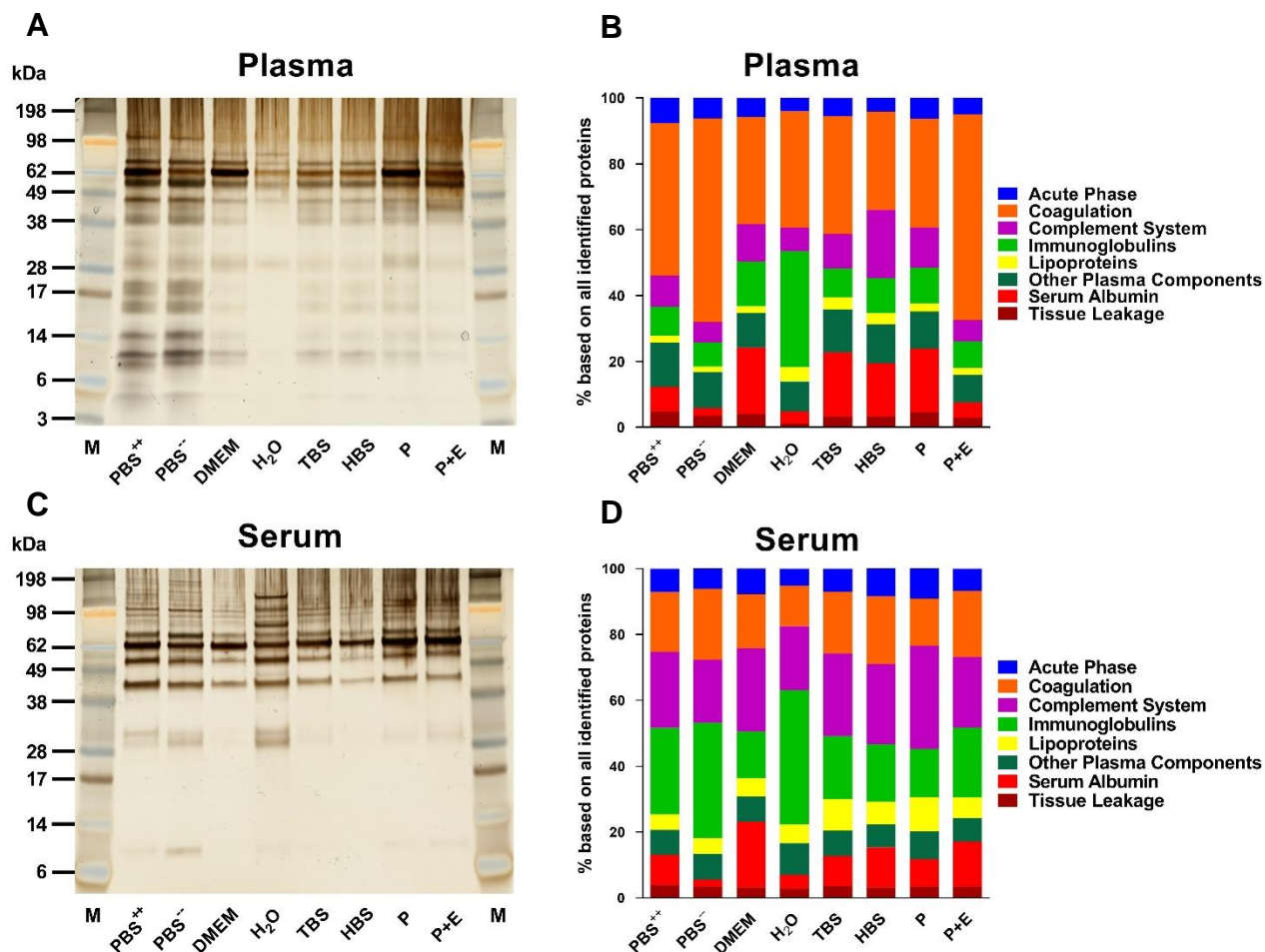


Figure 2.2: Protein Corona Analysis of mgHES by SDS-PAGE and LC-MS. After the incubation of blood plasma/serum and washing, the proteins were desorbed and separated from the nanocarrier by desorption buffer and magnetic force. Afterwards, the protein quantification was measured by Pierce 660 nm assay and 2 μ g of protein corona samples and 5 μ L of marker (M) were applied for SDS-PAGE (run for 110 min at 100 V) followed by silver staining. A and C show the results of the protein coronas of the nanocarriers with eight different washing solutions in citrate plasma and serum, respectively. In B and D, the percentage based on all identified proteins of both citrate plasma and serum, respectively, analyzed by LC-MS is shown ($n = 3$, technical replicates).

Strikingly, washing with H₂O results in an altered protein corona composition compared to the other media. As already investigated in literature, changing the nanocarrier system and thereby its composition and surface the chemistry leads to different protein adsorption profiles⁸⁹. Therefore, we additionally used silica and polystyrene based nanocarriers for our study. For all investigated nanocarriers, a significant effect of at least one of the chosen washing media

2. Preparation of the Protein Corona: how Washing Shapes the Proteome and Influences Cellular Uptake of Nanocarriers

was found (Figure 2.S2 – 2.S9). Furthermore, LC-MS analysis provided a quantitative insight into the exact protein corona composition. All identified proteins were further grouped into eight different classes. In general, there is a significant difference between plasma (Figure 2.2 B) and serum (Figure 2.2 D) incubation, which is also known from other literature reports. After the incubation of the serum, there is an increased amount of complement proteins detected in the corona of mgHES regardless of the chosen washing media. In contrast, after the incubation of the plasma, we found higher amounts of proteins, which were involved in the coagulation cascade. The complement and coagulation system function as multi-component protein networks, which protect the human body against pathogens or other invaders (e.g. nanocarriers) to ensure a successful host immune defense⁹⁰. Therefore, using anti-coagulated blood plasma, where the complexation of the calcium ions by citrate prevents complement activation, and serum, where the coagulation factors are depleted, enable the investigation of protein candidates for an artificial protein corona.

When comparing the corona composition for the eight washing media individually, quantitative differences between the protein groups are visible. For example, washing with water results in an enrichment of immunoglobulins that does not occur in any other group for plasma.

For a more detailed analysis, the most abundant proteins are highlighted in heat maps (Figure 2.3). In case of the plasma proteins (Figure 2.3 A), the by far most abundant protein found in each washing group is kininogen-1. However, its abundance varies between the different washing conditions. In general, kininogen-1 participates in the regulation of coagulation and platelet function⁹¹ and has also been detected as the most abundant corona protein for dextran-coated superparamagnetic iron oxide (SPIO) nanocarriers⁹². Regarding an artificial protein corona, kininogen-1 could be attached to the nanocarrier surface to transmit its functionality. For example, Jinfang Xu *et al.* show that the overexpression of kininogen-1 suppresses glioma progression by inhibiting the proliferation and promoting apoptosis of glioma cells⁹³.

Next to this, washing dependent alterations were also identified for serum albumin, plasma kallikrein, ceruloplasmin, and others. Especially, the washing with H₂O showed a higher enrichment of Ig kappa chain C region compared to the remaining washing media.

In general, the serum corona (Figure 2.3 B) mainly consisted of immunoglobulins, complement, and coagulation proteins. After washing with H₂O and PBS⁻, we detected higher amounts of Ig kappa chain C region and Ig mu chain C region in the protein corona, while the DMEM washing favored a strong binding of serum albumin. Among the detected proteins, the complement component C3 was highly enriched in the serum protein coronas for all washing

2. Preparation of the Protein Corona: how Washing Shapes the Proteome and Influences Cellular Uptake of Nanocarriers

conditions when compared to plasma protein coronas. It has been shown that the C3 binding to dextran-coated SPIOs favors their recognition by macrophages and leukocytes⁹⁴.

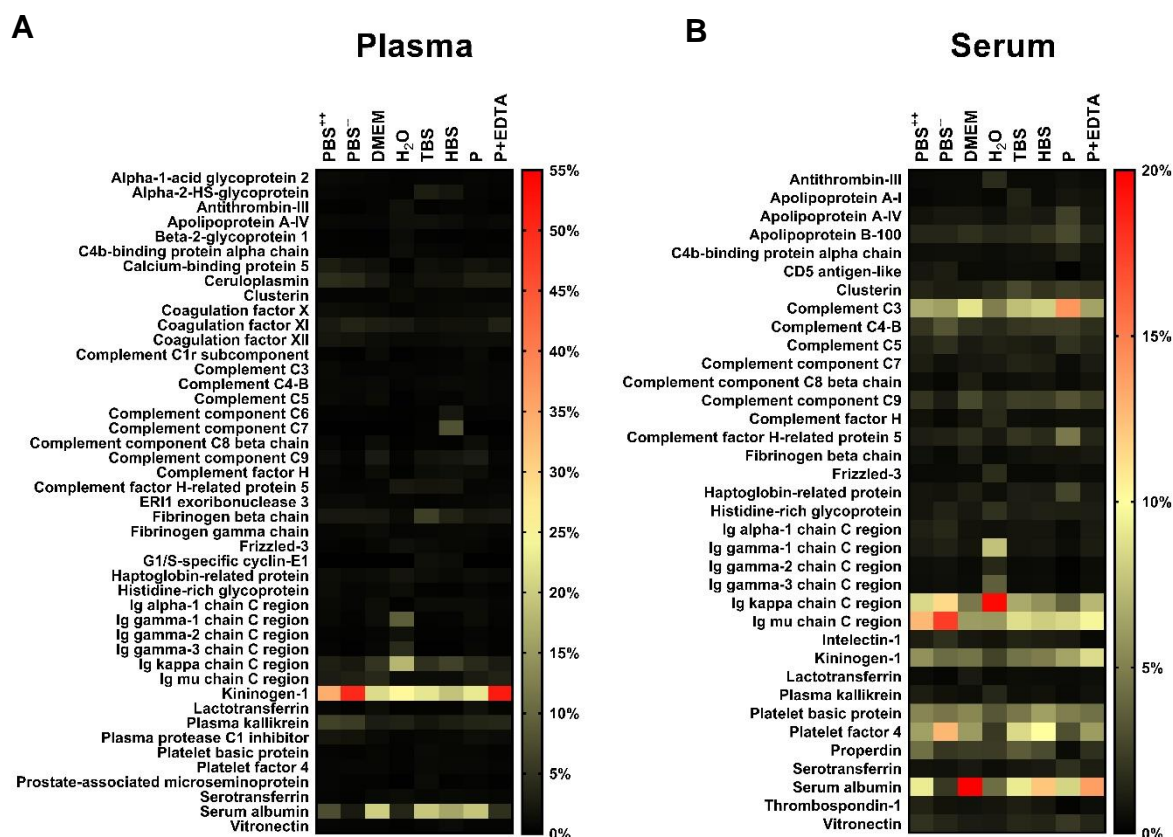


Figure 2.3: Washing Media Influences the Protein Corona Composition of mgHES Nanocarriers. Plasma and serum heat maps of the most abundant corona proteins are shown. Criteria for heat map generation are described in the material and method section. The values are expressed in percentage based on the total amount of all identified proteins ($n = 3$, technical replicates).

Exemplary shown for another nanocarrier type, the most abundant corona proteins for PS-COOH nanocarriers are summarized in heat maps in Figure 2.4. In general, similar trends were observed for the different washing media. Again, after washing with H₂O a strong enrichment of Ig gamma-1 chain C region and Ig kappa chain C was detected. The amount of the other most abundant corona proteins such as apolipoprotein E, beta-2-glycoprotein 1, clusterin, and vitronectin varied quantitatively for each washing condition as shown for mgHES nanocarriers.

In our previous studies, in which we used polystyrene (PS) nanocarriers with different surface functionalization (PS-plain, PS-NH₂, PS-COOH), vitronectin and clusterin also belonged to the most abundant corona proteins⁹⁵. While we have noticed that clusterin plays a crucial role in the mechanism of conveying stealth properties to PEGylated PS nanocarriers⁹⁶, vitronectin, on the other hand, has been shown to be involved in the nanocarrier cell surface interactions modulating fibroblasts viability and proliferation⁹⁷.

2. Preparation of the Protein Corona: how Washing Shapes the Proteome and Influences Cellular Uptake of Nanocarriers

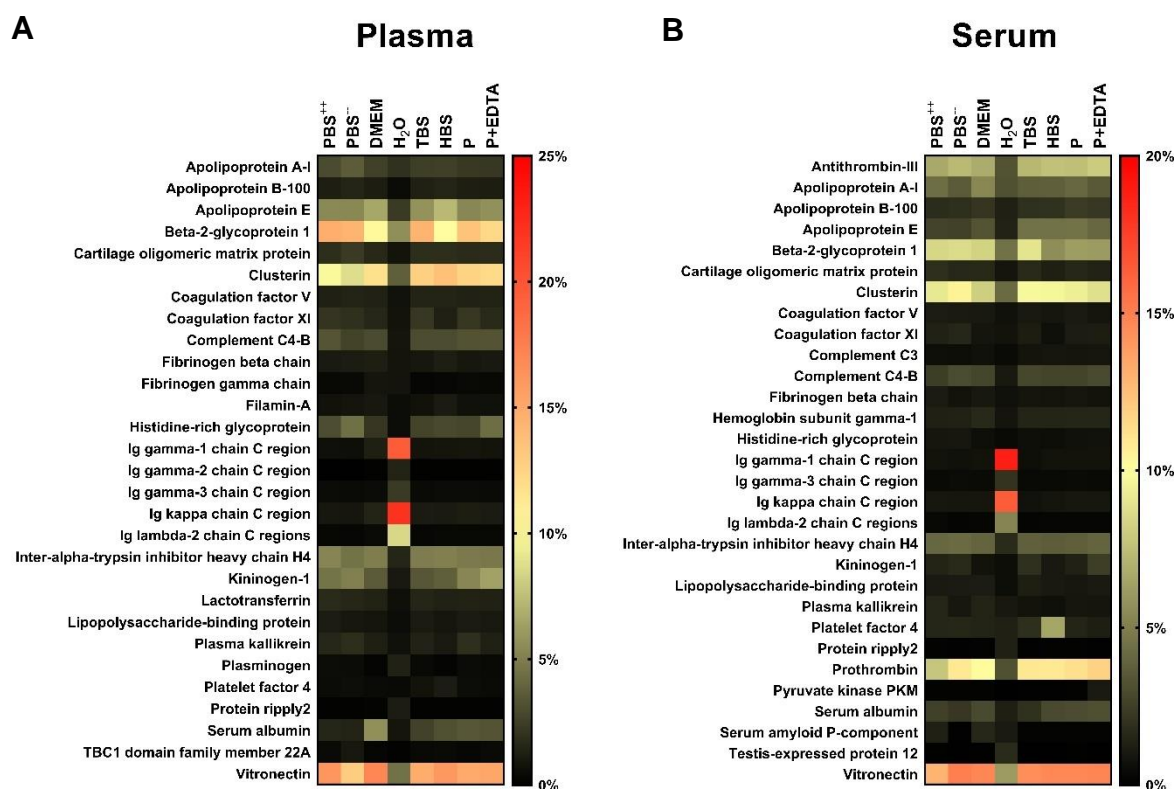


Figure 2.4: The Choice of Washing Media also Affects the Protein Corona Composition of PS-COOH Nanocarriers. Plasma and serum heat map of the most abundant corona proteins are shown. The criteria for the heat map generation is described in the material and method section. The values are expressed in percentage based on the total amount of all identified proteins ($n=3$, technical replicates).

Nevertheless, the set of adsorbed proteins that we detected for each washing condition could additionally be influenced by the nanocarrier concentration. In fact, Fedeli *et al.* demonstrate a correlation between the amount of nanocarriers and a variable protein pattern. Consequently, lower concentrations of their silica nanocarriers ($20, 40 \mu\text{g mL}^{-1}$) ended up with a homogeneous hard corona, whereas higher concentrations ($80, 160 \mu\text{g mL}^{-1}$) resulted in a heterogeneous hard corona⁹⁸. Moreover, Gunnarsson *et al.* also report about the importance of the nanocarrier concentration and surface area compared to aggregates that form during the shaping of the biomolecular corona^{99, 100}. In our size characterization analysis of the nanocarriers in the eight different washing media, we show that the hydrodynamic radii measured by dynamic light scattering (DLS) can be influenced by the washing procedure (SI Table 2.S1 and 2.S2). According to our results, this depends on the physicochemical properties of the nanocarrier as only the mgHES dispersed in water differs from the sizes measured in the other seven media (Table 2.S1). In addition, the hydrodynamic radii of PS-COOH nanocarriers are not influenced by any of the eight washing media. Being dispersed in water, the hydrodynamic radius of mgHES is observed to be twice as large ($356.5 \pm 7.19 \text{ nm}$) as being dispersed in one of the other media ($\sim 163.7 \text{ nm}$ for the other seven). We wondered if this might be due to the

2. Preparation of the Protein Corona: how Washing Shapes the Proteome and Influences Cellular Uptake of Nanocarriers

aggregation and performed the DLS measurement over time (Table 2.S2). Here, we show that mgHES nanocarriers do not increase in size, as it would be expected from aggregation, but rather decrease into an equilibrium state. Therefore, being dispersed in water, magnetic nanocarriers might form sphere-like trimers, which get stabilized while being incubated in a protein rich environment. This phenomenon was also observed by Gunnarsson *et al.* investigating the gold nanoparticle aggregation in cell culture media⁹⁹.

In order to support the reproducibility of the LC-MS findings, particularly the effect of washing with water, we additionally performed a quantification experiment. For this purpose, we picked the IgG from human serum as a protein source because only the hard corona of water washed nanocarriers is enriched with IgG molecules and incubated it with mgHES and PS-COOH to compare the total IgG amount after washing with H₂O and PBS⁻. We selected an IgG concentration (10.5 mg mL⁻¹) comparable to that of human plasma and serum^{101, 102} and incubated it with the two nanocarriers (see material and methods for a detailed experimental setup). After the three washing steps with H₂O and PBS⁻, the IgG hard corona was removed from the nanocarriers and quantified by Pierce. In the supporting information, the result of this experiment is shown in Figure 2.S12. According to our data, we show that washing with H₂O has a significant effect on the amount of IgG that remains on the nanocarriers compared to washing with PBS⁻ (mgHES P value 0.004** and PS-COOH P value 0.0002***). This further validates the reproducibility of the effect when washing with water as seen in our LC-MS findings.

Due to the significant impact of different washing media on the protein corona composition, we questioned whether this effect is based on an altered protein structure depending on the washing media. Therefore, we chose two of the most abundant blood proteins – serum albumin and IgG – and analyzed the influence of the washing media on the protein structure in the absence of any nanocarriers via nano differential scanning fluorimetry (nanoDSF). Both proteins were dissolved in the respective washing media and the unfolding of the proteins upon temperature increase was monitored. The nanoDSF uses the intrinsic fluorescence intensities of tryptophan or tyrosine residues in a protein, which highly depend on the structural conformation of the adjacent amino acids and are therefore altered by heat-dependent denaturation^{103, 104}. Note that for the nanoDSF experiment, the DMEM washing group is excluded, because it is composed of L-tryptophan (0.1 mM) and L-tyrosine (0.4 mM), which interfere with the nanoDSF method of measurement.

2. Preparation of the Protein Corona: how Washing Shapes the Proteome and Influences Cellular Uptake of Nanocarriers

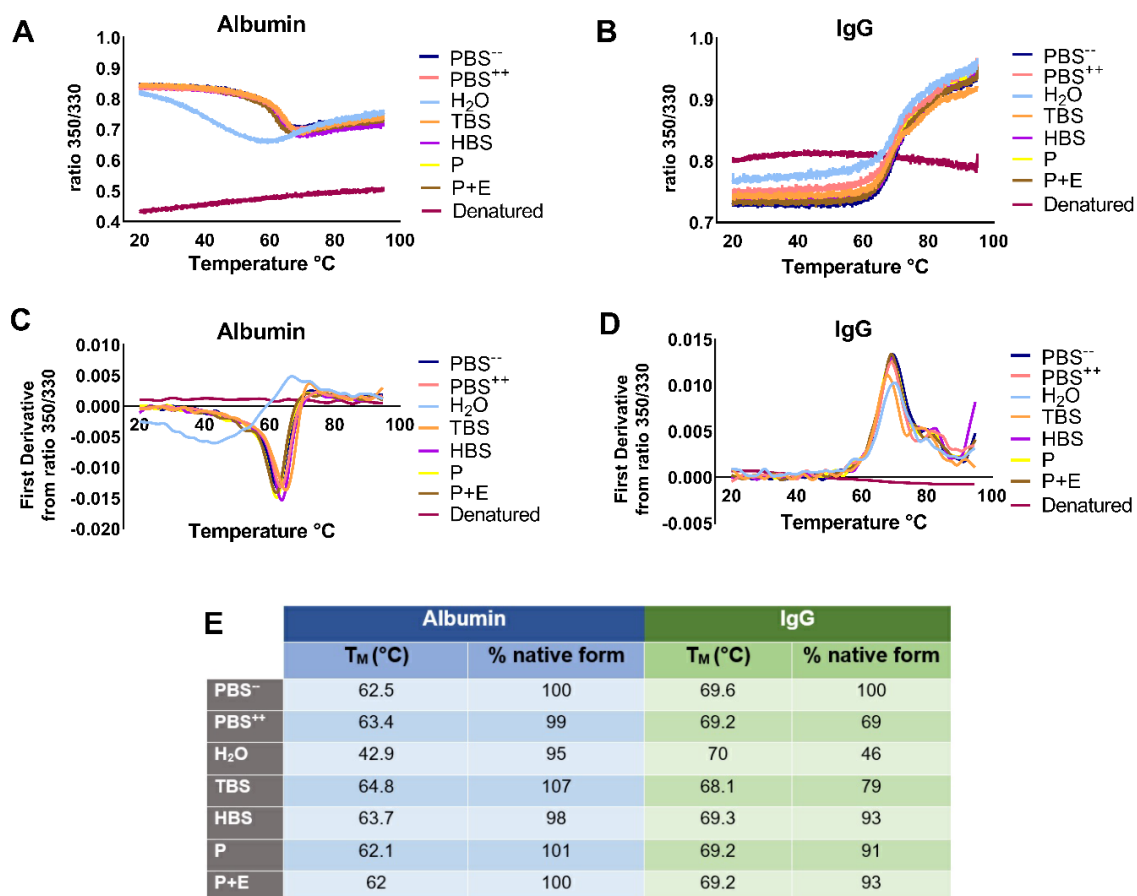


Figure 2.5: The Choice of Media Influences the Protein Stability. The Nano differential scanning fluorimetry (nanoDSF) was applied to illustrate the folding of human serum albumin (HSA) and IgG. (A,B) The fluorescence intensity ratio of 350/330 nm is plotted against the melting temperature (T_M) for each washing media. The melting temperature T_M is determined from the curve for the first derivative of the ratio plotted against the temperature (C,D). E) demonstrates the influence of the washing media on T_M and the denaturation degree. A representative measurement is shown. The experiment was repeated two to three times independently yielding similar results. A denatured control was generated by adding 2% SDS to the respective media and incubating it for 30 min at 95 °C before measurement.

Via the nanoDSF measurement, the characteristic melting temperature T_M of a protein, which is defined as the point where 50% of the protein is unfolded, is analyzed. This value is determined from the minimum/maximum of the first derivative for the ratio of the fluorescent intensity at 350/330 nm. Additionally, a denatured control was generated by dissolving the protein in 2% SDS and incubating it for 30 min at 95 °C. To calculate the denaturation degree (%), proteins in the PBS (--) solution were used as a reference and set to 100% meaning the protein is in its native folded state, whereas the denatured control was set to 0%. The detailed calculation is described in the material and methods section.

In general, for both proteins, we observed an influence of the washing media on the protein structure (Figure 2.5). Especially, H₂O had a major impact on the structure of human serum albumin and IgG. Compared to the PBS (--) control, the melting temperature for HSA in water

2. Preparation of the Protein Corona: how Washing Shapes the Proteome and Influences Cellular Uptake of Nanocarriers

is significantly lower ($H_2O = 42.9\text{ }^{\circ}C$ vs. $PBS (-) = 62.5\text{ }^{\circ}C$) which indicates structural alteration of HSA. In the case of IgG in H_2O , more than 50% of the protein is denatured in comparison to the PBS (-) control sample.

Upon protein unfolding and denaturation, the hydrophobic core of a protein becomes surface exposed. This process can further influence the adsorption properties towards a nanocarriers' surface and could explain the altered protein corona composition depending on the chosen washing media.

In vitro cell uptake experiments of mgHES nanocarriers

In order to investigate the effect of differently prepared protein coronas in a biological system, the uptake of mgHES nanocarriers was tested for two immortalized cell lines. Both represent a suitable model system for potential diagnostics and therapeutics of targeting cancer cells as well as investigating the interaction of nanocarriers with immune cells. Therefore, mgHES nanocarriers were incubated with HeLa and RAW264.7 cells and analyzed by flow cytometry (Attune™ NxT). Plain mgHES nanocarriers without protein corona were taken as a control and based on this, the relative median fluorescent intensity was calculated (see material/methods part).

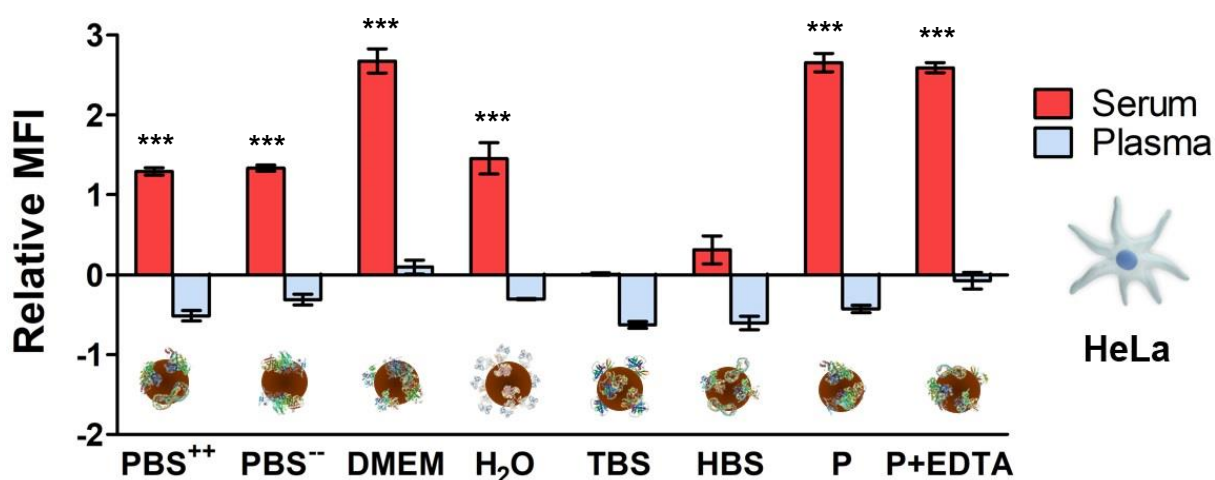


Figure 2.6: Washing Media Influences the Uptake of Differently Washed mgHES Nanocarriers by HeLa Cells.

The cells were incubated with differently washed mgHES nanocarriers containing a protein corona of either blood plasma or serum proteins at a concentration of $75\text{ }\mu\text{g mL}^{-1}$ for 4 h at $37\text{ }^{\circ}C$. Plain nanocarriers without a protein corona were used as a control representing the baseline at zero. The bars show the relative median fluorescence intensity (MFI) measurements generated by flow cytometry ($n = 3$ for each sample, \pm standard deviation) where each measured value is related to the control ($rMFI = 0$). $P < 0.001$ ***.

Therefore, a positive data point represents an increased uptake, and each negative data point a reduced uptake compared to nanocarriers without corona. There is a clear distinction between the uptake of nanocarriers, which were incubated with blood plasma in comparison

2. Preparation of the Protein Corona: how Washing Shapes the Proteome and Influences Cellular Uptake of Nanocarriers

to serum. While the plasma protein corona prevents uptake, the serum corona enhances internalization. This effect is quantitatively influenced based on the selection of the washing media with a significant increase observed for the serum corona after PBS⁺⁺, PBS⁻, DMEM, H₂O, P and P+E washing (P<0.001***).

Comparable results were found for the differently prepared nanocarriers, which were incubated with murine RAW 264.7 cells. Again, there was a significant difference between the plasma and the serum formed protein corona. Moreover, the chosen washing media quantitatively affected the uptake level (Figure 2.S11). Overall, this demonstrates that the chosen washing media step shapes hard corona composition and influences the cellular uptake behavior.

2.5 Supporting Information

commercially available			self-made					
DMEM Pen/Strep 1% + Glutamax 1%			PBS⁺⁺			TBS		
Component	mg/L	mM	Component	g/L	mM	Components	mM/L	
Amino Acids			(inorganic salts)			NaCl	150	
Glycine	30	0.4	CaCl ₂	0.1	0.9	Tris	10	
L-Arginine hydrochloride	84	0.4	MgCl ₂ ·6H ₂ O	0.1	0.493	pH	7.4	
L-Cystine 2HCL	63	0.2	KCl	0.2	2.667	HBS		
L-Histidine hydrochloride-H ₂ O	42	0.2	KH ₂ PO ₄	0.2	1.471	Components	mM/L	
L-Isoleucine	105	0.8	NaCl	8.0	137.9	NaCl	150	
L-Leucine	105	0.8	Na ₂ HPO ₄ ·7H ₂ O	2.1	8.060	HEPES	20	
L-Lysine hydrochloride	146	0.8		6		pH	7.4	
L-Methionine	30	0.2	pH 7.1 – 7.5			Phosphate		
L-Phenylalanine	66	0.4	PBS⁻			Components	mM/L	
L-Serine	42	0.4	Component	g/L		NaCl	150	
L-Threonine	95	0.8	(inorganic salts)			Phosphate	10	
L-Tryptophan	16	0.1	KCl	0.2		pH	7.4	
L-Tyrosine	72	0.4	KH ₂ PO ₄	0.2		Phosphate + EDTA		
L-Valine	94	0.948	NaCl	8.0		Components	mM/L	
Vitamines			Na ₂ HPO ₄ (anhydrous)	1.15		NaCl	150	
Choline chloride	4	0.03	pH	7.1 - 7.5		Phosphate	10	
D-Calcium pantothenate	4	0.01	Ultrapure MS water			EDTA	1	
Folic Acid	4	0.01				pH	7.4	
Niacinamide	4	0.03						
Pyridoxine hydrochloride	4	0.02						
Riboflavin	0.4	0.001						
Thiamine hydrochloride	4	0.01						
i-Inositol	7.2	0.04						
Inorganic Salts								
CaCl ₂ ·2H ₂ O	264	1.8						
Fe(NO ₃) ₃ ·9H ₂ O	0.1	2.5						
MgSO ₄ ·7H ₂ O	200	0.8						
KCl	400	5.3						
NaHCO ₃	3700	44						
NaCl	6400	110						
NaH ₂ PO ₄ ·2H ₂ O	141	0.9						
Others								
D-Glucose	1000	5.6						
Sodium Pyruvate	110	1						
pH	7.0 - 7.4							

Figure 2.S1: Composition of Used Washing Media. The commercially available media was purchased from Gibco (DMEM and PBS⁺⁺); Sigma (PBS⁻), and Biosolve (water ULC/MS – CC/SFC). DMEM was further supplemented with 1% penicillin (100 U mL⁻¹) and streptomycin (100 mg mL⁻¹) as well as 1% glutamine, all from Thermo. Self-made buffers were prepared in Ampuwa® water for injection with sodium chloride (VWR chemicals); Tris (Sigma); HEPES (Sigma); Phosphate (Fluka); EDTA (AppliChem) and adjusted to a pH of 7.4 with 1 mM NaOH and 1 mM HCl.

2. Preparation of the Protein Corona: how Washing Shapes the Proteome and Influences Cellular Uptake of Nanocarriers

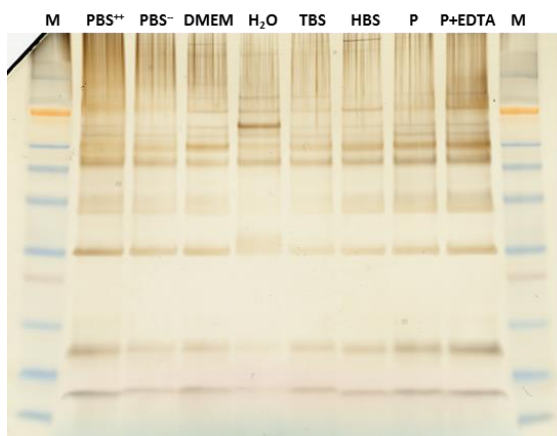


Figure 2.S2: Plasma PC of PS-COOH nanocarriers. After blood plasma incubation and washing, the proteins were desorbed and separated from the nanocarriers by desorption buffer. Protein quantification was measured by Pierce 660 nm assay and 2 μ g of protein corona samples and 5 μ L of marker (M) were applied for SDS-PAGE followed by silver staining.

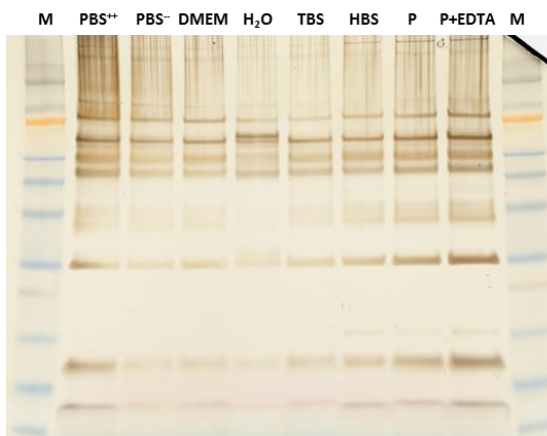


Figure 2.S3: Serum PC of PS-COOH nanocarriers. After blood serum incubation and washing, the proteins were desorbed and separated from the nanocarriers by desorption buffer. Protein quantification was measured by Pierce 660 nm assay and 2 μ g of protein corona samples and 5 μ L of marker (M) were applied for SDS-PAGE followed by silver staining.

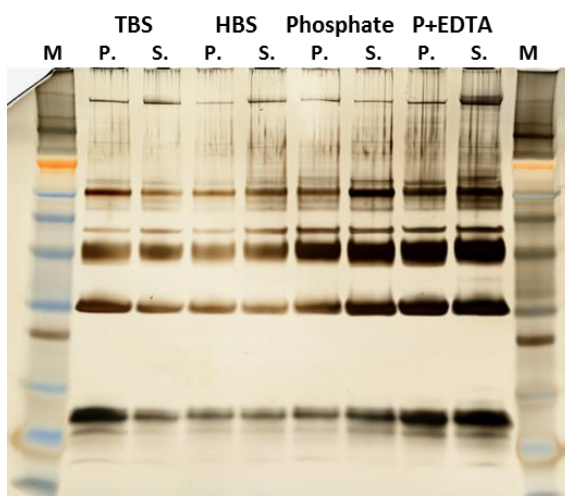


Figure 2.S4: SDS-PAGE of PS-plain nanocarriers. Plasma (P) and Serum (S) treated PS nanocarriers were washed with one of the four media indicated above the abbreviations. Afterwards, the proteins were desorbed and separated from the nanocarrier by desorption buffer. Protein quantification was measured by Pierce 660 nm assay and 2 μ g of protein corona samples and 5 μ L of marker (M) were applied for SDS-PAGE followed by silver staining.

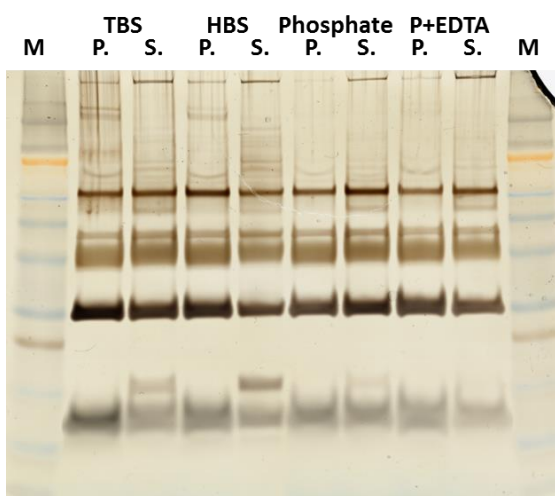


Figure 2.S5: SDS-PAGE of PS-NH₂ nanocarriers. Plasma (P) and Serum (S) treated PS nanocarriers were washed with one of the four media indicated above the abbreviations. Afterwards, the proteins were desorbed and separated from the nanocarrier by desorption buffer. Protein quantification was measured by Pierce 660 nm assay and 2 μ g of protein corona samples and 5 μ L of marker (M) were applied for SDS-PAGE followed by silver staining.

2. Preparation of the Protein Corona: how Washing Shapes the Proteome and Influences Cellular Uptake of Nanocarriers

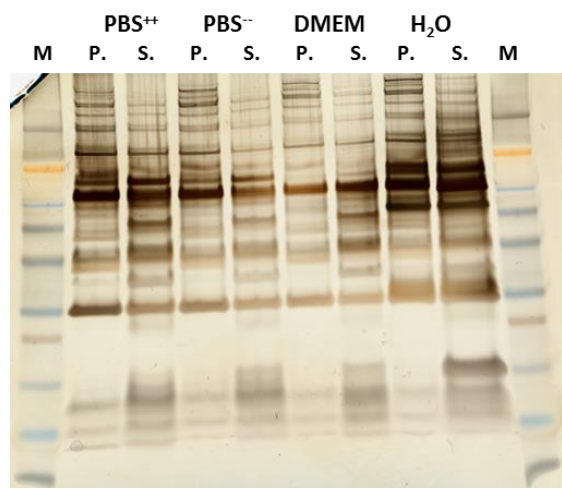


Figure 2.S6: SDS-PAGE of SiNC-O-Lutensol nanocarriers. Plasma (P) and Serum (S) treated PS nanocarriers were washed with one of the four media indicated above the abbreviations. Afterwards, the proteins were desorbed and separated from the nanocarrier by desorption buffer. Protein quantification was measured by Pierce 660 nm assay and 2 μ g of protein corona samples and 5 μ L of marker (M) were applied for SDS-PAGE followed by silver staining.

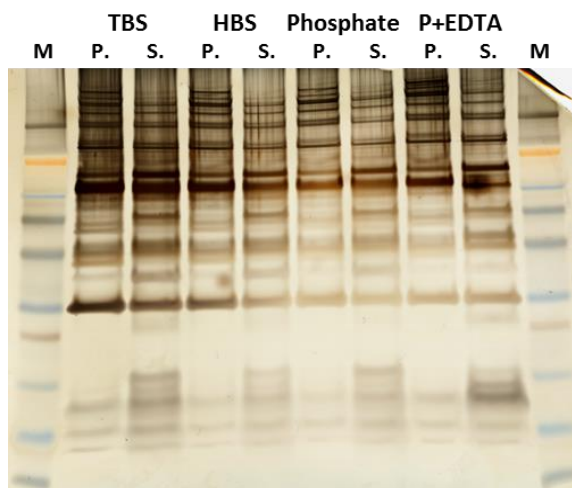


Figure 2.S7: SDS-PAGE of SiNC-O-Lutensol nanocarriers. Plasma (P) and Serum (S) treated PS nanocarriers were washed with one of the four media indicated above the abbreviations. Afterwards, the proteins were desorbed and separated from the nanocarrier by desorption buffer. Protein quantification was measured by Pierce 660 nm assay and 2 μ g of protein corona samples and 5 μ L of marker (M) were applied for SDS-PAGE followed by silver staining.

2. Preparation of the Protein Corona: how Washing Shapes the Proteome and Influences Cellular Uptake of Nanocarriers

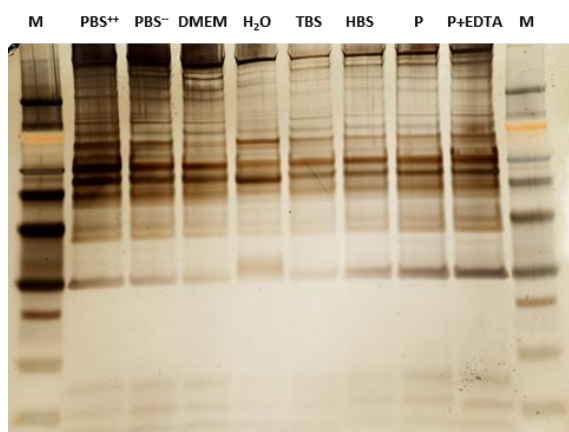


Figure 2.S8: Plasma protein corona of SiNC-O-CTAC-CI nanocarriers. Plasma (P) and Serum (S) treated PS nanocarriers were washed with one of the four media indicated above the abbreviations. Afterwards, the proteins were desorbed and separated from the nanocarrier by desorption buffer. Protein quantification was measured by Pierce 660 nm assay and 2 μ g of protein corona samples and 5 μ L of marker (M) were applied for SDS-PAGE followed by silver staining.

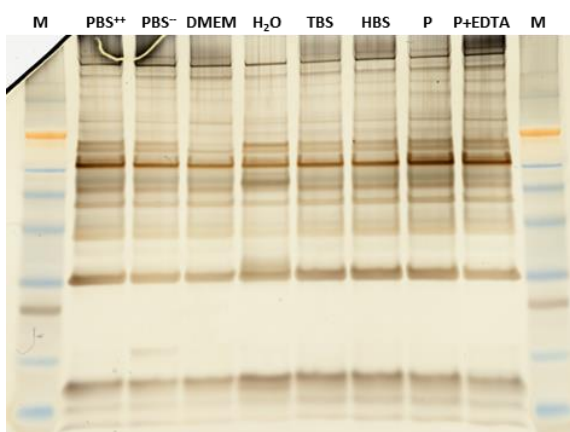


Figure 2.S9: Serum protein corona of SiNC-O-CTAC CI nanocarriers. Plasma (P) and Serum (S) treated PS nanocarriers were washed with one of the four media indicated above the abbreviations. Afterwards, the proteins were desorbed and separated from the nanocarrier by desorption buffer. Protein quantification was measured by Pierce 660 nm assay and 2 μ g of protein corona samples and 5 μ L of marker (M) were applied for SDS-PAGE followed by silver staining.

2. Preparation of the Protein Corona: how Washing Shapes the Proteome and Influences Cellular Uptake of Nanocarriers

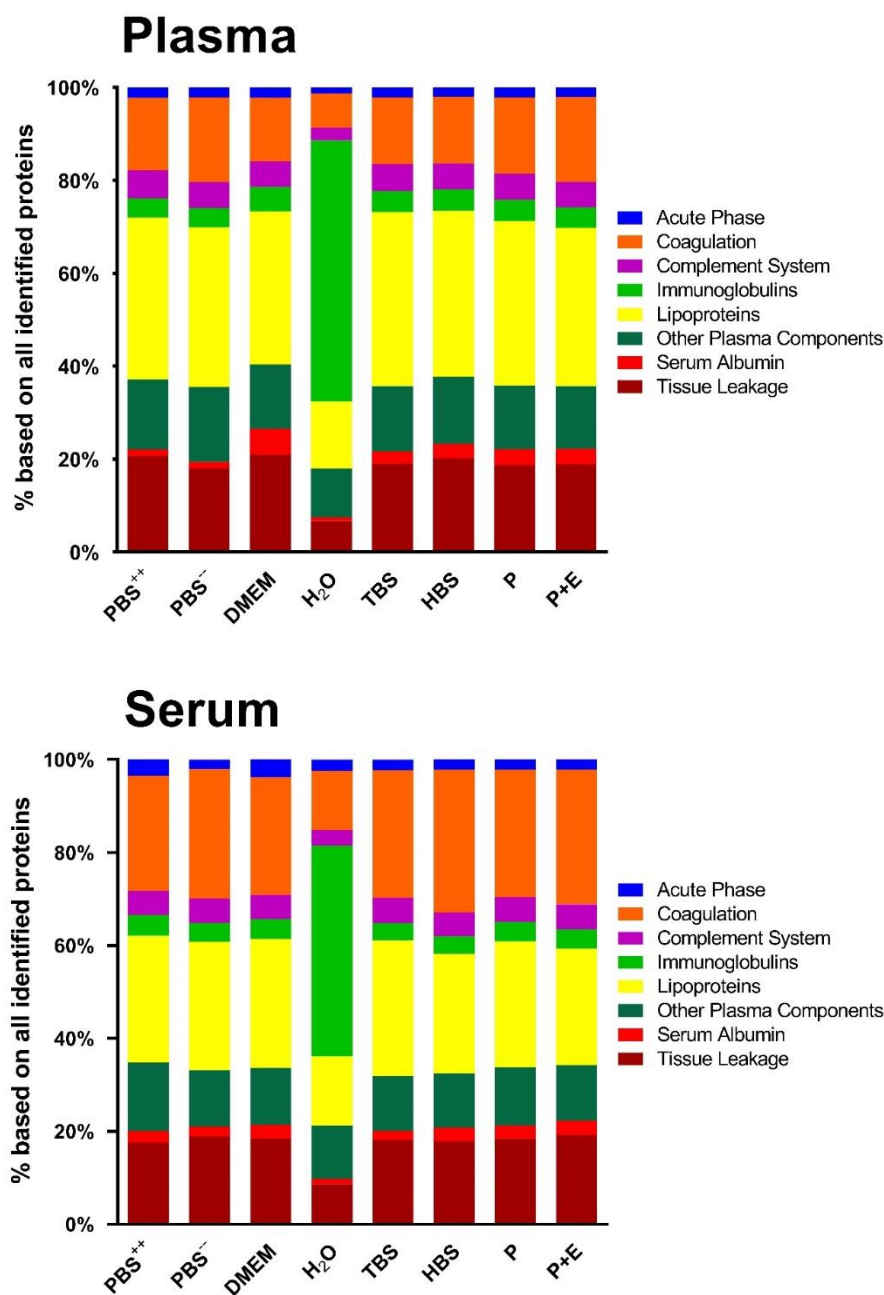


Figure 2.S10: Proteomic Analysis of the PS-COOH Protein Corona. The percentage based on all identified proteins of both citrate plasma and serum, respectively, analyzed by LC-MS is shown (n =3, technical replicates).

2. Preparation of the Protein Corona: how Washing Shapes the Proteome and Influences Cellular Uptake of Nanocarriers

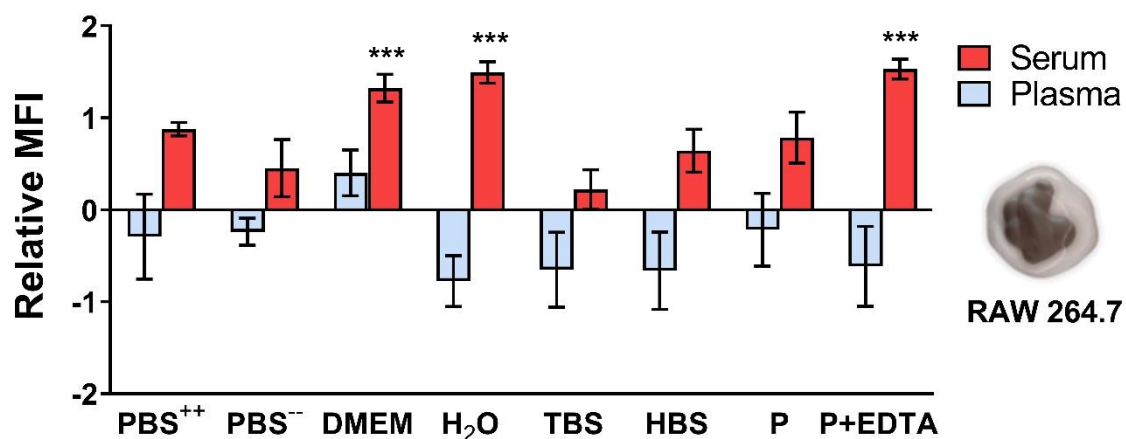


Figure 2.S11: Uptake of differently washed mgHES nanocarriers in RAW 264.7 macrophages. The cells were incubated with differently washed mgHES nanocarriers containing a protein corona of either blood plasma or serum proteins at a concentration of $75 \mu\text{g mL}^{-1}$ for 2 h at 37°C . Plain NPs without a protein corona were used as a control representing the baseline at zero. The bars show the relative median fluorescence intensity (MFI) measurements generated by flow cytometry ($n = 3$ for each sample, \pm standard deviation) where each measured value is related to the control ($= 0$). $P < 0.001$ ***.

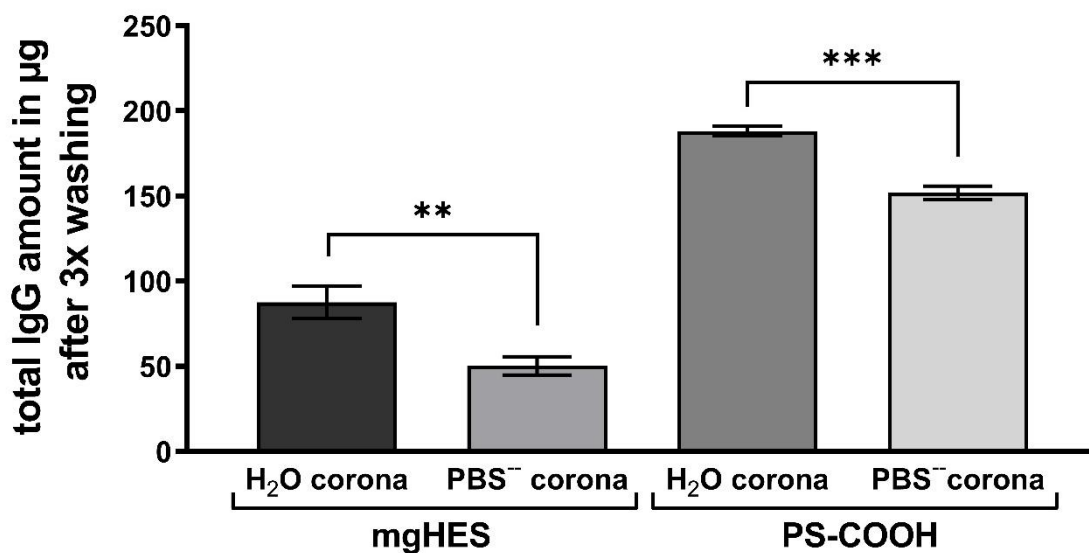


Figure 2.S12: Total IgG amount of mgHES and PS-COOH nanocarriers after 3x washing with H₂O and PBS. Human IgG was incubated with the nanocarriers for 1 h at 37°C shaking followed by three washing steps with either H₂O or PBS⁻⁻. Afterwards, the IgG corona was separated from the nanocarriers and the protein concentration determined by Pierce. The bars represent the mean value of the total IgG amount in micrograms ($n = 3$ for each sample, \pm standard deviation). mgHES P value 0.004 ** and PS-COOH P value 0.0002 ***. $P < 0.001$ ***.

2. Preparation of the Protein Corona: how Washing Shapes the Proteome and Influences Cellular Uptake of Nanocarriers

Table 2.S1: Hydrodynamic radii of magnetic (mgHES) and polystyrene (PS-COOH) nanocarriers dispersed in eight different washing media measured by dynamic light scattering. The average of three consecutive measurements \pm standard deviation is listed together with the polydispersity index in brackets.

	Hydrodynamic radius R_h in different dispersion media	
	mgHES	PS-COOH
PBS⁺⁺	162.7 \pm 2.04 nm (0.141 \pm 0.005)	122.3 \pm 1.21 nm (0.032 \pm 0.026)
PBS⁻	162.8 \pm 1.34 nm (0.098 \pm 0.005)	122.5 \pm 0.45 nm (0.031 \pm 0.025)
DMEM	165.5 \pm 1.12 nm (0.140 \pm 0.031)	124.4 \pm 0.55 nm (0.025 \pm 0.011)
H₂O	356.5 \pm 7.19 nm (0.141 \pm 0.020)	121.9 \pm 0.46 nm (0.014 \pm 0.012)
TBS	162.8 \pm 0.68 nm (0.108 \pm 0.033)	123.9 \pm 0.84 nm (0.031 \pm 0.040)
HBS	164.4 \pm 2.48 nm (0.116 \pm 0.009)	124.6 \pm 0.83 nm (0.025 \pm 0.024)
P	163.8 \pm 1.08 nm (0.097 \pm 0.008)	122.7 \pm 0.49 nm (0.042 \pm 0.017)
P+E	163.9 \pm 0.83 nm (0.118 \pm 0.025)	122.8 \pm 1.48 nm (0.019 \pm 0.014)

Table 2.S2: Hydrodynamic radii of magnetic (mgHES) and polystyrene (PS-COOH) nanocarriers dispersed in LC-MS water after 1 and 21 h measured by dynamic light scattering. The average of three consecutive measurements \pm standard deviation is listed together with the polydispersity index in brackets.

	Hydrodynamic radius R_h in LC-MS water over time	
	mgHES	PS-COOH
1 h	265.3 \pm 6.63 nm (0.309 \pm 0.015)	120.3 \pm 0.25 nm (0.036 \pm 0.023)
21 h	210.9 \pm 4.12 nm (0.262 \pm 0.025)	121.5 \pm 0.98 nm (0.033 \pm 0.022)

Chapter B – Surface-modification of nanocarriers with antibodies for a precise targeting of dendritic cells

The second chapter (**B**) of this dissertation divides into four subchapters. The first subchapter 3 describes the immunological research field on targeting dendritic cells with antibody-modified nanocarriers. In addition, it provides the theoretical aspects about the generation of antibody-nanocarrier-conjugates applied as targeting constructs *in vitro* as well as *in vivo*. The following three chapters 4 – 6 present each study individually [2 – 4].

[2] Maximilian Brückner*, Johanna Simon*, Katharina Landfester, Volker Mailänder. The conjugation strategy affects antibody orientation and targeting properties of nanocarriers. *Nanoscale*, **2021**, 13, 9816-9824.

[3] Johanna Simon*, Michael Fichter*, Gabor Kuhn*, **Maximilian Brückner**, Cinja Kappel, Jenny Schunke, Tanja Klaus, Stephan Grabbe, Katharina Landfester, Volker Mailänder. Achieving dendritic cell subset-specific targeting *in vivo* by site-directed conjugation of targeting antibodies to nanocarriers. *Nano Today*, bioRxiv, **2021**.

[4] Maximilian Brückner*, Michael Fichter*, Richard da Costa Marques, Katharina Landfester, Volker Mailänder. PEG spacer length substantially affects antibody-based nanocarrier targeting of dendritic cell subsets (preliminary title). To be submitted.

3. Theoretical background

3.1 Dendritic cells in cancer immunotherapy

Immunotherapies function by restoring the ability of the patient's immune system to detect and erase cancer cells and tumors, which otherwise hide from the immune system by numerous ways. In order to induce the detection and an effective killing of cancer cells, the strategies of a treatment by immunotherapy must intervene in the cancer-immunity cycle (Figure 3.1). Promising strategies, like immune checkpoint blockade (ICB), adoptive cell therapy (ACT) using tumor infiltrating leukocytes (TIL), and vaccine approaches aim at different steps in the cycle to enhance anticancer T lymphocyte responses. Within the cancer-immunity cycle, antigen-presenting cells (APCs), such as dendritic cells, initiate the cycle enabling the above-mentioned strategies to take effect.^{105, 106}

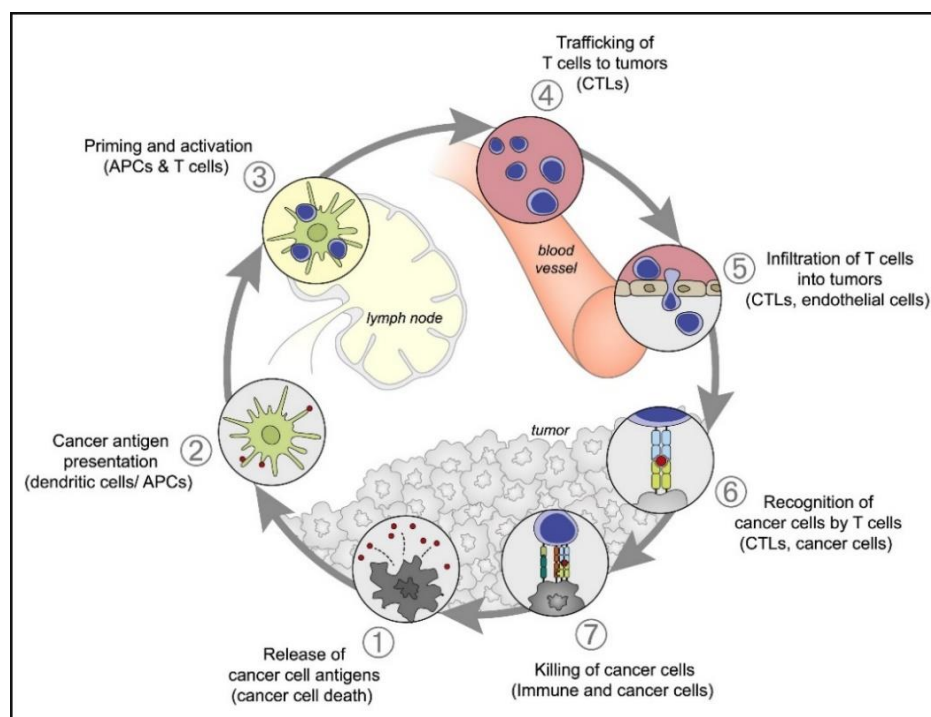


Figure 3.3: The seven steps of the cancer-immunity cycle. The seven steps of the cycle initiate with the release of antigens from the cancer cell and terminate with the killing of the cancer cells. Each step is shortly described above. APCs, antigen-presenting cells; CTLs, cytotoxic T lymphocytes. Reprinted with permission from Chen *et al.*¹⁰⁶. Copyright © 2022, Elsevier.

In general, the cancer-immunity cycle describes the recognition and killing of cancer cells in seven steps. At first, dendritic cells capture the released neoantigens generated by the formation of cancer cells for their subsequent processing into proteolytic peptides (step 1). At next, dendritic cells display the processed antigens on major histocompatibility class I (MHC I) and MHCII molecules to T cells (step 2). This presentation leads to the priming and activation

of effector T cell responses against cancer-specific antigens (step 3). Thereby, the T cells recognize the antigens and hence the cancer to be foreign. In the final steps, the activated T cells traffic to (step 4) and infiltrate the tumor site (step 5), where they recognize and bind to cancer cells via the interaction of their T cell receptors (TCRs) and its cognate antigen bound to MHC I (step 6), resulting in the killing of the cancer cells (step 7).¹⁰⁶ Acting as the starting points, dendritic cells play a major role in the cycle and thus are the target of dendritic cell-based immunotherapy (Figure 3.2).

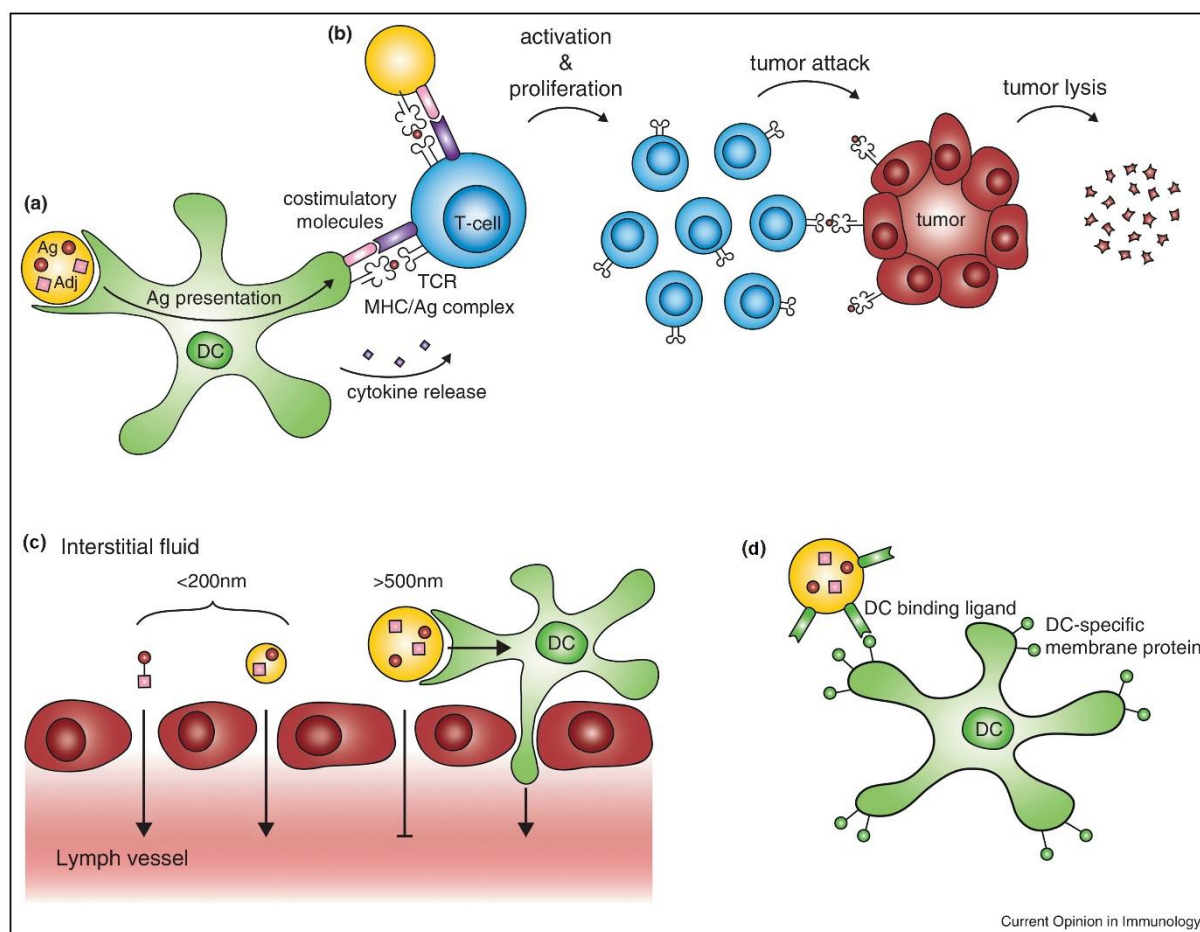


Figure 3.2: Nanocarriers vaccine delivery to dendritic cells for cancer immunotherapy. Nanocarriers (yellow) transport (a) tumor antigens (Ag, red) and adjuvants (Adj, pink) to dendritic cells (DCs, green). DCs process the antigens and present the peptides on major histocompatibility complex (MHC) molecules to the T cell receptor (TCR) on T cells (blue). In addition, nanocarriers can also directly present the tumor antigens to T cells (b). The antigen presentation combined with immune-stimulatory molecules (adjuvants) trigger tumor-specific T cell activation and expansion. Once activated, the T cells migrate to and recognize the tumor antigens resulting in tumor lysis. The nanocarrier transports the cargo either passively or actively to DCs. A passive targeting (c) depends on the nanocarrier size where smaller nanocarriers (< 200 nm) can diffuse from the intestinal fluid across the lymphatic endothelium into lymph vessels and larger nanocarriers (> 500 nm) require a dendritic cell transport into the lymph vessel. In the active targeting, ligand-functionalized (e.g. antibodies) nanocarriers precisely bind to DC surface receptors, enabling a DC uptake (d). Adapted with permission from Paulis *et al.*¹⁰⁷. Copyright © 2022, Elsevier.

Dendritic cells capture antigens and monitor the body's response through direct and/or indirect cytokine release. Presentation of the processed antigens into peptides on MHC I and MHC II on the dendritic cell surface induces immune responses by either CD8⁺ or CD4⁺ T cells, respectively¹⁰⁸. Consequently, dendritic cells as the major set of APCs orchestrate between innate and adaptive immune systems resulting in the control of both immune tolerance and response^{109, 110}. As a result, the immune system decides between an elimination of pathogens by CD8⁺ T cells and an induction of long-term memory by CD4⁺ T cells. Both outcomes essentially influence an anticancer treatment for the direct killing of the cancer cells by CD8⁺ T cells¹¹¹, but also for a long-lasting priming of memory CD4⁺ T cells¹⁰⁷. A state-of-the-art dendritic cell-based immunotherapy consists of the delivery of TAAs and immunomodulators (adjuvants) to dendritic cells by applying nanocarriers as transport vehicles. Nanocarriers enable a protection of the antigen and adjuvant payload from premature enzymatic digestion and control a dendritic cell uptake by means of passive or active targeting¹¹⁰. In case of a passive dendritic cell targeting, nanocarriers require a distinct set of physicochemical properties, including surface charge and hydrophobicity, morphology, and size¹¹². For instance, after subcutaneous injection, nanocarriers below 200 nm in diameter might diffuse into lymph vessels interacting with lymph node-resident dendritic cells, whereas larger nanocarriers above 500 nm require an uptake by skin-resident dendritic cells following transportation to lymph nodes¹¹³. Contrary, decorating the nanocarrier surface with antibodies enables an active dendritic cell targeting. Thereby, the antibody ligand on the nanocarrier surface aims at the precise interaction with one of the multiple surface receptors present on the dendritic cell surface or inside the cytosol¹¹⁴. These receptors scan the body for the recognition of pathogenic structures enabling dendritic cells to induce immunity-related functions, like antigen-specific T-cell responses, pro-inflammatory signaling pathways, and dendritic cell maturation^{115, 116}. Dendritic cell receptors include phagocytic or scavenging receptors, integrins that activate signal transduction pathways, and surface and intracellular pattern recognition receptors (PRRs)¹¹⁶.

Addressing these receptors by an antibody-directed nanocarrier transport improves a localized cargo delivery to specific cell populations by receptor-specific internalization leading to possible downstream effects dependent on the receptor of interest¹¹⁷. In fact, the heterogeneous population of dendritic cells characterize by their developmental origin and the set of surface marker expression leading to subpopulations with distinct functions. Thereby, dendritic cells divide into four major subsets, namely monocyte-derived dendritic cells (mDCs), plasmacytoid dendritic cells (pDCs), and conventional type 1 and 2 dendritic cells (cDC1s and cDC2s)¹¹⁸. Especially, the cDC1 subset represents a promising target for cancer immunotherapy because it demonstrates an elevated cross-presentation of exogenous antigen

and subsequent CD8⁺ T cell activation¹¹⁹. Therefore, antibody-decorated nanocarriers require a distinct surface receptor to target the desired dendritic cell population.

3.2 Targeting of dendritic cells with antibody-modified nanocarriers

Through their combination, antibodies transfer their huge antigen-binding repertoire onto the nanocarrier system. Consequently, antibodies are widely used from biotechnological and biomedical applications, including fluorescence activated cell sorting, bioseparation, protein purification, nanocarriers as biosensors, *in vivo* diagnosis, and in human therapy as drug carriers^{120, 121}. Especially, in the biomedical field of nanomedicine, it is critically important how the antibody is bound to the surface¹²². This positioning highly affects the intended functionality of the antibody nanocarrier conjugate (Figure 3.3).

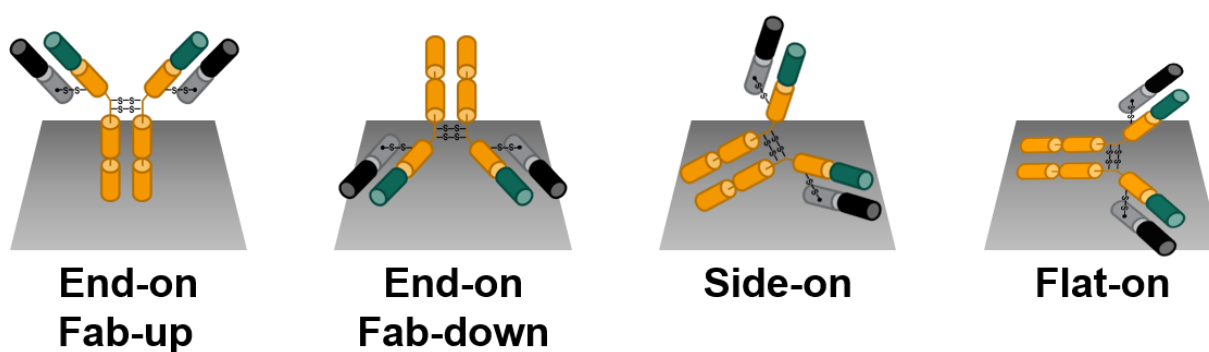


Figure 3.3: Antibodies positioned on the nanocarrier surface, either adsorbed or covalently bound, can adopt different orientations. The heavy chains are demonstrated in orange (constant) and green (variable), and the light chains in grey (constant) and black (variable). In the desired and biological active orientation, the antibody positions end-on with the Fab-up.

In general, the surface-modification requires a precise and controlled immobilization of the antibody molecule onto the surface without interfering with the antigen binding regions (F_{abs}) of the antibody hence its bioactivity. An incorrect attachment of the antibody can lead to a non-specific uptake in undesired regions. Therefore, the antibody conjugation strategy needs a careful preparation because of the asymmetric composition of antibody molecules leading to different spatial orientations on the nanocarrier surface¹²³. Conventional strategies involve the attachment onto the nanocarrier surface via EDC/NHS crosslinker chemistry^{124, 125} through the manifold primary amine termini of the lysine residues^{126, 127}. Due to the abundance of lysine residues all over the antibody, the conjugation results in random orientations of the molecules hindering their full potential of antigen recognition¹²⁸⁻¹³⁰. Consequently, a state-of-the-art attachment must result in an oriented positioning of the antibody molecule on the surface. For this purpose, the antibody is covalently bound to the nanocarrier surface through its F_c region. While the F_c part forms the foundation on the surface and is sterically inaccessible, the two F_{ab}

domains point away from the surface and are thus freely accessible to bind their corresponding antigen¹³¹. Most commonly, an oriented attachment is transmitted through the binding of thiol groups of the antibody, through biotin- or F_c-binding proteins, or binding through the sugar chains of the antibody¹³². In general, every nanocarrier conjugation strategy involves the basic understanding of the structure and function of the antibody molecule.

3.3 Structure and function of antibodies

Being part of the adaptive immune response, antibodies represent exclusively B cell produced glycoproteins that either act as B cell antigen receptors or neutralize their target antigen when being in the secreted form¹³³. Within the immune system, antibodies intervene in main processes such as opsonisation, complement dependent cytotoxicity (CDC), phagocytosis, and antibody-dependent cytotoxicity (ADCC)¹³⁴. Throughout the variety of species, the antibody or immunoglobulin (Ig) commonly consist of a Y-shaped, quaternary structure (Figure 3.4)¹³⁵.

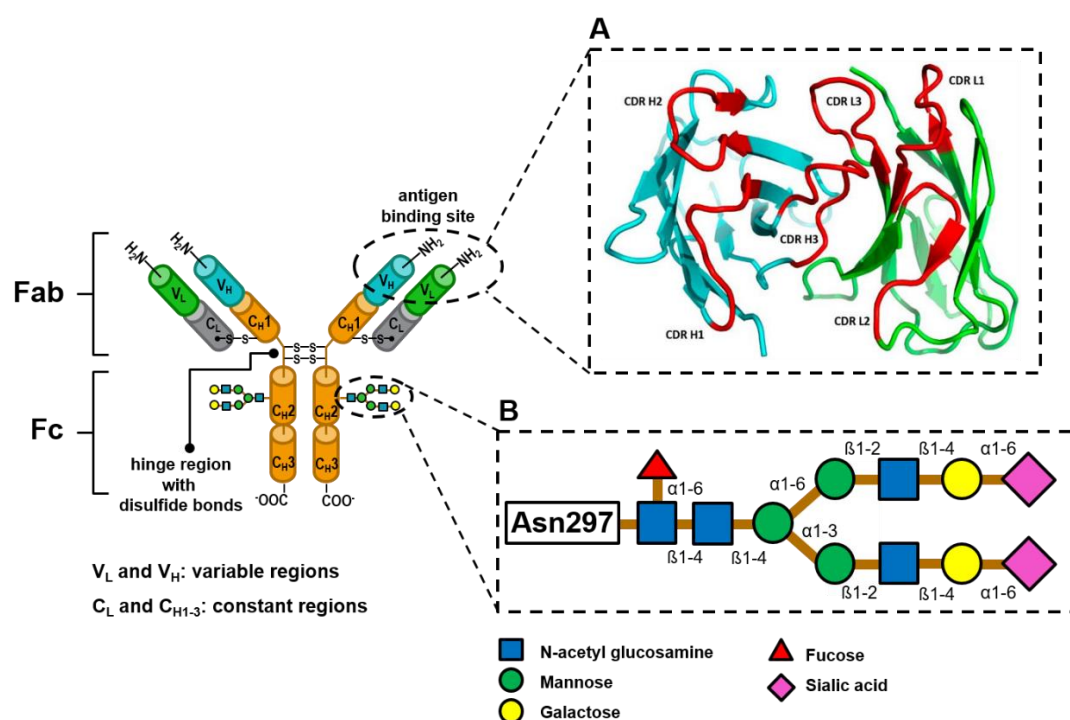


Figure 3.4: Schematic presentation of a regular IgG structure. The IgG is composed of the heavy chain (V_H and C_{H1-3}) and light chain (V_L and C_L), which are connected by disulfide bonds within the hinge region. The fragment antigen-binding domains (F_{abs}) represent the upper region, whereas the fragment crystallizable (F_c) region forms the lower part of the IgG. Within the antigen-binding site, the V_H (blue) and V_L (green) build the complementarity-determining region (CDR, in red) composed of three hypervariable regions for each V_H (CDR H1, H2, H3) and V_L (CDR L1, L2, L3) (A). The CDR is reprinted with permission from Chiu et al.¹³⁵. The glycosylation site of a typical IgG locates within the C_{H2} region at the asparagine 297 (Asn297) in the F_c region and is mostly represented as a biantennary structure (B).

This structure is typically composed of two identical heavy chains and two identical light chains. The pairing of each light chain with each heavy chain is forming two identical heterodimers that create the intact Ig. Disulfide bridges link the light chain and heavy chain of the heterodimer and the two heavy chains of the heterotetramer. Each light chain has two domains, a constant domain (C_L) and a variable domain (V_L). The mammalian light chain can be of the kappa (κ) or lambda (λ) class, which are functionally similar. Oppositely, the heavy chain defines the isotype of the antibody, which in mammals can be one of five types (IgA, IgD, IgE, IgG, and IgM). The IgA, IgD, and IgG have three constant domains (C_{H1} , C_{H2} , and C_{H3}) and one variable domain (V_H), while the IgE and IgM have four constant and one variable domain. An additional J-chain in the IgA and IgM isotypes enables the organization into dimers and pentamers. All other isotypes are monomers with each a pair of the heavy and light chain heterodimer.^{135, 136} Typically, the two heavy chains are glycosylated with two covalently bound oligosaccharide groups. In particular, the N-linked glycosylation site of the IgG isotype positions at the amino acid asparagine 297 located in the C_{H2} domain of the F_c region. From a structural point of view, these sugar chains form a biantennary structure composed of N-acetyl glucosamine, fucose, mannose, galactose, and sialic acid¹³⁷. Based on the Y-shaped structure, antibodies possess three distinct functional regions. The two fragment antigen-binding domains (F_{abs}) and the fragment crystallizable (F_c) part. The hinge region connects both domains, which provides the F_{abs} with additional flexibility in conformation regarding the F_c . For a precise antigen targeting, each F_{ab} domain generates an antigen-binding site, which is composed of the variable domains of the heavy and light chains, namely the complementarity-determining region (CDR). In detail, each variable domain contributes three hypervariable regions, namely the CDR L1, L2 and, L3 from the V_L and CDR H1, H2, and H3 from the V_H domain.^{135, 136} Next to the targeting ability, the constant F_c part of the antibody mediates a distinct effector function profile. Based on the binding between the F_c and, for example, complement proteins and specialized F_c -receptors, antibody effector functions play a crucial role in the humoral immune response and critically connect innate and adaptive immunity¹³⁸.

3.4 A site-directed strategy for the immobilization of whole antibodies onto the nanocarrier surface

The antibody molecule offers several modification approaches based on the repertoire of their natural amino acid residues positioned at the backbone of each glycoprotein. Modification strategies commonly focus on the innate chemical reactivity of amino acids such as lysine, cysteine, and glutamic/aspartic acid. The preference for these modification sites relies on their ease in functionalization due to well-established chemistries². However, these traditional

chemical methods lack in a site-specific modification leading to a random and heterogeneous mixture of modified antibody species. These methods include, for example, modifying the amines on lysine residues and the N-termini, or the thiols of the cysteine residues by acylation, or alkylation, respectively¹³⁹. For instance, non-specific antibody modifications in antibody constructs like antibody drug conjugates (ADC) lead to complex mixtures with positional isomers and different drug-to-antibody ratios¹⁴⁰. The same applies when conjugating antibodies onto a nanocarrier surface, where random conjugation strategies interfere with the targeting efficiency of the construct¹⁴¹. In the random conjugation process, antibodies lose their biological activity and specificity due to multiple sites of modifications leading to structural changes at the F_{ab} arms hence their CDRs responsible for their antigen binding function^{142, 143}. Consequently, a nanocarrier to antibody conjugation strategy must avoid modifications of the antibody interfering with their biological function to covalently-bind the molecule in a site-specific and homogeneous manner under mild reaction conditions. Likewise, the nanocarrier of interest also needs a precise modification to position the antibody specifically as a targeting ligand on the surface (Figure 3.4).

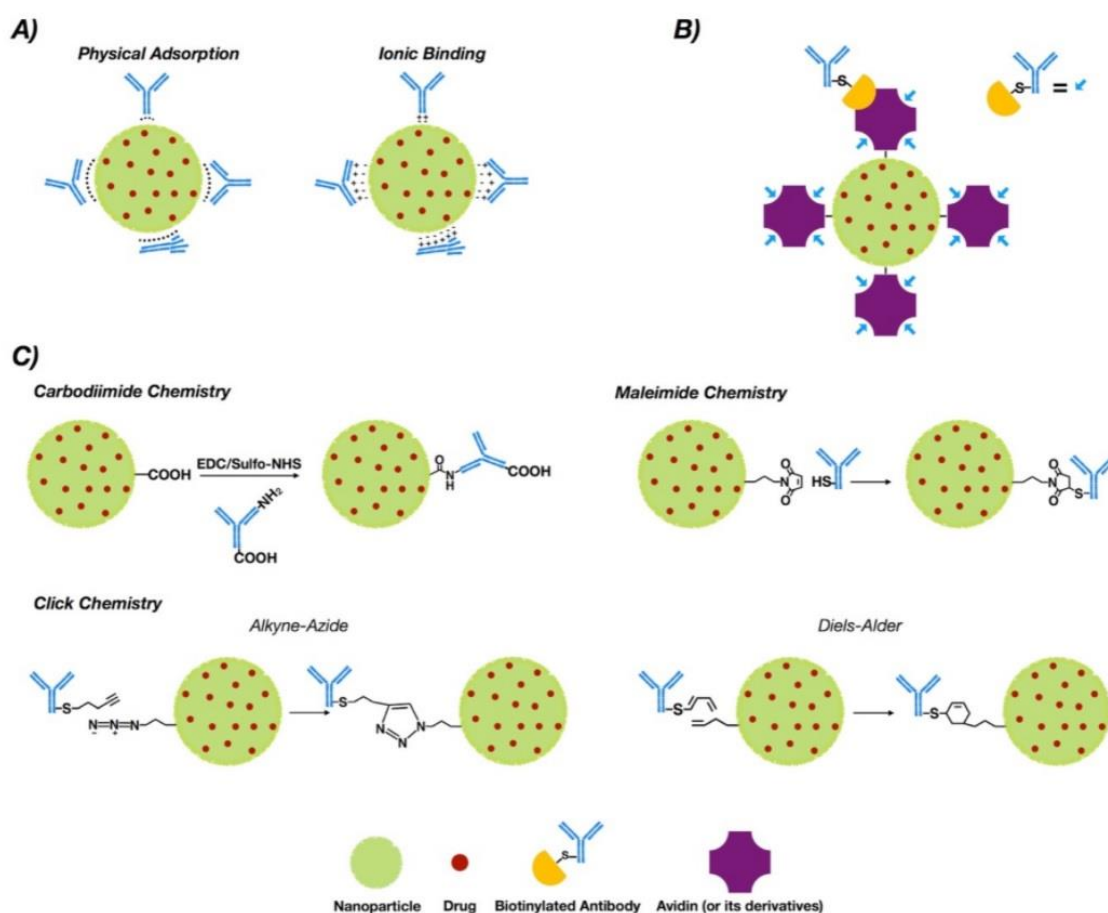


Figure 3.4: Surface-modification strategies for the generation of antibody-functionalized nanocarriers. Common strategies involve adsorption (A), the use of adapters (B), and covalent attachment (C). Reprinted with permission from Juan *et al.*³.

This modification happens either by non-covalent or covalent technologies. While non-covalent techniques apply a surface-to-ligand interaction by intermolecular attraction or physisorption, covalent modifications introduce a chemical functional group to the nanocarrier surface for the attachment². In comparison, covalently bound antibody nanocarrier conjugates show a greater *in vivo* stability than most of the non-covalent conjugates⁴. Furthermore, engineering the nanocarrier surface with a particular number and density of reactive sites for a covalent attachment enables a distinct control over the position and orientation of the antibody molecules. This strategy works best when combined with a site-specifically modified antibody. Several functional groups enable the covalent attachment of antibodies onto the surface, including amines, carboxylic acids, alcohols, thiols, aldehydes, maleimides, alkynes, and azides. However, besides the commonly used conjugation approaches, like carbodiimide chemistry, or maleimide chemistry, the click chemistry might be the most promising covalent coupling reaction¹⁴⁴.

Generally, the term “click chemistry” describes a set of simple chemical reactions with high efficiency and stereospecificity. In particular, Sharpless *et al.* coined the click terminology to be modular reactions with a wide scope and high yield, producing minimal and easily removable by-products, under benign solvent conditions¹⁴⁵. In sum, click chemistry comprises four classifications, namely nucleophilic ring-openings, additions to carbon-carbon multiple bonds, carbonyl chemistry of the non-aldol type, and cycloadditions¹⁴⁶. Out of these four, the cycloaddition reaction represents the most frequently applied conjugation technique for the generation of antibody-nanocarrier-conjugates, using the copper-catalyzed azide-alkyne cycloaddition (CuAAC), strain-promoted alkyne-azide cycloaddition (SPAAC), and inverse electron demand Diels-Alder reactions¹⁴⁷.

4. The conjugation strategy affects antibody orientation and targeting properties of nanocarriers

Copyright:

The content in the upcoming subchapter 4 was published in a peer-reviewed journal [2]. For this reason, the presented text is a word-by-word reproduction of the peer-reviewed and published paper. All results are reprinted with permission from the Royal Society of Chemistry, Nanoscale. Copyright © 2022 Royal Society of Chemistry.

[2] **Maximilian Brückner***, Johanna Simon*, Katharina Landfester, Volker Mailänder. The conjugation strategy affects antibody orientation and targeting properties of nanocarriers. *Nanoscale*, **2021**, 13, 9816-9824.

Aim:

Establishing a conjugation strategy for a nanocarrier system is fundamentally important for a precise antibody-based targeting. This targeting ability must be of high specificity towards the desired antigen with low influence of F_c -mediated uptake to undesired tissues and cells. Therefore, antibodies targeting the CD11c receptor on dendritic cells are covalently attached onto the nanocarrier surface by two different conjugation strategies. This study aims to identify the conditions that are necessary for a covalent attachment of antibodies onto a nanocarrier surface resulting in a precise targeting of dendritic cells. Thereby, it sets the foundation for future targeted nanocarriers and highlights how an uncontrolled antibody attachment leads to an undesired F_c -mediated cell uptake.

Contribution:

I, Maximilian Brückner, performed the synthesis of the two conjugation chemistries between the nanocarriers and the antibodies (nanocarrier functionalization and antibody modification) as well as all cellular uptake experiments (flow cytometry and cLSM). The protein corona analysis was partly carried out by Dr. Johanna Simon (LC-MS) and me (Pierce Assay, SDS-PAGE). Christine Rosenauer measured the multi-angle DLS, Elke Muth the ζ -Potential, and the TEM image analysis was performed by Francesca Mazzotta and Dr. Ingo Lieberwirth. Stefan Schuhmacher designed the table of contents and Karolin Eberle helped in revising the final readings of the manuscript. Dr. Johanna Simon, Prof. Dr. Volker Mailänder, and Prof. Dr. Katharina Landfester supervised the project.

4.1 Abstract

Antibody-modified drug delivery systems in the nano-range have the ability to overcome current challenges for treating diseases due to their high specificity towards the targeted body region. However, no antibody-bound nanocarrier has been clinically approved to date. This missing clinical approval may be a result of the conjugation strategy that influences the spatial orientation of the attached antibody on the nanocarriers' surface. What is not missing, however, is a diverse selection of antibody to nanocarrier conjugation strategies that determine the success of an antibody functionalized drug delivery system. In this paper, two antibody conjugation strategies were compared by conjugating the surface of cross-linked starch iron oxide nanocarriers with specifically modified CD11c monoclonal antibodies. The antibody nanocarrier conjugates, synthesized either by the chemistry of thiol-maleimide coupling or copper-free click chemistry, were analyzed by flow cytometry to determine their binding affinity towards a murine dendritic cell line (DC2.4). In the cell uptake, different antibody amounts on the nanocarrier could induce a dendritic cell uptake for both conjugation strategies. However, blocking experiments further highlighted the importance of the orientation of the antibody on to the nanocarriers' surface. While the antibodies which were attached via the copper-free click chemistry were oriented, maleimide synthesized conjugates presented their antibodies randomly on the surface. Lastly, to evaluate the *in vivo* properties of the antibody-modified nanocarriers, targeting experiments with mouse plasma were performed, and it was proven that the biomolecular corona does not diminish the targeting efficiency.

4.2 Introduction

The attachment of an antibody to the surface of a nanocarrier is the transfer of the specific and selective recognition ability of the antibody towards a nanocarrier. In return, nanocarriers offer a stable drug encapsulation, reduce toxicity, and control drug release¹⁴⁸. Therefore, it is of great interest to maintain the antibodies targeting ability to recognize its antigen for a site- and cell-directed delivery of a nanocarrier. Also, the non-binding parts like the constant region (F_c) of the antibody should not be exposed because F_c parts can enhance the mistargeting of nanocarriers to F_c -receptor containing cells like macrophages¹³⁸. Therefore, it is essential that an appropriate conjugation and orientation of the antibody on the nanocarriers' surface is ensured for a targeted drug delivery via nanocarriers¹⁴⁹.

Over the past decades, numerous strategies have been developed to attach antibodies to the surface of nanocarriers. These strategies include the physical adsorption, covalent bonding, adapter molecules or the combination of these concepts¹⁵⁰. Despite the simplicity or straightforwardness of these conjugation concepts in theory, the implementation is challenging¹⁵¹. For instance, the F_{ab} regions of the antibody should remain unaffected during the modification and immobilization process, as this region mediates the antigen recognition¹⁵².

The major goal of the synthesized antibody nanocarrier conjugates is the targeted transport of the cargo. As an example, in the field of immunotherapy, the nanocarrier can allow a co-delivery of different immunomodulators (e.g. adjuvant and antigen). The targeted transport of both substances to specific cells (e.g. antigen presenting cells, APCs) will further influence all down-stream processes, e.g. an antigen-specific cytotoxic T-lymphocyte (CTL), which can eventually enable a tumor regression¹⁵³. In this process, dendritic cells, which are APCs, play a crucial role because they initiate and regulate these immune responses¹⁵⁴.

The aim of this study was to compare two bioconjugation methods for the attachment of an antibody on a nanocarriers' surface. For this purpose, we used red-fluorescent nanocarriers that are composed of a magnetite core because of their ease in detection and magnetic separation. These nanocarriers are further equipped with a shell of cross-linked hydroxyethyl starch with amino groups on the surface. Anti-CD11c antibodies were either attached via the chemistry of thiol-maleimide coupling or via copper-free click chemistry on the surface of magnetic nanocarriers to specifically target dendritic cells. In our study, we found that both, the amount of functionalized antibody on the nanocarriers' surface and the conjugation chemistry, had a significant influence on the spatial orientation of the covalently bound antibody and thus on the targeting efficiency.

4.3 Material and Methods

Culturing of Dendritic Cells. Murine DC2.4 Dendritic Cells (Merck, Germany) were cultured in Iscove's Modified Dulbecco's Medium (Sigma-Aldrich, U.S.A), supplemented with 5% fetal bovine serum (FBS), 1% penicillin (100 U mL^{-1}) and streptomycin (100 mg mL^{-1}), as well as 1% 2-Mercaptoethanol (100X), in an incubator with $37 \text{ }^\circ\text{C}$ and 5% CO_2 humidity (CO_2 Incubator C200, Labotect). The confluence of the cells was checked under the microscope. When reaching a confluence greater than or equal to 80% the cells were passaged. The consumed media of the cells was discarded, and the cells were briefly washed with 10 mL PBS. For the detachment of the cells, 10 mL of cold PBS containing 2 mM EDTA were applied for 10 minutes at $4 \text{ }^\circ\text{C}$. Then, 10 mL of FBS containing medium were added to the flask and pipetted up and down to detach all cells. The resulting cell suspension was transferred into a 50 mL tube and centrifuged at 300 g for five minutes. The supernatant was discarded, and the cell pellet was resuspended in 10 – 20 mL of FBS containing medium. Cell viability was checked with trypan blue, by mixing 20 μL of cell suspension to 20 μL of trypan blue solution of which 10 μL were pipetted onto a counting slide and the live count was measured by an automated cell counter (TC10, Bio-Rad). Dependent on the live count, the cell suspension was used for experimental procedures or for keeping the cells in culture.

Nanocarrier Functionalization. The BNF-Starch-redF nanocarriers (micromod, Germany) were functionalized with either the Sulfo-SMCC linker (Thermo, Waltham/U.S.A.) for thiol-maleimide chemistry or the DBCO-PEG₄-NHS linker (Bioscience, Germany) for copper-free click chemistry. For the thiol-maleimide chemistry, nanocarrier to linker ratios were calculated based on 3 nmol mg^{-1} amino groups on the nanocarrier (micromod data sheet). Therefore, the number of NH_2 groups per mg nanocarriers were multiplied by the molecular weight of the Sulfo-SMCC linker and the desired linker ratio (example calculation below). The linker solutions had to be prepared freshly for each experiment and were not stored over a longer period due to the risk of oxidation. Before starting the linker reaction, the media of the nanocarriers was exchanged to 1 mM PBS-EDTA pH 7.4 utilizing magnetic force. Subsequently, the respective amount of maleimide-linker was added to the nanocarriers and incubated for 1 h at room temperature under shaking. Afterwards, the mixture was washed three times with 1 mM PBS-EDTA pH 7.4 by applying a magnet (strong neodymium magnet, Germany) to separate unbound linker moieties. The remaining pellet was resuspended in 1 mM PBS-EDTA pH 7.4 and quantified by fluorescence calibration. For the copper-free click approach, 10 mg of the DBCO-PEG₄-NHS linker were resuspended in 500 μL of DMSO to obtain a stock solution with 20 mg mL^{-1} . This stock solution could be used for several months being stored at $-20 \text{ }^\circ\text{C}$. As before, linker ratios were calculated based on 3 nmol mg^{-1} amino groups on the nanocarrier. For example, 1 mg of nanocarriers (100 μl) was reacted with

4. The conjugation strategy affects antibody orientation and targeting properties of nanocarriers

1.95 μg DBCO-PEG₄-NHS linker (1 μL of 2 mg mL⁻¹ DBCO-PEG₄-NHS linker stock solution) for a 1:1 ratio, 19.5 μg DBCO-PEG₄-NHS linker (9.75 μL of 2 mg mL⁻¹ DBCO-PEG₄-NHS linker stock solution) for 1:10 ratio and so forth. The reaction was incubated overnight under constant shaking at room temperature. The next day, the mixture was washed three times with PBS by applying the neodymium magnet to separate unbound linker moieties. The remaining pellet was resuspended in PBS and quantified by fluorescence calibration.

Nanocarrier Quantification. To determine the amount of nanocarrier and nanocarrier-conjugates, a fluorescence calibration of the nanocarrier was conducted. The unfunctionalized nanocarriers were utilized as a standard and the samples diluted based on the initial mass used. All probes, including the standard, were prepared as duplicates in deionized water. Fluorescence was measured by the Infinite M1000 plate reader (Tecan) with an excitation wavelength of 552 nm and emission of 580 nm.

Traut's Modification of Antibody-Lysine Residues. The procedure for thiolation of the antibodies (mouse α -hamster CD11c clone N418, and α -hamster IgG isotype control clone HTK888, both Biolegend, U.S.A) lysine residues was partially adapted from the Traut's reagent and Micromod's Technote 201 manufacturer's instructions. In summary, a buffer exchange to 1 mM PBS-EDTA pH 8.0 was conducted for the antibodies with a Zeba™ Desalting Column after the manufacturer's instructions. Subsequently, the antibody concentration was quantified by Pierce 660 nm and the respective amount of Traut's reagent was calculated dependent on the obtained antibody concentrations. The Traut's reagent was prepared as a stock solution in 1 mM PBS-EDTA pH 8.0 (14 mM stock = 2 mg mL⁻¹). For example, 147 μg (490 μL) of antibody were reacted with 7 μL of the 14 mM Traut's stock solution for a 100x molar excess of Traut's reagent. The modification of antibodies with the Traut's reagent was conducted for 1 h at room temperature. Conclusively, the Traut's reagent was removed from the modified antibody by performing another buffer exchange, followed by a final determination of the concentration by Pierce 660 nm. The modified antibodies were directly tested for thiolation or conjugated to functionalized nanocarriers via thiol-maleimide chemistry.

Enzymatic Modification of Antibody Glycans. The azide modification of the antibodies (α -CD11c, α -IgG isotype) was conducted according to the manufacturer's instructions (Site Click™ Antibody Azido Modification Kit). Briefly, the carbohydrate domain at the F_c region of the concentrated antibody was modified by cleaving the galactose residues via β -galactosidase for 6 h at 37 °C. Afterwards, the azide group was attached by applying the GalT (Y289L) enzyme in combination with the UDP-GalNAz donor in an overnight reaction at 30 °C. Finally, the azide-modified antibody was purified and concentrated for further

experiments, including Pierce 660nm Protein Assay, testing for azide modification as well as conjugation to functionalized nanocarriers via copper-free click chemistry.

Antibody Quantification. The total amount of antibody or protein concentrations were quantified by using the Pierce 660nm protein assay according to the manufacturer's instructions. BSA (bovine serum albumin) was used as a standard by preparing a dilution series in demineralized water. The Infinite M1000 plate reader (Tecan) measured all samples at an optical density of 660 nm, including the standard, in duplicates.

Detection of Antibody Modification. Comparison between modified and unmodified antibodies in combination with a linker of known mass was achieved by applying SDS-PAGE in combination with either silver staining or Coomassie staining. For each chemistry, a specific linker was applied. The MeO-PEG-Mal (5 kDa) linker (Sigma, U.S.A.) for thiol-maleimide chemistry and the DBCO-mPEG (5 kDa) linker (Iris Biotech, Germany) for copper-free click chemistry. In case of the thiol-maleimide chemistry, the thiolation detection was calculated based on the assumption of five possible thiol groups to be conjugated. For the copper-free click chemistry, the azide detection was calculated based on four azide groups to be linked. Conjugation with the respective detection linker was conducted overnight at room temperature under shaking. Analysis by SDS-PAGE was conducted either under reduced or non-reduced conditions. Samples were prepared in a total volume of 40 or 60 μ L. The desired antibody amount was adjusted with demineralized water to a total volume of 26 μ L for the 40 μ L approach (all volumes can be adjusted to the 60 μ L approach by multiplying the volume with 1.5). Furthermore, 4 μ L of NuPAGE™ sample reducing agent (4 μ L demineralized water for non-reduced samples) and 10 μ L of NuPAGE™ LDS sample buffer were added and incubated at 70 °C for 10 min. The samples were transferred into the chambers of a Bolt™ 10% Bis-Tris Plus Gel submerged in 1X NuPAGE™ MES SDS Running Buffer and run for 1 – 6 h at 110 – 120 V. SeeBlue™ Pre-Stained Standard was used as molecular weight marker. The visualization of the proteins was conducted by applying either silver staining (SilverQuest™) or Coomassie staining (SimplyBlue™ SafeStain) according to the manufacturer's instructions.

Antibody to Nanocarrier Conjugation. The Sulfo-SMCC linker with its maleimide group was binding the terminal sulfhydryl groups of the modified antibody to form the conjugate via thioether bonding. In case of the DBCO-linker, the copper-free click reaction between the alkyne group of the DBCO and the azide group of the modified antibody was employed to generate the conjugate with a stable triazole formation. Maleimide functionalized nanocarriers were synthesized with the thiolated antibodies for three hours at room temperature under shaking (in 0.1 mM PBS-EDTA pH 7.4). DBCO-functionalized nanocarriers were overnight conjugated with the azide-modified antibodies at room temperature under shaking (in PBS).

After incubation, the maleimide or DBCO conjugates were washed three times with 0.1 mM PBS-EDTA pH 7.4 or PBS, respectively, by using a magnet. Finally, the conjugates were resuspended in the respective media and utilized for further experiments or stored at 4 °C. Before testing the nanocarrier conjugates in the dendritic cell uptake experiments, they were analyzed by flow cytometry to detect the covalently bound antibodies. This was performed by utilizing a secondary FITC labeled anti-hamster antibody and the unfunctionalized nanocarriers as a negative or positive control, respectively.

Detection of Unbound Antibodies. For the detection of unbound antibodies after the Antibody to Nanocarrier Conjugation, each magnetically separated wash fraction was collected and analyzed in the DC2.4 cell line via flow cytometry. For this purpose, the supernatant and washes were collected and concentrated to a final volume of 350 μL in PBS-EDTA (thiol-maleimide chemistry) or PBS (copper-free click chemistry) using the Savant DNA120 SpeedVac Concentrator (Thermo Fisher). The supernatants and washes of the CD11c and IgG conjugates with an antibody amount of 7.5 μg were analyzed. For the detection of unbound antibodies, 1.5×10^5 cells mL^{-1} were used for each condition in 100 μL PBS in 1.5 mL tubes. All samples were analyzed in triplicates ($n = 3$). In the first step, the cells were centrifuged at 300 g for 5 min and the cell pellets were resuspended in 100 μL of the supernatants and/or the three washes. After an incubation time of 30 min at 4°C, the cells were centrifuged again at 300 g for 5 min. Then, the cell pellets were resuspended in 100 μL PBS containing 0.5 μg (1 μL , 1:100) of the secondary FITC Goat anti-hamster (Armenian) IgG antibody (polyclonal antibody clone Poly4055, Biolegend). After an incubation time of 30 min at 4 °C, the cells were centrifuged at 300 g for 5 min. Finally, the cell pellet was resuspended in 1 mL PBS and analyzed by flow cytometry.

Dendritic Cell Uptake Experiments. For the cell uptake experiments, 1.5×10^5 cells mL^{-1} were seeded per well in a 24-well plate and left to attach overnight in a humidified incubator at 37 °C and 5% CO_2 . The next day, dependent on the experiment, the FBS containing medium was exchanged to medium without FBS and left for one to two hours so that the cells could adapt to the serum-free environment. In case of FBS dependent experiments, the medium was exchanged to a new FBS containing medium and left for one to two hours. All samples were prepared in triplicates if not stated otherwise and incubated for 2 h with a concentration of 75 $\mu\text{g mL}^{-1}$ in 250 μL of medium per well. For the mouse plasma incubation, each sample was pre-incubated for one hour at 37 °C shaking in a 1:1 ratio with the plasma source. Afterwards, the plasma was exchanged to IMDM without FBS by using a magnet and 75 $\mu\text{g mL}^{-1}$ in 250 μL of medium were incubated with the dendritic cells. After the two-hour incubation, the cells were washed with 1 mL PBS and detached via 250 μL 2 mM PBS-EDTA for 10 min at 4 °C. Afterwards, the cells were transferred from the well into a 1.5 mL micro tube by adding 250 μL

of FBS containing medium to the cells in the well and pipetting it up and down to detach as many cells as possible. For the cell viability assay, the cells were centrifuged at 300 g for 5 min and the cell pellet was resuspended in 100 μ L Zombie Agua (Biolegend, U.S.A/ previously diluted 1:500 in PBS). After 15 min of incubation at 4 °C in the dark, the cells were centrifuged again at 300 g for 5 min and the cell pellet was resuspended in 1 mL PBS ready to be analyzed by flow cytometry.

Blocking Experiments. All blocking experiments were performed in 250 μ L IMDM medium without FBS for 30 minutes at 4 °C. The CD11c (monoclonal antibody clone N418, Thermo Fisher) blocking was first tested with four different antibody concentrations (Figure 4.S6). After blocking, a fluorescence-conjugated CD11c antibody (CD11c monoclonal antibody clone N418, PECyanine7, Thermo Fisher) was used to check for free or blocked CD11c integrins on the cell surface, respectively. This validation resulted in a final CD11c blocking concentration of 7.5 μ g mL⁻¹ before the antibody nanocarrier conjugates cell uptake. The antibody nanocarrier conjugates cell uptake was conducted with a sample concentration of 75 μ g mL⁻¹ for 30 – 40 min at 4 °C for both, the CD11c and non-blocking reference.

Flow Cytometry. Quantification of nanocarriers or conjugates taken up by cells as well as the detection of the attached antibodies by secondary antibody testing was analyzed by flow cytometry. The red fluorescence of the nanocarriers was detected by the YL1 channel with an excitation laser of 561 nm and a 585/16 nm band pass filter for emission. Cell viability with the Live/Dead fixable Zombie Agua (Biolegend, U.S.A) was performed by using the VL2 channel with an excitation laser of 405 nm and a 512/25 nm band pass filter for emission. Data analysis was performed by applying Attune™ NxT Software. Here, the cell population was selected with a FSC/SSC scatter plot, excluding cell debris populations. The gated events of viable cells were evaluated by the fluorescent signal expressed as median fluorescence intensity (MFI) or as the percentage of gated events/cells. For the secondary antibody testing, 2 μ g of sample were added to 1 μ g of secondary antibody in 20 μ L PBS and incubated for 30 min at 4 °C in the dark. Unfunctionalized nanocarriers with and without the secondary antibody were applied as controls. After incubation, the samples were added up to 1 mL PBS and analyzed by flow cytometry. The FITC detection of the secondary antibody was performed by using the BL1 channel with an excitation laser of 488 nm and a 530/530 nm band pass filter for emission.

Visualization of Intracellular Localization by cLSM. In order to demonstrate the internalization effect of antibody functionalized nanocarriers in cells, confocal laser scanning microscopy (cLSM) was employed. Experiments were conducted on the LSM SP5 STED Leica Laser Scanning Confocal Microscope (Leica, Germany), composed of an inverse fluorescence

microscope DMI 6000CS equipped with a multi-laser combination using a HCX PL APO CS 63 x 1.4 oil objective. Nanocarriers were excited with the excitation laser 561 nm and detected with an emission filter at 570 – 599 nm. The cell membrane was stained with CellMask DeepRed (5 mg mL⁻¹, Thermo) using the excitation laser 633 nm, detected at 660 – 700 nm. For the visualization of the CD11c blocking experiment, 5 x 10⁴ cells in 200 µL IMDM with 5% FBS were seeded in a well of a 15 µ-Slide 8 well glass bottom (ibidi). After an overnight incubation at 37 °C and 5% CO₂ in the incubator, the cells were blocked with 7.5 µg mL⁻¹ CD11c antibodies (monoclonal antibody clone N418, Thermo Fisher) in IMDM medium without FBS. After the incubation, the wells were washed with PBS and an antibody nanocarrier conjugate uptake with 75 µg mL⁻¹ was performed for 30 min at 4 °C. Then, the wells were washed with PBS and the cells fixed for 15 min with 4% paraformaldehyde (PFA). Afterwards, the cells were stored in PBS at 4 °C until being further processed for image acquisition. For the visualization of intracellular localization, 5 x 10⁴ cells in 200 µL IMDM with 5% FBS were seeded in a well of a 15 µ-Slide 8 well glass bottom (ibidi). After an overnight incubation at 37 °C and 5% CO₂ in the incubator, the cells were treated with the respective sample in medium with 5% FBS as well as pre-incubated with mouse plasma proteins. After the two-hour incubation with a concentration of 75 µg mL⁻¹, the wells were washed with PBS and the cells fixed for 15 min with 4% paraformaldehyde (PFA). Afterwards, the cells were stored in PBS at 4 °C until being further processed for image acquisition. Cell membrane staining was conducted shortly before the cLSM analysis for 5 min in the dark (1:1.000 in PBS).

Incubation and Visualization of Mouse Plasma. SDS-PAGE and silver staining visualized adsorbed mouse plasma proteins on nanocarrier conjugates. First, the samples were incubated with the mouse plasma (GeneTex, California, U.S.A) at a 1:1 volume ratio for 1 h at 37 °C under shaking. After the incubation, the plasma was removed and the samples were washed three times with PBS, using a magnet. For the protein desorption, the washed pellet was resuspended in 100 µl desorption buffer (2% (w/v) SDS + 62.5 mM Tris-HCl in 3 mL deionized water) and incubated for 10 min at 70 °C under shaking. Afterwards, the magnet was applied to separate desorbed proteins from the nanocarriers. The denatured proteins containing supernatants were quantified by Pierce 660nm Protein assay and 3 µg were used for SDS-PAGE, visualized by silver staining.

Size and Charge of Antibody Nanocarrier Conjugates. The determination of size and charge of synthesized conjugates is important to estimate differences between unfunctionalized nanocarriers and those that are conjugated to a linker with and without the antibody. Light scattering measurements were performed on an ALV spectrometer consisting of a goniometer and an ALV-5004 multiple-tau full-digital correlator (320 channels) which allows measurements over an angular range from 30° to 150°. A He-Ne Laser (wavelength of

632.8 nm) is used as light source. For temperature-controlled measurements the light scattering instrument is equipped with a thermostat from Julabo. 1 μL of unfiltered dispersion was diluted with 1 ml PBS which was previously filtered through membrane filters with a pore size of 0.20 μm (GS Millipore). Measurements were performed at 20 °C at 7 (dynamic) angles ranging from 30° to 150°. The zeta (ζ) potential of the nanocarriers and synthesized conjugates (10 μL sample) was measured with a Zetasizer Nano – Z Series (Malvern, Germany) in 1 mM potassium chloride solution (1 mL KCl). The results of the measurements are listed in the table 4.S1.

TEM Measurements. The morphology of the particles was investigated using a FEI Tecnai F20 transmission electron microscope operating at voltage of 200 kV. The different samples were diluted to a 75 $\mu\text{g mL}^{-1}$ particle concentration in the solvent of interest, 4 μL were deposited on a carbon coated grid and the excess solvent was blotted away with filter paper.

In solution digestion. First, SDS was removed from protein solutions by applying Pierce detergent removal columns (Thermo Fisher, Germany). The digestion was based on previously established protocols^{84, 85}. Briefly, ProteoExtract protein precipitation kit (CalBioChem, Germany) was used to precipitate proteins overnight according to the manufacturer's instructions. Proteins were isolated by centrifugation (14.000 g, 10 min), followed by several washing steps and resuspension in RapiGest SF (Waters Cooperation, Germany) dissolved in ammonium bicarbonate (50 Mm) buffer. Then, the samples were incubated at 80 °C for 15 min. Protein disulfide bonds were reduced using Dithiothreitol (Sigma, Germany) at a final concentration of 5 mM. The reaction was executed for 45 min at 56 °C. Iodoacetamide (final concentration 15 mM, Sigma, Germany) was used for alkylation of proteins in the dark for 1 h. A protein:trypsin ratio of 50:1 was chosen for digestion and the reaction was performed over 14 h at 37 °C. The reaction was quenched by adding 2 μL hydrochloric acid (Sigma, Germany). Ultimately, degradation products of RapiGest SF were removed by centrifugation of the peptide samples at 14.000 g for 15 min (4 °C).

Liquid chromatography-electrospray ionization mass spectrometry (LC-MS). For absolute protein quantification, all specimen were diluted with 0.1% formic acid and spiked with 50 fmol μL^{-1} Hi3 E. coli standard (Waters Cooperation)⁸⁶. In a nanoACQUITY UPLC system, the tryptic peptides were transferred to a C18 analytical reversed phase column (1.7 μm , 75 μm x 150 mm) and a C18 nanoACQUITY trap column (5 μm , 180 μm x 20 mm). For separation, two mobile phases with (A) consisting of 0.1% (v/v) formic acid in water and 0.1% (v/v) formic acid with acetonitrile and a gradient of 2% to 37% of mobile phase (B) were applied for a time period of 70 min. The nanoACQUITY UPLC system was connected to a Synapt G2-Si mass spectrometer and electrospray ionization (ESI) was performed in positive ion mode

using a NanoLockSpray source. A sample flow rate of $0.3 \mu\text{l min}^{-1}$ was selected and Glu-Fibrinopeptide, as a reference component, was infused with $150 \text{ fmol } \mu\text{l}^{-1}$ at a flow rate of $0.5 \mu\text{l min}^{-1}$. The Synapt G2-Si was operated choosing the resolution mode and data-independent acquisition (MSE) experiments were conducted. The data was acquired for a time of 90 min with a mass to charge range of 50 – 2000 Da, a scan time of 1 s and ramped trap collision energy from 20 to 40 V. Data acquisition and processing was performed using MassLynx 4.1.

Protein identification. The continuum data was post lock mass corrected and further processed by Progenesis Q1 (2.0) applying a reviewed mouse data base (Uniprot) for peptide and protein identification. Noise reduction thresholds were set to 120, 25, and 750 counts by using several processing parameters for low energy, high energy and peptide intensity. For absolute quantification, the Hi3 *E. coli* standard sequence information was added to the mouse data base. Following criteria were chosen for protein and peptide identification: one missed cleavage, maximum protein mass 600 kDa, fixed carbamidomethyl modification for cysteine, variable oxidation for methionine and protein false discovery rate of 4%. At least two assigned peptides and five assigned fragments are required for protein identification. Peptide identification relies on three assigned fragments. Identified peptides with a score parameter below 4 were discharged. The TOP3/Hi3 approach provided the amount of each protein in fmoI^{87} .

Statistical Analysis. Using GraphPad Prism 5, two-way analysis of variance (ANOVA) was performed with Bonferroni's post-hoc-test choosing a confidence interval of 99.9% ($P < 0.001^{***}$) and 95% ($P < 0.05^*$) significance.

4.4 Results and Discussion

Two conjugation strategies were compared to covalently attach a targeting antibody onto a nanocarriers' surface (Figure 4.1). First, the amine groups on the nanocarriers' surface were functionalized with two different linkers via NHS chemistry (size and charge of the nanocarrier and synthesized nanocarrier conjugates are listed in Table 4.S1). Each linker provides a specific reactive moiety, which is necessary for the antibody attachment. The modification of the antibodies was carried out by either the random thiolation through Traut's Reagent (2-Iminothiolan) or by a site-directed enzymatic modification at the F_c region. In a second step, the linker-functionalized nanocarriers were conjugated to the modified antibodies by using either the thiol-maleimide or the copper-free click chemistry. The targeting efficiency of the resulting nanocarrier conjugates was analyzed in a cell-based assay via flow cytometry and confocal laser scanning microscopy (cLSM).

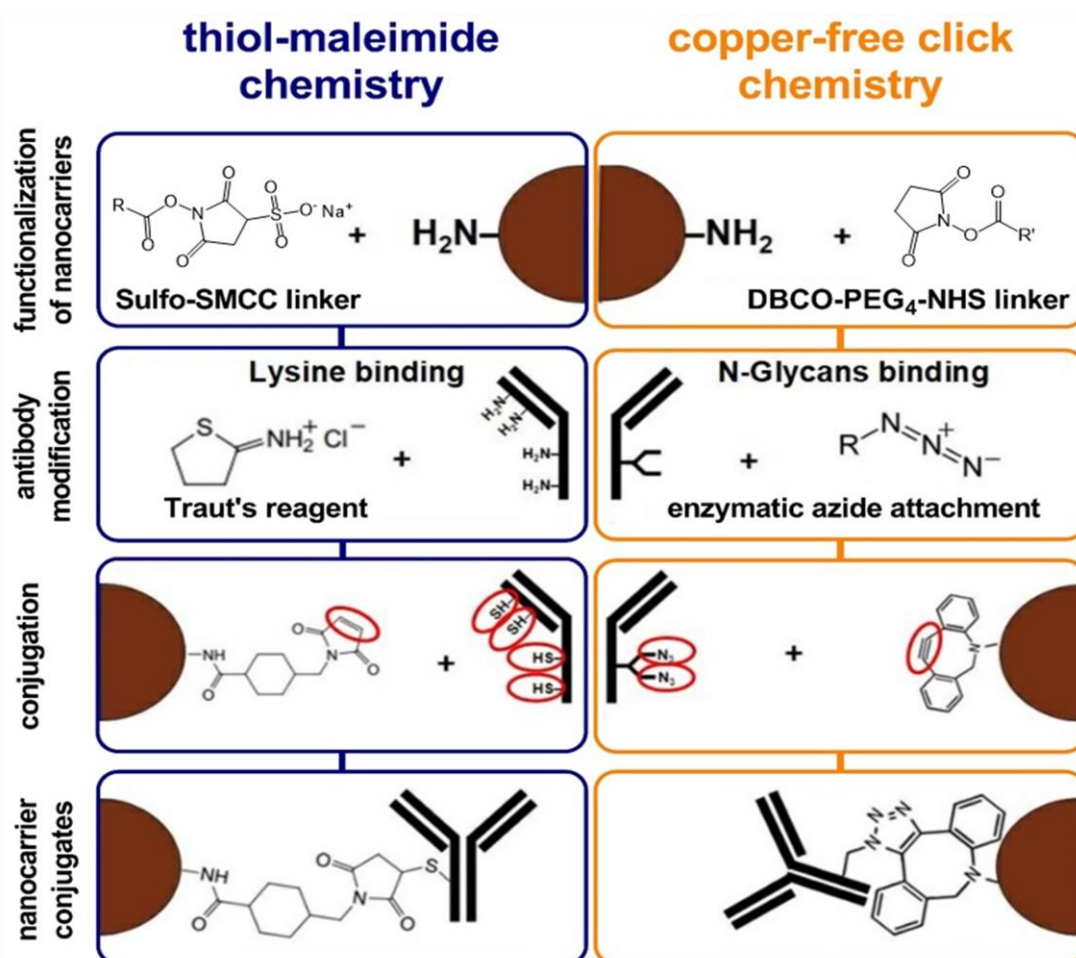


Figure 4.1: The schematic workflow of generating antibody nanocarrier conjugates based on two different chemical strategies. Magnetic nanocarriers are shown in brown, targeting antibodies in black. Chemical formulas are not fully represented. This illustration is not suited for scaling. R = Sulfo-SMCC (Thermo, Cat. No.: 22122), R' = DBCO-PEG₄-NHS ester (Jena Bioscience, Cat. No.: CLK-A134-10).

The modification of monoclonal CD11c antibodies

In the case of the thiol-maleimide chemistry, antibodies were chemically modified by reacting the primary amines of lysine residues with Traut's reagent in the absence of a regiochemical control, generating antibodies with free sulfhydryl groups. For the copper-free click chemistry, antibodies were enzymatically modified at their N-glycans, which are positioned at the F_c region to generate antibodies with free azido groups.

The validation of the antibody modification was investigated by SDS-PAGE and visualized by silver staining (Figure 4.2).

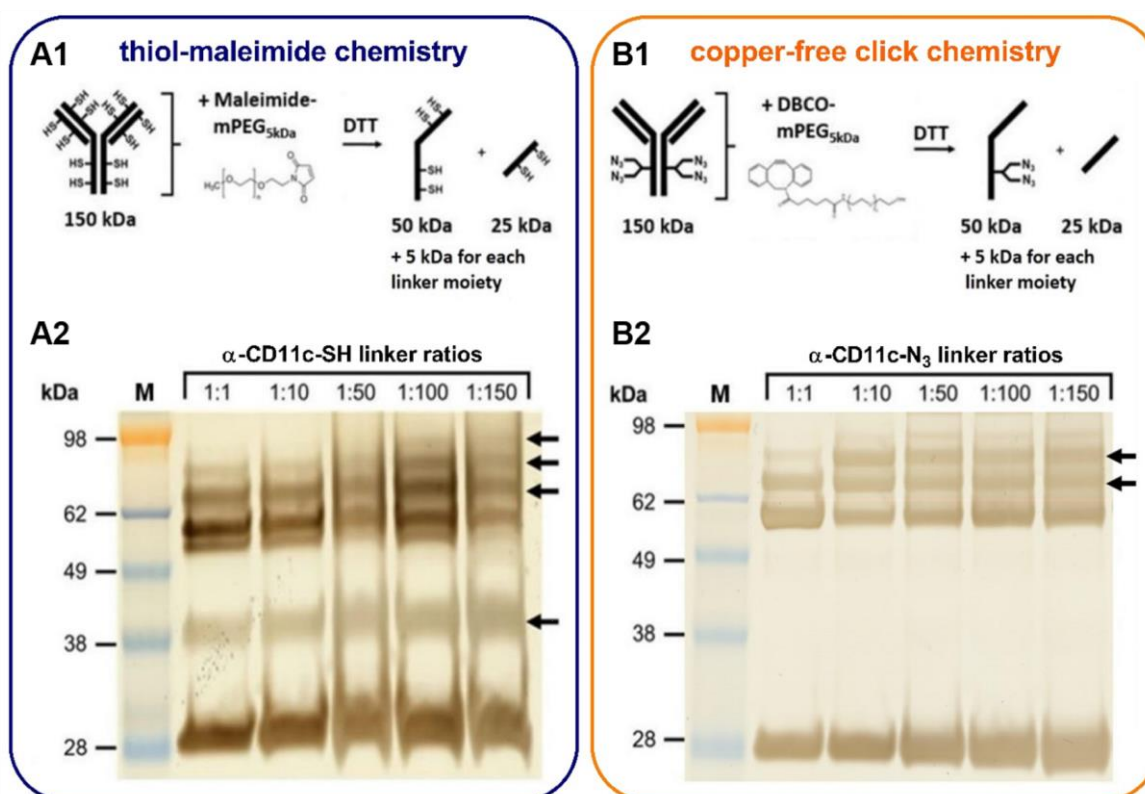


Figure 4.2: The detection of antibody modification. The antibody linker reaction scheme for the thiol-maleimide chemistry is shown in **A1** and for the copper-free click chemistry in **B1**. Here, the previously modified antibodies (150 kDa) were conjugated to the respective 5 kDa linkers following the reduction by Dithiothreitol (DTT), which enables the visualization of conjugation of the linkers to the heavy (50 kDa) or light (25 kDa) chain. For the thiol-maleimide conjugation, first, the antibodies were modified with Traut's reagent and then coupled to five different Maleimide-mPEG_{5kDa} linker ratios overnight (**A2**). Antibodies were enzymatically modified and reacted to five different DBCO-mPEG_{5kDa} linker ratios overnight (**B2**). All samples were prepared according to reduced SDS-PAGE instructions and boiled for 10 min at 70°C. The molecular weight marker (M) was applied with 5 µL and each sample was loaded with 3 µg onto a 10% Bis-Tris Plus gel and run for 60 min at 120 V. The visualization was conducted by silver staining.

For this concept, modified antibodies were reacted with a functional linker (PEG_{5kDa}-Maleimide or PEG_{5kDa}-DBCO) and further applied to SDS-PAGE under reducing conditions (A1 and B1).

This enabled a mass-based separation of the different antibody linker species and a distinguishable observation between the heavy and the light chain modification of the antibody. The thiol-maleimide chemistry approach showed next to the unconjugated heavy chain at 50 kDa up to three additional heavy chain linker species ranging between 55, 60, and 65 kDa (A2, black arrows). This modification was achieved at equal molar ratios (1:1), carrying up to two linker moieties. At the lower molecular weight region, the light chain was observed at around 30 kDa. An additional band at around 40 kDa was detected, representing a conjugation of two linker units to the light chain (A2 black arrow). In contrast, via the use of the copper-free click chemistry the antibody was only modified at the heavy chain (B2 black arrows) and not the light chain. The addition of the PEG_{5ka}-DBCO linker molecule generated two additional heavy chain linker species at 55 and 60 kDa for all tested linker ratios. The linker attachment efficacy was also demonstrated for the whole antibody molecules (150 kDa) and for the isotype control antibodies under non-reducing conditions (4.S1 – 4.S5).

The results therefore show that the antibody modification via Traut's reaction for the thiol-maleimide conjugation was mainly unspecific and modified the heavy and light chain. This broad modification can be explained by the high number of lysine residues (~80) on an antibody with around 10 of them being chemically accessible¹⁵⁵. This availability of lysine residues indicates that a precise control of the conjugation site cannot be guaranteed with the lysine amide coupling approach. For instance, some of the lysine residues are positioned in the antigen recognition, and therefore, a modification could potentially reduce the binding affinity of the antibody. Moreover, the abundance of lysine residues increases the number of conjugated antibody-nanocarrier configurations, which might have an impact on pharmacokinetics, pharmacodynamics, and cytotoxicity, as it has been observed for antibody-drug conjugates¹⁵⁶. Especially, antibodies attached with the two F_{ab} regions onto the surface of the nanocarrier will exhibit the F_c part of the antibody and therefore, can promote a mistargeting.

On the contrary, the enzymatic antibody modification for the copper-free click reaction was highly site-specific because only the heavy chain was modified (B2, black arrows). In this case, antibodies were selectively modified on the sugar residues present at the F_c region. All immunoglobulin G (IgG) subclasses are N-glycosylated at a single, conserved region at the F_c portion. This glycosylation site is positioned within the heavy chains CH2 domain at the amino acid asparagine 297 (N297)¹⁵⁷. The attached carbohydrate chain has a predominantly biantennary complex structure, which is usually composed of N-acetylglucosamine (GlcNAc) and mannose, followed by a variable addition of galactose (Gal), N-acetylneuraminic acid (NeuNAc), fucose (Fuc), as well as bisecting GlcNAc residues¹⁵⁸. In our case, using this site for the conjugation involved the unmasking of the GlcNAc residues by removing the terminal

Gal residues with β -Galactosidase, followed by the enzymatic β -galactosyl transferase reaction. The mutant bovine enzyme (Y289L-Gal-T1) transfers N-azidoacetylglucosamine (GalNAz) selectively to the unmasked GlcNAc residues of the N-linked IgG glycans^{159, 160}. The resulting azide-modified tags can then be used for the strain-promoted copper-free click reaction between the alkyne-functionalized (DBCO) nanocarrier and the azide-modified antibody. This strategy is of great advantage because it can be applied for any IgG isotypes with various N-glycosylation profiles¹⁵⁶.

In summary, the enzymatic modification provides the ability to attach a linker molecule to the antibody in a site-specific manner under mild reaction conditions without altering the antigen binding sites. In contrast, conventional attachment strategies, like the lysine approach, result in a non-specific antibody functionalization^{151, 156, 161}.

The amount of antibodies on the nanocarrier is crucial for a specific dendritic cell uptake.

In a next step, different antibody amounts were attached onto the nanocarriers' surface in order to investigate the lowest quantity that still evokes a specific cell response towards the murine dendritic cell line DC2.4. For this purpose, the integrin α X or CD11c was chosen as a target surface receptor because of its wide use as a defining marker for dendritic cells¹⁶² and its ability to mediate phagocytosis of, for example, antibody-bound nanocarriers¹⁶³. The CD11c antibody-based targeting was performed with an additional isotype control antibody, which exhibits a similar composition to that of the CD11c antibody, however, it lacks in a specific target binding. This allows to determine the contribution of non-specific binding via the F_c region of the antibody contrary to a specific binding via the F_{ab} region.

For this investigation, five different antibody quantities of 0.05 μ g, 0.5 μ g, 2.5 μ g, 7.5 μ g, and 12.5 μ g were chosen to be conjugated to 500 μ g of nanocarriers (Figure 4.3). In a first step, all nanocarrier conjugates were tested for the presence of the antibody on the surface using a labeled secondary antibody and analyzed by flow cytometry (Figure 4.3, A1 and B1). For the nanocarrier conjugates using the thiol-maleimide or the copper-free click chemistry, the CD11c and isotype antibodies were detected in a concentration dependent manner (Figure 4.3, A1 and B1).

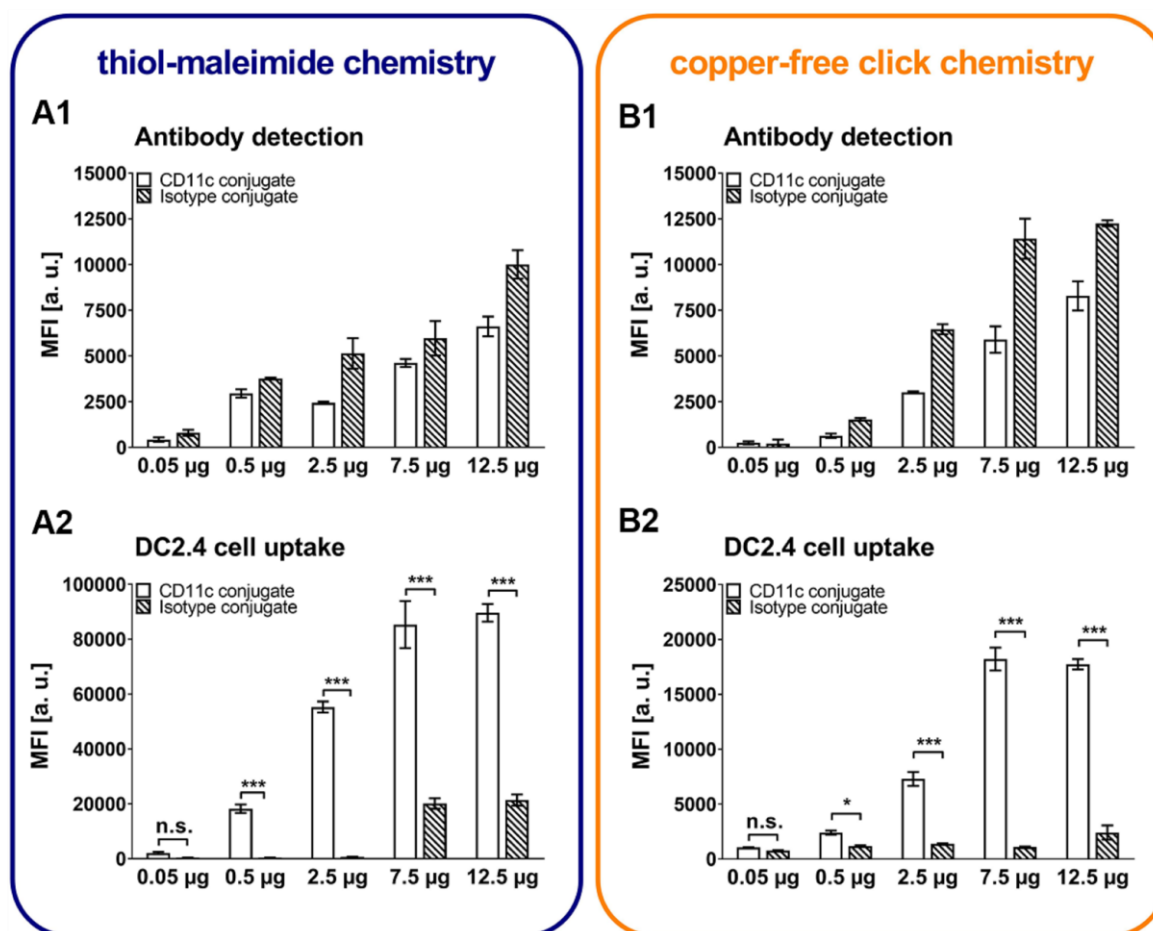


Figure 4.3: The amount of conjugated antibody on a nanocarrier is crucial for a precise dendritic cell targeting. For the secondary antibody test by flow cytometry (A1, B1), 2 µg of sample were reacted with 1 µg secondary antibody in PBS in a total volume of 20 µl. Values are given as mean ± SD (n = 2). The linker-functionalized nanocarriers as well as the conjugates were synthesized according to the respective chemistry. For the conjugation, 500 µg were conjugated with 0.05, 0.5, 2.5, 7.5, and 12.5 µg of respective antibody. The dendritic cell uptake (A2, B2) was conducted with a sample concentration of 75 µg mL⁻¹ in 250 µL of IMDM with 5% FBS for 2 h at 37 °C and 5% CO₂. Only viable cells are gated and analyzed by flow cytometry. Values are given as mean ± SD (n = 3). MFI [a.u.] = median fluorescence intensity [arbitrary units], n.s. = no significance, P<0.001***, P<0.05*.

The DC2.4 dendritic cell uptake was conducted with 1.5×10^5 cells mL⁻¹ in a culture medium containing fetal bovine serum (FBS) (Figure 4.3, A2 and B2). Additional serum proteins in the medium lead to the formation of a biomolecular corona around the surface of the nanocarriers representing a more physiological environment¹⁶⁴. The lowest antibody quantity on the thiol-maleimide nanocarrier conjugates showed no significant uptake by the dendritic cells. Starting at an antibody amount of 0.5 µg, a significant cell uptake of the CD11c conjugate compared to the isotype conjugate was observed (P<0.001***). This specificity increased for the 2.5 µg group to an even higher median fluorescence intensity (MFI). However, for higher antibody quantities of 7.5 and 12.5 µg, the unspecific cell uptake of the isotype conjugates was also increased.

4. The conjugation strategy affects antibody orientation and targeting properties of nanocarriers

In case of the copper-free click chemistry, the lowest antibody amount of 0.05 μg showed no significant cell uptake (Figure 4.3, B2). Starting from the 0.5 μg CD11c conjugate group, a slightly increased intensity was detected, compared to the corresponding isotype conjugate ($P < 0.05^*$). For the higher antibody amounts, the cellular uptake was strongly increased with an amount of 2.5 μg and reached a maximum at 7.5 μg ($P < 0.001^{***}$).

In a nutshell, different amounts of antibodies on the nanocarrier's surface showed that there is a certain antibody amount acting as a threshold that leads to a specific cell targeting. In fact, the actual amount of antibody molecules on a nanocarrier, which are believed to initiate an intended cell-based response, is an important value. However, reports about the introduction of a precise and controllable number of antibodies per nanocarrier are largely missing. Nevertheless, it is possible to generate nanocarriers with exactly one or two conjugated antibodies. In this attempt, gold nanocarriers with only one attached antibody suggested the best targeting efficiency in mice bearing MCF-7 xenografts¹⁶⁵. Furthermore, bioanalytical systems and biosensors have also demonstrated a better antigen-capturing activity for lower antibody densities on nanocarriers^{166, 167}.

Blocking dendritic targeting sides reveals a spatial orientation of the antibody on the nanocarrier

To further investigate the specific targeting ability of the nanocarrier conjugates additional blocking experiments were conducted. This included the blocking of the targeted CD11c ligands on dendritic cells. For the blocking experiment, a CD11c antibody concentration of 7.5 $\mu\text{g mL}^{-1}$ with an incubation time of 30 min at 4 °C prior to the cell uptake has been proven to be sufficient (Figure 4.S6). All tested conjugates were synthesized with an antibody amount of 7.5 μg (Figure 4.4, Figure 4.S7). Blocking CD11c had virtually no effect on the thiol-maleimide generated nanocarriers, because there was no difference between the unblocked condition (Medium^{-Serum}, white bar) and the blocked condition (grey bar). According to our data, which showed that the CD11c thiol-maleimide conjugates were taken up to a significant higher amount compared to the isotype conjugate, it can be assumed that an alternative uptake mechanism is addressed. This difference highlights that CD11c thiol-maleimide conjugates have a heterogeneous antibody arrangement on their surface. As soon as the CD11c integrin is blocked and targeting through the F_{ab} region of the antibody is no longer possible, the misplaced antibodies pointing their F_c region to the outside will cause the cell uptake by F_c receptors. Therefore, thiol-maleimide generated antibody nanocarriers compensate the uptake mechanism by a different arrangement of the antibody molecules on their surface. Moreover, copper-free click generated CD11c conjugates are effectively blocked to a comparable level of the unspecific isotype conjugate (4B). In addition, the visualization of the blocking

4. The conjugation strategy affects antibody orientation and targeting properties of nanocarriers

experiment by confocal laser scanning microscopy revealed the same outcome (Figure 4.S7). Blocking had no influence on the thiol-maleimide generated conjugates (high uptake for both CD11c conjugate and IgG conjugate), whereas the copper-free click generated conjugates showed almost no uptake (low uptake for both CD11c conjugate and IgG conjugate).

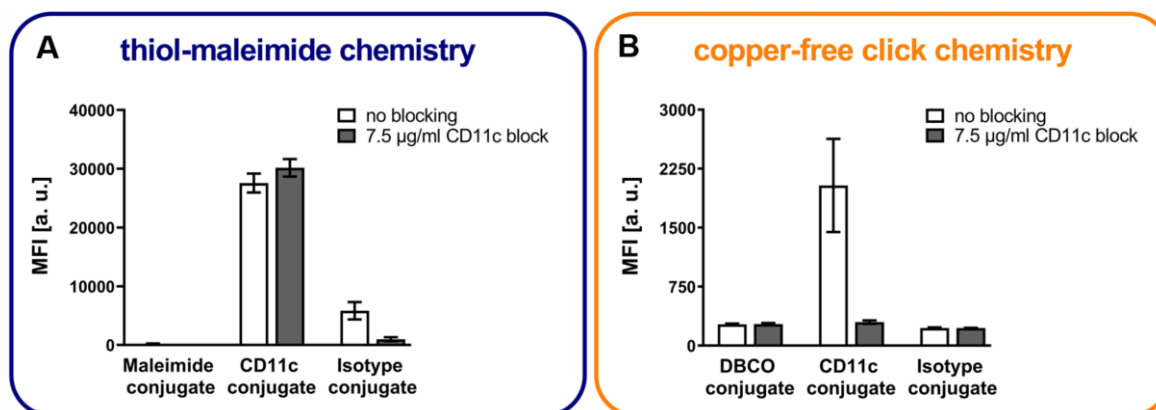


Figure 4.4: A proper conjugation influences site-directed targeting of dendritic cells. All linker-functionalized nanocarriers as well as the conjugates were synthesized according to the respective chemistry, either thiol-maleimide chemistry (A) or copper-free click chemistry (B). Blocking was conducted with a CD11c concentration of $7.5 \mu\text{g ml}^{-1}$ in $250 \mu\text{l}$ IMDM medium without FBS for 30 min at 4°C , followed by the cell uptake experiment with a sample concentration of $75 \mu\text{g mL}^{-1}$ in $250 \mu\text{l}$ IMDM medium without FBS per well for 30 minutes at 4°C . Only viable cells are gated and analyzed by flow cytometry. Values are given as mean \pm SD ($n = 3$). MFI [a.u.] = median fluorescence intensity [arbitrary units].

Furthermore, we investigated the detection of unbound antibodies in the supernatant and washes (Figure 4.S8) to attribute the F_{ab} -mediated targeting efficiency of the copper-free click generated CD11c conjugates to their spatial orientation. This investigation should highlight that there is no difference in the number of conjugated antibodies between the two conjugation chemistries. As a result, we demonstrated that in each magnetically separated wash fraction, the level of unbound antibodies was on a comparable detection level for each conjugation chemistry (Figure 4.S8 A) and that a certain amount of nanocarriers was lost during the washing process (Figure 4.S8 B).

Therefore, the conjugation strategy of linking an antibody on to the nanocarrier had a significant influence on the spatial orientation of the antibody molecule. In case of the copper-free click attached antibodies, this spatial orientation is referring to the conjugation of the antibody via its azido-modified N-glycans of the F_c region with the DBCO-functionalized nanocarrier surface. Given this spatial orientation, the unspecific F_c region is hidden from any cell surface interactions, while the specific F_{ab} region is pointing away from the surface being accessible to target the CD11c surface receptors.

Mouse plasma incubation influences the targeting ability of CD11c nanocarriers

To investigate the targeting efficiency of the antibody nanocarrier conjugates in a more physiological context, cellular experiments using mouse plasma were performed. In the biological environment, e.g. in blood, proteins are in constant interactions with the surface of the nanocarrier, forming the biomolecular corona¹⁶⁴. Therefore, it is of great importance to examine the binding affinity of the antibody nanocarrier conjugates in the presence of the biomolecular corona. In Figure 4.5, the cellular uptake experiments were performed using three different cell culture conditions. There was no significant difference for the conditions with and without FBS. The pre-coating of the nanocarrier conjugates with mouse plasma slightly reduced the cellular uptake, however, it did not diminish the targeting efficiency. In literature, it is shown that different protein sources alter the physicochemical properties of nanocarriers^{33, 44}, which can affect the antigen-antibody interaction, cellular targeting, and uptake behavior^{54, 168, 169}. Furthermore, it is important to consider a possible loss of antigen binding ability or a complete change of antibody nanocarrier functionality due to the corona. Indeed, our group already showed this effect for coupled and adsorbed antibodies on polystyrene nanocarriers. We demonstrated that pre-adsorbed CD63 antibodies keep their targeting ability and are not covered by the biomolecular corona compared to conjugated antibodies¹⁷⁰.

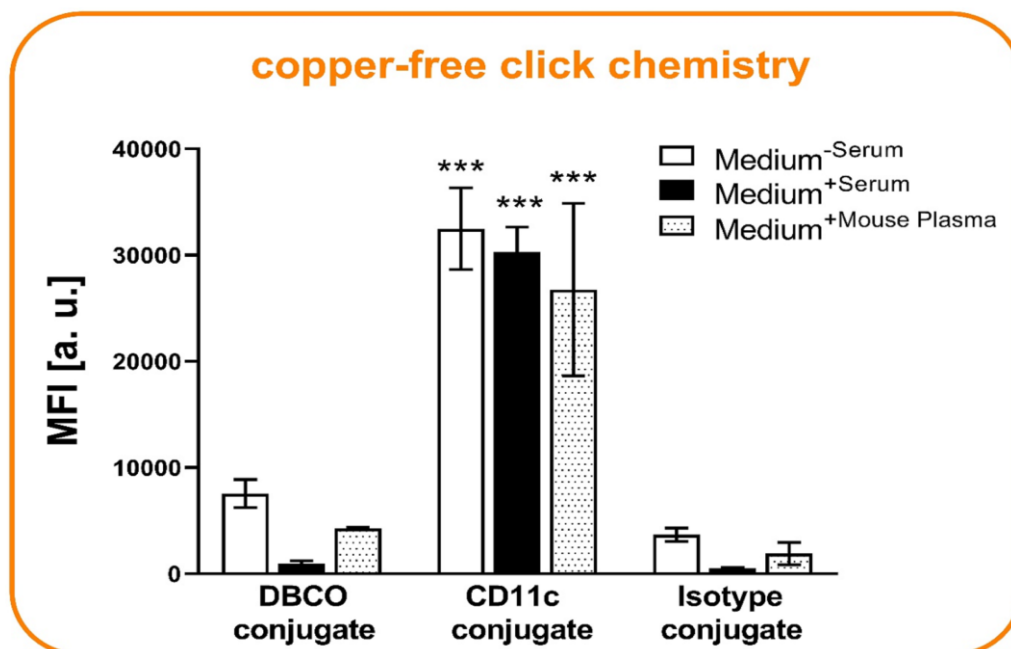


Figure 4.5: The influence of mouse plasma on the dendritic cell uptake. The dendritic cell uptake with a sample concentration of $75 \mu\text{g mL}^{-1}$ in $250 \mu\text{L}$ of IMDM with and without FBS for 2 h at 37°C and $5\% \text{CO}_2$ is shown. The mouse plasma samples are pre-incubated in the protein source for 1 h at 37°C . After a magnetic separation from the mouse plasma, the samples are diluted in IMDM without FBS for the cell uptake. Only viable cells are gated and analyzed by flow cytometry. Values are given as mean \pm SD ($n = 6$). MFI [a.u.] = median fluorescence intensity [arbitrary units]. ($P < 0.001^{***}$).

4. The conjugation strategy affects antibody orientation and targeting properties of nanocarriers

To additionally verify the intracellular localization of the nanocarrier-conjugates, confocal laser scanning microscopy images were taken (Figure 4.6). Two cell culture conditions, one being a medium with 5% FBS and the other being pre-incubated with mouse plasma were analyzed. Because there were no visual differences between these conditions, only mouse plasma incubated samples are representatively shown in the Figure 4.6. Additional images are summarized in Figure 4.S9.

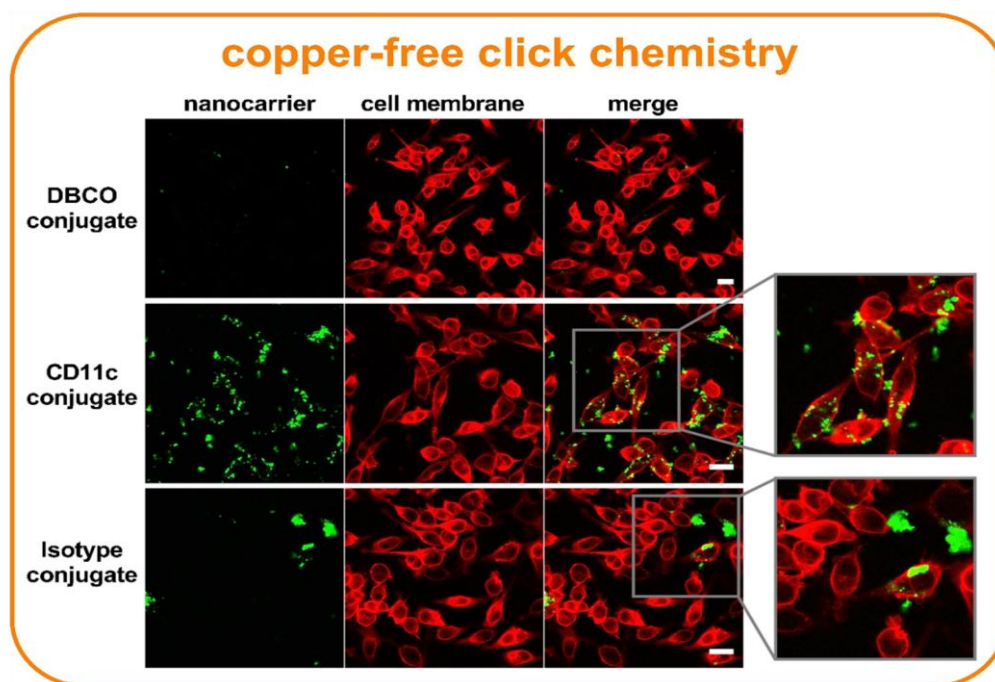


Figure 4.6: Site-directed targeting of dendritic cells by antibody nanocarrier conjugates. For the image acquisition, 5×10^4 cells per well were treated with $75 \mu\text{g mL}^{-1}$ pre-incubated mouse plasma samples in $200 \mu\text{l}$ IMDM without FBS. After the two-hour incubation, the wells were washed with PBS and the cells fixed for 15 min with 4% paraformaldehyde (PFA). Nanocarriers were excited with the laser 561 (emission filter 570 – 599 nm) and the cell membrane was excited with the laser 633 (emission filter 660 – 700 nm). All scale bars represent $20 \mu\text{m}$.

The images clearly indicate the difference between the targeting specificity of the CD11c conjugates in contrast to the isotype control or the DBCO linker-attached nanocarrier. No uptake was detected in the case of linker-functionalized nanocarriers (first row). The CD11c conjugates are mostly internalized in dendritic cells, with some of them being randomly attached to the surface of the cells (second row, enlarged image). The isotype conjugates are only taken up by a few dendritic cells or form clusters outside of the cells (third row, enlarged image). We additionally visualized the nanocarriers by TEM to confirm their colloidal stability in cell culture media under the same sample concentration (Figure 4.S10). According to our data, we observed that the pristine and antibody-modified nanocarriers formed small clusters that approx. matched in size to the values obtained by multi angle DLS (Table 4.S1).

4. The conjugation strategy affects antibody orientation and targeting properties of nanocarriers

Studies have shown that the cell uptake significantly increases during the first minutes and gradually slows down until reaching a plateau within two to three hours¹⁷¹⁻¹⁷³. Therefore, in the first phase, antibody nanocarrier conjugates might directly adsorb onto the cell membrane, while at a later state, internalization through an endocytic pathway is initiated. CD11c conjugates which have been incubated for two hours show this behavior as some are still attached to the cell membrane, while others are already internalized (Figure 4.6).

For a quantitative analysis of the murine biomolecular corona, the label-free mass spectrometry was applied to identify and characterize the biological identity of the antibody targeted nanocarriers. In Figure 4.7, all identified proteins were divided into nine groups, and the respective values were plotted as a percentage.

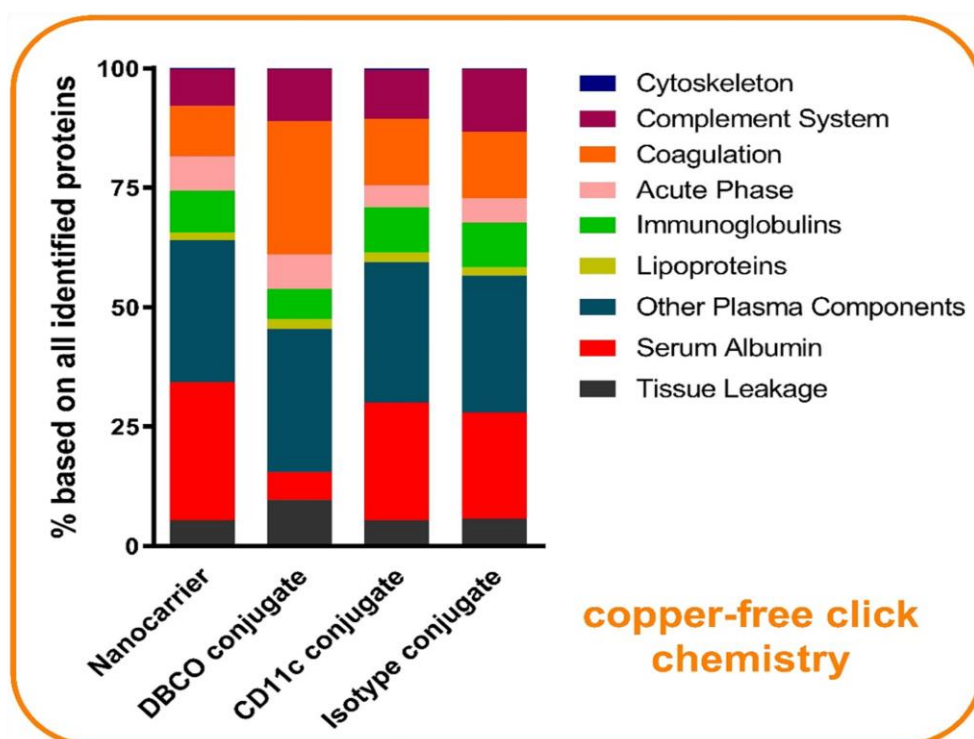


Figure 4.7: The antibody-functionalization of nanocarriers has almost no influence on the protein surface adsorption. The percentage based on all identified proteins analyzed by LC-MS is shown. $n = 2$ with each technical triplicates.

The comparison of the individual groups illustrated almost no difference between the identified proteins of the nanocarrier and the antibody conjugated nanocarrier groups. Only for the DBCO linker-functionalized nanocarrier conjugate without the antibody, lower amounts of serum albumin and higher amounts of coagulation proteins were observed. Serum albumin is not only the most abundant murine corona protein found on our antibody nanocarrier conjugates, but moreover, it is the most abundant serum protein for many species, including mouse and human^{102, 174}. Dai *et al.* have examined the targeting ability of antibody-mimetic

4. The conjugation strategy affects antibody orientation and targeting properties of nanocarriers

ligand-functionalized nanocarriers under different conditions using human serum or human serum albumin alone. They showed that the mixture of different proteins in the human serum corona inhibited cell association, while human serum albumin alone enhanced the targeting ability of the nanocarriers³⁹. In comparison to their findings, we detected a general enrichment of murine serum albumin on our targeted nanocarriers, which could potentially support an uptake by dendritic cells. However, having a complex mixture of murine plasma proteins acting as a corona, the balance between the targeting ability of the conjugated antibody in cooperation with serum albumin or other candidates, either facilitates or impedes a precise cell targeting. For a more detailed analysis, the top 20 most abundant proteins are highlighted in a heat map (Figure 4.8).

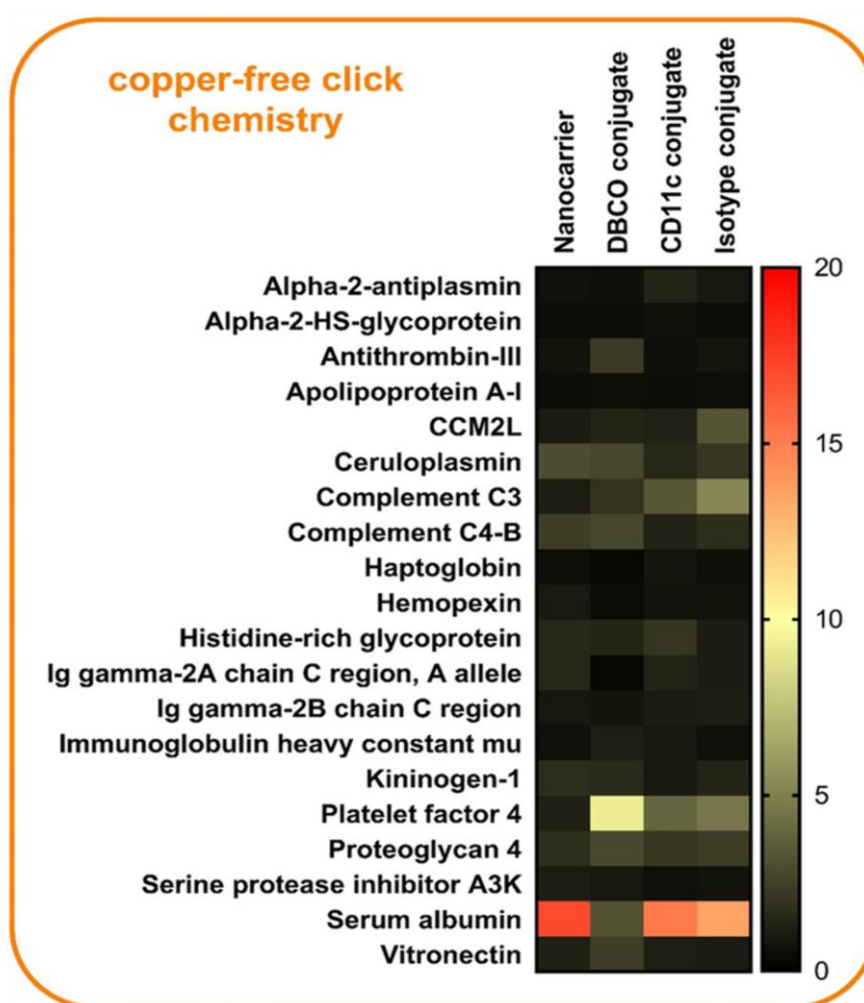


Figure 4.8: Serum albumin is the most abundant protein found on targeted nanocarriers. A heat map of the top 20 most abundant corona proteins. Values are expressed in % based on the total amount of all identified proteins. n = 2 with each technical triplicates. CCM2L = Cerebral cavernous malformations 2 protein-like.

As already shown in the identified protein groups, serum albumin is the most abundant protein detected in the corona of the antibody nanocarrier conjugates. Linker-functionalized nanocarrier conjugates (DBCO conjugate) highly adsorbed platelet factor 4. Additional

4. The conjugation strategy affects antibody orientation and targeting properties of nanocarriers

abundant mouse plasma proteins included ceruloplasmin, complement C3 and complement C4-B, histidine-rich glycoprotein, kininogen-1, serine protease inhibitor A3K as well as vitronectin. Other murine biomolecular corona studies on differently composed nanocarriers have also identified these proteins to be commonly adsorbed^{174, 175}.

In general, the findings of the murine biomolecular corona suggest that the targeting ability of CD11c antibody conjugated nanocarriers is not induced by corona proteins, although they influence the targeting process. Therefore, antibody targeted nanocarrier conjugates must be examined in the *in vivo* mouse model.

4.5 Supporting Information

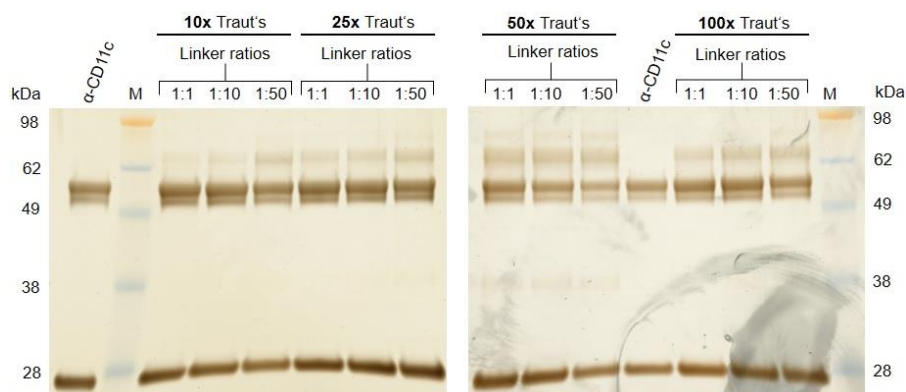


Figure 4.S1: Evaluation of thiolated and linker-reacted CD11c antibodies under reduced conditions. For the analysis, 10 μL of $\alpha\text{-CD11c}$ (21 μg) were reacted with 1; 2.5; 5; and 10 μL of Traut's reagent (1.4 mM) for 1 h at room temperature, representing a Traut's excess of 10; 25; 50 and 100 mol to $\alpha\text{-CD11c}$, respectively. For the overnight coupling, 4 μg of modified $\alpha\text{-CD11c-SH}$ (20 μL) were reacted for each Traut's group in an $\alpha\text{-CD11c-SH}$ to maleimide linker ratio of 1:1; 1:10 and 1:50 (0.65 $\mu\text{g } \mu\text{L}^{-1}$ linker stock = 1:1 ratio of linker to $\alpha\text{-CD11c}$). All samples were prepared according to reduced SDS-PAGE instructions (40 μL approach) and boiled for 10 min at 70 $^{\circ}\text{C}$. The molecular weight marker (M) was applied with 5 μL and each sample at 2 μg onto a 10% Bis-Tris Plus gel and run for 111 min at 120 V. Visualization was conducted by silver staining.

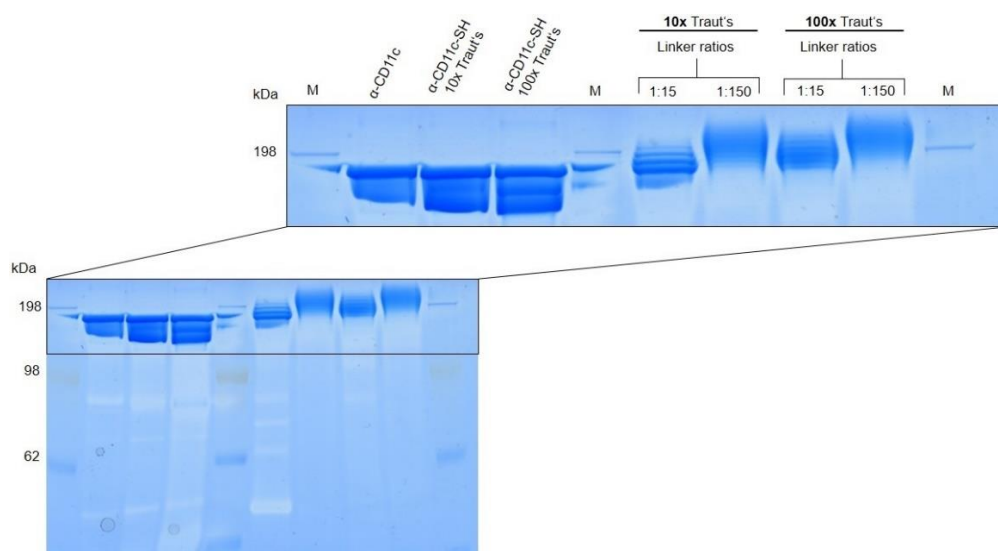


Figure 4.S2: Evaluation of thiolated and linker-reacted CD11c antibodies. For the Traut's modification, 74 μg of $\alpha\text{-CD11c}$ ($\sim 245 \mu\text{L}$) were reacted with 0.4 and 4 μL of Traut's reagent (14 mM) for 1 h at room temperature, representing a Traut's excess of 10 and 100 mol to $\alpha\text{-CD11c}$, respectively. For the overnight coupling, 7 μg of modified $\alpha\text{-CD11c-SH}$ ($\sim 30 \mu\text{L}$) were reacted for each Traut's group in an $\alpha\text{-CD11c-SH}$ to maleimide-linker ratio of 1:15 and 1:150 (1.25 $\mu\text{g } \mu\text{L}^{-1}$ linker stock = 1:1 ratio of linker to $\alpha\text{-CD11c-SH}$). Modified samples were prepared according to SDS-PAGE instructions (60 μL approach). Unmodified $\alpha\text{-CD11c}$ was prepared at a 40 μL approach. All samples were boiled for 10 min at 70 $^{\circ}\text{C}$. The molecular weight marker (M) was applied with 5 μL , the unmodified and thiolated $\alpha\text{-CD11c}$ groups with 7 μg and the linker-reacted groups with 3.5 μg onto a 10% Bis-Tris Plus gel and run for ~ 6 h at 120 V. Visualization was conducted by Coomassie Staining.

4. The conjugation strategy affects antibody orientation and targeting properties of nanocarriers

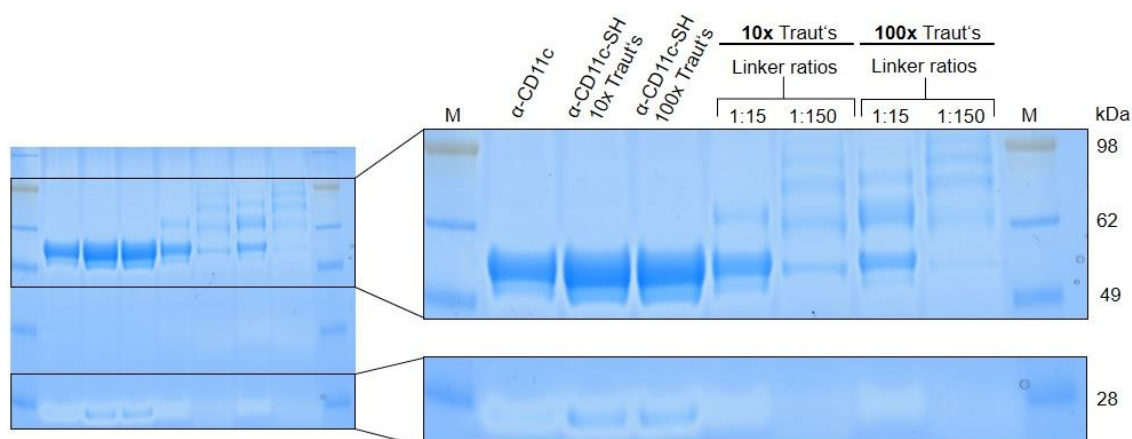


Figure 4.S3: Evaluation of thiolated and linker-reacted CD11c antibodies under reduced conditions. For the Traut's modification, 74 μg of $\alpha\text{-CD11c}$ ($\sim 245 \mu\text{L}$) were reacted with 0.4 and 4 μL of Traut's reagent (14 mM) for 1 h at room temperature, representing a Traut's excess of 10 and 100 mol to $\alpha\text{-CD11c}$, respectively. For the overnight coupling, 7 μg of modified $\alpha\text{-CD11c-SH}$ ($\sim 30 \mu\text{L}$) were reacted for each Traut's group in an $\alpha\text{-CD11c-SH}$ to maleimide-linker ratio of 1:15 and 1:150 (1.25 $\mu\text{g} \mu\text{L}^{-1}$ linker stock = 1:1 ratio of linker to $\alpha\text{-CD11c-SH}$). Modified samples were prepared according to SDS-PAGE instructions (60 μL approach). Unmodified $\alpha\text{-CD11c}$ was prepared at a 40 μL approach. All samples were boiled for 10 min at 70 $^{\circ}\text{C}$. The molecular weight marker (M) was applied with 5 μL , the unmodified and thiolated $\alpha\text{-CD11c}$ groups with 7 μg and the linker-reacted groups with 3.5 μg onto a 10% Bis-Tris Plus gel and run for 111 min at 120 V. Visualization was conducted by Coomassie staining.

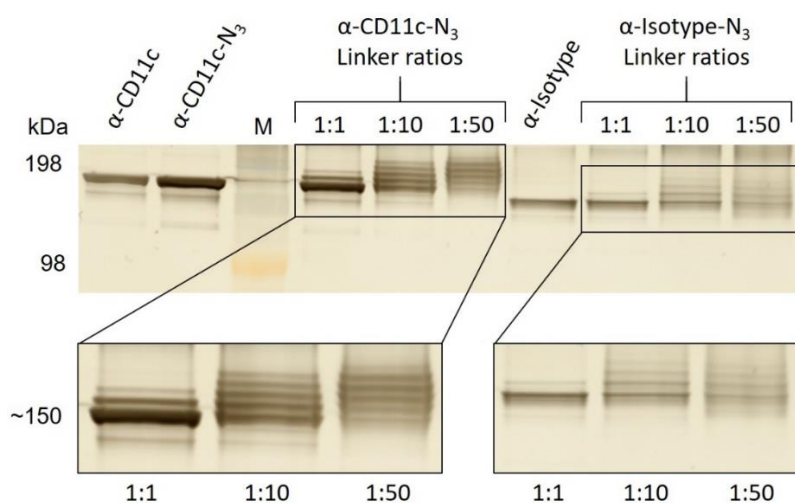


Figure 4.S4: Detection of azide-modified antibodies. For the overnight coupling, 1 μg azide-modified antibody (1 μL of $\alpha\text{-CD11c-N}_3$ or $\alpha\text{-isotype-N}_3$) was reacted with the respective amount of DBCO-mPEG 5 kDa linker (0.15 $\mu\text{g} \mu\text{L}^{-1}$ linker stock = 1:1 ratio of linker to antibody). Three linker ratios were tested for each modified antibody. All samples were prepared according to 40 μL SDS-PAGE instructions and boiled for 10 min at 70 $^{\circ}\text{C}$. The molecular weight marker (M) was applied with 5 μL , the unmodified $\alpha\text{-CD11c}$ with 1 μg , the modified $\alpha\text{-CD11c-N}_3$ with $\sim 2 \mu\text{g}$, the modified $\alpha\text{-isotype-N}_3$ with $\sim 1 \mu\text{g}$ and the linker coupled samples with $\leq 0.5 \mu\text{g}$ onto a 10% Bis-Tris Plus gel and run for ~ 5 h at 110 V. Visualization was conducted by silver staining.

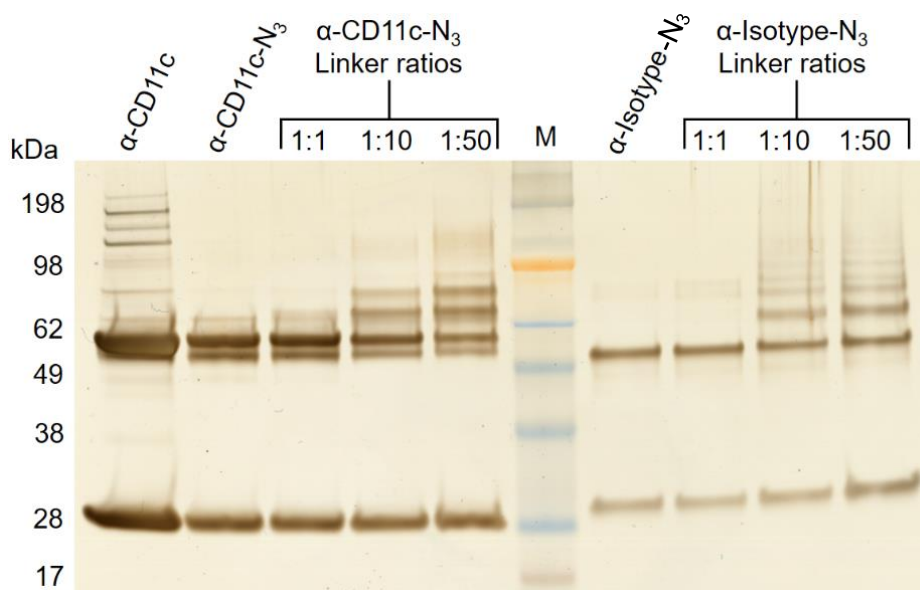


Figure 4.S5: Detection of azide-modified antibodies under reduced conditions. For the overnight coupling, 1 μg azide-modified antibody (1 μl of $\alpha\text{-CD11c-N}_3$ or $\alpha\text{-Isotype-N}_3$) was reacted with the respective amount of DBCO-mPEG 5 kDa linker (0.15 $\mu\text{g } \mu\text{L}^{-1}$ linker stock = 1:1 ratio of linker to antibody). Three linker ratios were tested for each modified antibody. All samples were prepared according to 40 μL reduced SDS-PAGE instructions and boiled for 10 min at 70 $^\circ\text{C}$. The molecular weight marker (M) was applied with 5 μL , the unmodified $\alpha\text{-CD11c}$ with 1 μg , the modified $\alpha\text{-CD11c-N}_3$ with $\sim 2 \mu\text{g}$, the modified $\alpha\text{-Isotype-N}_3$ with $\sim 1 \mu\text{g}$ and the linker coupled samples with $\leq 0.5 \mu\text{g}$ onto a 10% Bis-Tris Plus gel and run for 70 min at 110 V. Visualization was conducted by silver staining.

CD11c blocking

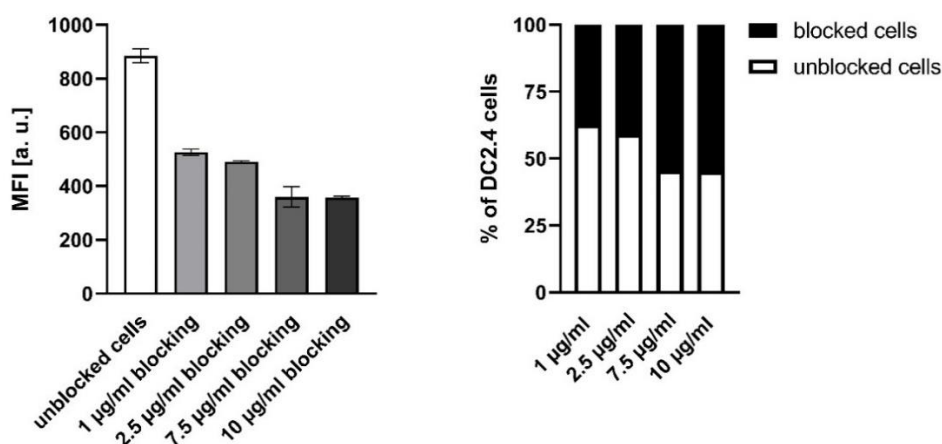


Figure 4.S6: Concentration-dependent blocking of CD11c integrins on dendritic cells. DC2.4 dendritic cells were initially blocked with CD11c antibodies (unlabeled) for 30 min at 4 $^\circ\text{C}$, followed by the detection of free CD11c integrins by fluorescence-labeled CD11c antibodies also for 30 min at 4 $^\circ\text{C}$. Only viable cells are gated and analyzed by flow cytometry (A). Values are given as mean \pm SD (n = 2). MFI [a.u.] = median fluorescence intensity [arbitrary units]. For a percentage representation of the results, the MFI value of unblocked cells was used as 100% and the individual groups were calculated accordingly (B).

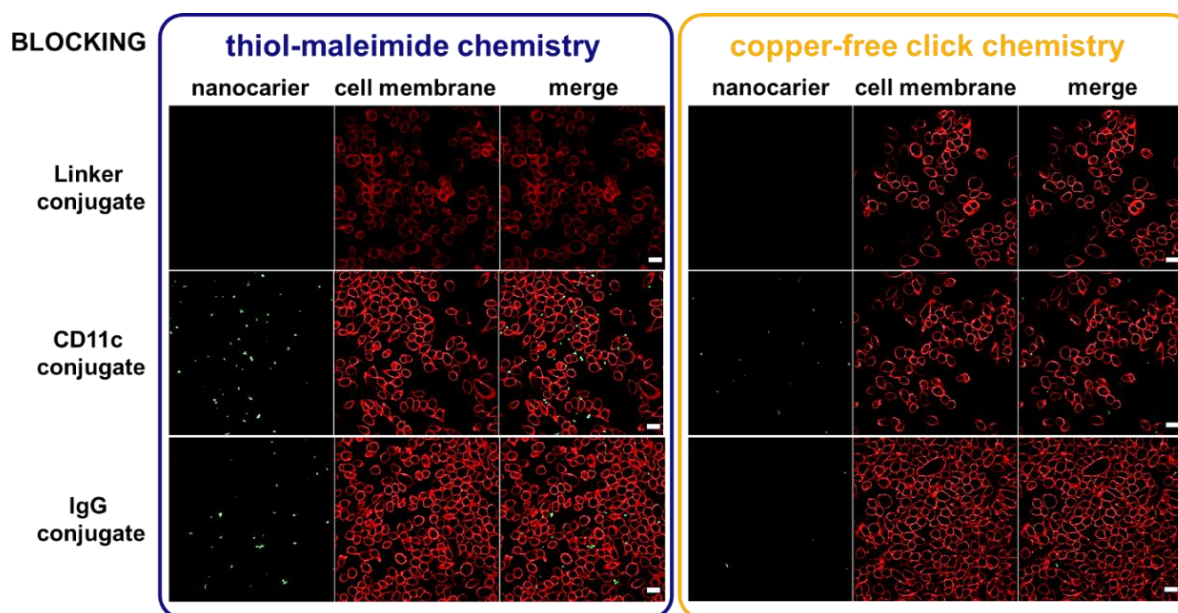


Figure 4.S7: Visualization of blocking CD11c prior to an antibody nanocarrier conjugate uptake. For the image acquisition, 5×10^4 cells per well were pre-treated with $7.5 \mu\text{g mL}^{-1}$ CD11c antibodies in $200 \mu\text{L}$ IMDM without FBS for 30 min at 4°C . After the incubation, the wells were washed with PBS and the antibody nanocarrier conjugates uptake was performed with $75 \mu\text{g mL}^{-1}$ in $200 \mu\text{L}$ IMDM without FBS for 30 min at 4°C . After the incubation, the wells were washed with PBS and the cells were fixed for 15 min with 4% paraformaldehyde (PFA). Nanocarriers were excited with the laser 561 (emission filter 570 – 599 nm) and the cell membrane was excited with the laser 633 (emission filter 660 – 700 nm). All scale bars represent $20 \mu\text{m}$.

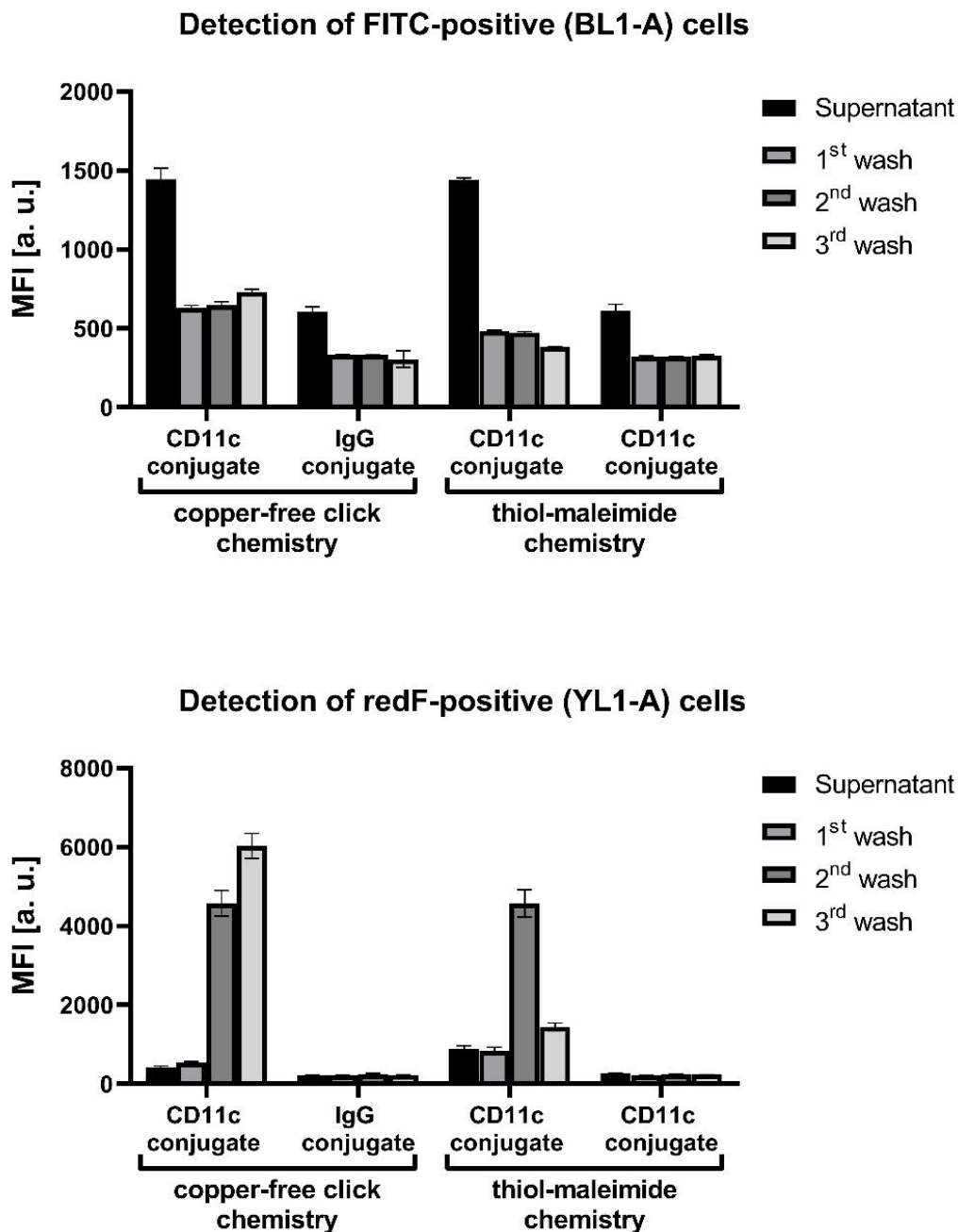


Figure 4.S8: Detection of unbound antibodies and free nanocarriers in each magnetically separated fraction. For the detection of unbound antibodies and nanocarriers in each wash fraction, 1.5×10^5 cells were incubated (30 min, 4 °C) in 100 μ L of the respective supernatant or one of the three washes. Unbound CD11c or IgG isotype antibodies were detected by a secondary FITC anti-hamster antibody (30 min, 4 °C). The CD11c and IgG conjugates with an antibody amount of 7.5 μ g are analyzed by flow cytometry. The detection of FITC-positive (BL1-A) cells represents unbound antibodies in each wash fraction that bound to the cell surface and are detected by the secondary FITC antibody (A). The detection of redF-positive (YL1-A) cells represents free nanocarriers in each wash fraction that were not magnetically purified and attached to the cells (B). Values are given as mean \pm SD (n = 3). MFI [a.u.] = median fluorescence intensity [arbitrary units].

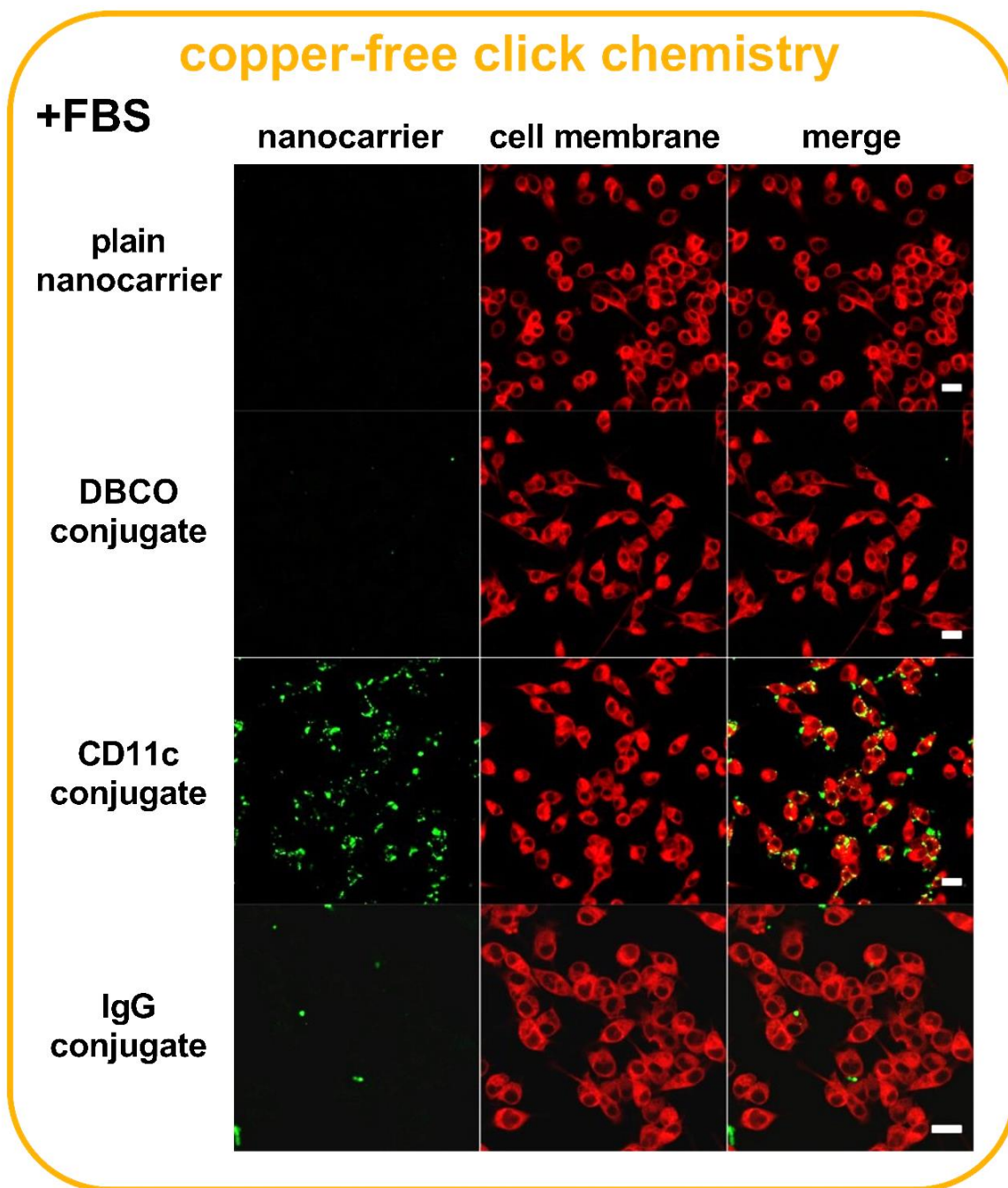


Figure 4.S9: Site-directed targeting of dendritic cells by antibody nanocarrier conjugates. For the image acquisition, 5×10^4 cells per well were treated with $75 \mu\text{g mL}^{-1}$ samples in $200 \mu\text{l}$ IMDM with 5% FBS. After the two-hour incubation, the wells were washed with PBS and the cells fixed for 15 min with 4% paraformaldehyde (PFA). Nanocarriers were excited with the laser 561 (emission filter 570 – 599 nm) and the cell membrane was excited with the laser 633 (emission filter 660 – 700 nm). All scale bars represent $20 \mu\text{m}$.

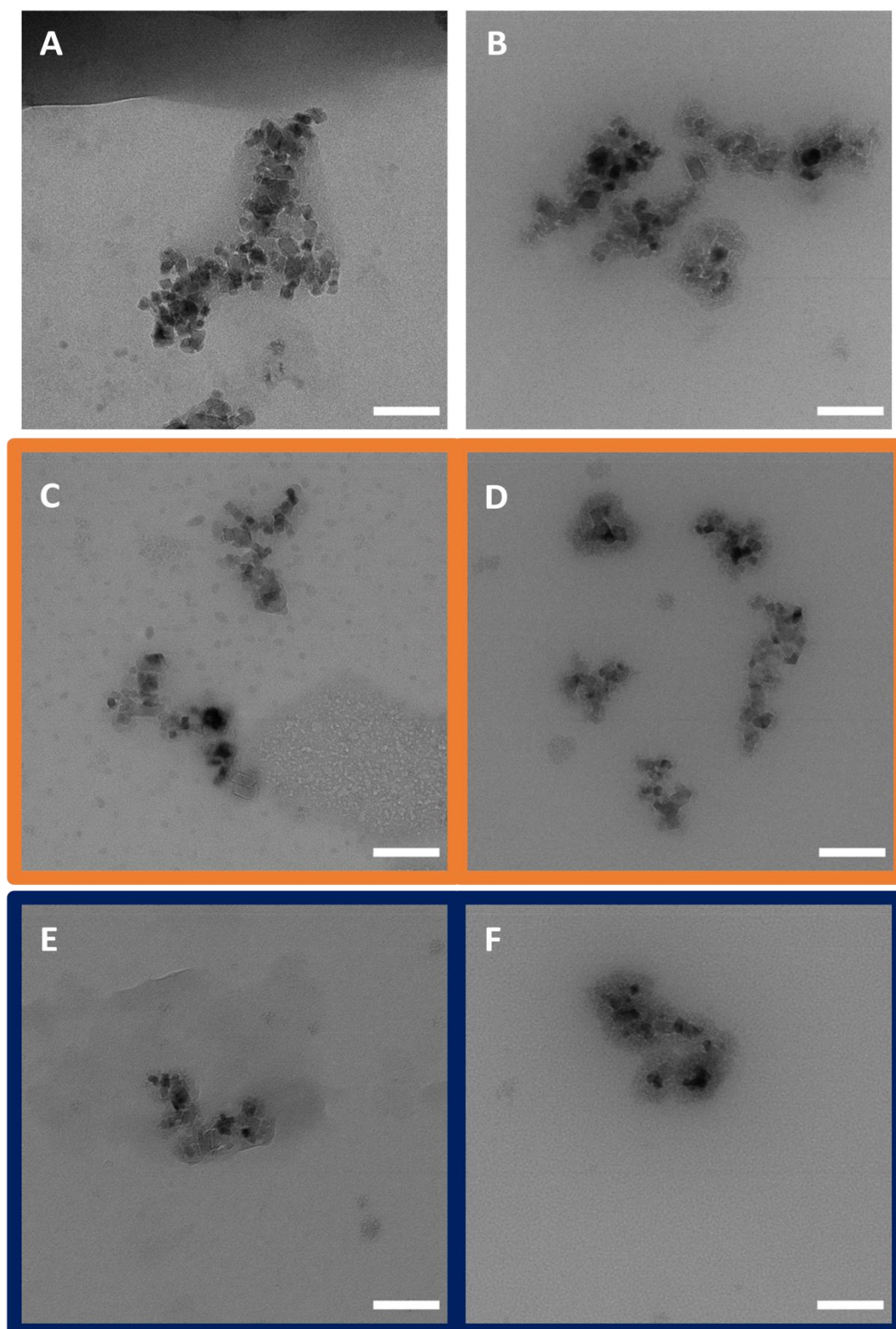


Figure 4.S10: TEM images of antibody-modified nanocarriers in cell culture medium. The images show small clusters of the nanocarriers in different conditions with a sample concentration of $75 \mu\text{g mL}^{-1}$. Nanocarriers in water (A) and in IMDM with 5% FBS (B) are shown. Antibody-modified nanocarrier conjugates ($7.5 \mu\text{g}$ antibody amount for all tested conjugates) obtained via copper-free click chemistry in orange with CD11c (C) or IgG (D) antibody and those obtained via thiol-maleimide chemistry in blue with CD11c (E) or IgG (F) antibody are shown. All scale bars represent 100 nm.

4. The conjugation strategy affects antibody orientation and targeting properties of nanocarriers

Table 4.S1: Average size and charge of synthesized nanoconjugates. Light scattering measurements were performed on an ALV spectrometer with 10 μ L of sample in 1 mL PBS ($n = 1$, with an experimental error of 10%). The ζ -potential was measured at the Zeta-Sizer – Z (Malvern) in 1mM KCl (1mL) with an average of three measurements ($n = 3$). Thiol-maleimide generated conjugates were synthesized with a nanocarrier to linker ratio of 1:150 and copper-free click conjugates with a nanocarrier to linker ratio of 1:10. Different nanocarrier to antibody ratios/amounts were investigated (20:1 [25 μ g]; 67:1 [7.5 μ g]; and 200:1 [2.5 μ g]).

Sample name	Average diameter in PBS ^a	PDI in PBS ^a	ξ -potential [mV]	ξ -deviation [mV]
BNF Starch redF (pristine nanocarrier)	210 nm	0.148	-5.77 \pm 1.73	4.38 \pm 0.46
Thiol-maleimide generated conjugates:				
Maleimide linker conjugate	244 nm	0.216	-15.5 \pm 0.17	3.59 \pm 0.39
α -CD11c conjugate [25.0 μ g]	298 nm	0.396	-11.3 \pm 0.61	4.10 \pm 1.29
α -CD11c conjugate [7.5 μ g]	190 nm	0.266	-14.37 \pm 0.15	3.46 ^b \pm 0.42 ^b
α -CD11c conjugate [2.5 μ g]	198 nm	0.150	-12.8 \pm 1.82	7.53 \pm 7.08
α -IgG conjugate [25.0 μ g]	/ ^c	/ ^c	-10.62 \pm 3.63	3.74 \pm 0.85
α -IgG conjugate [7.5 μ g]	234 nm	0.205	-11.40 \pm 2.44	5.24 \pm 1.05
α -IgG conjugate [2.5 μ g]	230 nm	0.122	-13.00 \pm 0.26	4.38 \pm 0.58
Copper-free click generated conjugates:				
DBCO linker conjugate	210 nm	0.200	-10.3 \pm 0.1	5.39 \pm 3.47
α -CD11c conjugate [25.0 μ g]	202 nm	0.080	-9.75 \pm 0.65	3.81 \pm 0.60
α -CD11c conjugate [7.5 μ g]	204 nm	0.060	-9.35 \pm 0.19	3.81 \pm 0.60
α -CD11c conjugate [2.5 μ g]	204 nm	0.168	-9.09 \pm 1.41	3.94 \pm 0.62
α -IgG conjugate [25.0 μ g]	238 nm	0.260	-8.67 \pm 0.54	5.03 \pm 0.92
α -IgG conjugate [7.5 μ g]	228 nm	0.169	-8.97 \pm 1.10	5.70 \pm 0.23
α -IgG conjugate [2.5 μ g]	208 nm	0.168	-9.82 \pm 0.68	3.50 \pm 0.36

^a Determined by multi angle DLS (at scattering angles of 30° to 150°)

^b ($n = 2$)

^c not measurable (macroscopic aggregates)

5. Achieving dendritic cell subset-specific targeting *in vivo* by site-directed conjugation of targeting antibodies to nanocarriers

Copyright:

The subchapter 5 is published in a peer-reviewed journal [3] and demonstrates in most cases a complete reproduction of the published text. Accordingly, the presented results are reprinted with permission from Nano Today. Copyright © 2022, Nano Today, Inc. Published by Elsevier Ltd. All rights reserved.

[3] Johanna Simon*, Michael Fichter*, Gabor Kuhn*, **Maximilian Brückner**, Cinja Kappel, Jenny Schunke, Tanja Klaus, Stephan Grabbe, Katharina Landfester, Volker Mailänder. Achieving dendritic cell subset-specific targeting *in vivo* by site-directed conjugation of targeting antibodies to nanocarriers. Nano Today, **2022**, 43, 101375.

Aim:

The previously described conjugation strategy in chapter 4 demonstrates a desired attachment of whole antibodies specifically targeting dendritic cells *in vitro*. Consequently, in the next step, the current study aims to analyze the dendritic cell subset-specific targeting effectiveness of the antibody-modified nanocarriers *in vivo*. This concern deals with the attachment of different dendritic cell subset-specific antibodies, as well as the influence of the biomolecular corona formed *in vitro* and *in vivo*.

Contribution:

I, Maximilian Brückner, synthesized all antibody nanocarrier conjugates composed of the 5 kDa NHS-PEG-DBCO linker, including the nanocarrier functionalization and antibody modification (CD11c, XCR1, CLEC9A, DEC205, IgG_{2b}). Dr. Michael Fichter investigated these 5 kDa antibody-modified nanocarriers *in vivo* by flow cytometry (animal studies, uptake in different cell subpopulations). Dr. Johanna Simon prepared the antibody nanocarrier conjugates composed of the 0.65 kDa NHS-PEG-DBCO linker, including the nanocarrier functionalization and antibody modification (CD11c, and IgG) and performed the qualitative and quantitative measurements of the conjugates and the biomolecular corona (SDS-PAGE, LC-MS, DLS, ζ -Potential). Gabor Kuhn investigated the 0.65 kDa conjugates *in vivo* (animal studies, flow cytometry). Christine Rosenauer measured the multi-angle DLS and Elke Muth the ζ -Potential of the 5 kDa antibody-modified nanocarriers. Prof. Dr. Volker Mailänder and Prof. Dr. Katharina Landfester supervised the project.

5.1 Abstract

The major challenge of nanocarrier-based anti-cancer vaccination approaches is the targeted delivery of antigens and immunostimulatory agents to the cells of interest, such as specific subtypes of dendritic cells (DCs), in order to induce robust antigen-specific anti-tumor responses. An undirected cell and body distribution of nanocarriers can lead to an unwanted delivery to other immune cell types like macrophages reducing the vaccine efficacy. An often-used approach to overcome this issue is the surface functionalization of nanocarriers with targeting moieties, such as antibodies, mediating cell type-specific interactions. Numerous studies could successfully prove the targeting efficiency of antibody-conjugated carrier systems *in vitro*, however, most of them failed when targeting DCs *in vivo* that is partly due to cells of the reticuloendothelial system unspecifically clearing nanocarriers from the blood stream via F_c receptor ligation. Therefore, this study shows a surface functionalization strategy to site-specifically attach antibodies in an orientated direction onto the nanocarrier surface. Different DC-targeting antibodies, such as anti-CD11c, anti-CLEC9A, anti-DEC205, and anti-XCR1, were conjugated to the nanocarrier surface at their F_c regions. Anti-mouse CD11c antibody-conjugated nanocarriers specifically accumulated in the targeted organ (spleen) over time. Additionally, antibodies against CD11c and CLEC9A proved to specifically direct nanocarriers to the targeted DC subtype, conventional DCs type 1. In conclusion, site-directed antibody conjugation to nanocarriers is essential in order to avoid unspecific uptake by non-target cells while achieving antibody-specific targeting of DC subsets. This novel conjugation technique paves the way for the development of antibody-functionalized nanocarriers for DC-based vaccination approaches in the field of cancer immunotherapy.

5.2 Introduction

Nanocarriers applied as drug delivery vehicles protect the cargo in an unprecedented way, as exemplified these days with the newly approved preventive SARS-CoV-2 vaccines developed by BioNtech or Moderna loaded with highly fragile loads like mRNA. This revolutionizes the current strategy for preventing viral diseases or treating cancer¹⁷⁶⁻¹⁸⁰. Also, an unwanted body distribution can be skewed towards a more desired one. To this end, a specific transport of the drug to cells of interest via the nanocarrier can be achieved through the functionalization of the nanocarrier surface with targeting ligands such as antibodies specific for cell surface antigens^{181, 182}. Antibody-conjugated nanocarriers have the potential to improve the drug selectivity, reduce systemic side effects, and increase the therapeutic potential¹⁸³.

Already in the 90s, the first nanocarrier system (DOXIL®), a polyethylene glycol (PEG)-functionalized liposomal formulation of doxorubicin, was approved by the FDA for treating cancer^{184, 185}. To date, however, no antibody-conjugated nanocarrier system has been clinically approved. Even though numerous reports could successfully prove the targeting specificity of antibody-conjugated nanocarriers *in vitro*¹⁸⁶⁻¹⁹¹, the majority of these studies failed *in vivo* (see e.g.¹⁹²⁻¹⁹⁴). Additionally, there is a lot of publications showing an antibody-mediated delivery of antibody-antigen-conjugates to dendritic cells, but only a few studies reporting a specific uptake of antibody-functionalized nanometer-sized particles in DCs *in vivo*^{195, 196}. A major factor responsible for these discrepancies is the phenomenon of blood protein adsorption on the nanocarrier surface following intravenous injection forming the biomolecular corona^{44, 197}. Due to this process, the targeting ligand can be completely covered up by corona proteins preventing an interaction between the antibody conjugated onto the nanocarrier and its targeted cell receptor^{198, 199}. A second significant confounding factor which enhances unspecific uptake by especially macrophages is F_c receptor ligation by the F_c region of antibodies non-specifically conjugated to the nanocarrier surface. We have shown before that this can be avoided by an F_c region-directed coupling strategy²⁰⁰. Thus, there is a great need for site-specific conjugation of targeting antibodies to ensure correct orientation hindering F_c receptor ligation.

To overcome current challenges, this study presents a surface functionalization strategy for the attachment of dendritic cell-specific antibodies onto a nanocarrier surface allowing a specific, targeted cell interaction *in vivo* with minimal non-specific F_c-mediated nanocarrier clearance. The effect of protein corona formation was studied both *in vitro* as well as *in vivo*, and the targeting properties of the designed antibody-conjugated nanocarriers were not affected. This approach can be transferred to a broad range of nanocarriers and antibodies. As a proof of concept, an anti-mouse CD11c antibody was conjugated to the surface of

5. Achieving dendritic cell subset-specific targeting *in vivo* by site-directed conjugation of targeting antibodies to nanocarriers

magnetic nanoparticles. The CD11c receptor is expressed by all subtypes of dendritic cells²⁰¹ present in the liver²⁰² and the spleen²⁰³. Targeting dendritic cells is of great interest in the field of cancer immunotherapy²⁰⁴, as DCs play a crucial role in activating the immune system to fight cancer²⁰⁵ and other diseases²⁰⁶. CLEC9A and DEC205 define subgroups of CD11c⁺ DCs. But not all DC subtypes support an anti-viral or anti-tumor response in the same effective way. CLEC9A⁺ and DEC205⁺ DCs are thought to define subgroups which are crucial for an effective immune response. This study demonstrates that anti-mouse CD11c-, CLEC9A-, as well as DEC205-functionalized nanocarriers specifically bind to distinct subtypes of dendritic cells *in vivo*, whereas nanocarriers conjugated to an IgG control antibody exhibited no interaction with the targeted cell population.

5.3 Material and Methods

Nanocarriers. Hydroxyethyl starch-coated magnetic nanoparticles (BNF-Starch) with amino groups on the surface (named as mgHES-NH₂) were obtained from micromod. Nanoparticles either contained the fluorophores Dy-750 (for *in vivo* imaging) and Dy-633 (for *in vitro* assays) or redF (for the comparison of different DC-targeting antibodies). Nanoparticles were synthesized via the core-shell method according to literature^{207, 208} with a solid content of 5 mg mL⁻¹ and 3 nmol mg⁻¹ amino groups per mg nanoparticle.

Enzymatic modification of antibodies. Antibodies (anti-mouse CD11c (clone N418), anti-mouse CLEC9A (clone 7H11), anti-mouse/rat XCR1 (clone ZET), anti-mouse DEC205 (clone NLDC-145), or IgG isotype controls (Armenian Hamster IgG or Mouse IgG2b, κ) all from Biolegend) were modified with azide groups via the Site Click™ Antibody Azido Modification Kit (Thermo Fisher Scientific) according to the manufacturer's instructions. Briefly, the carbohydrate domain at the F_c region of the concentrated antibody was modified by cleaving the galactose residues using β-galactosidase for 6 h at 37 °C. Afterwards, the azide group was attached by applying the GalT (Y289L) enzyme in combination with the UDP-GalNAz donor in an overnight reaction at 30 °C. The azide-modified antibody was purified via Zeba™ Spin columns, concentrated and the protein concentration was determined.

Protein quantification. The total amount of antibody or protein concentrations were quantified by using the Pierce 660 nm protein assay according to the manufacturer's instructions. Bovine serum albumin (BSA) was used as a standard by preparing a dilution series in demineralized water. The optical density at 660 nm of samples and standards was measured in duplicates using an Infinite M1000 plate reader (Tecan).

Nanocarrier functionalization with antibodies. mgHES-NH₂ nanoparticles (200 mg, 40 mL) were functionalized with either DBCO-PEG₄-NHS linker (3.9 mg, 10 x molar excess, 20 mg mL⁻¹ stock solution in DMSO, Jena Biosciences) or DBCO-PEG_{5kDa}-NHS linker (150 mg, 50x molar excess, 20 mg mL⁻¹ stock solution in DMSO, Nanocs Inc., USA). The reaction was incubated overnight at room temperature. The following day, the nanoparticle dispersion was washed three times with 1 mL of PBS by applying a neodymium to separate unbound linker moieties. DBCO-functionalized nanocarriers (mgHES-DBCO, 67 mg) were incubated with azide-modified antibodies (1 mg) at room temperature under shaking overnight. The following day, the dispersion was washed three times with PBS to remove unconjugated antibodies.

5. Achieving dendritic cell subset-specific targeting in vivo by site-directed conjugation of targeting antibodies to nanocarriers

Nanocarrier quantification. To determine the amount of nanocarrier and nanocarrier-conjugates, a fluorescence calibration of the nanocarrier was conducted. The non-functionalized nanocarriers were applied as a standard and the samples diluted based on the initial mass used. All probes, including the standard, were prepared as duplicates in deionized water. Fluorescence was measured using an Infinite M1000 plate reader (Tecan) with an excitation wavelength of 552 nm or 633 nm and emission of 580 nm or 647 nm for redF-labelled or Dy-633-labelled mgHES nanocarriers, respectively.

Dynamic light scattering. The size (diameter in nm) and size distribution (PDI) of all nanocarriers were measured by dynamic light scattering (DLS, Malvern Instruments GmbH, Herrenberg, Germany) at 25 °C at an angle of 90°. The nanocarriers (10 µL, 10 mg mL⁻¹) were diluted in PBS and measurements were performed in technical triplicates. Multi-angle light scattering measurements were performed on an ALV spectrometer consisting of a goniometer and an ALV-5004 multiple-tau full-digital correlator (320 channels) at 20 °C and 7 (dynamic) angles ranging from 30° to 150°. A He-Ne Laser (wavelength of 632.8 nm) was used as light source. 1 µl of unfiltered dispersion was diluted with 1 ml PBS which was previously filtered through membrane filters with a pore size of 0.20 µm (GS Millipore).

Zeta potential. Measurements were performed with a Zeta Sizer Nano Series (Malvern Instruments GmbH, Herrenberg, Germany) and nanocarriers (10 µL, 10 mg mL⁻¹) were diluted in an 1 mM potassium chloride solution (1 mL). Each measurement was performed in technical triplicates.

In vivo animal studies. Wild type C57BL/6J mice and C57BL/6 albino mice (B6N-Tyrc-Brd/BrdCrCrI) were kept in the animal facility of the Translational Animal Research Center at the University Medical Center of the Johannes Gutenberg University Mainz under pathogen-free conditions on a standard diet. All procedures were approved by the regional animal care committee (Landesuntersuchungsamt Rheinland-Pfalz) and performed according to the EU Directive 2010/63/EU. Nanocarriers (1 mg in 500 µL PBS or 500 µg in 200 µl PBS (for comparing different antibody-functionalized nanocarriers) were administered intravenously via tail vein injection. As a control, animals were treated with PBS. After 1 min, 10 min, 60 min, or 120 min blood was isolated via cardiac puncture. Animals were sacrificed and all organs (lung, spleen, liver, and kidney) were prepared and imaged via small animal fluorescence imaging (IVIS® SpectrumCT, Perkin Elmer). For the comparison of different DC-targeting antibodies conjugated onto the nanocarrier surfaces, mice were sacrificed 24 h after injection via cervical dislocation and spleens were dissected and dissociated for subsequent flow cytometric analyses.

Isolation of spleen cells. Spleen cells were prepared as previously described²⁰⁹. Briefly, the

5. Achieving dendritic cell subset-specific targeting in vivo by site-directed conjugation of targeting antibodies to nanocarriers

spleens of C57BL/6J mice were isolated and mechanically disrupted by grinding through a 40 μm cell strainer. Subsequently, erythrocytes within the cell suspension were lysed using a hypotonic buffer (155 mM NH_4Cl , 10 mM KHCO_3 , 100 μM EDTA-disodium, pH 7.4) for 30 s and subsequently washed using Iscove's Modified Dulbecco's Medium (IMDM) supplemented with 5% fetal bovine serum (FBS) and 1% penicillin (100 U mL^{-1}) and streptomycin (100 mg mL^{-1}). Spleen cells were stained with antibodies to discriminate the different cell populations and the amount of nanocarrier positive cells was determined by flow cytometry.

Spleen cell staining. First, cells were washed (1% FBS in PBS) and a live/dead staining was performed using Live/Dead Fixable Aqua (1:1000 in PBS; Thermo Fisher Scientific) for 20 min at 4 $^\circ\text{C}$. F_c receptors were blocked with anti-CD16/CD32 (clone 2.4G2) for 10 min. To differentiate the cell types via flow cytometry, spleen cells were incubated with fluorophore-labelled cell type-specific antibodies for 30 min: anti-CD11c (clone N418), anti-CD11b (clone M1/70), anti-CD172a (clone P84), anti-CD8 α (clone 53-6.7), anti-I-A/I-E (MHCII, clone M5/114.15.2), anti-F4/80 (clone BM8), anti-CD4 (clone GK1.4), anti-Siglec-H (clone 551), anti-CD19 (clone 6D5), anti-CD3 ϵ (clone 145-2C11), anti-CD14 (clone Sa14-2), anti-NK1.1 (clone PK136), anti-Ly6G (clone 1A8). Flow cytometric analysis was performed with the Attune NxT (Thermo Fisher Scientific) and analyzed with FlowJo software v10.7.1.

Isolation of liver cells. Non-parenchymal liver cells of C57BL/6J mice were isolated by an organ perfusion method as previously described²¹⁰. Therefore, mice were anesthetized using ketamine/xylazine and the abdominal cavity was opened. The liver was flushed through the portal vein with 20 ml of Ca^{2+} - and Mg^{2+} -free HBSS (Hank's Balanced Salt Solution, Thermo Fisher Scientific) containing 5% FBS, collagenase A (100 U L^{-1} ; Sigma-Aldrich) and DNase I (10 μg mL^{-1} ; Sigma-Aldrich). The liver was subsequently cut into pieces, incubated in the perfusion solution for 15 min at 37 $^\circ\text{C}$ in a 50 ml tube, and mechanically disrupted with a 70 μm nylon cell strainer. The enzymatic reaction was stopped by adding a cell culture medium (Dulbecco's Modified Eagle Medium (DMEM)/F-12, 5% FBS, 1% P/S). Hepatocytes were pelleted and removed via centrifugation (30 g for 15 min) and the remaining cells in the supernatant were purified by 30% Histodenz-HBSS gradient centrifugation as previously described²¹¹. Non-parenchymal liver cells were obtained, stained with antibodies, and the frequency of nanocarrier positive cells was determined by flow cytometry.

Liver cell staining. First, cells were washed (1% FBS in PBS) and F_c receptors were blocked with anti-CD16/CD32 (clone 2.4G2) for 10 min. To discriminate the cell types, non-parenchymal liver cells were incubated with cell type-specific antibodies for 30 min: anti-CD45 (clone 30-F11), anti-CD31 (clone 390), anti-CD11c (clone N418) and anti-F4/80 (clone BM8).

***In vivo* protein corona.** Nanocarriers were recovered from the blood stream 1 min, 10 min,

5. Achieving dendritic cell subset-specific targeting *in vivo* by site-directed conjugation of targeting antibodies to nanocarriers

60 min, or 120 min after intravenous injection via cardiac puncture followed by magnetic separation. The resulting nanocarrier pellet was washed with PBS (three times) to remove loosely bound and unbound proteins. Afterwards, the firmly attached proteins were desorbed from the surface using 2% SDS (with 62.5 mM Tris*HCl) and heated up to 95 °C for 5 min. The nanocarrier pellet was magnetically separated and the resulting protein supernatant was analyzed by Pierce Assay, SDS-PAGE, and liquid chromatography-mass spectrometry (LC-MS).

Ex vivo protein corona. Blood was isolated from C57BL/6J mice via cardiac puncture (~500 µL – 1 mL) and supplemented with heparin (2 µL, 5,000 units). Nanocarriers (1 mg) were incubated with 2 mL of whole blood for 1 min and the *ex vivo* protein corona was purified as described above (*in vivo* protein corona).

In vitro protein corona. Mouse serum and plasma, derived from anti-coagulation with EDTA, heparin, or citrate, was prepared from blood of C57BL/6J mice. Nanocarriers (1 mg) were incubated with serum or plasma (1 mL) for 1 min at 37 °C. The *in vitro* protein corona around the nanocarriers was purified as described above (*in vivo* protein corona).

SDS-PAGE. Corona proteins (1 - 2 µg) were mixed with NuPAGE™ LDS sample buffer and NuPAGE™ sample reducing agent, incubated at 95 °C for 5 min, and further applied to a NuPAGE™ 10% Bis-Tris protein gel (Thermo Fisher Scientific). The gel was run in NuPAGE™ MES SDS running buffer at 120 V for 1 h with dithiothreitol (DTT) and SeeBlue Plus2 Pre-Stained Standard was used as a molecular marker. Proteins were visualized using the SilverQuest™ Silver Staining kit (Thermo Fisher Scientific) according to the manufacturer's instruction.

In solutions digestion. Proteins were digested according to previous reports^{212, 213}. First, SDS was removed via Pierce detergent removal columns (Thermo Fisher Scientific). Furthermore, proteins were precipitated overnight using the ProteoExtract® Protein Precipitation Kit (Millipore) according to the manufacturer's instruction. The protein pellet was re-suspended in an ammonium bicarbonate (50 mM) buffer supplemented with RapiGest SF (Waters Cooperation). Subsequently, proteins were reduced (DTT, 5 mM, Sigma-Aldrich) for 45 min at 56 °C, alkylated with iodoacetoamide (15 mM, Sigma-Aldrich) for 60 min at room temperature and finally trypsin was added. A protein:trypsin ratio of 50:1 was used and the digestion was carried out for 14 h to 18 h at 37 °C. The reaction was quenched with 2 µL hydrochloric acid (Sigma-Aldrich).

Liquid chromatography coupled to mass spectrometry (LC-MS). The reference peptide standard Hi3 E.coli (Waters Cooperation) was spiked into all peptide samples at a

5. Achieving dendritic cell subset-specific targeting *in vivo* by site-directed conjugation of targeting antibodies to nanocarriers

concentration of 50 fmol μL^{-1} for absolute protein quantification⁸⁶. Measurements were performed with a nanoACQUITY UPLC coupled to a Synapt G2-Si mass spectrometer (Waters Cooperation). Ionization was carried out with a NanoLockSpray source in positive ion mode and the Synapt G2-Si was operated in resolution mode performing data-independent acquisition (MS^E) experiments. For data analysis MassLynx 4.1 and Progenesis QI (2.0) was used. A murine database was downloaded from Uniprot. Proteins were quantified based on the TOP3/Hi3 providing the absolute amount of each protein in fmol⁸⁷. For further analysis, the relative amount in % based on all identified proteins was calculated.

Cell culture. Murine DC2.4 dendritic cells (Merck) were cultured in IMDM supplemented with 5% FBS, 1% P/S, and 50 μM 2-Mercaptoethanol at 37 °C and 5% CO₂. Cells were regularly split (2-3 times per week) when reaching a confluence of about 80%.

***In vitro* DC2.4 cell uptake.** Cells (100.000 per well) were seeded in a 24-well plate with a regular cell culture medium containing FBS and incubated overnight. The next day, cells were washed with PBS and FBS-free medium was added (1 mL per well). Cells were incubated for 2 h. Nanocarriers left untreated, pre-treated with mouse serum/plasma (ratio see *in vitro* protein corona) or isolated after *in vivo* intravenous injection were added to cells at a concentration of 37.5 $\mu\text{g mL}^{-1}$ in cell culture medium without FBS for 2 h. Cells were washed with 1 mL PBS and detached with 2 mM EDTA in PBS. After centrifugation (300 g, 5 min), the resulting cell pellet was resuspended in 1 mL of PBS + 2% FBS and analyzed by flow cytometry using the Attune™ NxT (Thermo Fisher Scientific). Cells were selected on a FSC/SSC scatter plot, excluding cell debris populations and the median fluorescence intensity (MFI) or the percentage of gated events/cells was determined. The red fluorescence of the nanocarriers was detected by the RL1 channel with an excitation laser of 638 nm and a 670/14 nm band pass emission filter.

***Ex vivo* nanoparticle-blood interaction.** Blood was isolated from C57BL/6 albino mice via cardiac puncture (~500 μL - 1 mL) and supplemented with heparin (2 μL , 5,000 units). Nanocarriers (5 μL , 50 μg) were incubated with whole blood (1 μL) for 1 min. The NP-blood mixture was diluted with 1 mL of PBS and analyzed by flow cytometry using the NxT No-Wash No-Lyse Filter Kit (Thermo Fisher Scientific). Therefore, the Attune NxT flow cytometer was equipped with an additional side scatter channel off of the violet laser, which allowed the immunophenotyping of whole blood without the lysis of red blood cells and antibody staining.

5.4 Results and Discussion

The main pre-requisite for effective antibody-based DC targeting *in vivo* is represented by ensuring accessibility of the antigen-binding site at the F_{ab} region while avoiding non-specific immune cell interactions by F_c receptor ligation. Therefore, a site-specific antibody-nanocarrier conjugation strategy was chosen to achieve correct antibody orientation²⁰⁰. The antibody was enzymatically modified in a two-step reaction at the F_c part with a maximum of four azide groups (two N_3 -groups per heavy chain). This functionalization strategy takes advantage of the characteristic N-glycosylation pattern at the F_c region (CH_2 domain at the amino acid asparagine 297 (N297)), which is present at all immunoglobulins. First, galactose residues were enzymatically removed and, in a second step, using a transferase, the azide-modified sugar component N-azidoacetylglucosamine (GalNAz) was attached resulting in a site-specific modification (Figure 5.1A). With this strategy, the antigen binding region of the antibody remains unmodified, therefore, mediating specific binding towards the targeted cell receptor.

The mgHES nanocarriers carrying amino groups on the surface were functionalized via NHS-chemistry with an alkyne-modified DBCO-PEG-linker (Figure 5.1 B). Finally, the azide-modified antibody was coupled using copper-free click chemistry to DBCO-functionalized nanocarriers representing a quantitative²¹⁴ and bio-orthogonal conjugation process^{215, 216} (Figure 5.1 B). Altogether, this functionalization strategy allows the precise attachment of an antibody to the surface of a nanocarrier. In addition, this attachment protocol can be transferred to any nanocarrier with amino groups on the surface.

Non-functionalized and functionalized nanocarriers were physico-chemically characterized using dynamic light scattering and zeta potential measurements. Antibody coupling resulted in a minor size increase (~30 nm) and slightly reduced zeta potential (Figure 5.1 C). For the initial characterization of antibody functionalization, an anti-mouse CD11c antibody binding to CD11c-expressing dendritic cells was used. Dendritic cells represent key players for the induction of antigen-specific anti-tumor responses in vaccination approaches and are of great interest as a target cell population using nanocarrier-based antigen delivery²¹⁷. Additionally, an isotype control antibody was selected to demonstrate the cellular targeting specificity of the anti-mouse CD11c-modified nanocarriers.

5. Achieving dendritic cell subset-specific targeting *in vivo* by site-directed conjugation of targeting antibodies to nanocarriers

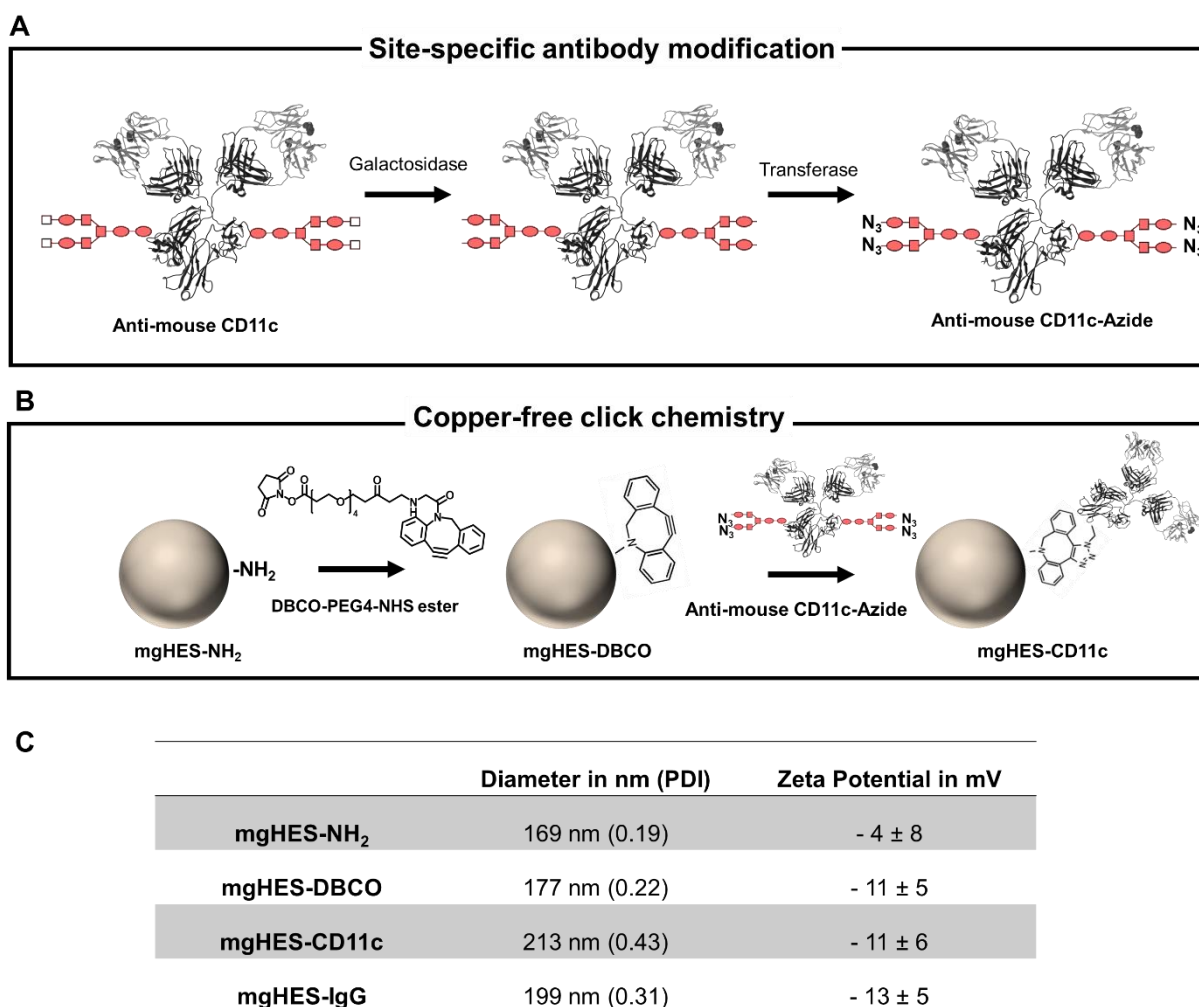


Figure 5.4: Site-specific antibody modification and the functionalization of nanocarriers. **A)** Antibodies were enzymatically modified with a maximum of four azides on the F_c region. **B)** Nanocarriers were functionalized with a DBCO linker via NHS-chemistry and further via copper-free click reaction the antibody was attached on the nanocarrier surface. **C)** Physico-chemical properties of all nanocarriers before and after functionalization.

Wild type C57BL/6J mice were treated with antibody-modified nanocarriers (1 mg) or with PBS as a control. The blood was isolated after 1 min, 10 min, 60 min, or 120 min to determine the blood circulation time of the antibody-modified nanocarriers (Figure 5.2 B). Next to this, the nanocarriers remaining in the blood were magnetically recovered to determine the proteins, attached onto the nanocarrier surface after *in vivo* circulation (Figure 5.2 A). At distinct time points, mice were sacrificed, organs were isolated and analyzed using the IVIS® SpectrumCT imager to investigate the biodistribution.

5. Achieving dendritic cell subset-specific targeting *in vivo* by site-directed conjugation of targeting antibodies to nanocarriers

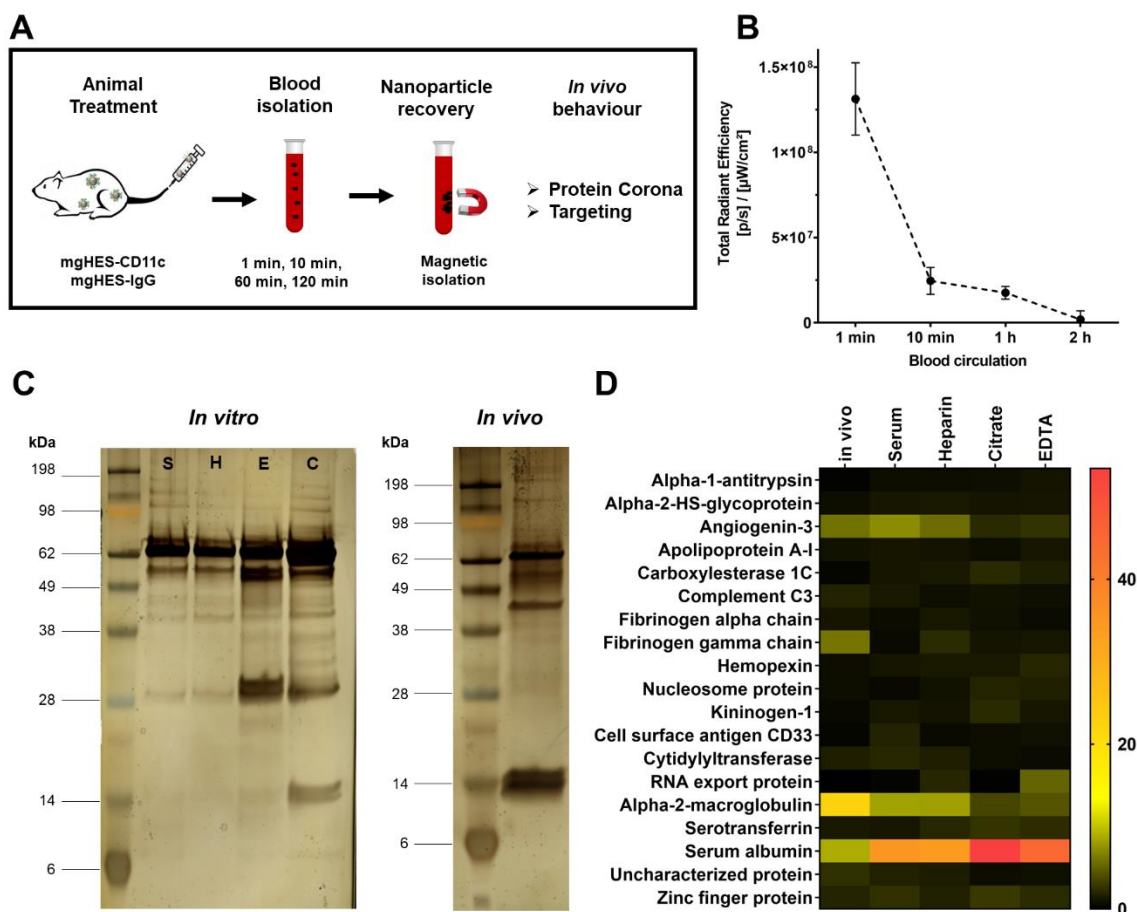


Figure 5.5: *In vivo* protein corona formation. **A)** Experimental workflow **B)** Blood circulation time of antibody-functionalized nanocarriers. Mice were treated with mgHES-CD11c nanocarriers or PBS as a control. At different time points blood was isolated and analyzed via the IVIS® SpectrumCT. Background fluorescence measured from PBS-treated mice was subtracted. **C)** SDS-PAGE of the protein corona of antibody-functionalized nanocarriers incubated under *in vitro* conditions for 1 min (S = Serum, H = Heparin Plasma, E = EDTA Plasma, C = Citrate Plasma) or after recovery from the blood stream after 1 min (*in vivo*). **D)** LC-MS analysis of the protein corona of antibody-functionalized nanocarriers. The relative amount of each protein in % is calculated based on the total amount of all identified proteins determined in fmol. $n = 3$, for all *in vivo* samples.

It has been shown that the adsorption of corona proteins onto the surface of antibody-modified nanocarriers can significantly affect their binding properties to the targeted cells *in vitro*^{218, 219}. However, only few studies have characterized the protein corona formation of nanocarriers after *in vivo* application and it has been shown that there is a significant difference in the protein composition compared to the *in vitro* situation²²⁰⁻²²². Therefore, the proteins adsorbing onto the nanocarriers in the blood stream *in vivo* were analyzed via SDS-PAGE and proteomic high-resolution mass spectrometry. Additionally, the protein pattern after *in vivo* circulation was compared to the protein corona pattern after *in vitro* incubation with serum or plasma. Most importantly, the protein analyses revealed a significant difference in the corona proteome of nanocarriers incubated under *in vitro* conditions compared to the *in vivo* situation (Figure 5.2 C and D). This effect was observed for both control (mgHES-IgG) and targeting nanocarriers

5. Achieving dendritic cell subset-specific targeting *in vivo* by site-directed conjugation of targeting antibodies to nanocarriers

(mgHES-CD11c) under either *in vitro* (Figure 5.S1) or *in vivo* (Figure 5.S2) conditions. For all nanocarriers, alpha-2 macroglobulin was enriched in the protein corona after *in vivo* circulation, whereas primarily serum albumin was bound to nanocarriers after *in vitro* incubation (Figure 5.S2). These results indicate that studies characterizing the protein corona forming after *in vitro* incubation do not fully reflect the complex situation present in biological fluids such as the blood stream or interstitial fluid. Additionally, these findings give hints to explain the great discrepancy between successful *in vitro* studies and failing *in vivo* experiments aiming to target specific cell populations. To overcome this issue, we developed a method to mimic the *in vivo* corona in a more precise fashion²²⁰. Therefore, nanocarriers were incubated with mouse whole blood and the protein corona was prepared (indicated as *ex vivo*). High-resolution mass spectrometry demonstrated that the protein corona pattern after *ex vivo* incubation is highly comparable to the *in vivo* pattern (Figure 5.S2). This finding indicates that the *ex vivo* strategy allows to mimic the *in vivo* protein corona.

A five-step protocol was implemented investigating the efficiency of antibody-functionalized nanocarriers to specifically address target cells *in vivo*. In a first step, nanocarriers recovered from treated mice after *in vivo* blood circulation were incubated with dendritic cells (DC2.4) expressing the CD11c receptor on their cell surface *in vitro* (Figure 5.3 A). These experiments served to delineate the effects of the *in vivo* protein corona upon the antibody-functionalized nanocarriers' targeting properties *in vitro*. As a control, nanocarriers were left untreated (w/o corona) or pre-treated with either serum or plasma to allow *in vitro* protein corona formation or with whole blood for *ex vivo* incubation (w/ corona). The cellular binding affinity of all nanocarriers was analyzed. Flow cytometry revealed that all anti-CD11c-functionalized nanocarriers specifically bound to DC2.4 cells irrelevant of pre-treatment, whereas the IgG control nanocarriers showed a significantly reduced cell binding (Figure 5.3 A). Comparable results were also obtained for anti-CD11c-functionalized nanocarriers after *ex vivo* blood incubation.

5. Achieving dendritic cell subset-specific targeting *in vivo* by site-directed conjugation of targeting antibodies to nanocarriers

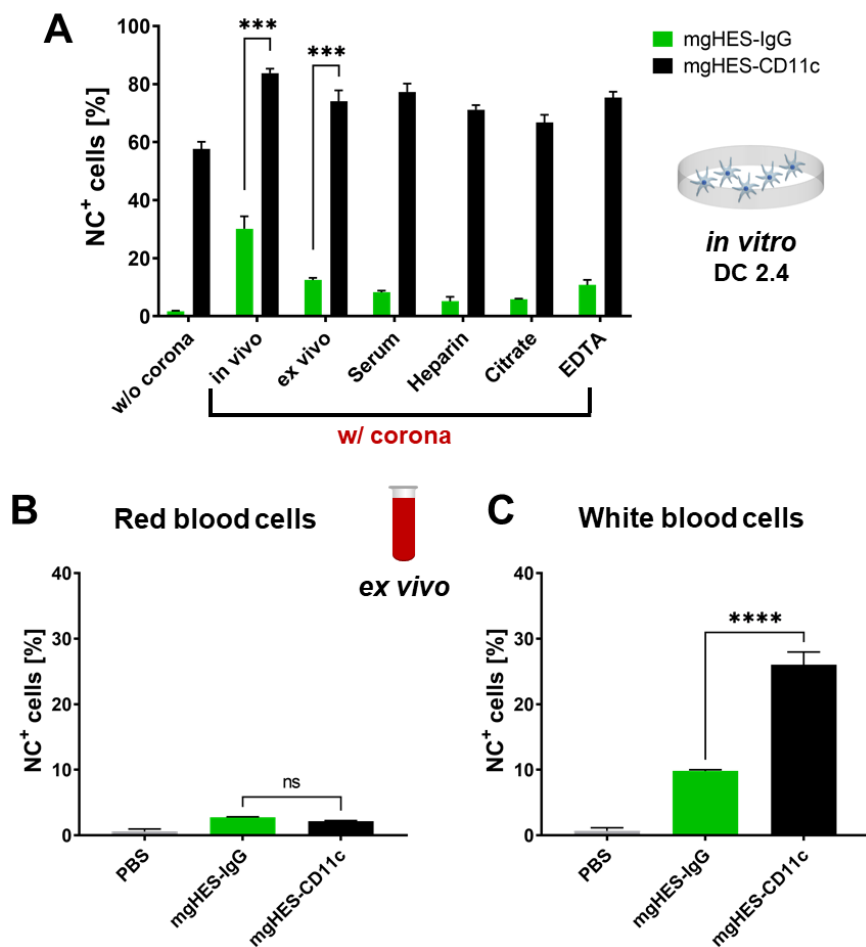


Figure 5.3: *In vitro* and *ex vivo* targeting properties of anti-CD11c-functionalized nanocarriers. **A)** DC2.4 cells were incubated with antibody-functionalized nanocarriers ($37.5 \mu\text{g mL}^{-1}$) without protein corona coating (indicated as *w/o corona*), after *in vivo* circulation (1 min, indicated as *in vivo w/ corona*), after *ex vivo* protein coating for 1 min (indicated as *ex vivo*), or after *in vitro* protein coating for 2 h (indicated as Serum, Heparin, Citrate, EDTA *w/ corona*). Data represent mean \pm SD. *In vivo* and *ex vivo* protein corona-coated mgHES-CD11c were compared to mgHES-IgG, respectively, and significance was given with $p < 0.05$ (Welch's *t* test). $p < 0.001$ ***. **B+C)** Interaction of whole blood components with antibody functionalized nanocarriers. The whole blood was analyzed via flow cytometry and the interaction of antibody-functionalized nanocarriers with red blood cells (**B**) and white blood cells (**C**) was measured using flow cytometry. Data represent mean \pm SD and significance was given with $p < 0.05$ (one-way ANOVA). *ns* = not significant, $p < 0.0001$ ****.

This finding proves that even after *in vivo* circulation or *ex vivo* blood incubation the antibodies on the nanocarrier surface retained their targeting properties. It also highlights that even in the presence of the protein corona the antibody-functionalized nanocarriers are able to bind to the targeted cells.

In a second step, an *ex vivo* approach was developed. Therefore, mouse whole blood was incubated with antibody-functionalized nanocarriers. White and red blood cells were differentiated in whole blood by flow cytometry due to distinct light-scattering properties²²³. A detailed protocol is provided in the method section. Interactions of anti-CD11c-functionalized

5. Achieving dendritic cell subset-specific targeting in vivo by site-directed conjugation of targeting antibodies to nanocarriers

nanocarriers with erythrocytes could not be observed (Figure 5.3 B). This is of great importance as it has been shown that some nanocarriers favor the interaction with red blood cells and hereby induce hemolysis and severe side effects^{224, 225}.

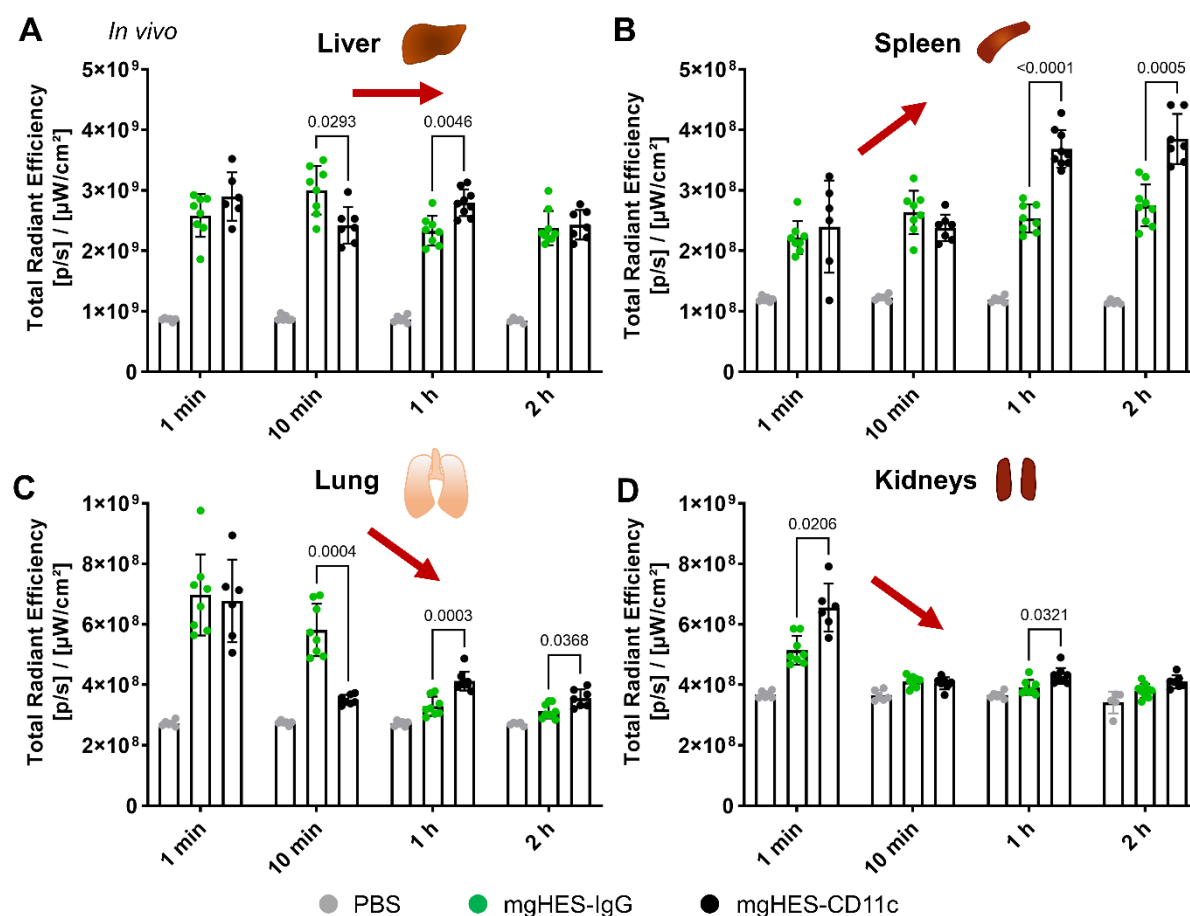


Figure 5.4: Biodistribution of antibody-functionalized mgHES nanocarriers into different organs over time. A) – D) Animals were intravenously injected with mgHES-IgG or mgHES-CD11c nanocarriers (1 mg). Liver (A), spleen (B), lung (C), and kidneys (D) were dissected at different time points post injection (1 min – 2 h) and imaged using the IVIS® SpectrumCT. Data represent mean ± SD. mgHES-CD11c nanocarriers were compared to the IgG control (mgHES-IgG) and significance was given with $p < 0.05$ using a mixed-effects analysis followed by a Šidák's multiple comparison test. Individual p values are indicated in the graph.

Furthermore, anti-CD11c-functionalized nanocarriers specifically bound to white blood cells composed of a mixture of different cell types including CD11c⁺ cells, while the frequency of mgHES-IgG⁺ cells was significantly reduced²²⁶.

In a third step, the targeting efficacy of the anti-CD11c-functionalized nanocarriers was investigated on organ level. Therefore, mgHES-CD11c- or mgHES-IgG-treated mice were sacrificed, and all relevant organs were dissected. Liver, spleen, lung, and kidneys were subsequently analyzed for nanocarrier accumulation using small animal fluorescence imaging (Figure 5.4).

5. Achieving dendritic cell subset-specific targeting *in vivo* by site-directed conjugation of targeting antibodies to nanocarriers

Foremost, both nanocarrier formulations primarily accumulated in the liver (Figure 5.4 A). This phenomenon has already been reported for a great number of studies^{194, 226-228} and is based on the physiological function of the liver as a filter organ clearing the bloodstream from foreign particulate material²²⁹. This can lead to off-target effects and unwanted side effects^{229, 230}. Nevertheless, CD11c⁺ dendritic cells also reside within the liver. Therefore, the binding of anti-CD11c-functionalized nanocarriers towards CD11c⁺ and CD11c⁻ non-parenchymal liver cells was determined in order to investigate the specificity of nanocarrier targeting within the liver (Figure 5.5).

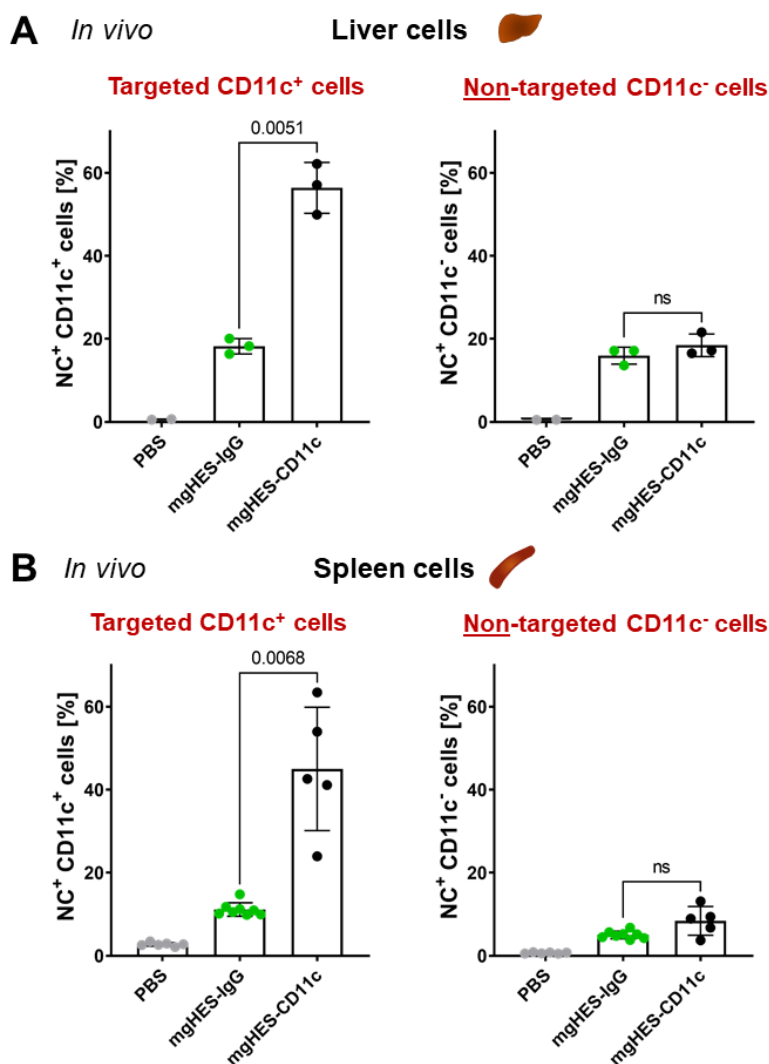


Figure 5.5: Targeting CD11c⁺ liver and spleen cells *in vivo*. Antibody-functionalized nanocarriers were intravenously injected into mice. Non-parenchymal liver cells (**A**) were isolated 2 h and splenocytes (**B**) 1 min after injection and nanocarrier uptake by CD11c⁺ or CD11c⁻ cells was analyzed using flow cytometry. Data represent mean \pm SD. mgHES-CD11c nanocarriers were compared to the IgG control (mgHES-IgG) and significance was given with $p < 0.05$ using a Welch's *t* test. *ns* = not significant. Individual p values are indicated in the graph.

For the spleen, additionally harboring CD11c⁺ cells, the fluorescence signal of the anti-CD11c-functionalized nanocarriers steadily increased from 1 min to 120 min following

5. Achieving dendritic cell subset-specific targeting *in vivo* by site-directed conjugation of targeting antibodies to nanocarriers

injection, while no significant increase in IgG control nanocarriers could be observed (Figure 5.4 B). This finding indicates an anti-CD11c-specific accumulation of nanocarriers in the targeted organ over time. In contrast, the nanocarrier-based fluorescence signal in the non-targeted organs (lung and kidney) decreased over time (Figure 5.4 C and D).

As described above, in a fourth step (Figure 5.5), the targeting efficiency of the antibody-functionalized nanocarriers *in vivo* towards CD11c⁺ and CD11c⁻ liver or spleen cells was investigated. This allowed determining the binding specificity of anti-CD11c-functionalized nanocarriers and indicated binding to targeted or non-targeted cells. Flow cytometric analyses revealed that anti-CD11c-functionalized nanocarriers specifically bound to CD11c⁺ cells, both in the liver and in the spleen, while the frequency of cells positive for IgG control nanocarriers was significantly reduced in both organs (Figure 5.5 A and B and Figure 5.S3). Targeting specificity *in vivo* was additionally proved by analyzing CD11c⁻ cells showing no significant differences in binding of either anti-CD11c- or IgG control-functionalized nanocarriers (Figure 5.5 A and B and Figure 5.S3). In conclusion, this proves that the here presented anti-CD11c-functionalized nanocarriers were able to reach the targeted cells *in vivo*.

In the final step, additional DC subtype-specific antibodies were conjugated onto the mgHES nanocarriers in order to evaluate their capacity for nanocarrier-based targeting of relevant DC subpopulations. CD8 α ⁺ conventional DCs type 1 (cDC1) are of great interest for the targeted delivery of antigens in vaccination approaches due to their high cross-presenting potential and efficiency to prime anti-tumor CD8⁺ T cells^{217, 231}. Next to the pan DC marker CD11c, cDC1 cells express XCR1, CLEC9A, and DEC205 on their cell surface, which have been exploited as targeting receptors in vaccination studies either as antibody-antigen fusion proteins or as antibody-functionalized nanoparticles²³²⁻²³⁶. Therefore, antibodies against these receptors present on cDC1 cells were conjugated onto mgHES nanocarriers using the method described above and their targeting efficacy towards different cell types within the spleen was analyzed.

IgG control- and anti-CD11c-functionalized nanocarriers were applied as negative and positive controls, respectively, and led to similar frequencies of NC⁺ CD11c⁺ (Figure 5.6 A) and CD11c⁻ (Figure 5.6 B) cells compared to the results described above (Figure 5.5 B). In addition to the analysis of pan DC populations (CD11c⁺; Figure 5.6 A), anti-CD11c-functionalized nanocarriers bound to all analyzed CD11c⁺ DC subtypes in an elevated manner (Figure 5.6 C - E). Notably, functionalization of nanocarriers with anti-XCR1 did not result in an elevated uptake by any of the cell types investigated (Figure 5.6). While anti-DEC205 nanocarriers did not improve binding to cDC1, plasmacytoid DCs and cDC2 showed an increased binding (Figure 5.6 D and E). DEC205 is often exploited as a targeting receptor for cDC1, however, there is good evidence that also cDC2 express this endocytic C-type lectin molecule at a high extent^{237, 238}. The most pronounced elevation in targeting of cDC1 and

5. Achieving dendritic cell subset-specific targeting *in vivo* by site-directed conjugation of targeting antibodies to nanocarriers

plasmacytoid DCs was achieved with anti-CLEC9A-functionalized nanocarriers that even exceeded the effects induced with CD11c targeting (Figure 5.6 C and E). CLEC9A has been found to be differentially expressed on conventional DCs type 1, but also on plasmacytoid DCs¹⁸⁸. Moreover, antibody-functionalized nanocarriers were evaluated regarding their toxicity profile after 24 h incubation *in vivo* (Figure 5.S4). All of the applied nanocarrier formulations showed a high frequency of viable cells with about 90% regardless of whether analyzing whole splenocyte populations or gating on CD11c⁺ splenocytes that bound mgHES nanocarriers.

5. Achieving dendritic cell subset-specific targeting *in vivo* by site-directed conjugation of targeting antibodies to nanocarriers

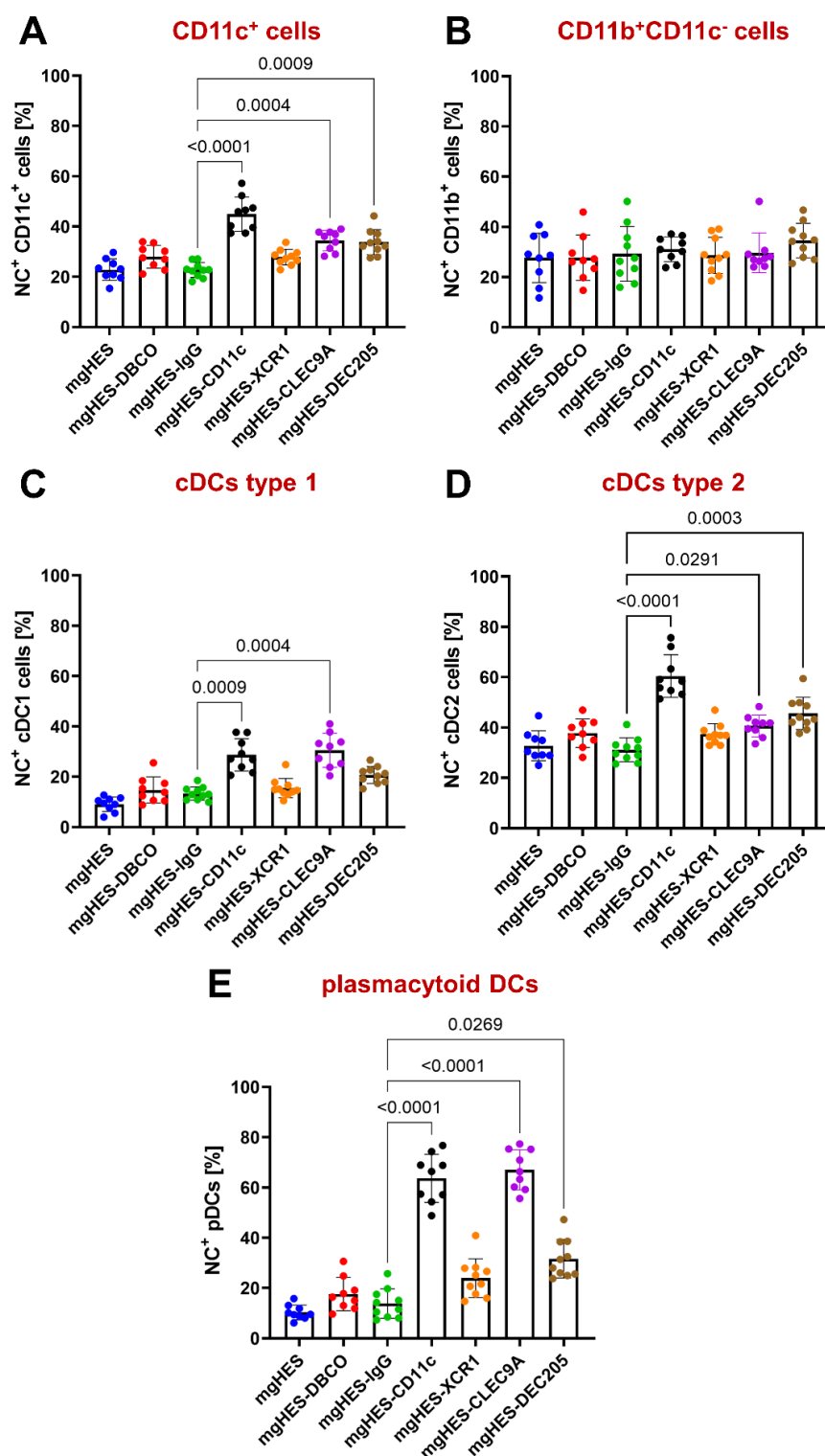


Figure 5.6: Targeting of dendritic cell subsets *in vivo*. Mice were treated with mgHES nanocarriers functionalized with different DC-targeting antibodies. Nanocarrier uptake by (A) CD11c⁺ cells, (B) CD11b⁺CD11c⁻ macrophages, (C) conventional DCs type 1, (D) conventional DCs type 2, and (E) plasmacytoid DCs within the spleen was determined using flow cytometry. Data represent mean ± SD. All nanocarrier formulations were compared to the IgG control (mgHES-IgG) and significance was given with $p < 0.05$ using a Kruskal-Wallis test followed by a Dunnett's multiple comparison test. Individual p values are indicated in the graph.

5.5 Supporting Information

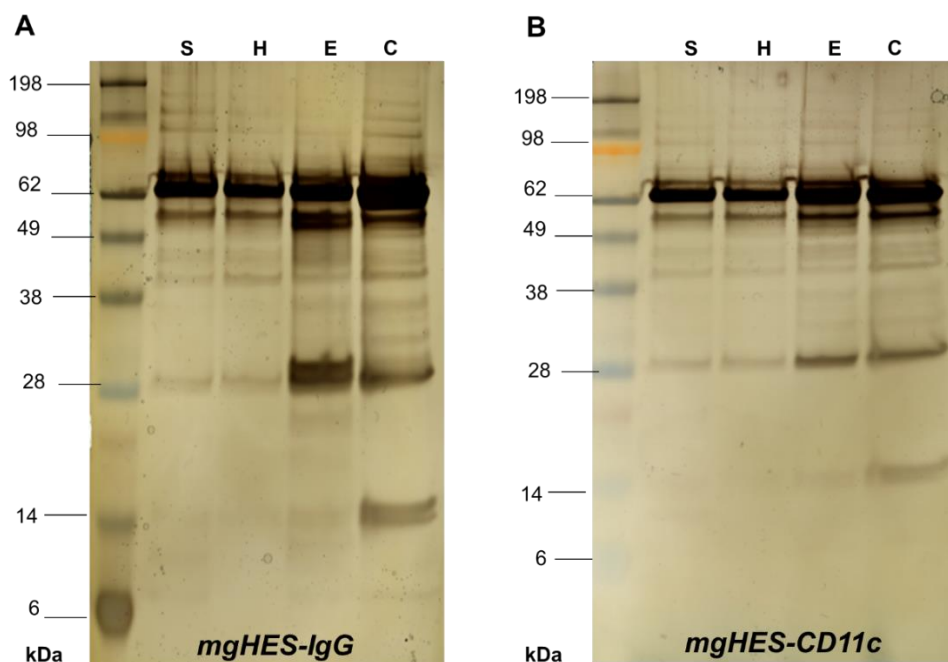


Figure 5.S1. SDS-PAGE of the protein corona of antibody-functionalized nanocarriers incubated under *in vitro* conditions for 1 min (S = Serum, H = Heparin plasma, E = EDTA plasma, C = Citrate plasma). **A)** mgHES-IgG nanocarriers vs. **B)** mgHES-CD11c nanocarriers.

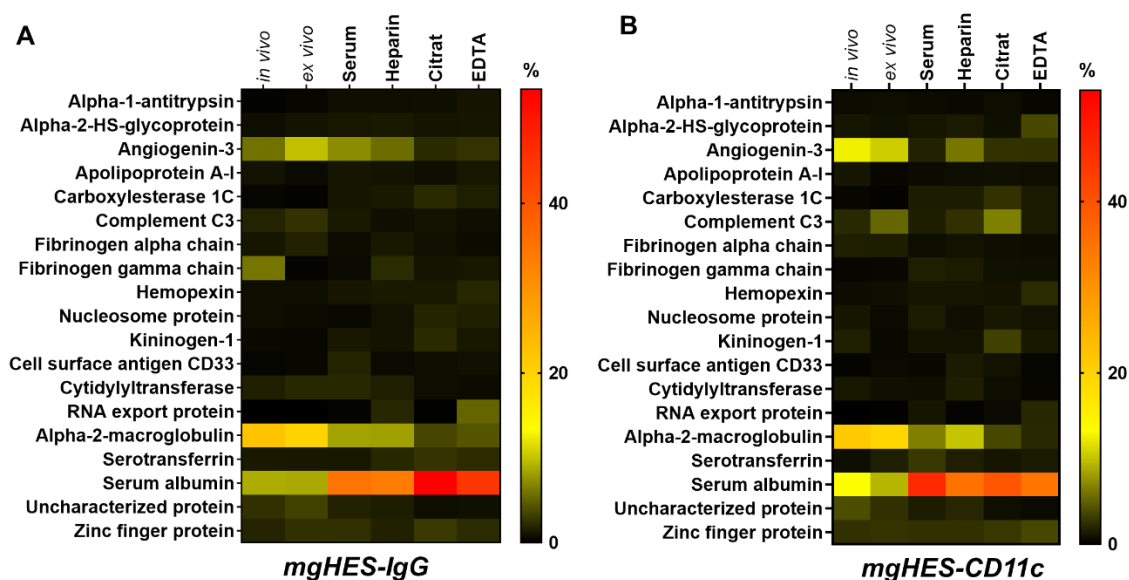


Figure 5.S2. LC-MS analysis of the protein corona. The relative amount of each protein in % is calculated based on the total amount of all identified proteins determined in fmol ($n = 3$, for all *in vivo* samples). **A)** mgHES-IgG nanocarriers vs. **B)** mgHES-CD11c nanocarriers.

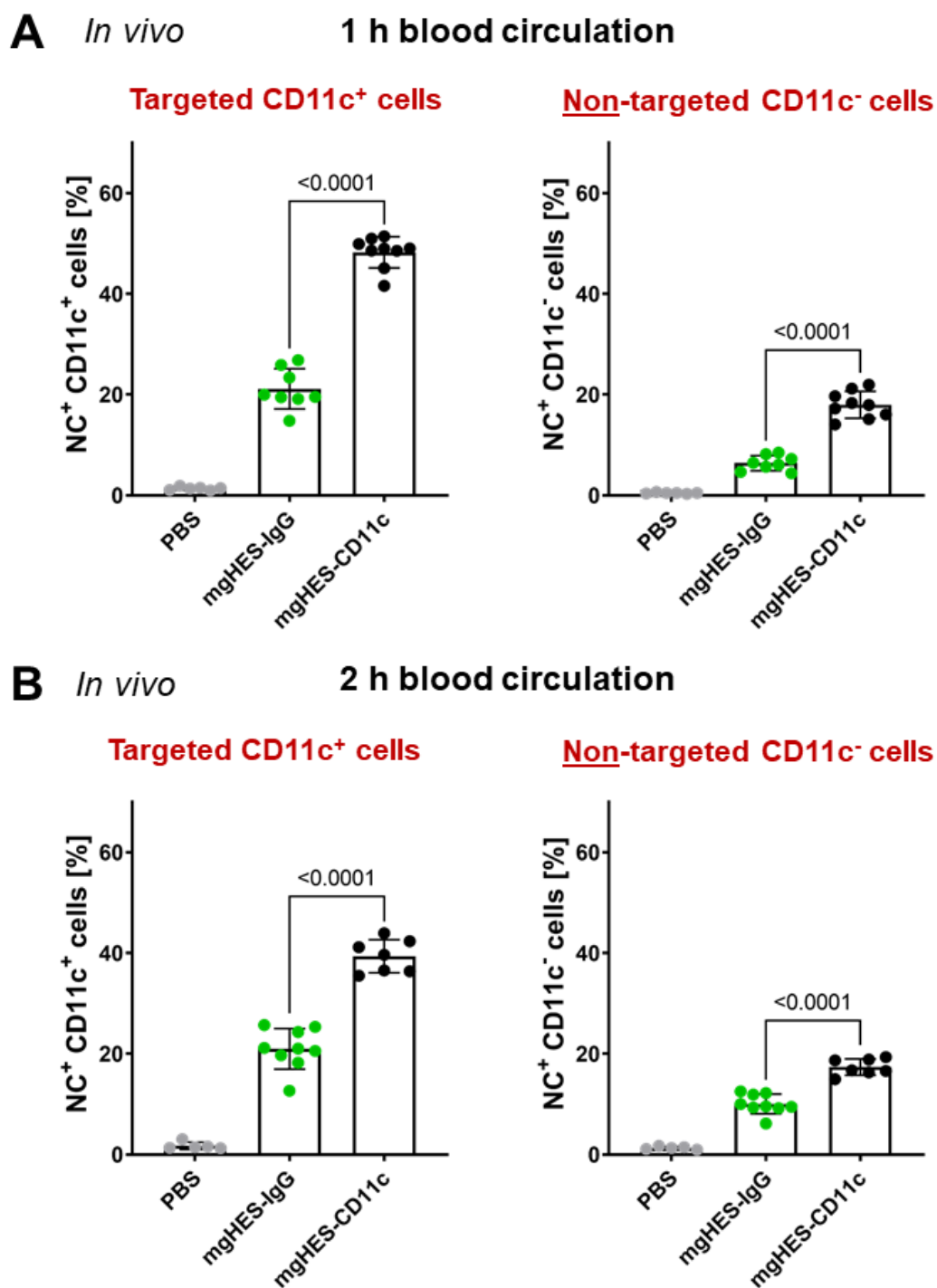


Figure 5.S3. Targeting CD11c⁺ spleen cells *in vivo*. Mice were treated with antibody-conjugated nanocarriers for 1 h (A) or 2 h (B), subsequently sacrificed and the spleen was dissected. Binding of antibody-conjugated nanocarriers towards CD11c⁺ and CD11c⁻ cells was analyzed by flow cytometry. Data represent mean \pm SD. mgHES-CD11c nanocarriers were compared to the IgG control (mgHES-IgG) and significance was given with $p < 0.05$ using a Welch's t test. Individual p values are indicated in the graph.

5. Achieving dendritic cell subset-specific targeting *in vivo* by site-directed conjugation of targeting antibodies to nanocarriers

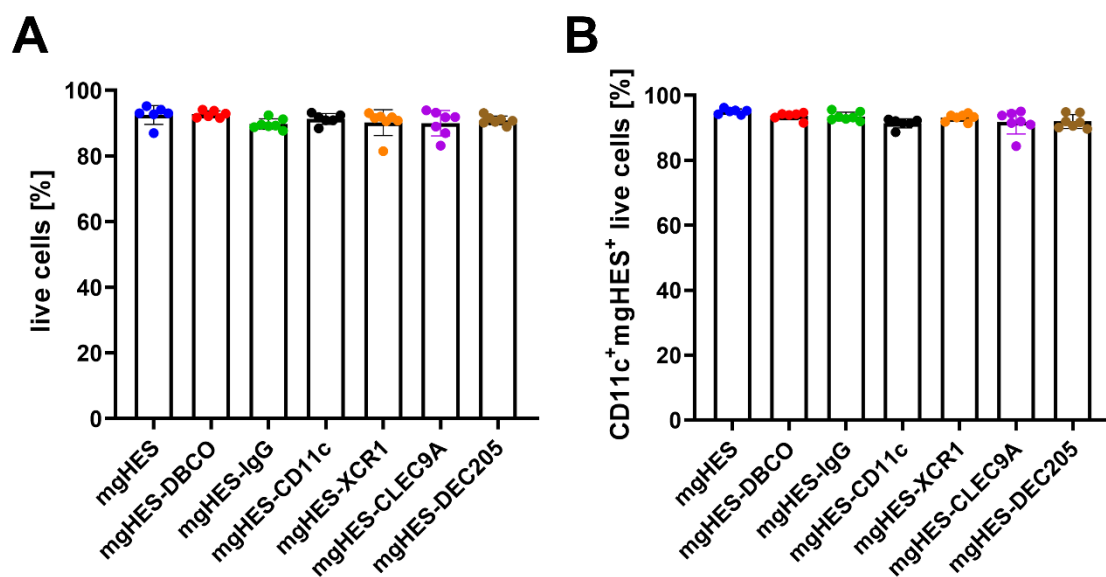


Figure 5.S4. Toxicity of nanocarriers *in vivo*. Mice were treated with antibody-conjugated nanocarriers for 24 h, subsequently sacrificed and the spleen was dissected. Viability is depicted A) as percentage of live cells based on all splenocytes and B) as percentage of live cells based on CD11c⁺ mgHES⁺ splenocytes. All nanocarrier formulations were compared to the IgG control (mgHES-IgG) and significance was given with $p < 0.05$ using a Kruskal-Wallis test followed by a Dunnett's multiple comparison test.

Table 5.S1: Physico-chemical characterization of antibody-functionalized mgHES nanocarrier.

Sample name	Average diameter in PBS ^a	PDI in PBS ^a	ξ -potential [mV]	ξ -deviation [mV]
mgHES-NH ₂	290 nm	0.161	-2.21 ± 0.88	3.23 ± 0.17
mgHES-PEG _{5kDa} -DBCO	396 nm	0.233	-4.22 ± 0.40	3.75 ± 0.34
mgHES-PEG _{5kDa} -IgG	238 nm	0.129	-4.63 ± 0.25	3.28 ± 0.26
mgHES-PEG _{5kDa} -CD11c	208 nm	0.076	-3.84 ± 0.10	3.46 ± 0.42
mgHES-PEG _{5kDa} -XCR1	288 nm	0.145	-4.79 ± 0.22	4.43 ± 0.50
mgHES-PEG _{5kDa} -CLEC9A	308 nm	0.186	-4.85 ± 0.37	4.46 ± 0.81
mgHES-PEG _{5kDa} -DEC205	220 nm	0.194	-6.82 ± 0.58	5.12 ± 1.31

^a Determined by multi-angle DLS (at scattering angles of 30° to 150°)

6. PEG spacer length substantially affects antibody-based nanocarrier targeting of dendritic cell subsets

Aim:

The previous two chapters, 4 and 5, introduced a site-directed antibody modification strategy combined with the surface-functionalization of nanocarriers. This precise conjugation strategy highlighted the importance of a controlled orientation of the antibody to target specifically dendritic cells *in vitro* and dendritic cell subsets *in vivo*. As a follow-up study, the presented work [4] in subchapter 6 aims to investigate the previously established conjugation strategy regarding the use of different length PEG linkers. These heterobifunctional PEG linkers distance the antibody molecule from the nanocarrier surface enabling a certain flexibility in the positioning of the molecule. Hence, we investigated the influence of this spacing with a focus on targeting dendritic cells from cell lines and dendritic cell subsets from primary cells. In addition, the PEGylation of the nanocarriers without an antibody-modification further examined the stealth properties in macrophages and dendritic cells.

[4] Maximilian Brückner*, Michael Fichter*, Richard da Costa Marques, Katharina Landfester, Volker Mailänder. PEG spacer length substantially affects antibody-based nanocarrier targeting of dendritic cell subsets (preliminary title). To be submitted.

Contribution:

I, Maximilian Brückner, generated all PEGylated and antibody-decorated nanocarrier conjugates. In addition, I investigated the cell uptake experiments in the two cell lines (RAW264.7 and DC2.4 cell lines) using flow cytometry. These uptake experiments included the pre-incubation with mouse plasma and the visualization by cLSM. Dr. Michael Fichter performed the cell uptake experiments in primary cells (splenocytes and BMDCs) by flow cytometry. Richard da Costa Marques measured the biomolecular corona (LC-MS). Christine Rosenauer determined the average size of all nanocarrier samples (multi-angle DLS) and I examined the surface charge (ξ -potential). Kathrin Kirchhoff visualized the PEGylated nanocarriers in cell culture medium (TEM). Prof. Katharina Landfester and Prof. Volker Mailänder supervised the project.

6.1 Abstract

A successful dendritic cell (DC) targeting depends on the controlled positioning of DC-specific antibodies on the nanocarrier (NC) surface. Thus, an uncontrolled antibody immobilization results in an unintended cell uptake due to F_c -mediated cell interactions. Therefore, a precise immobilization of the F_c region towards the nanocarrier surface is needed with the F_{ab} regions maintaining freely accessible for antigen binding. Moreover, the antibody requires a certain distance to the nanocarrier surface, influencing the targeting performance after formation of the biomolecular corona. This can be achieved by using PEG linker molecules. However, dendritic cell targeting experiments with different linker lengths are largely missing. Consequently, we focused on the surface modification of nanocarriers with different molecular weight PEG linkers (0.65, 2, and 5 kDa) and their ability to reduce an undesired cell uptake while achieving efficient DC targeting via covalently immobilized antibodies (*stealth targeting*). As a result, our findings demonstrate a significant influence of the PEG linker length affecting an active dendritic cell targeting from cell lines (DC2.4) to primary cells (BMDCs, splenocytic conventional DCs type 1 (cDC1)). While antibody-functionalized nanocarriers with a shorter PEG length (0.65 kDa) showed the best targeting in DC2.4, a larger PEG length (5 kDa) was required to specifically accumulate in BMDCs and splenocytic cDC1. Therefore, our study highlights crucial aspects to consider when targeting dendritic cell subsets, which is of great importance in the field of cancer immunotherapy.

6.2 Introduction

The main goal of smart drug delivery is represented by a targeted nanocarrier transport of drugs or immunomodulatory molecules to the organ or cell type of interest without the clearance or accumulation in other compartments¹²². Controlling this nanocarrier-based delivery is key for the reduction of systemic side effects and the improvement of pharmacological profiles¹⁷⁶. Despite many years of research, tumor-targeting nanocarrier systems only achieve tumor accumulation rates with a median of 0.7% of the injected dose at the targeted site³⁰. Consequently, nanocarriers applied as nanomedicines have broadly failed in clinical trials with only a few exceptions, including albumin-stabilized paclitaxel nanoparticles (ABRAXANE®), or liposomal formulations of either doxorubicin (DOXIL®) or irinotecan (ONIVYDE®)^{31, 32, 239}. Nevertheless, nanocarriers inherit a great potential in revolutionizing targeted therapies, as demonstrated just recently by the use of lipid nanoparticle-based COVID-19 mRNA vaccines²⁴⁰.

Numerous factors influence a successful clinical translation into the medical market and must be overcome to learn from previously failed nanocarrier systems^{32, 239}. In this field, the nano-bio interface represents a great challenge to overcome³². In particular, the role of the biomolecular corona and its influence on antibody-based nanocarrier targeting³³ and drug release³⁴. In addition, many nanocarrier systems are rapidly cleared by the mononuclear phagocyte system (MPS) or the complement system²⁴¹. In this process, pristine nanocarriers are usually marked and identified by opsonins such as complement proteins or immunoglobulins, which can bind to opsonin receptors expressed on macrophages leading to nanocarrier phagocytosis²⁴². Hence, the immune system plays a critical role in the recognition and elimination of nanocarriers²⁴³.

Therefore, nanocarriers have been coated with an additional stealth layer that disguises the nanocarriers and prevents the recognition by opsonins reducing phagocytic removal. Among the stealth polymers, poly-(ethylene glycol) (PEG) is rated as the gold standard regarding the surface-modification of nanocarriers resulting in a reduced clearance by the MPS and complement system²⁴⁴. PEG has been shown to increase the hydrodynamic size and water solubility of nanocarrier systems, thereby, decreasing their self-aggregation and interaction with blood components of the MPS by means of steric repulsion^{245, 246}. As a result, PEGylated nanocarrier systems are rapidly growing in the field of nanomedicine and have already reached clinical trials or have been licensed by pharmaceutical regulatory authorities²⁴⁷. Across the PEGylated drugs or nanocarrier systems, the attached PEGs differ in their molecular weight ranging from 2 to 60 kDa²⁴⁶. Even though, these non-targeted nanocarriers demonstrated an

improved pharmacokinetic profile compared to the administration of free payload¹⁴⁴, as mentioned above, the average accumulation at the target site is low in case of tumor therapy³⁰.

Consequently, improving a selective accumulation of the nanocarrier system requires active targeting ligands, such as the surface-decoration with antibody molecules. Especially in the field of cancer vaccines and immunotherapy, a nanocarrier-based targeted delivery of tumor-associated antigens and immunomodulators (adjuvants) to dendritic cells (DCs) bears great potential to generate robust antigen-specific anti-tumor immune responses²⁴⁸. However, due to the poor success of DC-based anti-tumor vaccines in clinical trials, an efficient targeting of specific DC subsets is the prerequisite for the induction of strong anti-tumor responses²⁴⁹. In particular, conventional DCs type 1 (cDC1) inherit the potential to efficiently cross-present exogenous antigens enabling them to induce strong cytotoxic T cell responses against tumor cells²⁵⁰. Therefore, delivering cargo to cDC1 via nanocarriers functionalized with antibodies, such as anti-CLEC9A²⁵¹ and other targets, is a feasible approach. However, several limitations exist evidenced by only a small number of antibody-functionalized nanocarrier formulations undergoing clinical trials²⁵². Most commonly, the antibody surface-decoration of nanocarriers apply a PEG linker to locate the antibody molecule in a certain distance from the nanocarrier surface. Hence, the PEG length can influence the interactions of the attached targeting ligand and the cell receptor of interest^{253, 254}.

As investigated by Cruz *et al.*, a PEG linker length comparison on antigen-loaded and antibody-coated PLGA nanoparticles highlighted short PEG constructs (2 – 3 kDa) to result in stronger interactions with DCs inducing higher T cell proliferation compared to larger PEG constructs (6 – 20 kDa)²⁵⁵. In contrast, Kapadia *et al.* demonstrated a higher particle uptake and antigen presentation of peptide-decorated hydrogels when using a 5 kDa PEG linker compared to 2 and 10 kDa²⁵⁶. Due to this complexity, we aimed to investigate our previously developed antibody-nanocarrier conjugates, precisely targeting DCs both *in vitro*²⁰⁰ and *in vivo*²⁵¹, with respect to the influence of the applied PEG linker length (0.65, 2 and 5 kDa PEG). These investigations focused particularly on the targeting of the CD11c receptor on DCs in immortalized (DC2.4) or primary DCs (BMDCs, splenocytic cDC1s) and the impact of the biomolecular corona. The herein presented study delineates the differences in DC targeting between the three PEG linker constructs from cell lines to primary cells highlighting a greater antibody distance from the nanocarrier surface necessary for targeting DC subsets. In particular, the ability of nanocarriers to target cDC1 in primary cells required a 5 kDa PEG construct. Furthermore, our biomolecular corona analyses highlight the importance of the nanocarrier-antibody composition.

6.3 Material and Methods

Cell culture. The murine RAW264.7 macrophages (DSMZ, Germany) were cultured in Dulbecco's modified eagle medium (DMEM, Thermo, Germany) containing 10% fetal bovine serum (FBS), 100 U mL⁻¹ penicillin, 100 mg mL⁻¹ streptomycin, and 2 mM glutamine (all Invitrogen, Germany). The murine DC2.4 dendritic cells (Merck, Germany) were cultured in Iscove's Modified Dulbecco's Medium (IMDM, Sigma-Aldrich, USA), supplemented with 5% FBS, 100 U mL⁻¹ penicillin, 100 mg mL⁻¹ streptomycin, 2 mM glutamine, as well as 1% 2-Mercaptoethanol (100X). Both cell lines were maintained in an incubator with 37 °C and 5% CO₂ humidity (CO₂ Incubator C200, Labotect). For the passaging of cells, the consumed media was discarded and the cells were briefly washed with 10 mL PBS. RAW264.7 cells were detached at 37 °C with Trypsin-EDTA (Thermo, Germany) and DC2.4 cells at 4 °C with PBS containing 2 mM EDTA for 10 min. The cells were detached from the flask by pipetting 10 – 20 mL of FBS containing medium up and down, followed by centrifugation of the cell suspension at 300 g for five minutes. The resulting cell pellet was resuspended in medium with FBS and the cell viability was tested with trypan blue (1:1 dilution) by an automated cell counter (TC10, Bio-Rad).

Nanocarrier PEGylation and modification for the attachment of antibodies. The nanocarriers, namely bionized nanoferrite particles with a hydroxyethyl starch shell (micromod, Germany), were PEGylated to the surface amine groups via NHS chemistry based on the amount of NH₂ given by the manufacturer (3 nmol mg⁻¹). For this purpose, five different bifunctional linkers were investigated. Those include, the NHS-PEG-DBCO linker of 0.65 kDa (Jena Biosciences, Germany), the 2 kDa NHS-PEG-MeO and 5 kDa NHS-PEG-MeO (both from Iris Biotech GmbH, Germany), and the 2 kDa NHS-PEG-DBCO and 5 kDa NHS-PEG-DBCO (both from Nanocs Inc., USA). Each linker was conjugated onto the nanocarrier surface with three different molecular weight ratios (1:1, 1:10, 1:50) based on the amount of NH₂. For this, the number of NH₂ groups per mg nanocarrier were multiplied by the molecular weights of the different linkers and the desired linker ratio. All linker solutions were prepared freshly in DMSO (Merck) for each experiment. After overnight reaction under constant shaking at room temperature, all nanocarrier linker conjugates were washed (3x) with PBS using a strong magnet (neodymium magnet) to remove excess linker species. The final nanocarrier linker products were resuspended in PBS and their concentration was determined by fluorescence calibration. The DBCO-functionalized nanocarriers were overnight conjugated with the azide-modified antibodies (see site-directed antibody modification) at room temperature under shaking (in PBS). For this conjugation, the reaction was scaled based on a nanocarrier to azide-antibody ratio of 67:1. For example, 1 mg of nanocarriers were reacted with 14.93 µg of azide-antibody.

Fluorescence Calibration for Nanocarrier Quantification. The fluorescence calibration was performed to determine the amount and concentration of all nanocarrier conjugates. Pristine nanocarriers were used as a standard and diluted to a linear fit (100 µg mL⁻¹ down to 3.125 µg mL⁻¹). All probes were diluted based on the initial mass used. Measurements of the standard and samples were prepared as duplicates in PBS. The Infinite M1000 plate reader (Tecan) with an excitation wavelength of 552 nm and emission of 580 nm recorded the fluorescence.

6. PEG spacer length substantially affects antibody-based nanocarrier targeting of dendritic cell subsets

Validation of nanocarrier PEGylation. The surface PEGylation of the nanocarriers was qualitatively analyzed by two fluorescence-based methods via the plate reader (Infinite M1000, Tecan) and flow cytometry (Attune NxT, Thermo). For this purpose, an Alexa Fluor™ 647 NHS-Ester (Succinimidylester, Thermo) was applied. For the preparation, 100 µg of pristine and PEGylated nanocarriers were reacted with a 50-fold molar excess of the NHS-Ester (18.75 ng, 1.9 µL of a 10 ng/µL stock) for 1 h at room temperature while shaking. After the incubation, all samples were washed (3x) with PBS using a strong magnet. Pristine nanocarriers incubated with and without the NHS-Ester were utilized to differentiate between the negative background signal and the positive NHS-Ester signal representing the binding towards the primary amines on the nanocarriers. For the plate reader measurement, all samples were resuspended in a final volume of 0.1 mL PBS and 80 µL were pipetted into a black 96 well-plate (n = 2). The fluorescence was measured with an excitation of 651 nm and an emission of 672 nm. Data sets were calculated from the positive control. For the flow cytometry measurement, 1 µL of nanocarrier sample (~ 10 µg) were diluted in 1 mL PBS and analyzed by the RL1 channel with an excitation laser of 633 nm and a 670/14 nm band pass filter for emission.

Site-directed antibody modification. Antibodies (α-CD11c, clone N418, and α-IgG isotype, clone HTK888, both from Biolegend) were azide-modified based on the manufacturer's instructions (Site Click™ Antibody Azido Modification Kit, Thermo). In summary, the concentrated antibody was first reacted overnight with β-galactosidase at 37 °C to cleave the galactose residues present at the carbohydrate domains at the F_c region. At next, the azide groups were attached by incubating the antibody with the GalT (Y289L) enzyme in combination with the UDP-GalNAz donor in an overnight reaction at 30 °C. In a last step, the azide-modified antibody was purified and concentrated. The modified antibodies were further analyzed for their concentration (Pierce 660 nm Protein Assay), the validation of their azide-attachment, and the conjugation onto DBCO-functionalized nanocarriers via copper-free click chemistry.

Antibody quantification. The antibody concentrations were specified by using the Pierce 660nm protein assay according to the manufacturer's instructions. BSA (bovine serum albumin) was applied as a standard by setting up a dilution series in PBS. The Infinite M1000 plate reader (Tecan) was used to measure the standard and all samples at an optical density of 660 nm, in duplicates.

Cell line uptake experiments. For the nanocarrier cell experiments, 1.5×10^5 cells mL⁻¹ were cultivated in a 24-well plate in a humidified incubator at 37 °C and 5% CO₂. After overnight attachment, the cell culture medium was exchanged before each experiment to fresh medium with or without FBS for one to two hours. This medium exchange was performed so that the cells could adapt to the serum-free environment. All samples were prepared in triplicates and incubated for 2 h with a concentration of 7.5 or 75 µg mL⁻¹ in 250 µL of medium per well. The pre-incubation with mouse plasma was performed for 1 h at 37 °C shaking in a 1:1 nanocarrier to mouse plasma ratio. Afterwards, the mouse plasma was separated from the samples by using a magnet and 7.5 or 75 µg mL⁻¹ in 250 µL medium without FBS were incubated with the cells. After the incubation, 1 mL PBS was used to wash the cells. Then, the cells were detached via 250 µL 2 mM PBS EDTA for 10 min at 4 °C (DC2.4) or Trypsin-EDTA for 5 min at 37 °C (RAW264.7). At next, 250 µL of medium with FBS were added and the cells were transferred

6. PEG spacer length substantially affects antibody-based nanocarrier targeting of dendritic cell subsets

from the well into a 1.5 mL micro tube. The cell viability was determined by using the Zombie Aqua assay (Biolegend, USA). For this assay, the cells were centrifuged at 500 g for 5 min and the cell pellet was resuspended in 100 μ L Zombie Aqua solution (1:500 diluted in PBS). After an incubation of 15 min at 4 °C in the dark, the Zombie Aqua solution was separated from the cells by centrifugation at 500 g for 5 min and the cells were resuspended in 1 mL PBS for their analysis at the flow cytometer.

Flow cytometry. The measurement of nanocarriers taken up by cells or the detection of covalently bound antibodies on the nanocarrier surface was performed by flow cytometry (Attune™ NxT, Thermo). The nanocarriers were detected by their red fluorescence with the YL1 channel and an excitation laser of 561 nm and a 585/16 nm band pass filter for emission. Viability of the cells was determined by using the Live/Dead fixable Zombie Aqua (Biolegend, U.S.A) with the VL2 channel with an excitation laser of 405 nm and a 512/25 nm band pass filter for emission. The Attune™ NxT Software was applied for data analysis. In a first step, the cell population was selected with an FSC/SSC scatter plot, excluding cell debris. Only the gated events of viable cells were examined by the fluorescence signal expressed as the median fluorescence intensity (MFI) or as the percentage of gated events/cells. For the validation of a correct antibody surface-modification of the nanocarriers, a secondary fluorescence-labeled antibody, which was directed against the F_c region of the bound antibody, was chosen. The testing was performed with 2 μ g of sample and 1 μ g of secondary antibody in 20 μ L PBS, which were reacted at 4 °C in the dark for 30 min. The pristine nanocarriers with and without the secondary antibody were applied as adsorption controls. Following incubation, the probes were filled up to 1 mL PBS and analyzed by flow cytometry. After selecting the nanocarrier population by the FSC/SSC scatter plot, the red fluorescence (YL1) was plotted against the SSC. From this selected population, the MFI or the percentage of gated events of the secondary antibody channel were detected by using the BL1 channel with an excitation laser of 488 nm and a 530/30 nm band pass filter for emission.

Visualization of intracellular localization by cLSM. Nanocarrier cell interactions were visualized using the confocal laser scanning microscopy (cLSM). The experiments were performed on the LSM SP5 STED Leica Laser Scanning Confocal Microscope (Leica, Germany), composed of an inverse fluorescence microscope DMI 6000CS equipped with a multi-laser combination using a HCX PL APO CS 63 x 1.4 oil objective. The red fluorescence of the nanocarrier samples was excited with the excitation laser 561 nm and detected with an emission filter at 570 – 599 nm. The cell membrane of the cells was stained with CellMask DeepRed (Thermo) applying the excitation laser 633 nm with a detection at 660 – 700 nm. For the experimental setup, 5 x 10⁴ RAW264.7 cells in 200 μ L DMEM with 10% FBS were seeded in a well of a 15 μ -Slide 8 well glass bottom (ibidi). After overnight attachment in the incubator, the medium was exchanged for 60 – 90 min, followed by the sample incubation with 75 μ g mL⁻¹ for 2 h at 37 °C (DMEM medium with FBS, without FBS, and pre-incubated with mouse plasma and resuspended in medium without FBS). After the incubation, the cells were washed once with PBS and the cell membrane was stained for 5 min in the dark (1:1.000 in PBS) before the live cell imaging. The image acquisition was performed by using ImageJ (v1.52n).

Incubation and Visualization of Mouse Plasma. The murine biomolecular corona proteins of the nanocarriers were analyzed by SDS-PAGE and silver staining (both from Thermo). For this analysis,

6. PEG spacer length substantially affects antibody-based nanocarrier targeting of dendritic cell subsets

the samples were incubated with the mouse plasma (GeneTex, USA) at a 1:1 volume ratio for 1 h at 37 °C under shaking. Subsequently, the mouse plasma was removed and the samples were washed (3x) with PBS by using a magnet. Adsorbed mouse plasma proteins were detached from the samples by resuspending the nanocarrier pellet in 100 µL desorption buffer (2% (w/v) SDS + 62.5 mM Tris-HCl in 3 mL deionized water) for 10 min at 70 °C under shaking. Desorbed proteins were recovered from the nanocarrier samples by applying a magnet. The total amount of denatured proteins in the supernatant was quantified by Pierce 660nm protein assay and 2 µg were used for SDS-PAGE, visualized by silver staining.

Multi-angle dynamic light scattering. For the detection of the size (diameter in nm) and size distribution (PDI), all nanocarriers were analyzed by multi-angle dynamic light scattering. The measurements were performed on an ALV spectrometer consisting of a goniometer and an ALV-5004 multiple-tau full-digital correlator (320 channels) at 20 °C and 7 (dynamic) angles ranging from 30° to 150°. The light source was a He-Ne Laser (wavelength of 632.8 nm). The samples were prepared by diluting 1 µL of unfiltered dispersion with 1 mL PBS which was previously filtered through membrane filters (GS Millipore) with a pore size of 2.0 µm.

Zeta potential. The surface charge of the nanocarriers was detected using a Zeta Sizer Nano Series (Malvern Instruments GmbH, Herrenberg, Germany). All samples (10 µL) were diluted in a 1 mM potassium chloride solution (1 mL) and measured in technical triplicates.

TEM. The FEI Tecnai F20 transmission electron microscope (operating at a voltage of 200 kV) was used to investigate the morphology of the nanocarriers. For this investigation, all samples were diluted to a particle concentration of 75 µg mL⁻¹ in IMDM medium containing 5% FBS and 4 µL were pipetted on a carbon coated grid. The excess solvent was blotted away with filter paper.

In solution digestion. SDS was removed from the protein corona samples by using Pierce™ Detergent Removal Spin Columns (Thermo Scientific, Germany), according to the manufacturer's instructions. Next, protein samples were subjected to an in-solution tryptic digest as a preparation for the LC-MS proteomic measurements. The digestion protocol was carried out as described previously with modifications^{95, 257}. Briefly, 10 to 25 µg of protein were precipitated and washed twice by using the ProteoExtract Protein Precipitation Kit (CalBioChem, Germany), according to the manufacturer's instructions. After letting the protein pellet dry for 5 to 10 min, the protein was solubilized in 0,1% RapiGest SF surfactant (Waters Corporation, Germany, dissolved in 50 mM ammonium carbonate buffer) at 80 °C for 15 min. Disulfide bonds were reduced with a 5 mM final concentration of dithiothreitol (Sigma, Germany) at 56 °C for 45 min. Thiol alkylation was performed with a 500 mM final concentration of iodoacetamide (Sigma, Germany) at room temperature for 1 h in the dark. Subsequently, the digestion was carried out with trypsin in a mass ratio of 50:1 (protein:trypsin) at 37 °C for a maximum of 18 h. The digestion was stopped by lowering the pH of the peptide solution with 2 µL of hydrochloric acid (Sigma, Germany). To remove aggregates, the samples were centrifuged at 13 000g for 15 min at 4 °C and the supernatant was transferred to new tubes for measurement.

Liquid chromatography-electrospray ionization mass spectrometry (LC-MS). Peptide samples were spiked with 50 fmol μL^{-1} HI3 Ecoli Standard (Waters Corporation, Germany), and the total volume was adjusted with LC-MS grade water (Merck, Germany). The absolute quantification performed in these measurements is based on a previously published protocol²⁵⁸. The LC-MS measurements were carried out as previously described in the works of our group^{95, 245}. A nanoACQUITY UPLC system coupled to a Synapt G2Si mass spectrometer (both Waters Corporation, Germany) was utilized, operating the measurements with MassLynx 4.1 (Waters Corporation). The UPLC was equipped with a C18 nanoACQUITY trap column (5 μm , 180 μm \times 20 mm) and a C18 analytical reversed-phase column (1.7 μm , 75 μm \times 150 mm; both Waters Corporation, Germany). The samples were injected with a flow rate of 0.3 $\mu\text{L min}^{-1}$ and separated by a gradient of 2% to 37% of mobile phase B over 70 min. The solvents for the gradient consisted of (A) 0.1% (v/v) formic acid in LC-MS grade water and (B) 0.1% (v/v) formic acid in acetonitrile (Biosolve, Germany). The reference components Glu-Fibrinopeptide and LeuEnkephalin (both Sigma, Germany) were injected with a flow rate of 0.5 $\mu\text{L min}^{-1}$. The mass spectrometer was equipped with a NanoLockSpray for source by electrospray ionization (ESI) and configured for positive mode. The measurements were conducted in the resolution mode with data-independent acquisition (MS^E) in a mass to charge range of 50–2000 Da, scan time of 1 s, ramped trap collision energy from 20 to 40 V, and data acquisition of 90 min. All samples were measured in technical triplicates.

Protein identification. Protein identification was performed by using the Progenesis QI 2.0 software (Nonlinear Dynamics). The procedure was described previously²⁴⁵. Following settings were applied to process the data: Noise reduction threshold for low energy as 120 counts, elevated energy as 25 counts, and peptide intensity as 750 counts. The utilized protein database consisted of the human proteome with reviewed proteins which were downloaded from uniprot (swiss prot). The sequence information for the HI3 E. coli standard was added to the protein database file. Following settings were used to identify the proteins: one missed cleavage, maximum protein mass of 600 kDa, fixed carbamidomethyl modification for cysteine, variable oxidation for methionine, a minimum of three assigned fragments per peptide, a minimum of two assigned peptides per protein, a minimum of five assigned fragments per protein, and a score parameter below 4. A table with all identified proteins is provided as supplementary information.

Generation of bone marrow-derived dendritic cells. Bone marrow-derived dendritic cells (BMDC) were differentiated from progenitor cells (BM cells) isolated from bone marrow of 8- to 12-week old C57BL/6J mice as described before²⁵⁹. Briefly, bone marrow obtained by flushing the femur and tibia with cell culture medium (Iscove's Modified Dulbecco's Medium (IMDM) containing 5% FBS (PAN), 2 mM GlutaMax (Thermo Fisher Scientific), 100 U ml^{-1} penicillin, 100 $\mu\text{g ml}^{-1}$ streptomycin, and 50 μM β -mercaptoethanol (Sigma-Aldrich). BM cells were washed and seeded in non-TC-treated 10 cm-petri dishes (2 \times 10⁶ in 10 ml per dish). 50 % of cell culture medium was replenished on days 3 and 6. Non-adherent and loosely adherent immature BMDCs were harvested on day 7 and used for uptake experiments.

BMDC uptake experiments. Harvested BMDCs were washed with FBS-free cell culture medium and reseeded in 24-well suspension culture plates (10^5 per well) in 500 μ l cell culture medium either supplemented with 5% FBS or with 5 % mouse plasma. Subsequently, cells were incubated with 3 μ g mL⁻¹ of different nanocarrier formulations for 20 h at 37 °C and 7.5% CO₂, harvested and analyzed by flow cytometry.

Conventional DC type 1 uptake experiment. Spleen cells were prepared as previously described²⁶⁰. Briefly, spleens of C57BL/6 mice were dissected and mechanically grinded through a 40 μ m cell strainer. Red blood cells were subsequently lysed using a hypotonic buffer (155 mM NH₄Cl, 10 mM KHCO₃, 100 μ M EDTA-disodium, pH 7.4) for 30 s and washed using cell culture medium (Iscove's Modified Dulbecco's Medium (IMDM) supplemented with 5% fetal bovine serum (FBS) and 1% Penicillin (100 U mL⁻¹) and Streptomycin (100 mg mL⁻¹ (P/S)). Isolated spleen cells were subsequently seeded in 48-well plates (10^6 per well) in 500 μ l cell culture medium without FBS supplemented with 5% mouse plasma. Different nanocarrier formulations were added (3 μ g mL⁻¹) and cells were incubated for 20 h at 37 °C and 7.5% CO₂. Spleen cells were harvested and washed (1% FBS in PBS). F_c receptors were blocked with anti-CD16/CD32 (clone 2.4G2) for 10 min. To differentiate the cell types via flow cytometry, spleen cells were incubated with fluorophore-labelled cell type-specific antibodies for 30 min: anti-CD11c (clone N418), anti-CD11b (clone M1/70), anti-CD172a (clone P84), anti-CD8 α (clone 53-6.7), anti-I-A/I-E (MHCII, clone M5/114.15.2), anti-Siglec-H (clone 551), anti-CD19 (clone 6D5), anti-CD3 ϵ (clone 145-2C11), anti-CD14 (clone Sa14-2), anti-NK1.1 (clone PK136), anti-Ly-6G (clone 1A8). Flow cytometric analysis was performed with the Attune NxT (Thermo Fisher Scientific) and analyzed with FlowJo software v10.7.1. Conventional DCs type 1 were defined as CD19⁻ CD3⁻ CD14⁻ NK1.1⁻ Ly-6G⁻ MHCII⁺ CD11c⁺ CD11b⁻ CD172a⁻ CD8 α ⁺.

Statistical analysis. For the PEGylated nanocarrier uptake in the cell lines, the pristine nanocarriers of each medium condition (medium^{-FBS}, medium^{+FBS}, pre-incubated in mouse plasma) were statistically compared to the PEGylated samples from the corresponding medium condition using GraphPad Prism 9 and one-way analysis of variance (ANOVA) followed by a Dunnett's multiple comparison test with a confidence interval as indicated in each figure. The CD11c/isotype fold changes were statistically compared to each other using Brown-Forsythe and Welch ANOVA Test.

6.4 Results and Discussion

Outlining the experimental workflow, we first investigated the stealth effect by coating our magnetic and red-fluorescent nanocarriers (magnetic hydroxyethyl starch particles or mgHES) with different PEG ratios. These PEGylated nanocarriers were then examined in cell culture with macrophages and DCs. Based on these findings, the PEG-induced stealth effect was then combined with the DC targeting ability of antibodies and termed *stealth targeting*. Both, the stealth effect and stealth targeting nanocarriers, were analyzed based on their physicochemical characteristics (ζ -potential, MADLS, and TEM), their interaction with macrophages and DCs (flow cytometry and cLSM), and their proteomic biomolecular corona composition (SDS-PAGE and LC-MS).

Initially, two different PEG linkers (NHS-PEG_x-MeO) of 2 and 5 kDa molecular weight were covalently immobilized onto the surface of the amine-functionalized nanocarriers and three PEG excess ratios were examined in order to achieve a sufficient stealth effect. This stealth effect, namely a reduced uptake of the PEGylated samples compared to the pristine nanocarriers, was investigated in highly phagocytic cells (macrophage cell line, RAW264.7) as well as in the cells of interest (DC line, DC2.4) and analyzed by flow cytometry. In addition to this, primary DCs, such as bone marrow-derived DCs (BMDCs) and conventional DCs type 1 from the spleen, were analyzed for their potential to take up antibody-functionalized nanocarriers.

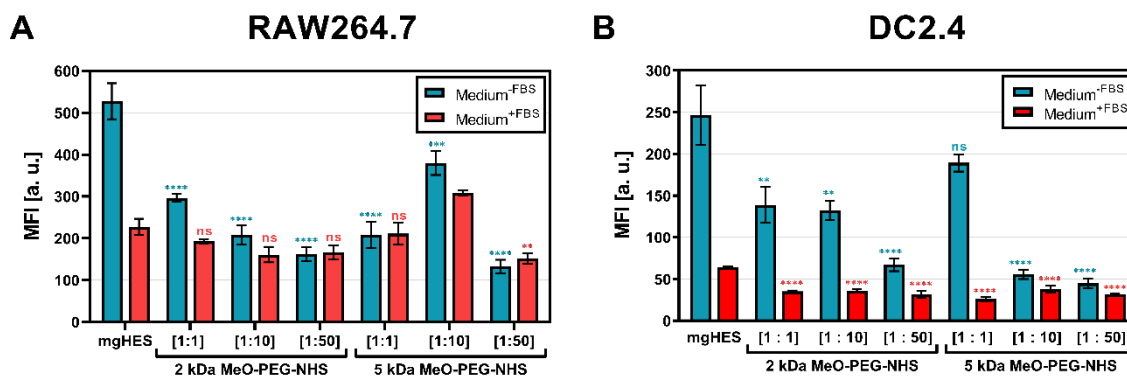


Figure 6.1: Stealth effect of PEGylated nanocarriers in macrophages and dendritic cells. The cell uptake study was conducted with a sample concentration of $7.5 \mu\text{g mL}^{-1}$ and an incubation for 2 h at 37°C . Auto fluorescence is subtracted from each data set. Only viable cells are gated. Values are given as mean \pm SD ($n = 3$). Each condition was compared to the respective control (pristine mgHES) and significance was given with $p < 0.05$ using a one-way ANOVA followed by a Dunnett's multiple comparison test. ns = not significant, $p < 0.0001$ ****.

First, three molar ratios of the linkers were evaluated (Figure 6.1 A and B). Furthermore, the use of culture medium with and without fetal bovine serum (FBS) highlighted the role of additional proteins that can form a biomolecular corona on the nanocarrier surface, potentially

influencing the nanocarrier cell interaction²⁶¹. Each PEG-modified (PEGylated) nanocarrier formulation was taken up to a lower rate by both cell lines when being incubated in medium without FBS (blue bars). Under this medium condition, the stealth effect was found to be more pronounced for both cell lines at higher PEG ratios than at lower ones. In medium supplemented with additional FBS proteins (red bars), the overall uptake of the samples was reduced compared to medium without FBS. Here, only slightly lower values, or slightly increased values (1:10 ratio of the 5 kDa sample in RAW cells, Figure 6.1 A) were detected. A similar finding could be observed when analyzing the frequency of NC⁺ cells (Supporting Information Figure 6.S1 A and B).

In this case, the nanocarrier PEGylation was limited to the amount of surface-NH₂ sites (3 nmol mg⁻¹) accessible for conjugation. Nevertheless, the cell uptake studies in both cell lines revealed that higher PEG ratios with sufficient reaction rates of NHS to NH₂ were able to better convey the stealth effect. Therefore, higher PEG to NH₂ ratios were able to fully saturate the NHS reaction on the nanocarrier surface. The difference in the PEGylation ratios could be demonstrated by the use of an Alexa FluorTM 647 NHS-ester. For this purpose, the difference in the fluorescence labeling between PEGylated and pristine nanocarriers was evaluated (see Material and Methods for a detailed description). Following the conjugation, the Alexa FluorTM 647-based nanocarrier fluorescence was measured by flow cytometry and the plate reader (Figure 6.S2 A and B). Thereby, a decreasing fluorescence signal was observed for increasing PEG ratios (10x and 50x) indicating that less primary amines were available to react with the Alexa FluorTM 647 NHS-ester compared to the equimolar ratio (1:1). Given the 3 nmol NH₂ per mg nanocarrier and assuming a sphere shape, in theory, the mgHES nanocarriers are equipped with 0.4 NH₂ target sites per nm². Therefore, at a full conversion of amines to NHS linker reactions, 0.4 PEG chains per nm² can be assumed. In summary, the best stealth properties could be achieved when PEGylation was performed at the molar ratio of NH₂ on nanocarriers to PEG linker ratio of 1:50. Li *et al.* showed that a PEG grafting density of 0.2 to 2.5 chains nm⁻² on polymeric ovalbumin nanocapsules with 2 kDa PEG was leading to the formation of an intermediate mushroom to a dense brush conformation²⁶². The ovalbumin nanocapsules evaluated in the respective study, that were modified with 5 kDa PEG, acquired the brush conformation even at a low density of 0.2 chains nm⁻² due to the higher molecular weight. In comparison to the ovalbumin nanocapsules, the herein analyzed PEGylated nanocarriers also seem to differ in their PEG conformation with a transition from the less-favorable mushroom conformation to the desired brush conformation resulting in the greatest stealth effect for a complete amine to PEG conversion in macrophages and DCs. Previous PEGylation studies showed that the PEG-induced stealth effect highly depends on the density and conformation of the surface PEG chains. These parameters affect the formation of a PEG barrier on the nanocarrier surface and hence decrease opsonization and increase circulation

time^{263, 264}. While the mushroom conformation with a larger PEG chain motion and unoccupied spaces on the surface is more susceptible to opsonins, the brush conformation with a limited PEG mobility and an increased surface coverage has been shown to reduce the interaction between the nanocarrier and the opsonins^{243, 265}.

In addition, the shortest PEG linker (0.65 kDa) applied in our previous studies²⁰⁰, was tested in terms of RAW264.7 cell uptake (Figure 6.S1 C and D). In comparison to the 2 and 5 kDa PEG linkers (Figure 6.1), the 0.65 kDa PEG linker showed higher uptake values (both for the MFI and frequency of NC⁺ cells) when FBS was present in the medium. This less pronounced stealth effect, compared to the 2 and 5 kDa PEGylated nanocarriers (50x excess), could also be influenced by the difference in the reactive group pointing to the cells. Namely, the methoxy (MeO) or the dibenzocyclooctyne (DBCO) groups, of which the latter one is necessary for clicking an azide-functionalized antibody onto the nanocarrier surface. With that in mind and according to the findings described above, we decided to further investigate the 50-fold molar excess ratio of the different PEGylated nanocarrier formulations with either the MeO (for the 2 and 5 kDa linkers) or the DBCO-reactive end group (for the 0.65, 2, and 5 kDa linkers) with respect to RAW264.7 cell uptake. Additionally, the PEGylated samples were pre-incubated with mouse plasma for one hour at 37 °C in order to mimic a more physiological condition (Figure 6.2).

As a result, we found that the PEGylated samples in medium without FBS and pre-incubated in mouse plasma almost showed no differences, indicating that the murine biomolecular corona is virtually not involved in conveying or preventing the stealth effect. Overall, the uptake analysis showed that in every sample group the frequency of NC⁺ cells was above 80% (Figure 6.S3). However, based on the MFI, we observe that the PEGylated samples were taken up to a much lower degree. For both, the medium without FBS and the mouse plasma pre-incubation, the greatest stealth effect could be observed for the higher molecular weight PEG linker (5 kDa) with the MeO end group. Carrying DBCO at the end group resulted in a generally higher uptake compared to MeO. This influence of the DBCO group was particularly evident for the shortest PEG linker. The FBS-containing medium showed weaker but comparable results to the other two medium conditions. However, the use of bovine-derived serum in a murine cell uptake study is rather artificial since it does not resemble a physiological environment and can bias the cell uptake results⁵³.

RAW264.7

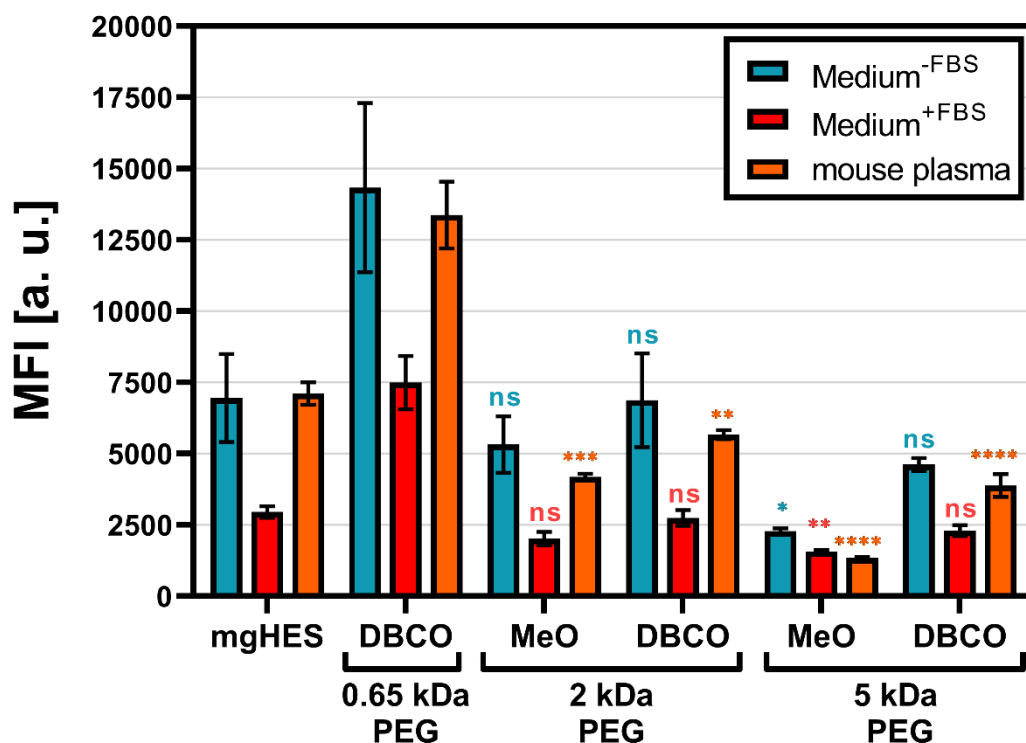


Figure 6.2: Longer PEG chains reduce nanocarrier uptake by RAW264.7 cells. Nanocarriers were incubated with RAW264.7 cells in either medium with or without FBS, or pre-incubated with mouse plasma with a sample concentration of $75 \mu\text{g mL}^{-1}$ and incubated for 2 h at 37°C . Autofluorescence was subtracted from each data set. Only viable cells were analyzed. Values are given as mean \pm SD ($n = 3$). Each PEGylated sample was compared to the pristine nanocarrier group (mgHES) and significance was given with $p < 0.05$ using a one-way ANOVA followed by a Dunnett's multiple comparison test. ns = not significant, $p < 0.0001$ ****.

In order to further depict the stealth effect and the cellular localization of our nanocarriers, either sticking to the cell membrane or being internalized, confocal laser scanning microscopy was performed (Figure 6.3). Therefore, the uptake of pristine and PEGylated nanocarriers, either pre-incubated in mouse plasma (no FBS present in medium) or in medium with 10% FBS was investigated in RAW264.7 cells (Figure 6.S4).

Visually, almost all nanocarrier formulations were internalized by the cells with only a few localized at the cell membrane. Only the 5 kDa PEGylated sample could be clearly distinguished from the other sample groups. Here, we found a lower number of nanocarriers as well as a weaker fluorescence signal. In comparison to the uptake in FBS-containing medium, a generally lower nanocarrier uptake of all samples could be observed. Here, also the longer PEG chains with 2 and 5 kDa led to a reduction in cell internalization. PEG linkers with the DBCO-reactive group could not visualize their stealth properties microscopically and were therefore not included for the 2 and 5 kDa linkers.

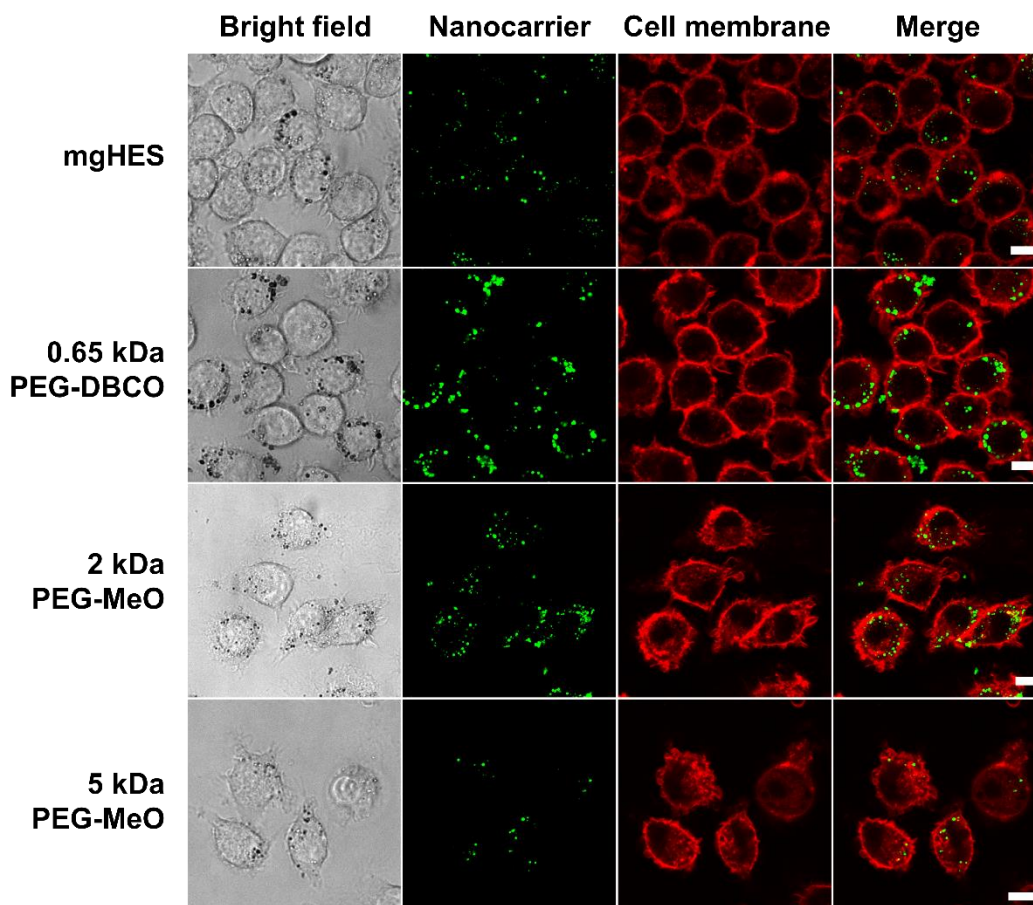


Figure 6.3: Longer PEG chains reduce internalization by macrophages. Mouse plasma pre-incubated nanocarriers were incubated with 5×10^4 RAW264.7 cells for 2 h at 37 °C with a sample concentration of $75 \mu\text{g mL}^{-1}$ in DMEM medium without FBS. Live cell images are shown. All scale bars represent 10 μm .

In a next step, the influence of the biomolecular corona on the stealth effect was determined by quantitatively analyzing the murine proteome of pre-incubated, PEGylated nanocarriers (all with a 50-fold molar excess of linker) via label-free mass spectrometry (LC-MS).

All identified proteins could be correlated to eight protein groups and the respective values were plotted as the percentage based on all identified proteins (Figure 6.4 A). In comparison to the composition of the mouse plasma control, the percentage of serum albumin within the protein corona of the pristine nanocarriers (mgHES) highly increased while the frequency of proteins of all other groups slightly decreased. A similar finding could be observed for all PEGylated samples irrespective of the PEG linker length used, even though the elevation in serum albumin content was not as pronounced as for the pristine nanocarriers. The qualitative analysis by SDS-PAGE further revealed serum albumin to be the strongest band with a molecular weight of about 62 kDa as detected by silver staining (Figure 6.S5 A).

6. PEG spacer length substantially affects antibody-based nanocarrier targeting of dendritic cell subsets

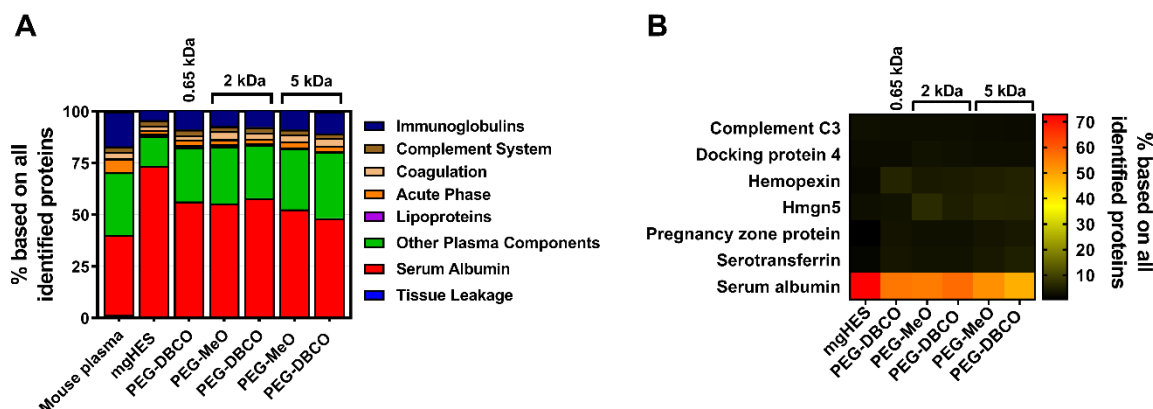


Figure 6.4: Nanocarrier PEGylation shows little influence on the adsorption profile of the biomolecular protein corona. Adsorbed corona proteins were analyzed by LC-MS and either sorted into eight protein groups (A) or individually plotted as a heatmap (B). Hmgn5 = High mobility group nucleosome-binding domain-containing protein 5.

Additionally, the top seven most abundant corona proteins detected in each group were plotted as a heatmap (Figure 6.4 B). In parallel to the protein group analysis, serum albumin was found to be by far the most abundant corona protein for every nanocarrier formulation. While serum albumin was detected with an abundance in the range from 48% (5 kDa PEG-DBCO) to 72% (mgHES), the other six most abundant proteins were observed with a relative abundance of less than 7% each. The whole mouse plasma control group showed a comparable distribution of most abundant proteins (Figure 6.S6).

Apart from Complement C3, none of the other abundant murine proteins is attributed to influence uptake by macrophages. C3 coated on nanocarriers, however, can lead to an increased internalization of NCs by macrophages through complement receptor ligation when being activated by pathway-specific C3 convertases^{266, 267}. However, the relatively low abundance of C3 on each nanocarrier formulation (~ 2%) indicates that C3-induced uptake by macrophages only plays a minor role for this carrier system. Walkey *et al.* demonstrated that higher PEG grafting densities control a decrease and change in the composition of the protein corona, where the nanoparticle size and the PEG density together determine the macrophage uptake²⁶⁸. On the contrary, PEGylation of the herein described nanocarrier formulations increased the rate of protein adsorption in comparison to the pristine nanocarriers (Figure 6.S7). Nevertheless, this increase in corona protein adsorption did not diminish the stealth effect of PEGylated nanocarriers. In addition, the physicochemical properties of the PEGylation with and without a protein corona were evaluated with respect to nanocarrier size and surface charge (Table S1). Multi-angle dynamic light scattering revealed a larger size of pristine nanocarriers compared to the PEGylated formulations in protein-free media and a smaller particle size under protein corona conditions. With regard to the surface charge of the nanocarriers, all samples presented a rather neutral zeta potential which consistently appeared

slightly negative for all mouse plasma pre-incubated nanocarrier formulations. In addition, TEM was used to visually confirm the nanocarrier size and morphology (Figure 6.S8). There were no visual differences between the pristine and PEGylated nanocarriers detectable. All formulations appeared to form small cluster duplets with a diameter of about 200 nm. In summary, the experiments conducted in the course of this study exhibited a reduced but not fully diminished protein corona formation following PEGylation of mgHES nanocarriers, which did not have an influence on the PEG-induced stealth properties.

Next to avoiding non-specific clearance of nanocarriers by phagocytes, conjugating active targeting moieties onto nanocarriers is the main prerequisite for a precise targeting of distinct DC subsets. Each DC subset is characterized by its capability of migration, cytokine secretion, and antigen presentation. Hence, the selection of a distinct subtype critically affects a sufficient DC vaccination approach. Applying the pan-DC marker CD11c as a target receptor has already underlined the role of DCs for enhancing humoral responses²⁶⁹⁻²⁷². Prior to the investigation of primary DCs, the influence of the length of the different DBCO-containing PEG linkers on the antibody-based targeting ability of herein used nanocarrier formulations were investigated in the DC2.4 cell line. In order to evaluate the stealth targeting, azide-modified CD11c antibodies were covalently bound onto the DBCO-functionalized surface as described previously²⁰⁰. Additionally, the corresponding CD11c isotype control antibody was included to control for non-specific, F_c -mediated uptake. This control antibody was conjugated to each NC-PEG_x-DBCO linker group to differentiate between a specific F_{ab} - and an undesired F_c -mediated cell binding. Conjugates with the 0.65 kDa PEG-DBCO linker were generated using a 10-fold molar excess of the linker, while the 2 kDa and 5 kDa molecular weight NC-PEG_x-DBCO linkers were conjugated with a 50-fold molar excess. Azide-modified antibodies were conjugated at a nanocarrier to antibody weight ratio of 67:1.

In order to validate the successful covalent binding of the CD11c and isotype antibodies on the PEG-DBCO linker-modified nanocarrier surface, flow cytometry was conducted (Figure 6.5, A and B). For this purpose, antibodies immobilized on the nanocarrier surface were stained with an anti-hamster FITC secondary antibody. The binding of the secondary antibody, either via adsorption onto the nanocarrier surface (no covalent-bound antibody present) or a positive, non-covalent binding towards the F_c region of the covalently-attached antibodies, enabled a qualitative detection method. Thereby, we confirmed the presence of the covalently-bound antibodies on the surface for each formulation.

6. PEG spacer length substantially affects antibody-based nanocarrier targeting of dendritic cell subsets

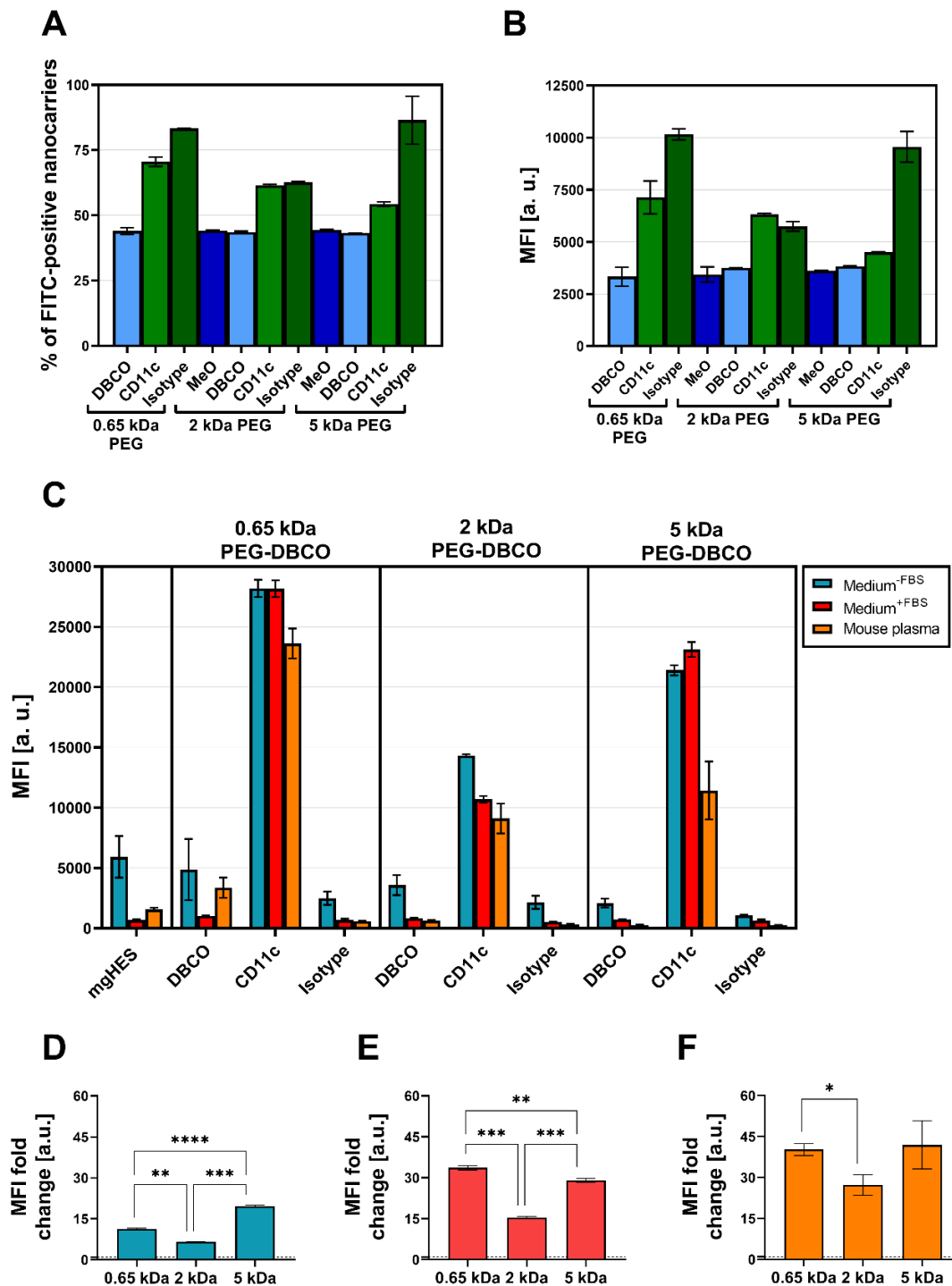


Figure 6.5: The PEG length affects antibody-based targeting in DC2.4 cells. Secondary antibody testing by flow cytometry qualitatively validated the presence of covalently-bound antibodies on the nanocarrier surface presented as the percentage of positive events (A) and as the median fluorescence intensity [arbitrary units] (MFI [a. u.]) (B). Values are given as mean \pm SD (n = 2). DC2.4 cells were incubated with nanocarriers (75 μ g mL⁻¹) functionalized with antibodies and PEG linkers of varying lengths (0.65 kDa, 2 kDa, 5 kDa) for 2 h in culture medium without FBS, with 5% FBS, or pre-incubated with mouse plasma and the uptake was quantified by analyzing the MFI (C). Values are given as mean \pm SD (n = 3). For each cell culture medium condition, the MFI values obtained by analyzing anti-CD11c-functionalized nanocarriers were normalized to its isotype controls and different PEG linker lengths were compared (without FBS (D), with FBS (E), pre-incubated in mouse plasma (F)). Significance was given with $p < 0.05$ using a Brown-Forsythe and Welch ANOVA test), $p < 0.05^*$, $p < 0.01^{**}$, $p < 0.001^{***}$, $p < 0.0001^{****}$.

6. PEG spacer length substantially affects antibody-based nanocarrier targeting of dendritic cell subsets

Subsequently, the CD11c targeting ability of functionalized nanocarriers was examined in terms of uptake by DC2.4 cells under three different medium conditions via flow cytometry (Figure 6.5 C). For each condition, the targeting ability of anti-CD11c-modified nanocarriers was clearly distinguishable from the isotype control-functionalized formulations. Only the CD11c nanocarrier conjugates showed a significant uptake by the DC2.4 cells, while the pristine nanocarriers, the corresponding DBCO linker conjugates, and the isotype conjugates remained at lower values. Comparing the three CD11c nanocarrier conjugate groups, the highest uptake was observed for the 0.65 kDa PEG-CD11c, followed by the 5 kDa PEG-CD11c, and 2 kDa PEG-CD11c being the weakest for culture medium with or without FBS. Applying mouse plasma pre-incubated nanocarriers only a minor difference between the 2 and 5 kDa PEG-CD11c could be observed, while the 0.65 kDa PEG-CD11c exhibited a substantial uptake. In order to evaluate the influence of different PEG chain length on the specificity of antibody-mediated targeting, the anti-CD11c/isotype control ratio based on the respective MFI values was calculated (Figure 6.5 D, E, and F). Among the three medium conditions, the ratio demonstrated a particularly low influence of the F_c region when using with the 5 kDa CD11c-functionalized nanocarriers, which was even more pronounced under medium conditions that led to protein corona formation (Medium^{+FBS} E, or mouse plasma pre-incubated F).

In parallel to the MeO-PEG-coupled nanocarriers, the influence of the biomolecular corona of anti-CD11c-functionalized nanocarriers upon their targeting ability was analyzed and quantitative LC-MS was performed. Again, all identified proteins were assigned to eight protein groups and the respective values were plotted as the percentage based on all identified proteins (Figure 6.6 A). No major differences between the three molecular weight PEG groups with either the CD11c targeting or the isotype control antibody could be detected. All of the individual groups exhibited serum albumin to be highly adsorbed onto the nanocarrier surface.

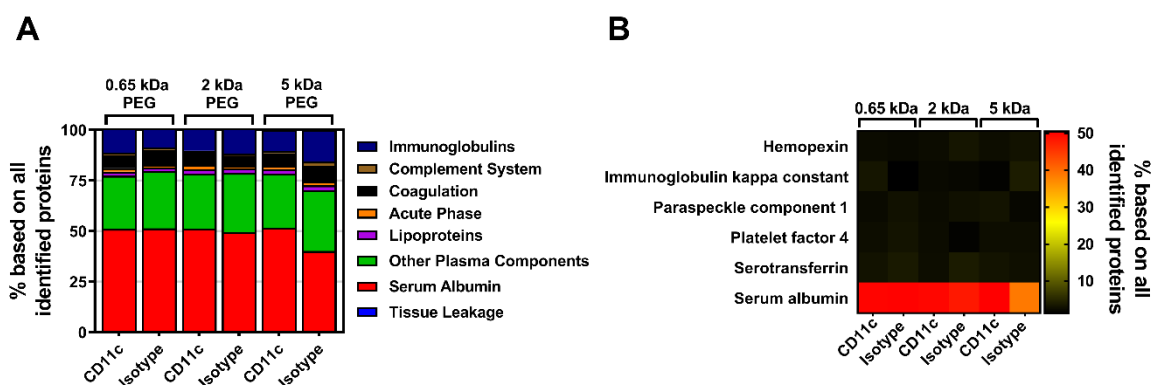


Figure 6.6: Antibody surface-modifications have no influence on the murine biomolecular protein corona composition. Adsorbed corona proteins were analyzed by LC-MS and either sorted into eight protein groups (A) or individually plotted as a heatmap (B).

Likewise, the qualitative SDS-PAGE detection of desorbed corona proteins showed serum albumin as the most abundant protein as visualized by silver staining (Figure 6.S5 B). Moreover, depicting the top six corona proteins further highlighted serum albumin to have the highest abundance of all identified proteins (Figure 6.6 B). As seen before with PEGylation, the analysis of the murine biomolecular corona showed that the surface-modification of the nanocarriers with PEG or in combination with antibodies only faintly influenced the protein adsorption profile. In general, only a low amount of proteins adsorbed onto the nanocarrier surface with very little influence on the stealth targeting ability.

Simultaneously to the uptake studies using the DC2.4 cell line, the influence of PEG linker length on the uptake of anti-CD11c-functionalized nanocarriers was analyzed in primary DCs, such as BMDCs and cDC1s of the spleen (Figure 6.7 A-E). In contrast to the uptake studies in DC2.4 cells, the targeting ability of anti-CD11c-functionalized nanocarriers was reduced when incubated with BMDCs (Figure 6.7 A). This was even more pronounced for the incubation in the presence of FBS. However, the targeting ability, in terms of the anti-CD11c/isotype control ratio, was significantly increased for longer PEG-DBCO linkers 2 kDa and 5 kDa by 4.0-fold and 4.75-fold, respectively, compared to 0.65 kDa PEG-DBCO (1.55-fold) (Figure 6.7 B). When analyzing cDC1s within whole splenocytes cultures, anti-CD11c-functionalized nanocarriers exhibited a substantial targeting ability compared to pristine, DBCO-, or isotype-functionalized nanocarriers (Figure 6.7 C-E). The uptake of IgG-functionalized nanocarriers was reduced to nearly background levels in contrast to BMDC cultures, in terms of frequency of NC⁺ cells (Figure 6.7 C) as well as MFI (Figure 6.7 D). In line with the data obtained from the incubation with DC2.4 cells and BMDCs, the PEG-DBCO linker length significantly influenced the anti-CD11c-mediated uptake of nanocarriers. While the 0.65 kDa linker only led to a 2.6-fold higher uptake rate compared to the isotype control, 2 kDa and 5 kDa resulted in significantly higher specific uptake by 6.6-fold and 7.5-fold, respectively (Figure 6.7 E). Additionally, the toxicity of different nanocarrier formulations was evaluated by coincubation with splenocytes for 20 h and staining of dead cells with LIVE/DEAD Aqua Dead Cell Stain (Figure 6.7 F). Flow cytometric analyses revealed no significant changes in the percentage of dead cells when comparing all applied nanocarrier formulations.

6. PEG spacer length substantially affects antibody-based nanocarrier targeting of dendritic cell subsets

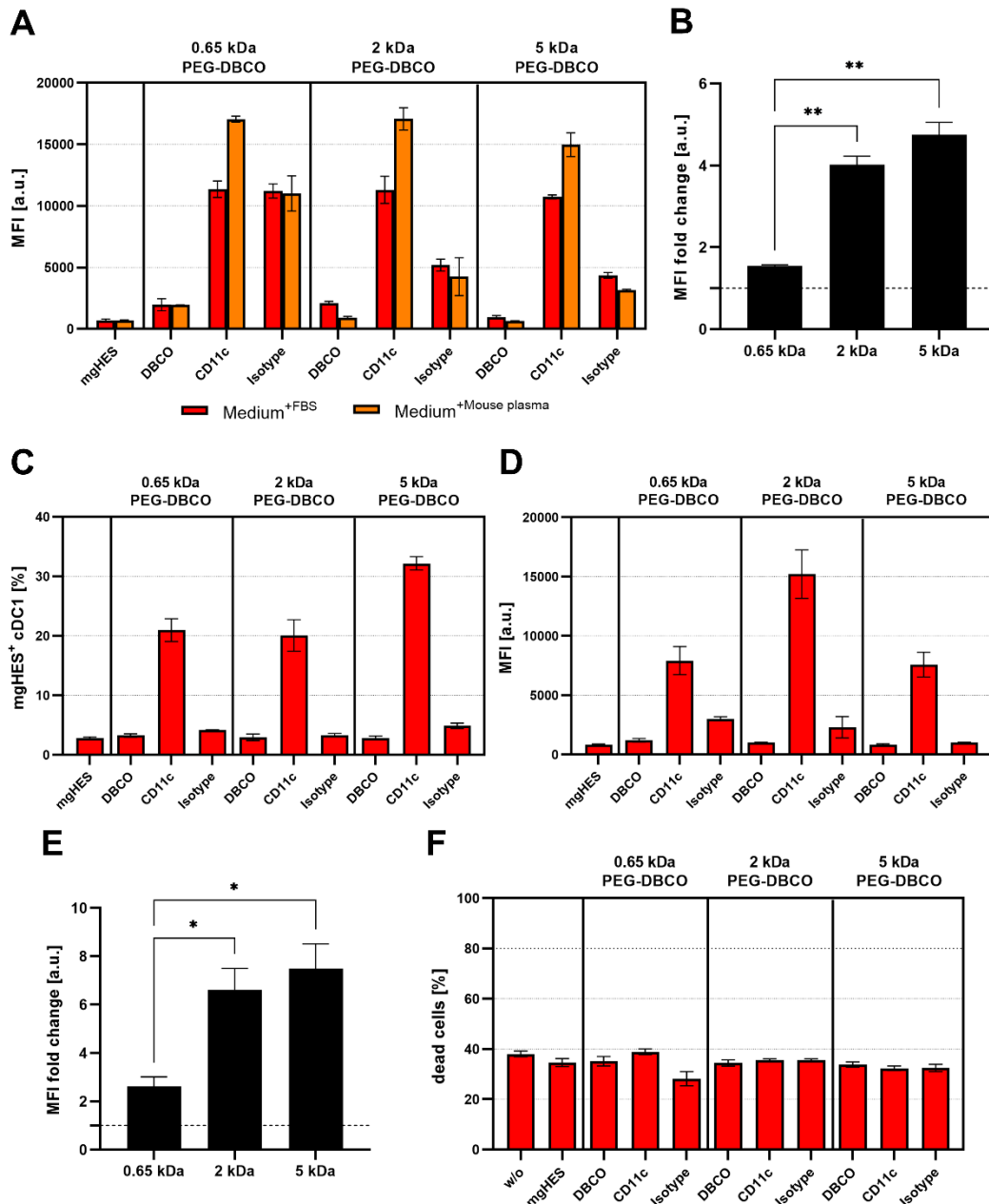


Figure 6.7: The PEG length affects antibody-based targeting in primary dendritic cells. **A**) BMDCs were incubated with nanocarriers ($3 \mu\text{g mL}^{-1}$) functionalized with antibodies and PEG linkers of varying lengths (0.65 kDa, 2 kDa, 5 kDa) for 20 h in culture medium containing either 5% FBS or 5% mouse plasma and uptake was quantified by analyzing the median fluorescence intensity (MFI) by flow cytometry. **B**) MFI values obtained by analyzing anti-CD11c-functionalized nanocarriers cultured in medium + 5% mouse plasma were normalized to its isotype controls and different PEG linker lengths were compared. Data represents mean \pm SD. Significance was given with $p < 0.05$ (Brown-Forsythe and Welch ANOVA test), $p < 0.01^{**}$. **C+D**) Splenocytes were incubated with nanocarriers ($3 \mu\text{g mL}^{-1}$) functionalized with antibodies and PEG linkers of varying lengths (0.65 kDa, 2 kDa, 5 kDa) for 20 h and uptake by conventional DCs type 1 (cDC1) was quantified by analyzing the percentage of NC⁺ cells (**C**) and MFI (**D**) by flow cytometry. **E**) MFI values obtained by analyzing anti-CD11c-functionalized nanocarriers were normalized to its isotype controls and different PEG linker lengths were compared. Data represents mean \pm SD. Significance was given with $p < 0.05$ (Brown-Forsythe and Welch ANOVA test), $p < 0.05^*$. **F**) Toxicity of nanocarrier formulations was documented by staining of splenocytes with LIVE/DEAD Fixable Aqua Dead Cell Stain after 20 h of coinubation and subsequent flow cytometric analyses.

6.5 Supporting Information

Table 6.S1: Physicochemical characterization of PEGylated and antibody-modified nanocarriers with and without a murine protein corona. The average size (diameter in nm) and size distribution (PDI) of the nanocarriers was determined by multi-angle dynamic light scattering, and the zeta (ξ) potential was measured.

	without a protein corona		pre-incubated with mouse plasma	
	Diameter in nm with PDI	ξ -Potential in mV with SD	Diameter in nm with PDI	ξ -Potential in mV with SD
Pristine nanocarriers				
mgHES	258 (0.156)	-0.90 (0.041)	208 (0.108)	-7.94 (0.601)
PEGylated nanocarriers				
0.65 kDa DBCO	232 (0.176)	-9.18 (0.154)	234 (0.158)	-11.9 (0.458)
2 kDa MeO	220 (0.126)	-4.90 (0.466)	218 (0.212)	-5.47 (1.670)
2 kDa DBCO	220 (0.107)	-5.02 (0.899)	220 (0.140)	-7.72 (0.893)
5 kDa MeO	202 (0.086)	-3.65 (0.574)	258 (0.211)	-4.95 (0.559)
5 kDa DBCO	198 (0.141)	-3.75 (0.665)	244 (0.214)	-7.29 (1.838)
Antibody-modified nanocarriers				
0.65 kDa CD11c	220 (0.235)	-6.28 (0.467)	206 (0.147)	-6.65 (0.120)
0.65 kDa Isotype	200 (0.186)	-4.98 (0.937)	168 (0.095)	-5.60 (0.675)
2 kDa CD11c	262 (0.217)	1.19 (0.0781)	170 (0.098)	-3.69 (0.0961)
2 kDa Isotype	196 (0.135)	0.165 (0.658)	200 (0.186)	-5.98 (0.411)
5 kDa CD11c	206 (0.210)	4.13 (0.137)	212 (0.117)	-4.81 (0.131)
5 kDa Isotype	218 (0.154)	5.05 (0.182)	168 (0.169)	-5.17 (0.192)

6. PEG spacer length substantially affects antibody-based nanocarrier targeting of dendritic cell subsets

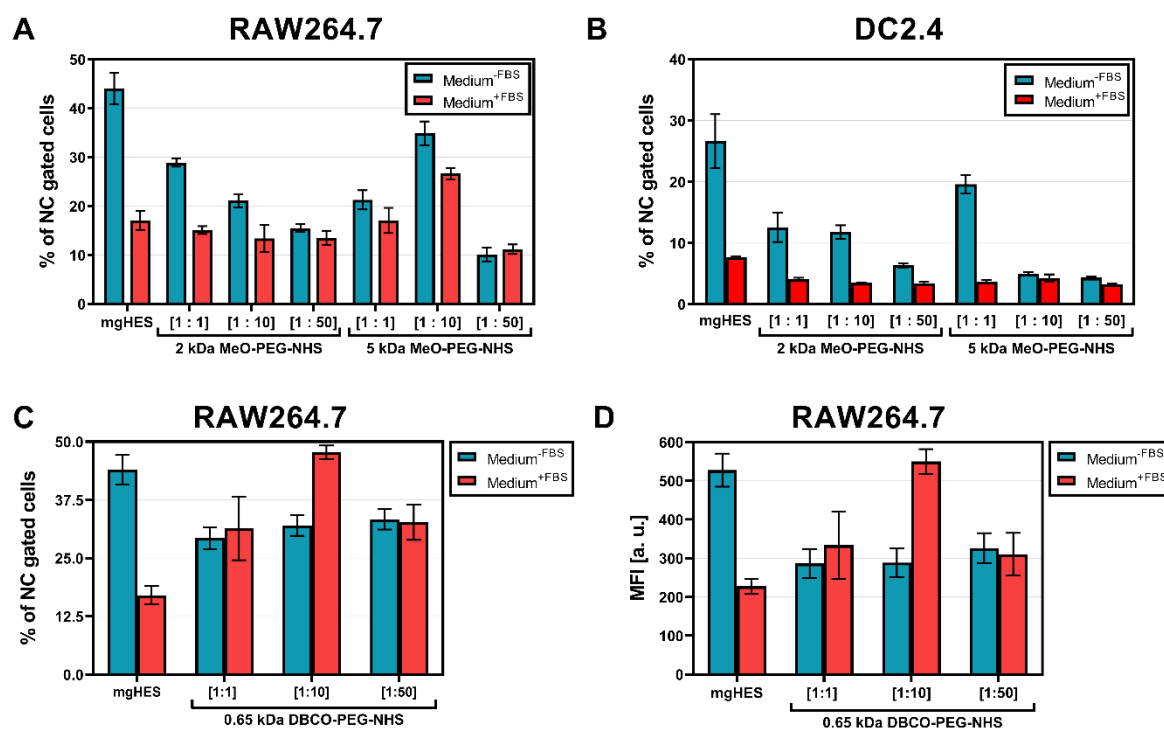


Figure 6.S1: PEGylated nanocarrier uptake analyzed by flow cytometry. Cell uptake of pristine nanocarriers (mgHES) and PEGylated samples with $7.5 \mu\text{g mL}^{-1}$ in medium with (red bars) or without (blue bars) FBS. PEGylation with the 2 and 5 kDa NHS-PEG-MeO linkers was performed with three molar reaction ratios (1:1, 1:10, 1:50) in either the RAW264.7 (A) or the DC2.4 (B) cell lines and analyzes by flow cytometry (percentage of nanocarrier gated cells). PEGylation with the 0.65 kDa NHS-PEG-DBCO linker was performed with the same three molar reaction ratios in the RAW264.7 cell line either analyzed as the percentage of nanocarrier gated cells (C) or as the median fluorescence intensity (D). Auto fluorescence is subtracted from each data set. Values are given as mean \pm SD ($n = 3$). Only viable cells are gated.

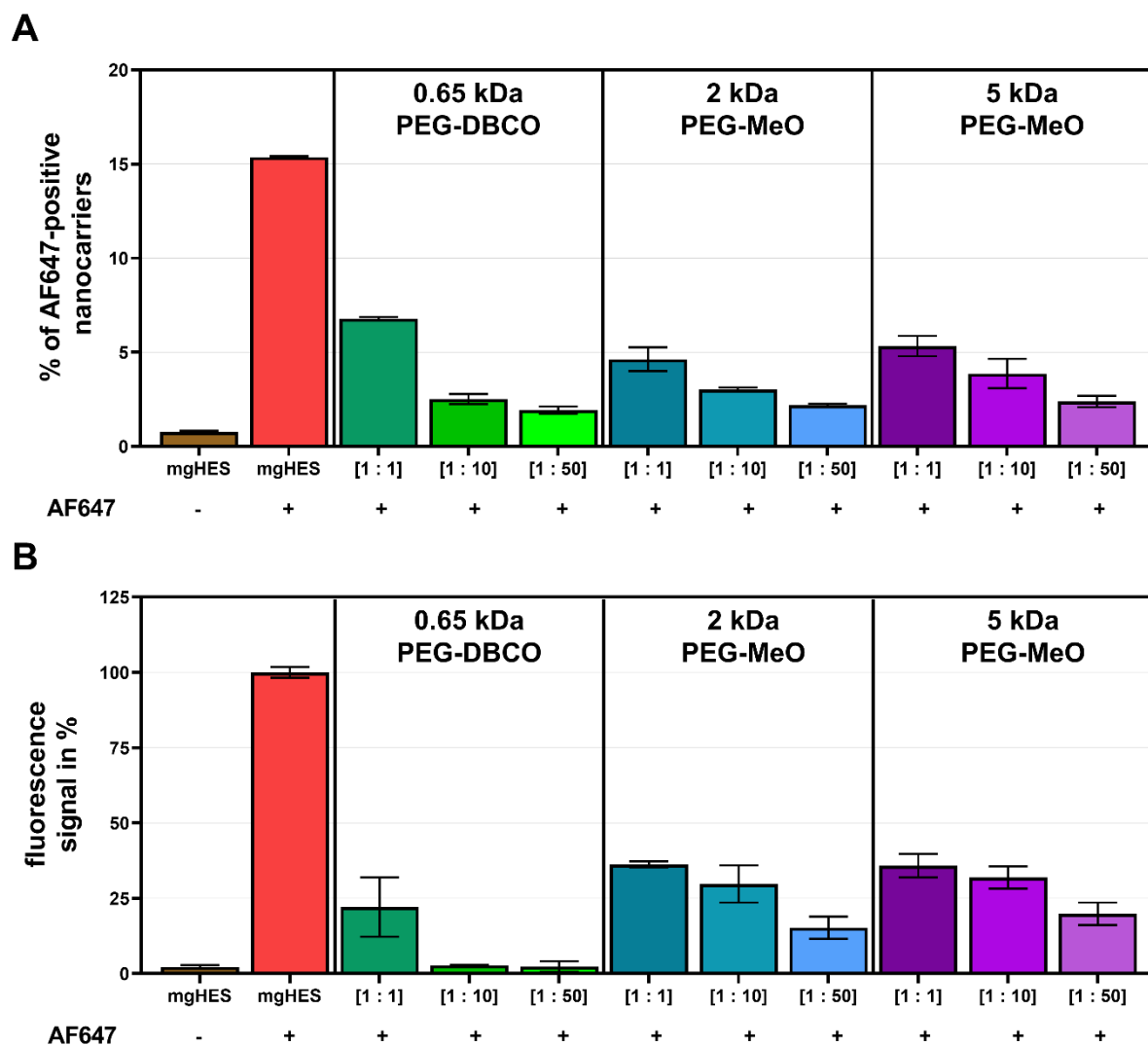


Figure 6.S2: Validation of nanocarrier PEGylation. The surface-modification of the nanocarriers with PEG was analyzed by flow cytometry (A) and plate reader (B). For this investigation, the pristine nanocarriers (mgHES) and the samples with different PEG ratios (1:1, 1:10, 1:50) were incubated with an Alexa Fluor 647 NHS-Ester followed by washing to remove unconjugated moieties. The fluorescence was then detected by the two devices mentioned above.

6. PEG spacer length substantially affects antibody-based nanocarrier targeting of dendritic cell subsets

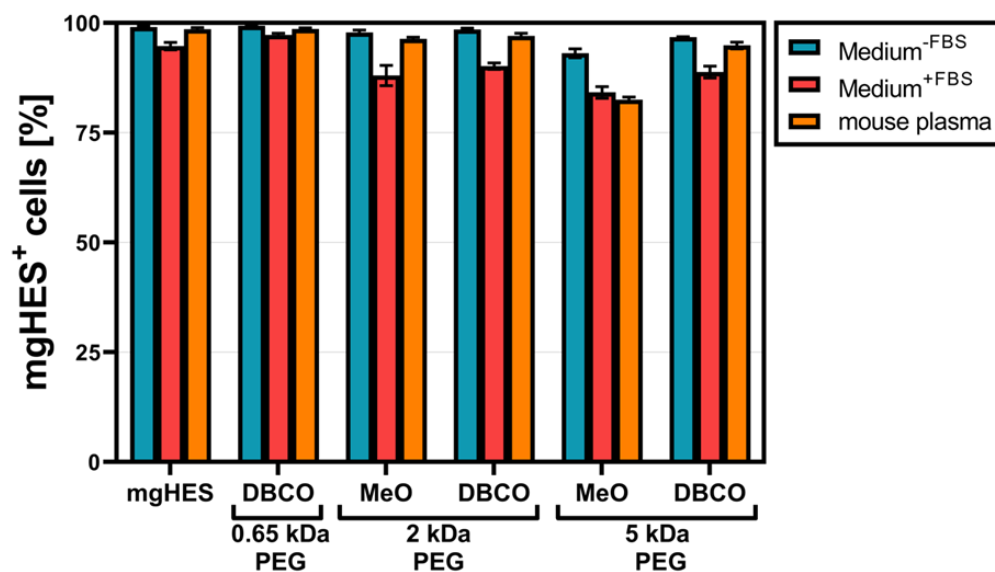


Figure 6.S3: RAW264.7 cell uptake of PEGylated nanocarriers. Nanocarriers were incubated with RAW264.7 cells in either medium with or without FBS, or pre-incubated with mouse plasma with a sample concentration of $75 \mu\text{g mL}^{-1}$ for 2 h at 37°C . Autofluorescence was subtracted from each data set. Only viable cells were analyzed. Values are given as mean \pm SD ($n = 3$).

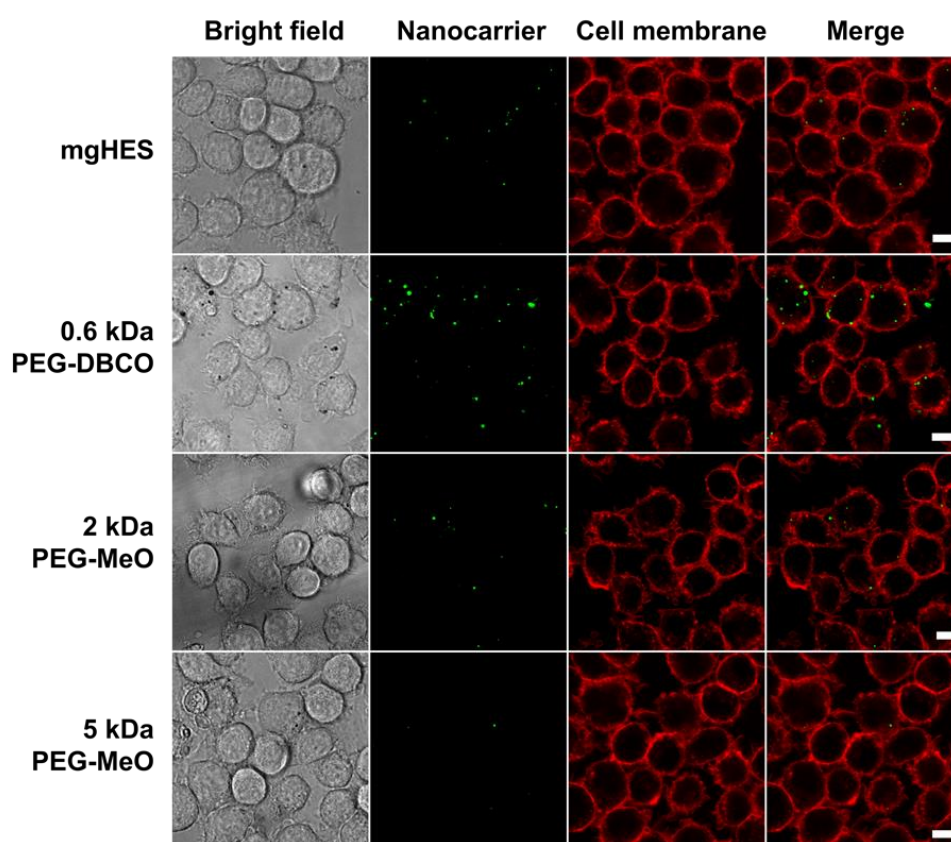


Figure 6.S4: A longer PEG chain reduces internalization by macrophages. Nanocarriers were incubated with the RAW264.7 cells for two hours at 37°C with a sample concentration of $75 \mu\text{g mL}^{-1}$ in DMEM medium with 10% FBS. Live cell images are shown. All scale bars represent $10 \mu\text{m}$.

6. PEG spacer length substantially affects antibody-based nanocarrier targeting of dendritic cell subsets

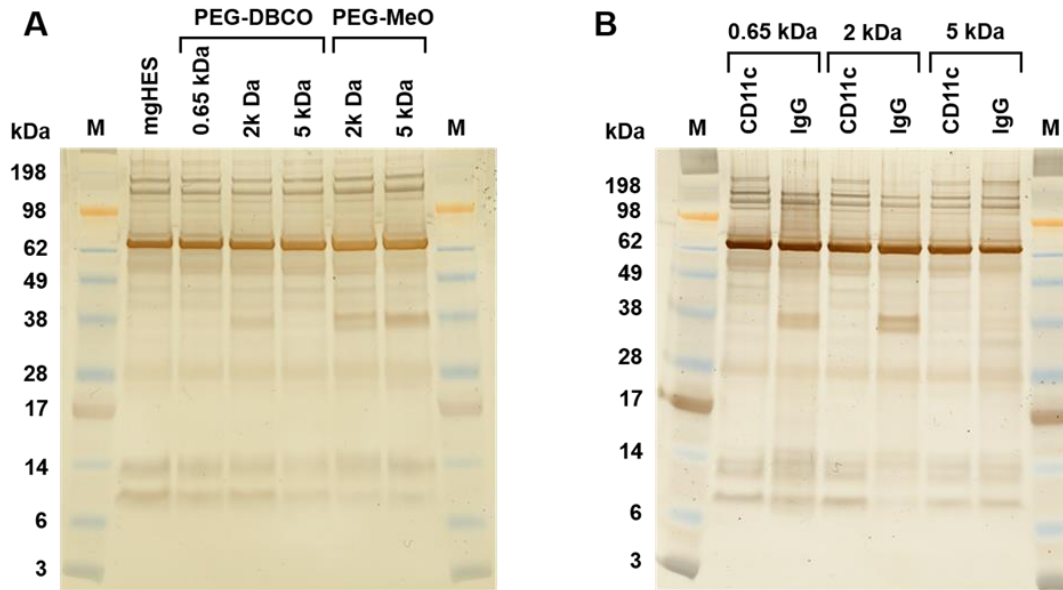


Figure 6.S5: Qualitative analysis of desorbed corona proteins. SDS-PAGE of PEGylated (A) and targeting (B) samples is shown. Following 1 h incubation in mouse plasma at 37 °C, murine proteins were desorbed and separated from the nanocarrier. The protein amount was quantified and 2 µg were used for the gel. The SDS-PAGE was run for 1 h at 120 V followed by silver staining.

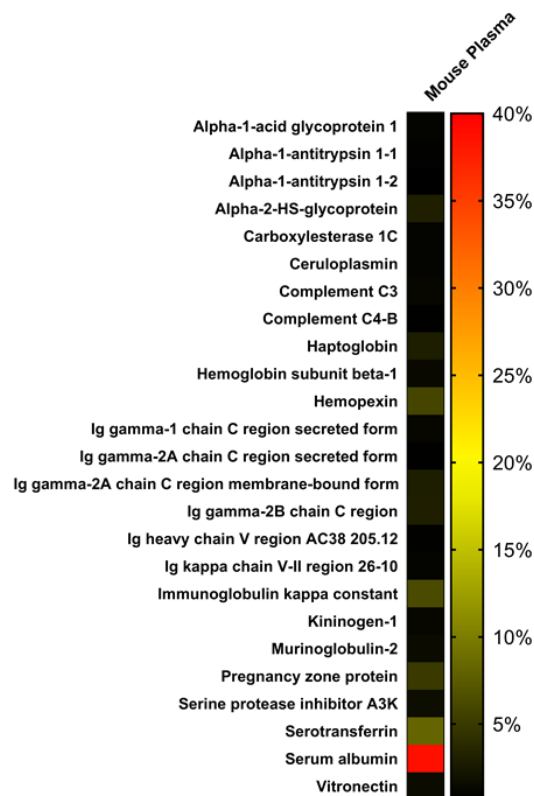


Figure 6.S6: Most abundant proteins detected in mouse plasma. Heat map of the top 25 most abundant proteins in mouse plasma are shown. The values are expressed in percentage based on the total amount of all identified proteins.

6. PEG spacer length substantially affects antibody-based nanocarrier targeting of dendritic cell subsets

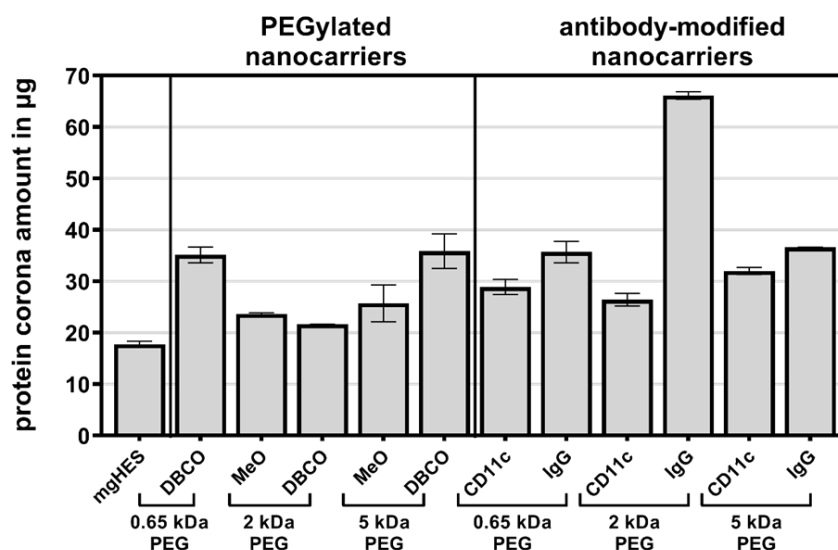


Figure 6.S7: Amount of desorbed corona proteins. After the pre-incubation with mouse plasma, the protein corona was desorbed from the nanocarriers by desorption buffer. The protein amount was determined by Pierce™ 660nm Protein Assay. Data is shown as mean \pm standard deviation ($n = 2$).

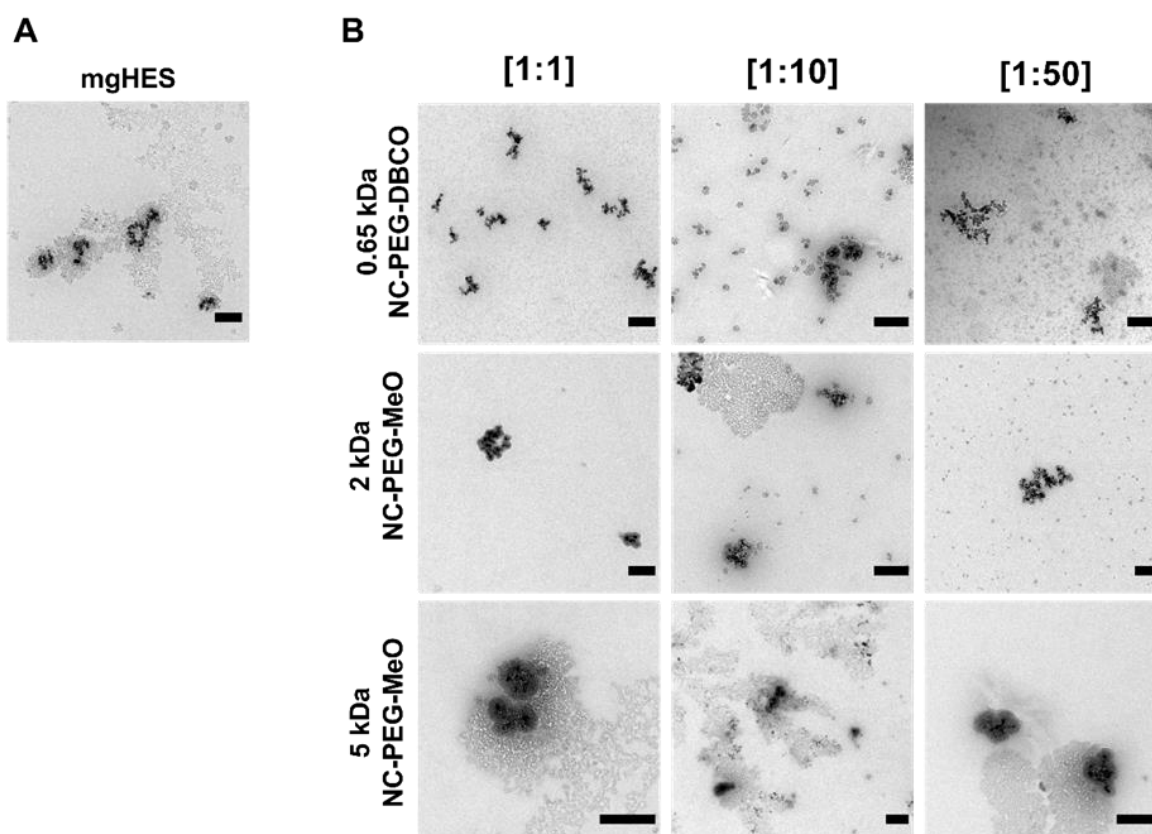


Figure 6.S8: TEM visualization of PEGylated nanocarriers in cell culture medium. Pristine nanocarriers (A) and PEGylated nanocarriers (B) were diluted to a concentration of $75 \mu\text{g mL}^{-1}$ in IMDM medium containing 5% FBS and were imaged by TEM. The PEGylation was performed with three different molecular weight linkers (0.65 kDa NHS-PEG-DBCO, 2 kDa and 5 kDa NHS-PEG-MeO) and three nanocarrier to linker molar reaction ratios (1:1, 1:10, 1:50). Grey clouds are most likely salt contaminations from the cell culture medium. The scale bars represent 200 nm.

Chapter C – Decoration of nanocarriers with antibody fragments to avoid an undesired F_c-mediated uptake

In the final chapter (C) of this dissertation, the subchapter 7 describes the generation of antibody fragments from whole IgG molecules and the use of nanobodies as targeting ligands. Therefore, subchapter 7 shortly introduces the theoretical background followed by the results presented in the structure of a publication. In general, the described work represents unpublished data possibly forming the basis for a future publication.

Aim:

Chapter B highlighted the importance of a correct immobilization of whole antibody molecules in a fixed orientation onto the nanocarrier surface. This antibody positioning directly influenced a precise targeting ability of the construct and determined the interactions with cells and organs *in vitro* and *in vivo*. Nevertheless, whole antibodies potentially trigger undesired immune reactions via their F_c region leading to a decrease in their targeting functionality and increased immunogenicity. Therefore, the aim of chapter C intends to examine the generation of antibody fragments and the binding ability of nanobodies that lack the F_c region as ligand alternatives to whole antibodies.

Contributions:

I, Maximilian Brückner, performed all antibody fragmentation experiments (pepsin digestion and reduction agent testings). Joshua Krehan analyzed the antibody fragments via the size exclusion chromatography (SEC) and Darijan Schüler via the matrix-assisted laser desorption/ionization time-of-flight (MALDI-TOF). The nanobody (VHH) experiments included the analysis of the VHH clone antigen binding (α -CD11c, α -CD40, and α -Clec9a), which was analyzed in the commercial cell lines (by me, Maximilian Brückner), and in the primary murine cells, including BMDCs (by Dr. Michael Fichter). Furthermore, I performed the TCEP treatment of the VHHs followed by the synthesis of nanocarrier-VHH-conjugates (nanocarrier-functionalization und VHH-modification). Dr. Michael Fichter analyzed the conjugates in primary cells (flow cytometry). Prof. Dr. Volker Mailänder and Prof. Dr. Katharina Landfester supervised the project.

7.1 Abstract

Antibody derivatives lacking the F_c region as targeting ligands on nanocarriers potentially eliminate the risk of unwanted immunogenic reactions and off-target effects within the body. This undesirable immunogenicity, including the nonspecific binding towards F_c receptors on phagocytes, and hampered targeting efficiency attribute to the F_c region of whole antibodies. Therefore, whole antibodies require a separation into distinct fragmentation products to remove the F_c region. Alternatively, the recombinant production of antibody derivatives, such as nanobodies, enables the generation of fragments lacking the F_c region. In general, the smaller size and lower complexity of antibody fragments in contrast to whole antibodies further facilitate a site-directed immobilization onto the nanocarrier surface. Consequently, this study demonstrates an enzymatic digestion approach to generate F_{(ab)₂} and, in combination with cysteamine, F_{ab}' fragments out of whole rat IgG₁. In addition, the investigation of commercially produced nanobodies highlighted antigen-binding differences in clones targeting the same surface receptor. Therefore, the established detection method for nanobody-to-antigen interactions enabled a differentiated selection of clones for their C-terminal cysteine tag (Cys-tag) production. Furthermore, nanobodies already carrying the Cys-tag allowed a first trial for their covalent-attachment onto the nanocarrier surface. This first experiment highlighted the importance of the nanobody quantity on the surface determining a desirable targeting. In conclusion, comparing different antibody formats applied as targeting ligands on the nanocarrier surface will decide which candidate demonstrates the best performance. Consequently, the combination of a sufficient antibody derivative with a suitable nanocarrier system will enhance the targeting efficiency resulting in a desired drug delivery.

7.2 Introduction

Despite the effectiveness of the described antibody-functionalized nanocarriers in chapter B, the challenge remains to guarantee a F_{ab} -mediated targeting and to avoid an unwanted cell uptake triggered by the F_c part of the immobilized antibody. Moreover, research on whole antibodies applied as targeting ligands on the nanocarrier surface shows to be impaired by poor stability, rapid elimination, F_c -induced immunogenicity, and unexpected targeting inefficiency². Therefore, antibody derivatives that lack their F_c part have the ability to overcome the limitations of their larger and more complex counterparts. For example, the F_c fragment of whole antibodies can trigger immunogenic responses by the F_c receptor binding on phagocytic cells leading to an undesired clearance before reaching the target site^{273, 274}. Due to their smaller size and lower structural complexity, antibody derivatives offer an easier site-directed modification and binding site density on the nanocarrier surface. In general, fragmentation protocols require a careful disassembly of the antibody molecule into its individual parts followed by a site-directed conjugation strategy onto the nanocarrier surface without compromising the binding activity of the fragment. Furthermore, it remains to clarify which antibody format on the nanocarrier elucidates an optimal binding to the target site without an accumulation in off-target cells or organs. As described in chapter B, the IgG molecule is a large macromolecule with a specific composition, structure, and function. This complexity can lead to undesirable side effects or a reduced antibody sensitivity for certain applications when being immobilized on a surface. Therefore, the IgG is intentionally disassembled into specific structures, like the $F_{(ab)_2}$, F_{ab} or F_{ab}' , and F_c fragments (Figure 7.1).

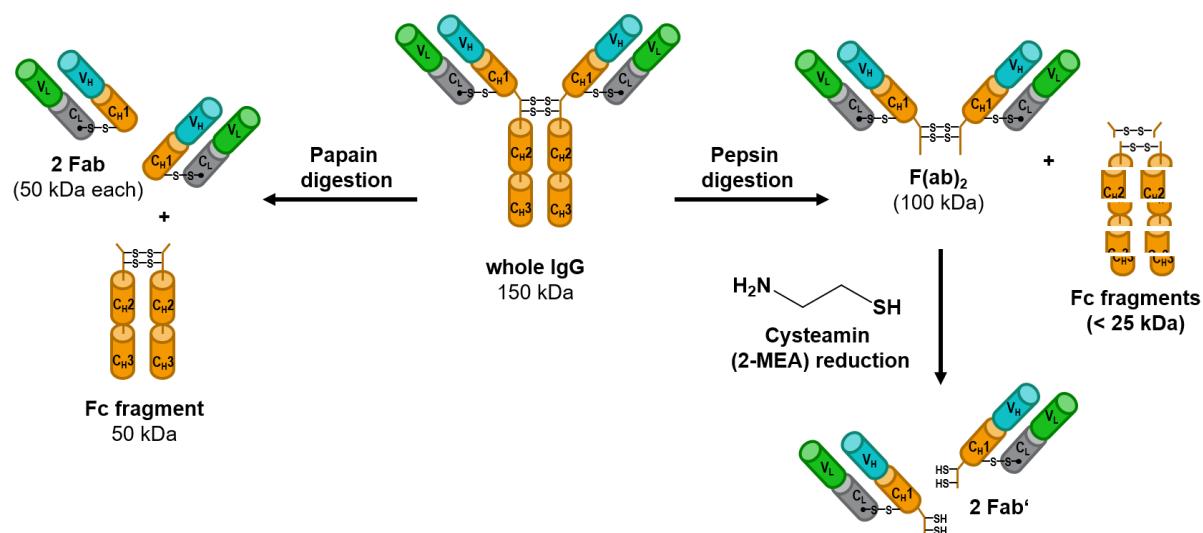


Figure 7.6: Fragmentation of whole IgGs into specific structures. The disassembly of a typical IgG into specific fragments ($F_{(ab)_2}$, F_{ab} , F_{ab}' , and F_c) is exemplary shown by enzymatic digestion (papain or pepsin) and reduction (cysteamin or 2-mercaptoethylamin (2-MEA)).

As a result, decorating nanocarriers with these IgG fragments leads to constructs with different functionalities. For example, the $F_{(ab)_2}$ and F_{ab} fragments possess at least one antigen-binding domain, which still enables them to actively bind their specific antigen. Without the influence of the F_c region, the $F_{(ab)_2}$ and F_{ab} fragments can focus their functionality exclusively on targeting.

For the generation of the fragments, different proteolytic enzymes digest the whole antibody leading to distinct formats. Hence, whole IgGs are digested either with papain to produce F_{ab} fragments or pepsin to produce $F_{(ab)_2}$ fragments²⁷⁵. Further, the enzymatic approach can be combined with mild reduction agents, like cysteamine or 2-mercaptoethylamine (2-MEA), to generate F_{ab}' fragments from $F_{(ab)_2}$ that, in contrast to F_{ab} , possess free thiol groups for their subsequent covalent attachment²⁷⁶. Adding to this, fragments are also recombinantly expressed which requires knowledge about the antibody sequence, or an intense production process from a host animal to the expression in *E. coli* via a bacteriophage^{277, 278}. Therefore, the enzymatic digestion is more straightforward in the generation of fragments from IgG molecules, although it still requires optimization for each antibody isotype and clone. This optimization focuses on the necessary conditions for fragment yield, digestion efficiency, and function²⁷⁷.

Another crucial factor is the removal of the F_c fragment after digestion. In general, the purification methods are classified into the fractionation via the physicochemical properties of antibodies in typical samples, into the specific binding of biological ligands towards particular antibody isotype classes, and into an antigen-specific affinity purification via the F_{ab} domains²⁷⁹.

Besides the $F_{(ab)_2}$ and F_{ab} fragments, so-called nanobodies (VHHs) or single-domain antibodies (sdABs) represent an even smaller antibody fragment (Figure 7.2).

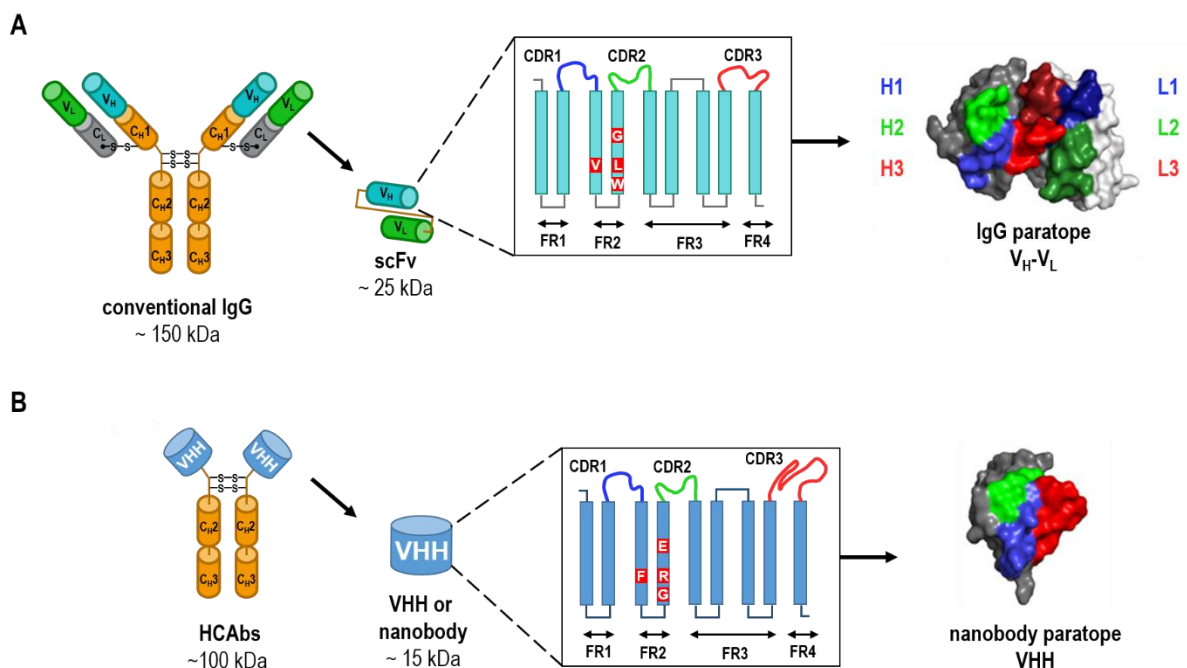


Figure 7.7: Structural differences between a conventional IgG and a camelid HCAb. The schematic IgG and single-chain variable fragment (scFv) structure, as well as the secondary structure of the V_H and the surface view of the IgG paratope is shown (A). In addition, the schematic heavy-chain only antibody (HCAb) and nanobody (VHH) structure, as well as the secondary structure and the surface view of the VHH paratope is shown (B). Both scFv and VHH secondary structures show 9 beta sheets distanced by loop regions. Three of these regions are hypervariable (CDR1 blue, CDR2 green, and CDR3 red). The variable loops are separated by four framework (FR) regions. The IgG FR2 embeds four highly conserved hydrophobic amino acids (V, valine; G, glycine; L, leucine; and W, tryptophan), which in the VHH FR2 are replaced by hydrophilic amino acids (F, phenylalanine; E, glutamic acid; R, arginine; G, glycine). The secondary structures are redrawn from Asaadi *et al.*²⁸⁰. The surface views are reprinted with permission from Mitchell and Colwell²⁸¹.

This recombinantly expressed antigen binding VHH is derived from the variable domains of heavy chain-only antibodies (HCAbs), which completely lack the light chains and are naturally produced in camelids²⁸². Besides their small size and molecular weight of around 12 to 15 kDa, they show structural differences to conventional IgGs due to the missing CH1 domain and light chain. Thus, VHHs bind their antigen or epitope only through their three CDRs unlike mammalian IgGs that bind via six CDRs (three from each of the V_H and V_L domain forming the paratope)^{283, 284}. The V_H CDR and VHH CDR share similar features in their secondary structure. Both domains consist of nine beta sheets distanced from each other by variable loop regions, of which three are hypervariable regions (CDRs) responsible for the antigen binding. The framework regions (FRs) one to four connect the CDRs and function as a scaffold. While the FR2 in the V_H domain more likely embeds hydrophobic amino acids, the FR2 of the VHH shows more hydrophilic amino acids^{280, 281}. Moreover, the enlarged CDR3 of the VHH represents the major difference to the CDR3 of the V_H domain. The greater length in the CDR3 loop enhances the strength in its interaction with the target antigen or epitope^{282, 285}, and enables the binding

to cavity-like epitopes²⁸⁶. Thereby, the CDR3 loop can reach and bind those regions, which are inaccessible for conventional IgGs, by the formation of finger-like protrusions recognizing conserved cleft and pocket regions^{285, 287}. In addition, VHHs possess a high thermoresistance and reversible refolding behavior, as well as an efficient tissue penetration and minimal immunogenicity *in vivo*²⁸⁸. Consequently, VHHs represent promising candidates for the surface-functionalization of nanocarriers enabling a specific and efficient dendritic cell targeting.

For these reasons, analyzing and comparing different antibody fragments on the nanocarrier surface as targeting ligands will highlight which antibody format targets most efficiently. Therefore, this chapter aims to identify the right conditions for the fragmentation of the IgG molecule into the $F_{(ab)2}$, F_{ab} and F_{ab}' fragments, as well as the validation of the detection of the VHH antigen binding and the modification for a covalent attachment onto the nanocarrier surface to precisely target dendritic cell subsets.

7.3 Material and Methods

Culturing of Dendritic Cells. The murine DC2.4 Dendritic Cells (Merck, Germany) were cultured in Iscove's Modified Dulbecco's Medium (Sigma-Aldrich, U.S.A), supplemented with 1% penicillin (100 U mL⁻¹) and streptomycin (100 mg mL⁻¹), 5% fetal bovine serum (FBS), as well as 1% 2-Mercaptoethanol (100X). In addition, the murine MutuDC1940 cells (abm®, U.S.A.) were maintained in Iscove's Modified Dulbecco's Medium, containing 5 mM ethylenediaminetetraacetic acid (EDTA) (AppliChem, Germany), 20 mM HEPES ((4-(2-hydroxyethyl)-1-piperazineethanesulfonic acid) (Sigma, Germany), 1% penicillin (100 U mL⁻¹) and streptomycin (100 mg mL⁻¹), 10% FBS, as well as 1% 2-mercaptoethanol (100X). All cell lines were stored in an incubator with 37 °C and 5% CO₂ humidity (CO₂ Incubator C200, Labotect). The confluence of the cells was checked under the microscope and passaging was conducted when reaching a confluence around 80%. For the passaging, the old media was discarded, and the cells were briefly washed with PBS. The detachment of the cells was conducted for the DC2.4 cells with PBS containing 2 mM EDTA and for the MutuDC1940 cells with PBS containing 5 mM EDTA and 20 mM HEPES for 10 min at 4 °C. After the incubation, the respective FBS containing medium was used to bring the detached cells into suspension. Then, the cell suspensions were centrifuged (DC2.4 cells at 300 g and MutuDC1940 cells at 290 g both for 5 min) and the supernatant was discarded. After resuspension in 5 – 10 mL of FBS containing medium, the cell viability was analyzed by measuring the live cell count using trypan blue and an automated cell counter (TC10, Bio-Rad). Based on the live count, the cells were utilized for experimental investigations or for maintaining the cells in culture.

Antibody pepsin fragmentation. In total, the pepsin (Thermo, Germany) digestion examined the fragmentation of three whole antibodies. Those include the Armenian hamster IgG isotype (clone HTK888), the purified α -mouse CD11c IgG (clone N418), and the purified rat IgG₁ isotype (clone RTK2071), all from Biolegend (U.S.A.). The digestion with pepsin included the fresh preparation of different digestion buffers, containing either 20 mM formic acid (Thermo, Germany) or 20 mM sodium acetate in Ampuwa® water (VWR chemicals). The pH of each buffer was adjusted to the required value by using 1 mM NaOH and 1 mM HCl. In a first step, 200 μ L of the immobilized pepsin equilibrated with 1.5 mL of the respective digestion buffer by using centrifugation (3x for 5 min at 1000 g). The final pepsin pellet was resuspended in 200 μ L of the respective digestion buffer. In the meantime, the antibody of interest was buffer exchanged to the respective digestion buffer by using a centrifugal filter with a 50 kDa molecular weight cut-off (MWCO) (Amicon®, Merck). For this purpose, the respective amount of antibody and digestion buffer were centrifuged (5000 g for 5 – 6 min) until reaching an end volume of around 200 μ L. After measuring the antibody concentration by the Pierce 660nm protein assay (see antibody quantification), 1 μ g of antibody reacted with 0.3 μ L of immobilized

pepsin (upscalable depending on the antibody quantity). The antibody-to-pepsin working solution required an antibody concentration of 1 mg/mL (adjusted with digestion buffer). After the desired incubation time (30 min, 1 h, 2 h, and 6 h) at 37 °C, a desalting column with a 7 kDa MWCO (Zeba™, Thermo) separated the digested antibody from the pepsin resin and buffer-exchanged to digested antibody to PBS according to the manufacturer's protocol. The fragmented antibodies were directly investigated by SDS-PAGE or stored at 4 °C.

F_(ab)₂ to F_{ab} reduction. Cysteamine, or 2-mercaptoethylamine (2-MEA), was applied for the reduction of the ~100 kDa F_(ab)₂ to the ~50 kDa F_{ab} fragment. For this purpose, different amounts of 2-MEA were dissolved in a reduction buffer containing 1 mM EDTA in PBS (pH ~7.1). The previously digested antibody, containing the F_(ab)₂, was reacted with different amounts of the 2-MEA containing reduction buffer for either 60 min or 90 min. Afterwards, the excess of 2-MEA was removed from the mixture by applying a buffer exchange to PBS via a 7 kDa MWCO desalting column (Zeba™, Thermo). After quantifying the protein concentration, the reduction products were visualized by SDS-PAGE.

Antibody Quantification. The Pierce 660nm protein assay (Thermo, Germany) quantified the total amount of antibody or nanobody protein according to the manufacturer's instructions. Bovine serum albumin (BSA) served as a standard by pipetting a dilution series in PBS. The Infinite M1000 plate reader (Tecan) measured all samples at an optical density of 660 nm, including the standard, in duplicates.

SDS-PAGE. The analysis of antibodies, fragments, and nanobodies was conducted with 2 µg of total protein. For a reduced SDS-PAGE analysis, 4 µL of NuPage Reducing Agent (DTT) was added (4 µL of VE-water under non-reduced condition), and 10 µL of NuPage LDS Sample Buffer, and VE-water to a total volume of 40 µL. The sample mixture was loaded on a 10% Bis-Tris-Protein Gels using NuPAGE MES SDS Running Buffer (all Novex, Thermo Fisher Scientific) and run for 2 h using SeeBlue Plus2 PreStained (Invitrogen) as a molecular marker. The marker consists of myosin (198 kDa), phosphorylase (98 kDa), BSA (62 kDa), glutamic dehydrogenase (49 kDa), alcohol dehydrogenase (38 kDa), carbonic anhydrase (28 kDa), myoglobin red (17 kDa), lysozyme (14 kDa), aprotinin (6 kDa), and insulin B chain (3 kDa). Silver staining (Thermo, Germany) visualized the protein band migration on the gels according to the manufacturer's instructions. In case of the visualization of the thiol-maleimide conjugation, a 5 kDa methoxypolyethylenglykol-maleimid (PEG-Maleimide, Merck) was reacted with 2 µg of the VHH (native or TCEP-treated) with different molecular weight ratios of the PEG-Maleimide linker (dissolved in DMSO at 20 mg/mL) overnight at room temperature. At the next day, the linker-reacted VHHs were prepared for the SDS-PAGE as mentioned above.

Size Exclusion Chromatography (SEC) for F_{(ab)₂} purification. For the rat F_{(ab)₂} purification, a Jasco PU-4085i inert HPLC system with a MD-4010 PDA detector was employed with ChromNav software for data acquisition and processing. After injection of 100 µL sample volume, separation was performed on a Cytiva Superose 6 Increase 10/300 GL column at a flow rate of 0.8 mL/min and using DPBS as eluent. Chromatograms were recorded at a wavelength of 280 nm.

Matrix-assisted laser desorption/ionization time-of-flight (MALDI-TOF/TOF). MALDI measurements were carried out on a rapiflex™ MALDI-TOF/TOF mass spectrometer (Bruker Daltonik GmbH). The instrument is equipped with a scanning smartbeam 3D 10 kHz Nd:YAG laser at a wavelength of 355 nm and a 10 bit 5 GHz digitizer. The acceleration voltage was set to 20 kV and the mass spectra were recorded in positive ion linear mode. Calibration was done with the Bruker peptide mix and the Bruker protein calibration standard I and II. Samples were measured with random walk ionization across the sample spot at a laser power of 100%. Typically, 8000 shots were averaged per spectrum. The rat F_{(ab)₂} sample was prepared in a concentrated sinapinic acid solution in acetonitrile:water (1:1) with a 0.1% trifluoroacetic acid matrix. This solution was further diluted with matrix solution (2:1). The data was analyzed with the open source mass spectrometry tool mMass.

Nanobodies. For the generation of nanobodies (VHHs) directed against the three selected murine surface receptors (CD11c, CD40, and CLEC9A), RD Biotech produced the respective recombinant proteins and QVQ developed the VHHs. For the recombinant protein production, RD Biotech performed the gene synthesis of the insert and cloning in an expression vector with His tag. After the amplification and quality controls, RD biotech produced the proteins in Chinese hamster ovary (CHO) cells and purified them by affinity chromatography, followed by quality controls (SDS-PAGE, Western blotting (anti His), and quantification). Then, RD Biotech sent the recombinant mouse proteins to QVQ Holding BV for the development of VHH fragments. The development of the VHHs included five steps, namely llama immunization, library construction, phage production and selection, generation of master plates, sequence analysis of VHHs, and finally, the production, purification, and dose response ELISA. In addition, α-DC-SIGN VHH (Q94c, QVQ) and α-HIV VHH (Q08c, QVQ) represented VHHs already carrying a Cys-tag, which enabled their covalent attachment onto the nanocarrier surface (see Nanocarrier surface-modifications for the attachment of VHHs).

Evaluation of VHH clone binding by flow cytometry. Validation of the VHH binding activity was examined by primary secondary binding experiments using fluorescence-labeled antibodies and flow cytometry. The VHH detection included the use of the rabbit IgG α-VHH (QE19, QVQ) in combination with the PE donkey α-rabbit IgG (minimal x-reactivity) antibody

(clone Poly4064, Biolegend), HyLight488-labeled rabbit IgG α -VHH (QE19-HyLight488, QVQ), FITC-labeled 6x-His Tag monoclonal antibody (clone AD1.1.10, Thermo), FITC-labeled Myc Tag monoclonal antibody (clone 9E10, abcam), and R-Phycoerythrin AffiniPure Goat α -Alpaca IgG, VHH domain (0.5 mg/mL, Jackson ImmunoResearch).

In control of the VHH binding, whole IgG antibodies targeting the same antigen were applied. Those included the purified α -mouse CD11c IgG (clone N418, Biolegend) in combination with the DyLight™ 649 goat α -hamster IgG (clone Poly4055, Biolegend), and the directly PE-labeled antibodies. Those PE-labeled antibodies involved the rat IgG_{2a} α -mouse α -CD40 (clone 3/23, BD Biosciences), α -rat-IgG_{2a} (clone RTK2758), rat IgG₁ α -mouse CLEC9A (clone 7H11), α -rat-IgG₁ (clone RTK2071), and the mouse IgG_{2c} α -mouse DC-SIGN (clone MMD3), all from Biolegend.

Binding of each VHH clone was performed by first transferring 1×10^5 – 1.5×10^5 cells into suspension in a 1.5 mL tube in PBS. For the F_c receptor blocked cells, the purified rat α -mouse CD16/CD32 antibody (clone 2.4G2, BD Biosciences) was incubated with the cells for 15 min at 4 °C (1 μ g/mL if not otherwise specified). Then, the respective amount of VHH was added to the cells and incubated for 30 min at 4 °C in the dark. After centrifugation (all centrifugations were performed for 5 min at 500 g), the supernatant was discarded, and the cell pellet was resuspended in 100 μ L PBS containing one of the above-mentioned detection antibodies. After 30 min incubation at 4° C, the cells were centrifuged and, in case of the rabbit IgG α -VHH incubated with another fluorescence-labeled antibody, or directly resuspended in 1 mL PBS for the subsequent analysis via flow cytometry (Attune™ NxT Flow Cytometer, Thermo).

A binding between cells and VHHs and/or antibodies (either directly or via primary-secondary approaches), correlated with the respective fluorophore-label of the detection antibody. Therefore, the fluorescence of FITC and DyLight488 was detected by the BL1 channel with an excitation laser of 488 nm and a 530/30 nm band pass filter for emission. In addition, the fluorescence of PE was detected by the YL1 channel with an excitation laser of 561 nm and a 585/16 nm band pass filter for emission. Furthermore, the fluorescence of DyLight649 was detected by the RL1 channel with an excitation laser of 638 nm and a 670/14 band pass filter for emission. The data analysis was conducted by using the Attune™ NxT software. In this analysis, the cell population required a selection by the FSC/SSC scatter plot to exclude cell debris populations. All gated cell events based on the fluorescence signal presented as median fluorescence intensity (MFI) or as the percentage of gated events/cells.

Nanocarrier surface-modifications for the attachment of VHHs. The conjugation between the VHHs with a Cys-tag and the amino-functionalized (3 nmol/mg NH₂) nanocarriers (BNF-Starch-redF from micromod, Germany) utilized a thiol maleimide chemistry. For this purpose, the VHHs required an incubation with the reduction agent TCEP (Carl Roth) (1 h at

room temperature) to separate VHH dimers formed due to the Cys-tags. This VHH treatment was performed with a 10-fold molecular excess of TCEP (1 μg VHH reacted with 0.2 μg TCEP). After the incubation, excess TCEP was removed by performing a buffer exchange to PBS (Zeba™ Spin Desalting column 7K, Thermo) and the VHH content was quantified by the Pierce 660nm protein assay. In the meantime, the nanocarriers required an exchange to PBS (0.01 M PBS diluted with VE-water) containing 1 mM EDTA and a pH 7.4 by using a magnet (strong neodymium magnet). Then, a 150-fold excess of the maleimide linker (Sulfo-SMCC, 436 g/mol, Thermo) dissolved in DMSO reacted with the buffer-exchanged nanocarriers (1 h shaking at room temperature). For example, 1 mg of nanocarrier carrying 3 nmol/mg NH_2 were multiplied with the molecular weight of the maleimide linker (436 g/mol) to obtain an equimolar ratio, which was further multiplied with the desired molecular weight ratio (1 mg x 3 nmol/mg = 3 nmol x 436 ng/nmol = 1308 ng = 1.308 μg x 150 = 196.2 μg). After the incubation, washing the maleimide linker-functionalized nanocarriers (3x with PBS using a magnet) removed excess of unbound linker molecules. The amount of functionalized nanocarriers was quantified by a fluorescence calibration. For the reaction between the VHHs' thiol groups and the maleimide-functionalized nanocarriers, 643 μg (77.5 μL) of the mgHES-maleimide conjugate reacted with different amounts of the VHHs for 3 h at room temperature in a total volume of 700 μL PBS-EDTA pH 7.4. The nanocarrier to VHH ratios determined the total amount of VHH for the conjugation. Investigated VHH ratios and amounts included the 67:1 nanocarrier to VHH ratio with 9.60 μg (32 μL of $\alpha\text{-DC-SIGN}$ and 48 μL of $\alpha\text{-HIV}$), the 600:1 ratio with 1.10 μg (3.67 μL of $\alpha\text{-DC-SIGN}$ and 5.5 μL of $\alpha\text{-HIV}$), and the 1200:1 ratio with 0.54 μg (1.8 μL of $\alpha\text{-DC-SIGN}$ and 2.7 μL of $\alpha\text{-HIV}$). After the incubation, all conjugates were washed (3x with PBS-EDTA) to remove unconjugated VHHs, resuspended to a desired concentration, and quantified by a fluorescence calibration.

Quantification of nanocarriers by fluorescence calibration. A fluorescence calibration determined the amount of pristine and surface-modified nanocarriers. For this quantification, pristine nanocarriers served as a standard and the samples were diluted in PBS based on the initial mass used. All samples, including the standard, were prepared as duplicates in PBS. The Infinite M1000 plate reader (Tecan) with an excitation wavelength of 552 nm and an emission of 580 nm detected the redF fluorescence of the nanocarriers.

Detection of VHH-binding on nanocarriers by flow cytometry. The goat R-Phycoerythrin AffiniPure Goat $\alpha\text{-Alpaca IgG}$, VHH domain ($\alpha\text{-VHH-PE}$) validated the presence of covalently bound VHHs on the nanocarrier surface by using the flow cytometer. For this purpose, 2 μg of sample reacted with either 1 μg (2 μL) or 0.5 μg (1 μL) of the $\alpha\text{-VHH-PE}$ in a total volume of 20 μL in PBS for 30 min at 4 °C. Pristine and maleimide-functionalized nanocarriers with and without the $\alpha\text{-VHH-PE}$ served as negative controls concerning the VHH-functionalized

nanocarriers. After the incubation, all samples were added up to 1 mL PBS and analyzed by flow cytometry, where the fluorescence of the nanocarriers and the PE was detected by the YL1 channel with an excitation laser of 561 nm and a 585/16 nm band pass filter for emission.

Generation of bone marrow-derived dendritic cells. Bone marrow-derived dendritic cells (BMDC) were differentiated from progenitor cells (BM cells) isolated from bone marrow of 8- to 12-week old C57BL/6J mice as described before²⁵⁹. Briefly, BM obtained by flushing the femur and tibia with cell culture medium (Iscove's Modified Dulbecco's Medium (IMDM) containing 5% FBS (PAN), 2 mM GlutaMax (Thermo Fisher Scientific), 100 U/ml penicillin, 100 µg/ml streptomycin, and 50 µM β-mercaptoethanol (Sigma-Aldrich). BM cells were washed and seeded in non-TC-treated 10 cm-petri dishes (2 x 10⁶ in 10 ml per dish). 50 % of cell culture medium was replenished on days 3 and 6. Non-adherent and loosely adherent immature BMDCs were harvested on day 7 and used for uptake experiments.

BMDC staining with TCEP-treated VHHs. BMDCs were harvested, washed with PBS and dead cells were stained with 100 µl Live/Dead Aqua (1:1000 in PBS) per sample for 20 min at 4 °C. Subsequently, cells were washed with PBS twice, F_c receptors were blocked by incubation with anti-CD16/CD32 antibody (clone 2.4G2, 5 µg/ml) in FACS buffer (PBS + 2% FBS + 2 mM EDTA) for 15 min. and incubated with either native or TCEP-pretreated DC-SIGN-VHH (1, 3, 10, 30, or 100 µg/ml) or with the control antibody anti-DC-SIGN-PE (1 µg/ml) for 30 min. at 4 °C. Finally, cells were washed with FACS buffer, fixed using 4% paraformaldehyde in PBS + 2 mM EDTA and analyzed for PE positive BMDCs by flow cytometry.

BMDC uptake experiments. Harvested BMDCs were washed with FBS-free cell culture medium and reseeded in 24-well suspension culture plates (10⁵ in 500 µl cell culture medium per well) either in cell culture medium. Subsequently, cells were incubated with either 30, 10, or 3 µg mL⁻¹ of different nanoparticle formulations for 20 h at 37 °C and 7.5% CO₂, harvested and analyzed by flow cytometry.

7.4 Results and Discussion

Fragmentation of the IgG molecule

In this study, the antibody fragmentation focused exclusively on the use of pepsin to produce the $F_{(ab)_2}$ fragment. Additional use of a reduction agent (cysteamine) aimed to further disassemble the $F_{(ab)_2}$ into the F_{ab}' fragment. Investigated IgGs included the Armenian hamster isotype (clone HTK888) and the CD11c targeting antibody (clone N418) of the same isotype, as well as the rat IgG₁ isotype (clone RTK2071). The fragmentation of the CD11c and the corresponding isotype into the $F_{(ab)_2}$ or F_{ab}' fragment aimed to compare the targeting ability between these fragments and the established whole CD11c antibody-modified nanocarriers described in chapter B. The same applied for the rat IgG, which represents the isotype of the CLEC9A targeting antibody.

Overall, the established conditions for the pepsin digestion were based on the systematic approach by Kinman *et al.*²⁷⁷. In their work, they present the procedure for the fragmentation by pepsin, including different conditions concerning the yield, digestion efficiency, and function of rat IgG antibodies. Therefore, the first fragmentation trial focused on the digestion with immobilized pepsin using a digestion buffer composed of formic acid with a pH of 2.8. For the digestion, the immobilized pepsin required a removal from the storage buffer and an equilibration into the digestion buffer. At the same time, the antibodies of interest, namely the hamster and rat isotype antibodies, needed also to be concentrated in the digestion buffer. Then, the buffer-exchanged antibodies and the activated pepsin reacted at a final antibody concentration of 1 mg/mL at 37 °C either for 2 or 6 h. After the incubation, the mixture required a removal of the pepsin resin from the digested antibody followed by the determination of the antibody concentration and visualization of the fragments by SDS-PAGE and silver staining (Figure 7.3).

As a result, the chosen conditions efficiently divided the rat isotype into four distinct fragment products. Those fragments included the possible $F_{(ab)_2}$ fragment at ~ 100 kDa, some digestion intermediates found ~ 70 – 80 kDa, possible F_{ab} fragments or heavy chain remains at ~ 50 kDa, and overdigested or degraded products, such as the light chains and F_c fragments at ~ 25 kDa (Figure 7.3 A a – d). These fragmentation products appeared also in the MALDI TOF analysis detecting the $F_{(ab)_2}$ around 100 kDa with the strongest signal intensity (Figure 7.3 B). Once treated with the reduction agent (DTT), only a single band appeared around 25 kDa (Figure 7.3 A red.). For the whole antibody (150 kDa), two specific bands usually appear after the reduction agent treatment at 50 kDa (heavy chain) and 25 kDa (light chain). Therefore, treating the pepsin-digested rat isotype antibody with the reduction agent leading to only one band

indicates a complete digestion of the hinge region. Without the hinge region, the reduction agent completely reduces the digested antibody into a mixture of only ~ 25 kDa fragments.

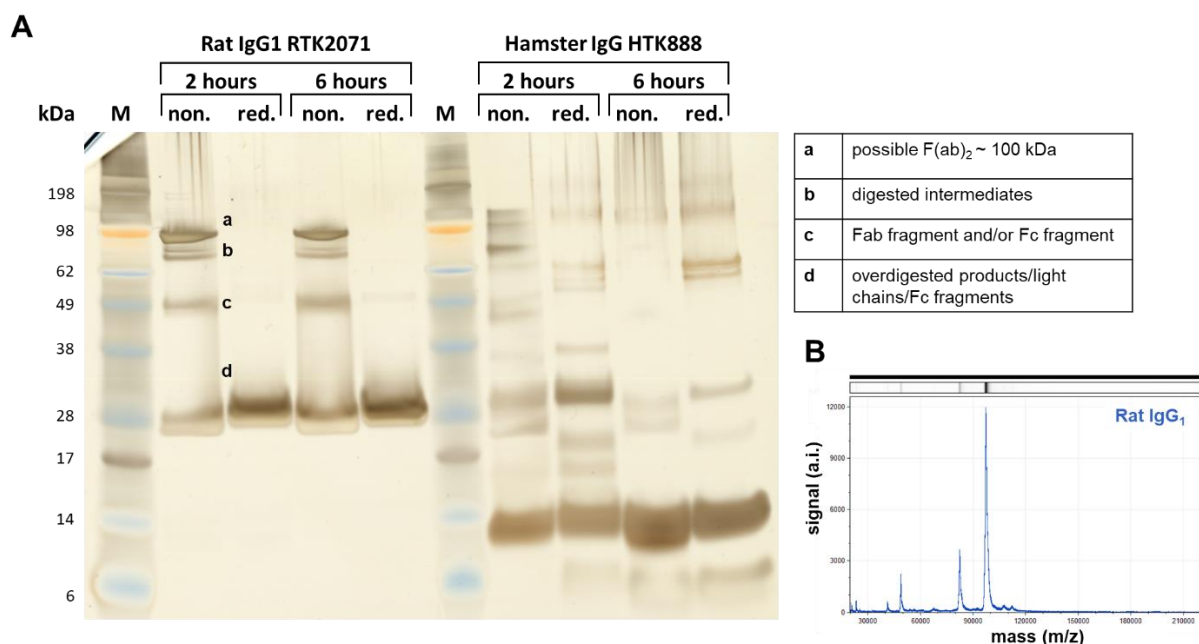


Figure 7.8: Visualization of fragmented isotype antibodies after pepsin digestion. Pepsin fragmented isotype control antibodies (rat IgG₁ and hamster IgG) are visualized by SDS-PAGE (**A**) and MALDI-TOF (**B**). For the SDS-PAGE, 2 µg of pepsin digested antibody (2 h or 6 h) were applied on the gel without (non.) or with (red.) reduction agent (DTT) and run for 1 h at 120 V. Silver staining visualized the protein bands according to the manufacturer's protocol. For the MALDI-TOF, the rat IgG₁ digested for 2 h was measured. M = marker.

Furthermore, the incubation time between the 2 and 6 h revealed no differences in the migration pattern on the SDS-PAGE. However, a longer pepsin incubation time might influence the binding ability of the antibody, although the isotype antibody has no specific target as such, which makes it difficult to analyze. Therefore, this enzyme influence on the targeting ability needs a testing with an epitope-binding antibody, such as the CLEC9A antibody. Contrary, the pepsin digestion of the hamster isotype after 2 and 6 h resulted in the generation of several digestion products (Figure 7.3 A). While the pepsin incubation for 2 h led to a mixture of several digested intermediates, the 6 h incubation completely overdigested the antibody into low molecular weight fragments primarily migrating around 14 kDa.

Concluding, the investigated conditions for the antibody fragmentation worked for the rat IgG₁ but were too harsh for the hamster isotype. Therefore, different conditions using a sodium acetate buffer (pH 4.0 and pH 4.5) with three pepsin incubation times (30 min, 1 h, and 2 h) examined the fragmentation of the hamster isotype and the CD11c antibody (Figure 7.4).

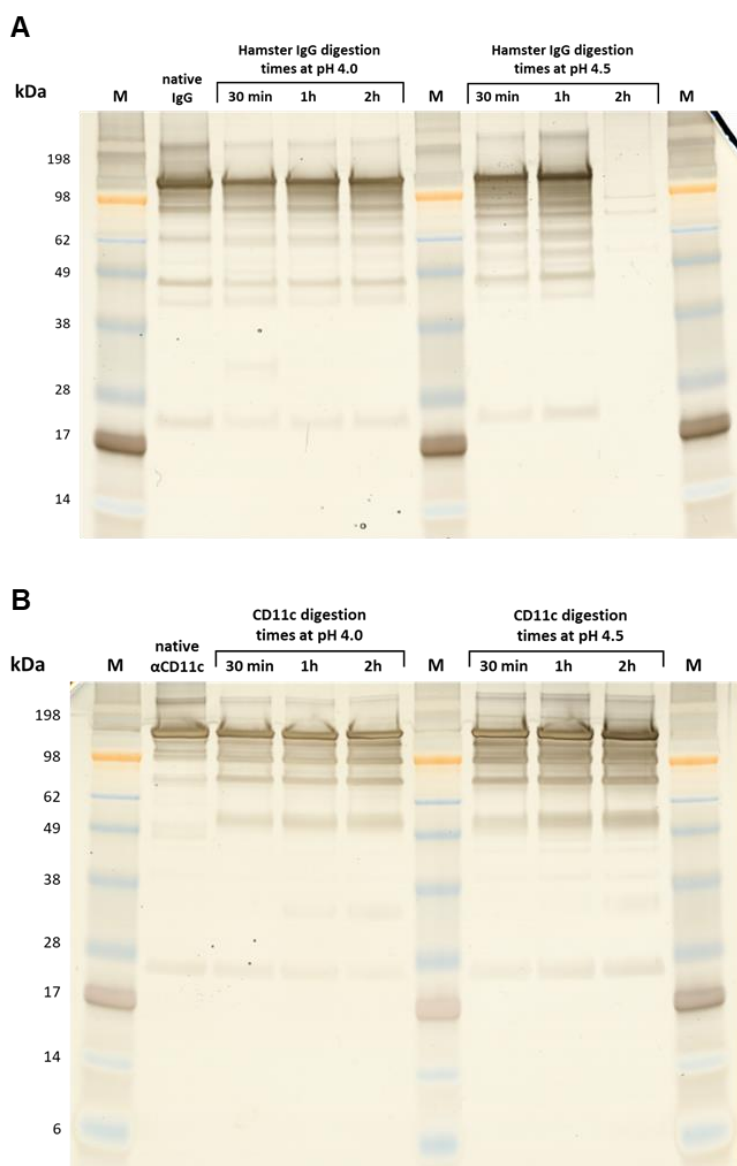


Figure 7.9: Pepsin digestion of the hamster IgG and CD11c antibody. SDS-PAGE visualization of the hamster isotype antibody (A) and CD11c antibody (B). Before the visualization, the antibodies were digested with pepsin for different time points (30 min, 1 h, and 2 h) in sodium acetate buffer (pH 4.0 or 4.5). Native antibodies were applied as a control. For the visualization, 2 μ g of sample were used for the SDS-PAGE without a reduction agent and run for 1 h at 120 V. Silver staining visualized the protein bands according to the manufacturer's protocol. M = marker.

Compared to the previous fragmentation condition, the most abundant hamster isotype band appeared at \sim 150 kDa (Figure 7.4 A). In respect to the undigested control (native IgG), virtually no differences in the migration pattern were observed after digestion at a pH 4.0 for all time points. Additional bands that also appeared in the undigested control prevented from distinguishing between fragmentation products or other proteins that act as stabilizers in antibody buffers during long-term storage, including bovine serum albumin and gelatin²⁸⁹. The digestion at a pH 4.5 led to a slightly more complex migration pattern, which might represent the generation of a few fragmentation products, although the 2 h incubation sample was lost. On the other side, the CD11c antibody fragmentation worked slightly better leading to

distinguishable bands in contrast to the undigested control (Figure 7.4 B). Here, the fragmentation products appeared slightly above 49 kDa and ~ 100 kDa, whereas the most abundant band was still detected around 150 kDa. Again, the incubation times and the difference in pH revealed only minor changes. Therefore, the new buffer condition with different pepsin incubation times showed not to be sufficient in the fragmentation of the hamster isotype and the CD11c antibody. In fact, some antibody classes or species like the mouse IgG_{1a} are not cleavable by pepsin, whereas mouse IgG_{2a} and IgG_{2b} are cleavable²⁹⁰. Consequently, it was decided to not further analyze these two antibodies but to take focus on the generation of the monovalent F_{ab}' out of the rat IgG₁ F_{(ab)₂} fragment. For this purpose, a mild reduction agent like cysteamine, also named 2-mercaptoethylamine (2-MEA), represents the advantage of generating F_{ab}' fragments with C-terminal thiol groups. Those thiols originate from the reduced disulfide bonds connecting the F_{(ab)₂} fragment. In contrast, the cleavage by papain would not produce such thiol groups. Therefore, 2-MEA represents the advantage of generating thiol groups as an active targeting site for conjugation. In the reduction procedure, different amounts of 2-MEA reacted with the rat IgG₁ F_{(ab)₂} fragment for different time points (Figure 7.5).

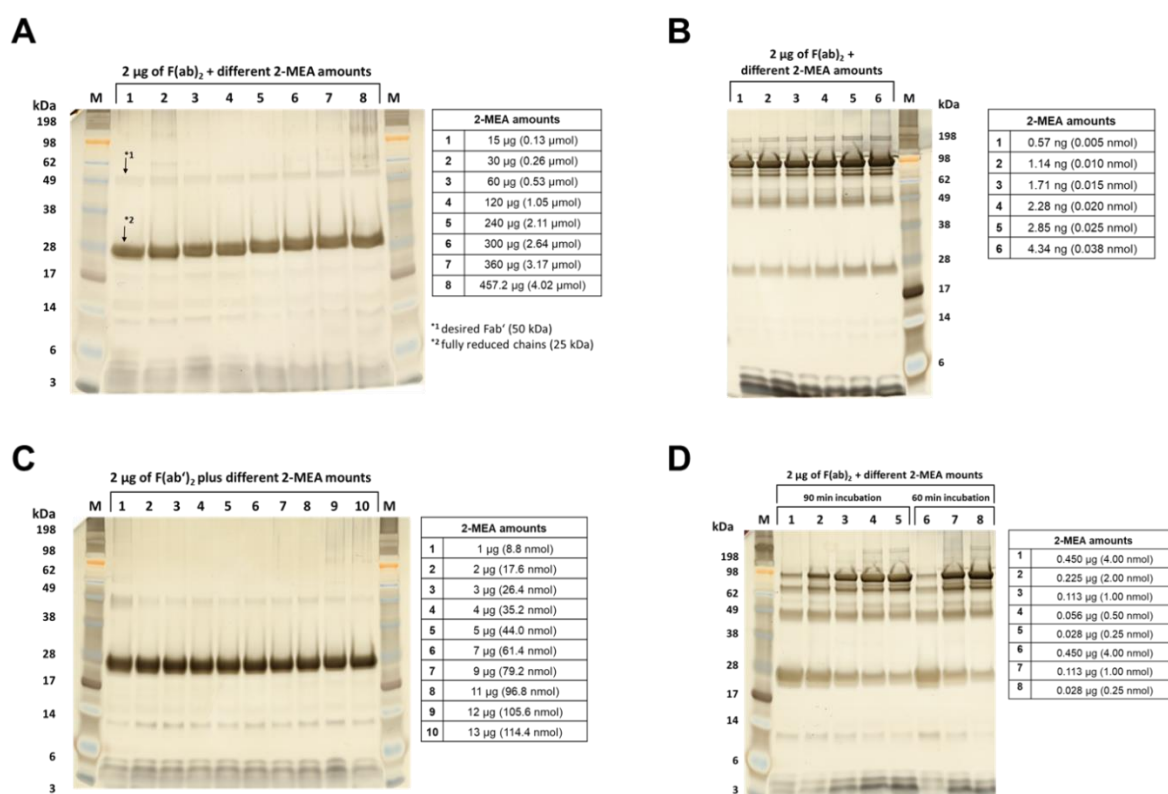


Figure 7.10: F_{(ab)₂} to F_{ab} reduction by 2-MEA. The pepsin digested rat IgG₁ F_{(ab)₂} fragment incubated with the reduction agent 2-MEA is visualized by SDS-PAGE. For the 2-MEA reduction, different amounts incubated with 2 μg of F_{(ab)₂} for 90 min at 37 °C, including 15 – 457.2 μg (A), 0.57 ng – 4.34 ng (B), 1 μg – 13 μg (C), and 0.450 μg – 0.028 μg for 90 and 60 min at 37 °C (D). The SDS-PAGE was performed with 2 μg of sample without DTT and run for 1 h at 120 V. Silver staining was conducted according to the manufacturer's protocol to visualize the protein band. M = marker.

In the first set of experiments (Figure 7.5 A), 2-MEA amounts of 0.13 μmol – 4.02 μmol incubated for 90 min at 37 °C almost fully reduced the $F_{(\text{ab})_2}$ into ~ 25 kDa fragments with only a weak band detected around 50 kDa, which potentially represented the desired F_{ab} ' fragment. Therefore, in the second trial (Figure 7.5 B), lower 2-MEA amounts (0.005 nmol – 0.038 nmol) incubated for 90 min at 37 °C had virtually no reduction effect on the $F_{(\text{ab})_2}$. In the third trial (Figure 7.5 C), the chosen 2-MEA amounts again almost completely reduced the $F_{(\text{ab})_2}$ (likewise to A) indicating either too high or too low 2-MEA amounts. Therefore, in the final trial (Figure 7.5 D), 2-MEA amounts of 0.25 nmol – 4 nmol incubated for either the usual 90 min or a shorter time of 60 min at 37 °C yielded the best reduction. In particular, 4 nmol of 2-MEA led to an even distribution of reduction products when comparing the band intensities. Lower 2-MEA amounts still showed the $F_{(\text{ab})_2}$ around 100 kDa to be the most abundant lane. Comparing the 60 min and 90 min incubation revealed no visual differences on the gel. In summary, the four 2-MEA trials highlighted a good $F_{(\text{ab})_2}$ to F_{ab} ' reduction range between 4 and 8.8 nmol. However, the gels indicated further reduction or fragmentation products besides the F_{ab} ' present in the mixture. Therefore, next to a proper 2-MEA amount for reduction, the removal of undesired antibody remnants from the antibody fragment of interest required a distinct purification method.

For this purpose, a preparative size exclusion chromatography (SEC), or gel permeation chromatography (GPC), examined the purification of the rat $F_{(\text{ab})_2}$ after the pepsin digestion (Figure 7.6). From the GPC, the rat $F_{(\text{ab})_2}$ digestion mixture divided into three main fractions (Figure 7.6 A) that were collected and analyzed by SDS-PAGE (Figure 7.6 B). Despite the separation by GPC, the visualization of each individual fraction showed not the desired single protein band but a mixture of different molecular weight fragments comparable to the pattern observed before the GPC. In this regard, Song *et al.* applied the SEC in a consecutive combination with a protein G resin to purify their F_{ab} fragment after the IgG papain digestion leading to highly purified F_{ab} fragments (33% yield)²⁹¹. Generally, protein A and G resins demonstrate a high affinity to the F_c region of many antibodies enabling an affinity-based removal of F_{ab} from F_c fragments in digested IgG mixtures²⁹². However, protein A shows almost no binding for rat IgG and protein G binds to both the F_{ab} and F_c region of rat IgGs, which prevents a purification by these techniques²⁹²⁻²⁹⁴.

As a result, the separation by GPC needs additional experiments to validate a complete purification of the desired $F_{(\text{ab})_2}$ from other fragments or contaminants. Once achieved, the purified fragment needs a testing for the conjugation onto the nanocarrier surface evaluating its targeting ability compared to whole antibodies.

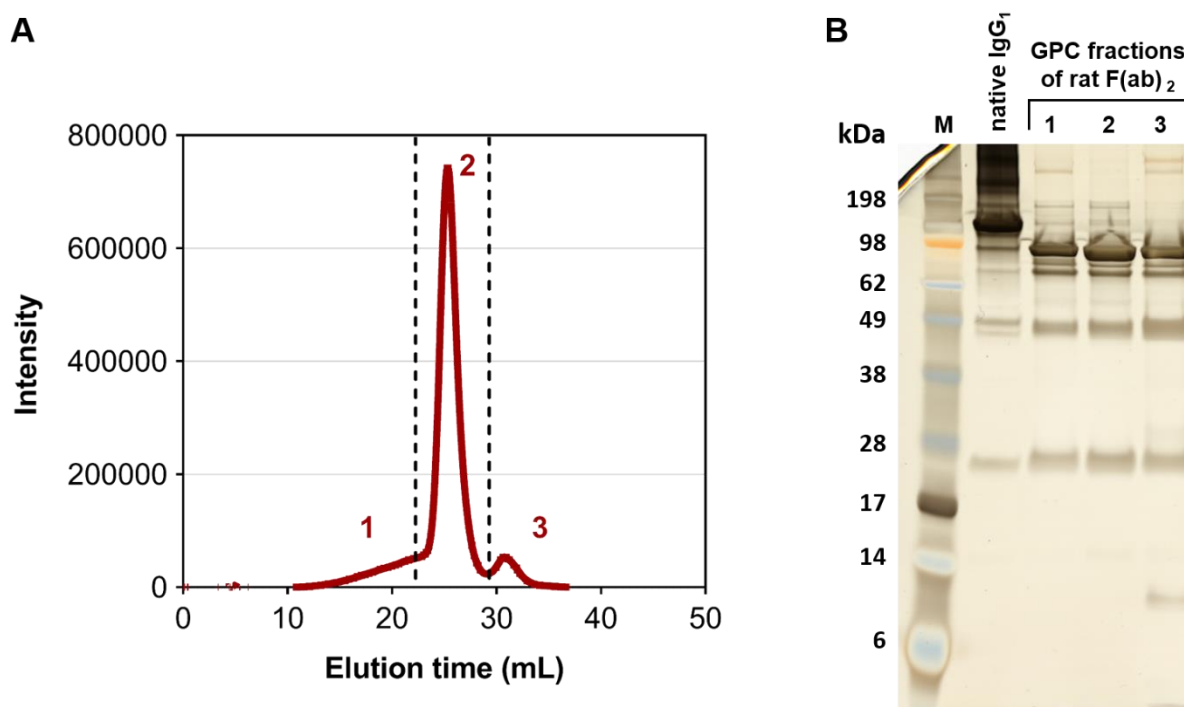


Figure 7.11: GPC separation of digested rat IgG₁. After the pepsin digestion, the mixture was separated by a preparative GPC (A) and the three fractions analyzed by SDS-PAGE (B). For the separation of the digested rat IgG₁ mixture, 100 μ L of sample volume were injected and separated on a Cytiva Superose 6 Increase 10/300 GL column at a flow rate of 0.8 mL/min using PBS as eluent. The chromatograms were recorded at a wavelength of 280 nm. Three distinct fractions were separated and collected for the analysis by SDS-PAGE and silver staining. All samples were pipetted with 2 μ g on the gel. M = marker.

Investigation on the antigen-binding ability of VHH clones

In the second aim of this study, the ability of binding the corresponding antigen in cell lines or primary cells distinguished which of the VHH clones showed the best targeting. For this purpose, different detection conditions using fluorescence-labeled whole antibodies highlighted the importance of how to identify a correct VHH antigen binding by flow cytometry. These preliminary studies form the basis for the envisioned covalent immobilization of the VHHs onto the nanocarrier surface.

After removing unbound clones, the cells with the antigen-bound VHH clones incubated with a secondary antibody directed against the VHH. Depending on whether this secondary antibody was fluorescence-labeled or not, the cells needed to be incubated with another fluorescence-labeled antibody and/or were finally washed for the detection by flow cytometry.

In the first three-step VHH antigen-binding detection (Figure 7.7), different conditions (indicated for each figure separately, Figure 7.7 A – G) showed the strongest binding for the CD11c VHH clone 1A6, followed by 1A9, and 1A1.

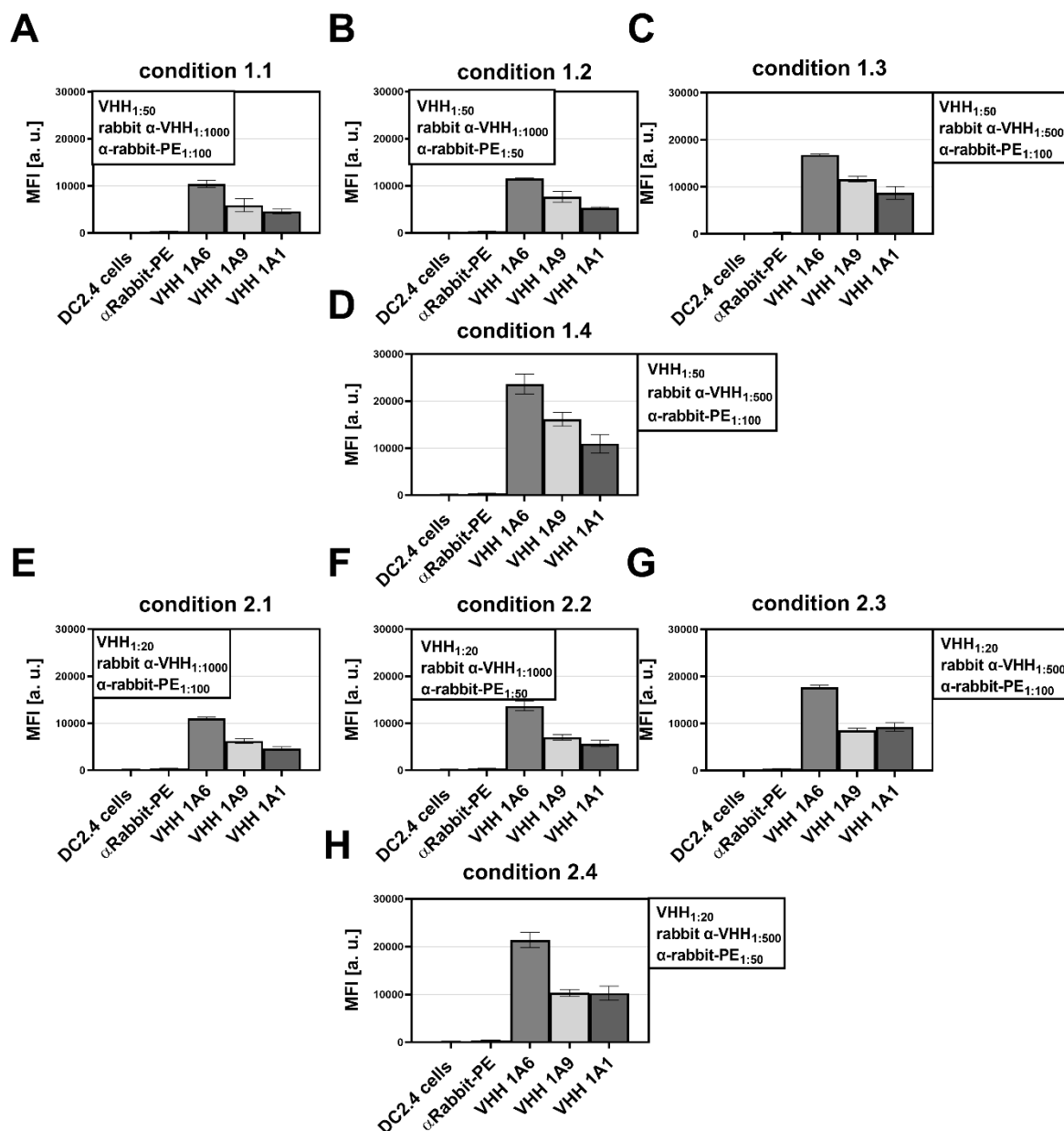


Figure 7.7: A three-step detection of the CD11c VHH clone antigen binding. Detection of the CD11c surface binding of three VHH clones (1A6 with 3 mg/mL, 1A9 3.6 mg/mL, and 1A1 with 2.1 mg/mL) on the DC2.4 cell line is analyzed via flow cytometry. For the experiment, 1×10^5 cells were transferred in 100 μ L PBS and incubated with different amounts of the VHH (1:50 or 1:20), the rabbit α -VHH (1:1000 and 1:500), and the α -rabbit-PE (1:100 and 1:50). These amounts were tested in combination as indicated in each image represented as conditions 1.1 – 2.4 (A – G). Every incubation step was performed for 30 min at 4 °C followed by centrifugation (500 g for 5 min). Values are given as mean \pm SD (n = 3). MFI [a.u.] = median fluorescence intensity [arbitrary units].

The conditions included the testing of two VHH dilutions (1:50 and 1:20), two rabbit IgG α -VHH dilutions (1:1000 and 1:500), and two goat α -rabbit-PE dilutions (1:100 and 1:50) incubated each for 30 min at 4 °C (no washing in between the steps). In total, eight conditions validated the binding where each VHH dilution incubated with both rabbit α -VHH dilutions and both α -rabbit-PE dilutions. The goat α -rabbit-PE secondary antibody showed virtually no unspecific binding towards the DC2.4 cell line. However, this validation missed a control where the rabbit

IgG α -VHH and the goat α -rabbit-PE incubated one after the other with the cells in the absence of a VHH clone.

Therefore, testing this control group with the VHH clone 1A9 and an F_cR blocking under the condition 1.1 revealed false-positive results due to the unspecific binding of the control group towards the DC2.4 cell line (Figure 7.8).

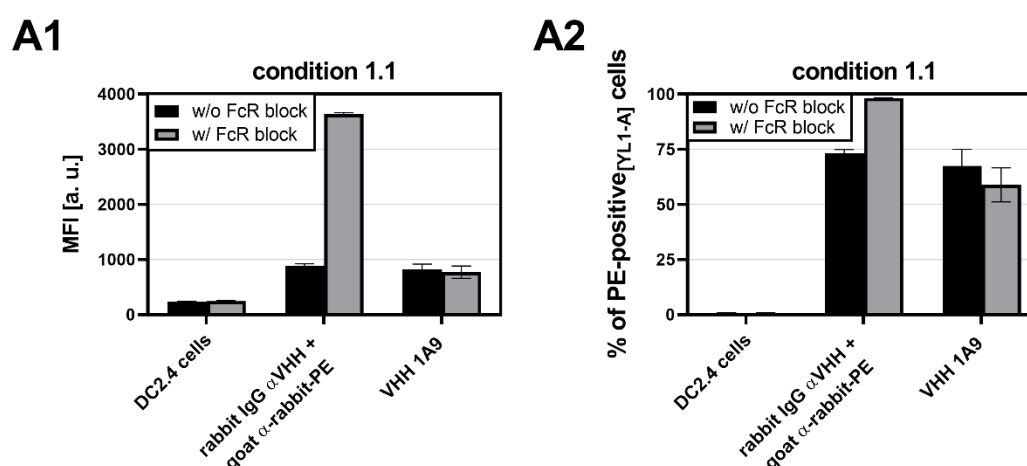


Figure 7.8: Unspecific binding of the rabbit IgG α -VHH. CD11c binding of the VHH clone 1A9 on DC2.4 cells is analyzed by flow cytometry. For the experiment, 1×10^5 cells were transferred in 100 μ L PBS and in case of the blocked group (w/ F_cR block, grey bars) incubated with the F_cR antibody (1 μ g/mL) for 30 min at 4 $^{\circ}$ C. Unblocked cells (w/o F_cR block, black bars) were incubated with PBS. Then, the cells were treated with the VHH (1:50), followed by the rabbit α -VHH (1:1000), and α -rabbit-PE (1:100). Each incubation was performed for 30 min at 4 $^{\circ}$ C with a centrifugation (500 g for 5 min) in between each step. In the control group, no VHH was applied. The flow cytometry data is represented as MFI [a.u.] = median fluorescence intensity [arbitrary units] (**A1**) or as the percentage of positive cells (**A2**). Values are given as mean \pm SD (n = 3).

In addition, the F_cR blocking of the cells with a rat anti-mouse CD16/CD32 antibody (clone 2.4G2) significantly increased the binding of the control group (grey bar), which likely occurred due to cross-reactivity. Despite of more than 50% of PE-positive gated cells (Figure 7.8 A2), the VHH clone 1A9 showed a weaker MFI (A1 compared to Figure 7.7 A).

For this reason, examining the control group and F_cR blocking together with the VHH clone 1A6 under the condition 1.4 additionally highlighted the role of the unspecific binding of the control group (Figure 7.9). Without the F_cR blocking, the VHH 1A6 clone showed a stronger MFI than the control group (Figure 7.9 A1 black bars). However, with F_cR blocking the binding of the 1A6 clone significantly reduced in MFI, while the control group significantly increased in MFI (Figure 7.9 A1). Adding to this, the percentage of PE-positive cells revealed almost no difference between the unspecific binding of the control group and a specific CD11c VHH clone 1A6 binding (Figure 7.9 A2).

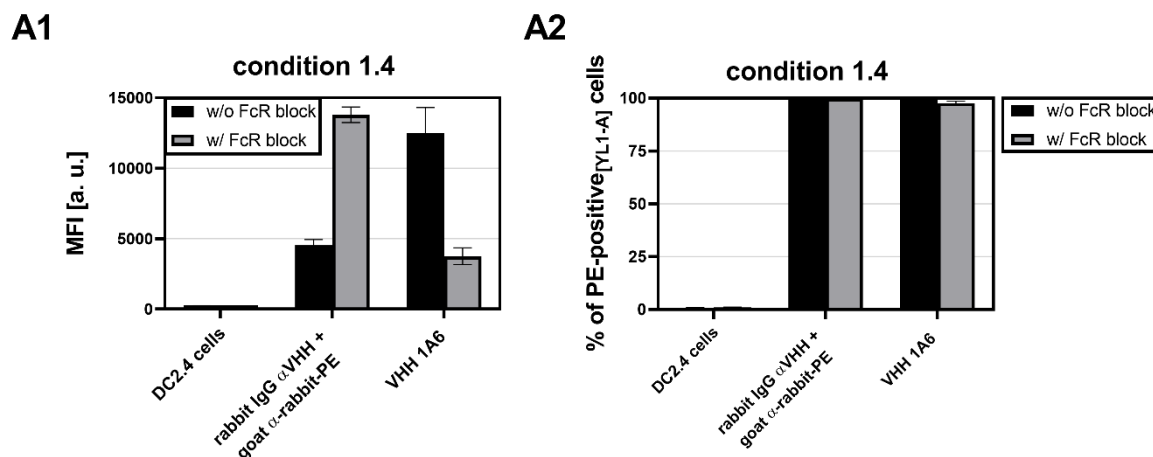


Figure 7.9: F_c receptor blocking impairs the CD11c VHH binding. CD11c binding of the VHH clone 1A6 on DC2.4 cells is analyzed by flow cytometry. For the experiment, 1×10^5 cells were transferred in 100 μ L PBS and in case of the blocked group (w/ F_cR block, grey bars) incubated with the F_cR antibody (1 μ g/mL) for 30 min at 4 °C. Unblocked cells (w/o F_cR block, black bars) were incubated with PBS. Then, the cells were treated with the VHH (1:50), followed by the rabbit α -VHH (1:1000), and α -rabbit-PE (1:100). Each incubation was performed for 30 min at 4 °C with a centrifugation (500 g for 5 min) in between each step. In the control group, no VHH was applied. The flow cytometry data is represented as MFI [a.u.] = median fluorescence intensity [arbitrary units] (**A1**) or as the percentage of positive cells (**A2**). Values are given as mean \pm SD (n = 3).

Due to this unspecific binding of the control group in combination with the F_cR block, starvation of the cells in cell culture medium without FBS and two rabbit IgG α -VHH dilutions tested the antigen-binding of the CD11c VHH clone 1A1 (Figure 7.10).

The FBS starvation of the DC2.4 cells before the antigen-binding experiment prevented the binding of proteins present in FBS that might be bound to the cell surface potentially causing the unspecific interaction between the control groups (rabbit IgG α -VHH and goat α -rabbit-PE). For example, Choi *et al.* demonstrate that cell culture medium components, such as FBS, amino acids and/or salts, prevented their antibody to antigen binding used in an ELISA²⁹⁵.

Therefore, the two dilutions of the two rabbit IgG α -VHHs examined to which degree the unspecific binding correlated with the amount used for the detection. Despite the FBS depletion, the control groups still bound comparably strong to the DC2.4 cell surface, where the F_cR blocked cells (Figure 7.10 A1) showed to interact stronger with the control groups than without the blocking (Figure 7.10 B1). Applying the rabbit IgG α -VHH with a lower amount reduced the unspecific binding. However, the experiment showed no specific CD11c binding of the VHH clone 1A1 for the investigated conditions also seen in the percentage of gated cells (Figure 7.10 A2 and B2).

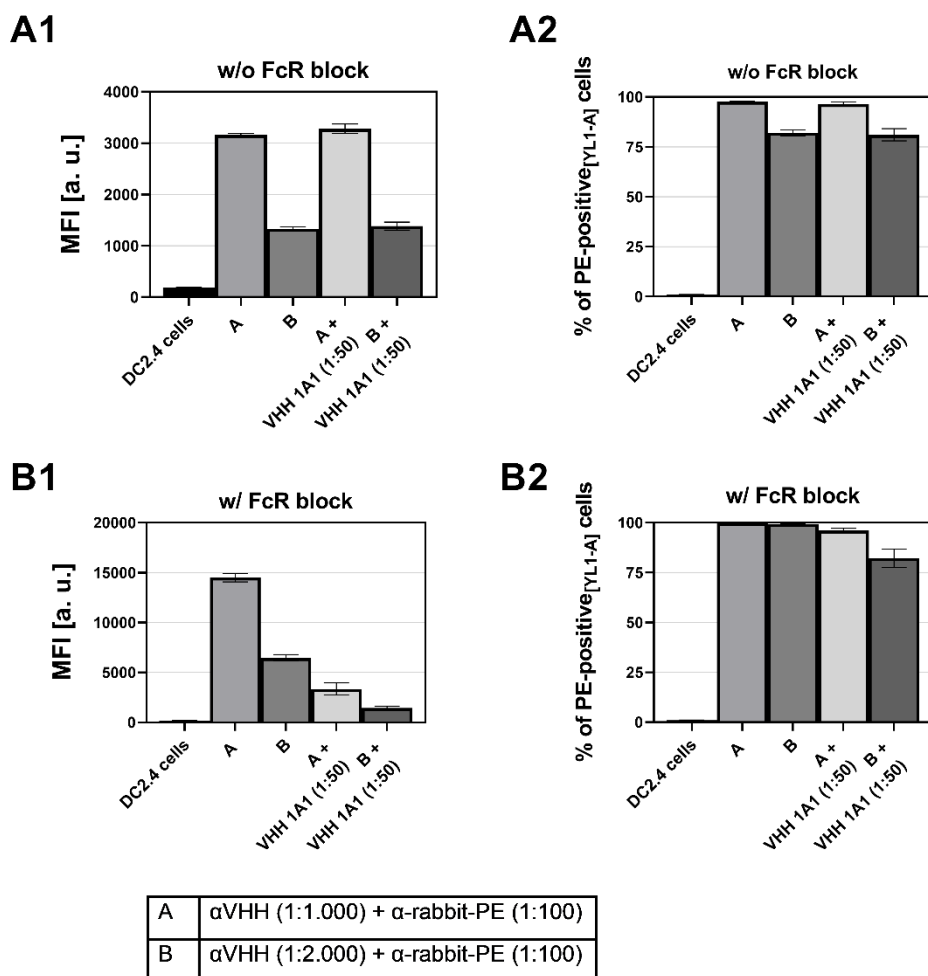


Figure 7.10: CD11c VHH binding of FBS-depleted DC2.4 cells. CD11c binding of the VHH clone 1A1 in FBS-depleted (~80 min in cell medium without FBS) DC2.4 cells is analyzed by flow cytometry. For the experiment, 1×10^5 cells were transferred in 100 μ L PBS and in case of the blocked group (w/ FcR block, grey bars) incubated with the FcR antibody (1 μ g/mL) for 30 min at 4 °C. Unblocked cells (w/o FcR block, black bars) were incubated with PBS. Then, the cells were treated with the VHH (1:50), followed by the rabbit α -VHH (1:1000 or 1:2000), and α -rabbit-PE (1:100). Each incubation was performed for 30 min at 4 °C with a centrifugation (500 g for 5 min) in between each step. In the control groups, no VHH was applied. The flow cytometry data is represented as MFI [a.u.] = median fluorescence intensity [arbitrary units] or as the percentage of positive cells either under unblocked (**A1** and **A2**, w/o FcR block) or Fc receptor blocked (**B1** and **B2**, w/ FcR block) conditions. Values are given as mean \pm SD (n = 3).

In the second two-step VHH antigen binding detection, the directly DyLight₄₈₈-conjugated rabbit IgG anti-VHH also showed no detection (Figure 7.11). According to the data, the DyLight₄₈₈-conjugated rabbit IgG α -VHH bound weakly to the cells when compared to the previous control groups although it was unable to detect a binding of the CD11c VHH 1A1 clone (Figure 7.11 A1 – B2).

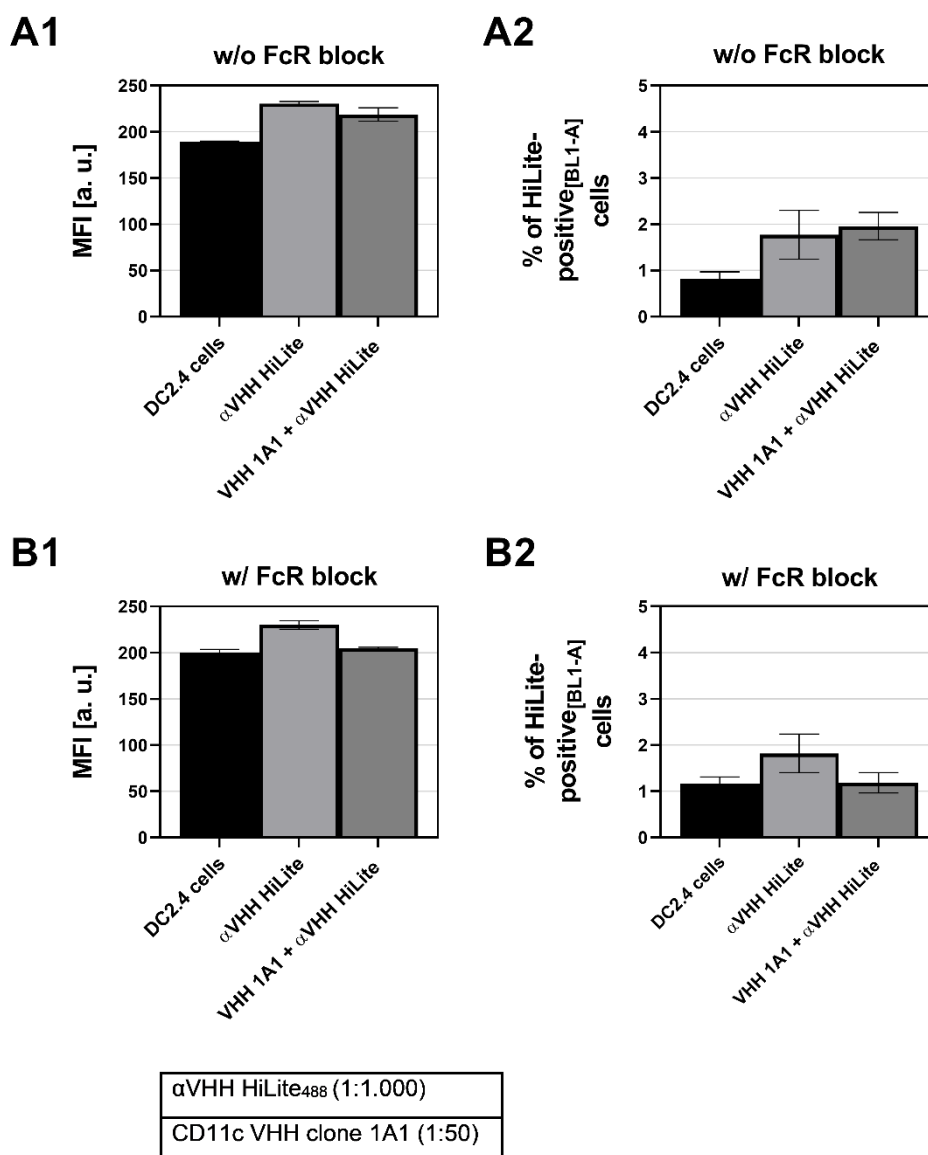


Figure 7.11: Two-step detection of CD11c VHH binding. CD11c binding of the VHH clone 1A1 in FBS-depleted (~80 min in cell medium without FBS) DC2.4 cells is analyzed by flow cytometry. For the experiment, 1×10^5 cells were transferred in 100 μ L PBS and in case of the blocked group (w/ FcR block, grey bars) incubated with the FcR antibody (1 μ g/mL) for 30 min at 4 °C. Unblocked cells (w/o FcR block, black bars) were incubated with PBS. Then, the cells were treated with the VHH (1:50), followed by the rabbit α -VHH HiLite₄₈₈ (1:1000). Each incubation was performed for 30 min at 4 °C with a centrifugation (500 g for 5 min) in between each step. In the control groups, no VHH was applied. The flow cytometry data is represented as MFI [a.u.] = median fluorescence intensity [arbitrary units] or as the percentage of positive cells either under unblocked (**A1** and **A2**, w/o FcR block) or Fc receptor blocked (**B1** and **B2**, w/ FcR block) conditions. Values are given as mean \pm SD (n = 3).

In another two-step detection attempt, sequence-specific antibodies (FITC-labeled) against the VHHs C-terminal Myc-tag or His-tag further showed no desirable detection (Figure 7.12).

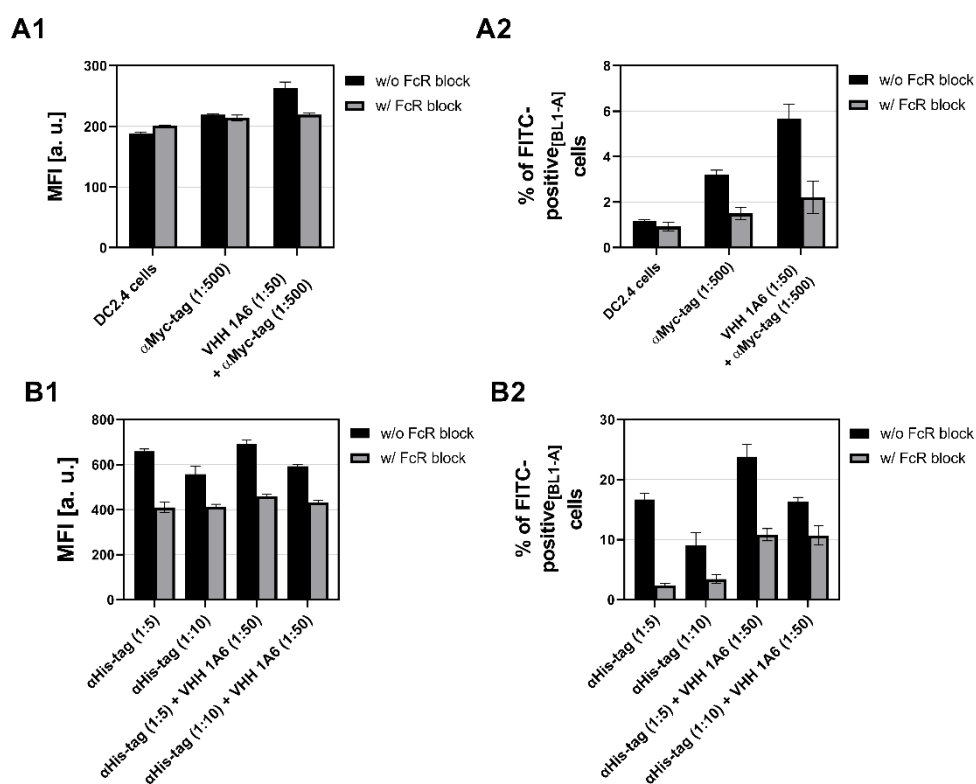


Figure 7.12: Two-step detection of CD11c VHH binding by sequence-specific antibodies. CD11c binding of the VHH clone 1A6 in DC2.4 cells is analyzed by flow cytometry. For the experiment, 1×10^5 cells were transferred in 100 μ L PBS and in case of the blocked group (w/ FcR block, grey bars) incubated with the FcR antibody (1 μ g/mL) for 30 min at 4 $^{\circ}$ C. Unblocked cells (w/o FcR block, black bars) were incubated with PBS. Then, the cells were treated with the VHH (1:50), followed by the incubation with either the α -Myc tag (1:500) (**A1** and **A2**), or the α -His tag (1:5 or 1:10) (**B1** and **B2**). Each incubation was performed for 30 min at 4 $^{\circ}$ C with a centrifugation (500 g for 5 min) in between each step. In the control groups, no VHH was applied. The flow cytometry data is represented as MFI [a.u.] = median fluorescence intensity [arbitrary units] or as the percentage of positive cells. Values are given as mean \pm SD (n = 3).

Finally, only the goat IgG α -VHH PE-conjugated (Jackson ImmunoResearch) secondary antibody enabled the establishment of a sufficient two-step detection protocol for the VHH clone antigen binding without an influence of the Fc receptor block antibody or an unspecific secondary antibody binding (Figure 7.13).

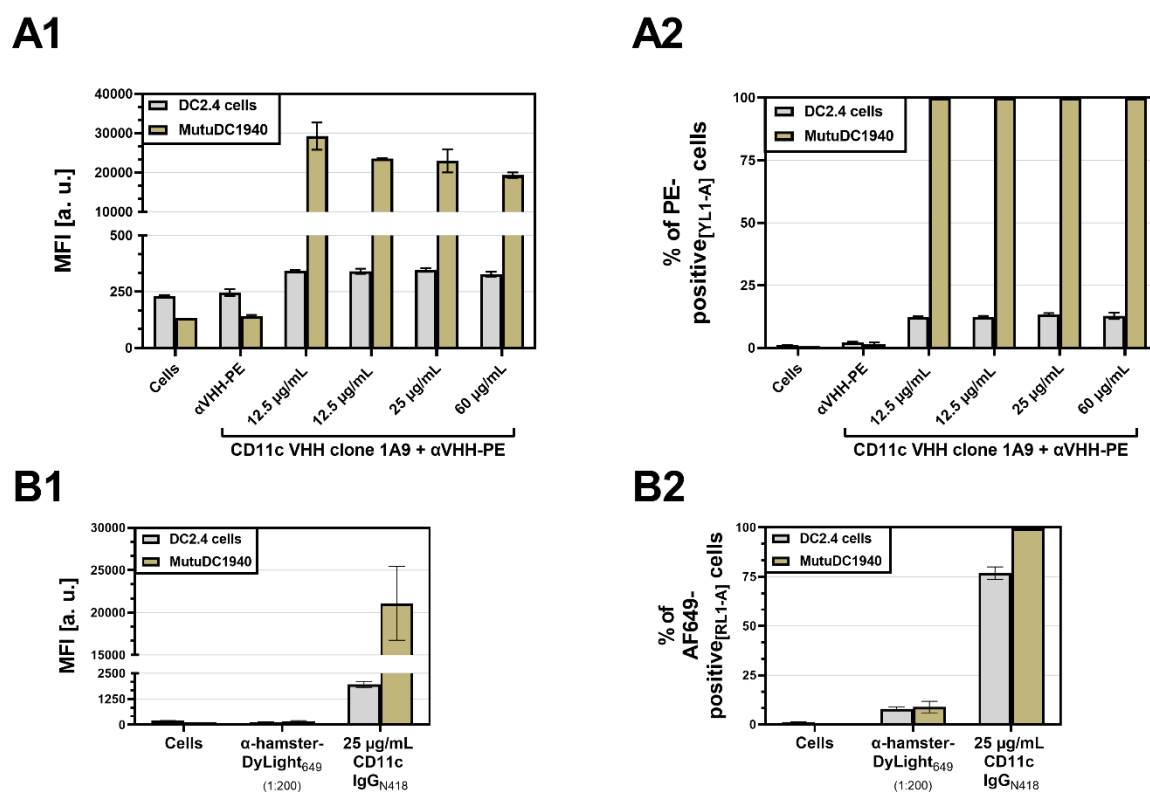


Figure 7.13: CD11c VHH binding differences in DC2.4 and MutuDC1940 cells. CD11c binding of the VHH clone 1A9 in DC2.4 and MutuDC1940 cells (**A1** and **A2**) is analyzed by flow cytometry. As a targeting control, the hamster α -mouse CD11c IgG (clone N418) and the α -hamster IgG DyLight₆₄₉ were applied (**B1** and **B2**). For the experiment, 1×10^5 cells were transferred in 100 μ L PBS and incubated with the F_cR antibody (5 μ g/mL) for 15 min at 4 °C. Then, the cells were treated with different concentrations of the VHH, followed by the incubation with the α -VHH-PE (1:200). Each incubation was performed for 30 min at 4 °C with 2 – 3 centrifugations (500 g for 5 min) in between each step to wash off unbound molecules. In the control groups, no VHH or IgG were applied. The flow cytometry data is represented as MFI [a.u.] = median fluorescence intensity [arbitrary units] or as the percentage of positive cells. Values are given as mean \pm SD (n = 3).

The detection protocol highlighted the difference in the CD11c VHH binding in the two investigated dendritic cell lines, namely the DC2.4 and the MutuDC1940 cells. While the CD11c VHH clone 1A9 bound relatively weak with less than 15% positive cells to the DC2.4 cell line (Figure 7.13 A1 and A2), the detected binding to the MutuDC1940 cells was strong with almost 100% of positive-gated cells. Furthermore, the titration of the 1A9 clone demonstrated that the optimal CD11c VHH antigen binding was stronger at lower concentrations than for higher ones (Figure 7.13 A1), which can be explained by VHH interference, cross-reactivity, or signal interference caused by high concentrations as described in the hook effect or prozone effect²⁹⁶. As a general control, detecting the antigen binding of a regular hamster IgG α -mouse CD11c via primary-secondary antibody detection worked without any influence of the F_cR block and a low unspecific binding of the secondary

antibody (Figure 7.13 B1 and B2). This IgG control testing demonstrated the differences in the CD11c expression of both cell lines, where the DC2.4 cells express around 75% and the MutuDC1940 cells around 100% CD11c-positive cells.

Based on the CD11c expression in the MutuDC1940 cell line, the established protocol examined the CD11c antigen binding of all VHH clones with two concentrations (Figure 7.14).

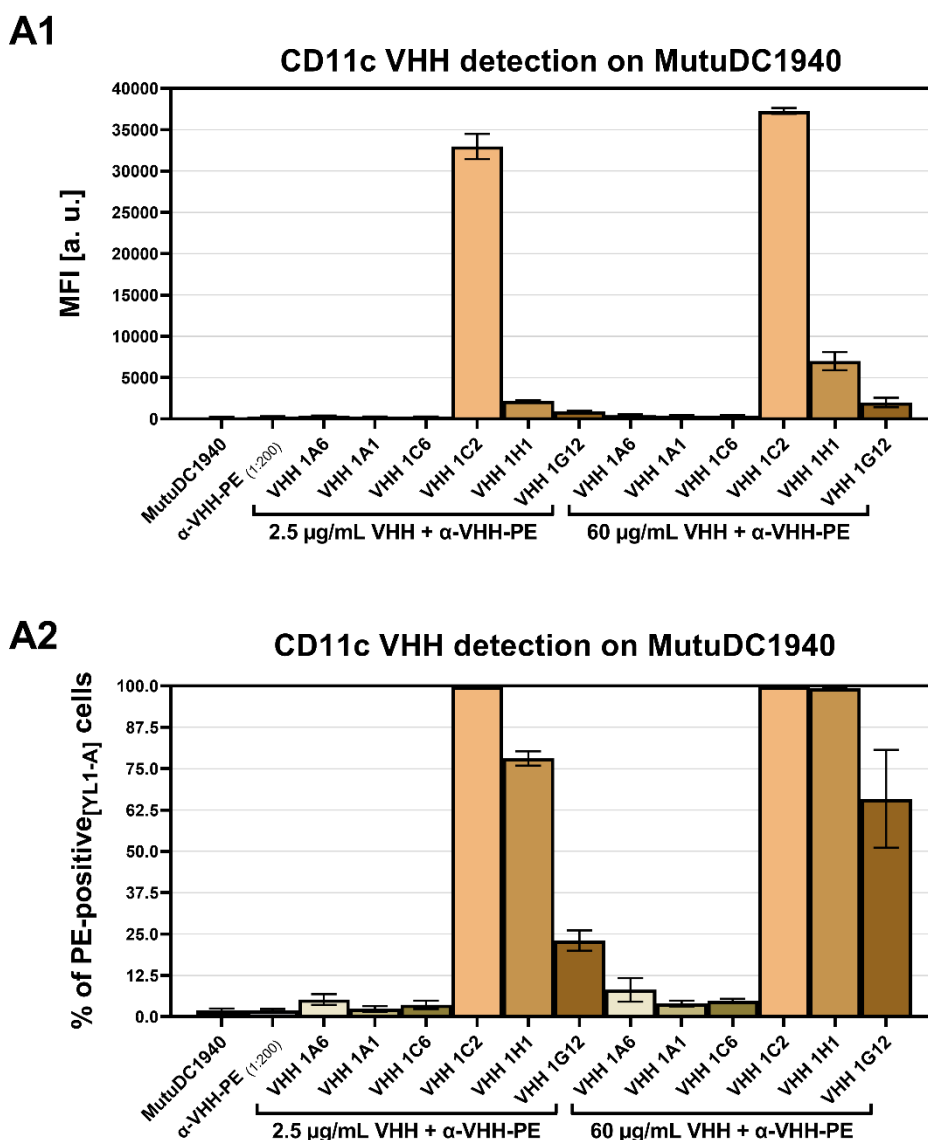


Figure 7.14: CD11c VHH clone detection on MutuDC1940 cells. CD11c binding of six VHH clones (1A6, 1A1, 1C6, 1C2, 1H1, and 1G12) in MutuDC1940 cells (A1 and A2) is analyzed by flow cytometry. For the experiment, 1×10^5 cells were transferred in 100 µL PBS and incubated with the FcR antibody (5 µg/mL) for 15 min at 4 °C. Then, the cells were treated with two concentrations (2.5 and 60 µg/mL) of the VHHs, followed by the incubation with the α-VHH-PE (1:200). Each incubation was performed for 30 min at 4 °C with 2 – 3 centrifugations (500 g for 5 min) in between each step to wash off unbound molecules. In the control group, no VHH was applied. The flow cytometry data is represented as MFI [a.u.] = median fluorescence intensity [arbitrary units] or as the percentage of positive cells. Values are given as mean ± SD (n = 3).

As a result, and in addition to the CD11c VHH clone 1A9, the CD11c antigen binding highlighted three out of the six VHH clones to be the best binders, namely 1C2, 1H1, and 1G12. Again, the CD11c VHH binding showed to be clone and concentration dependent.

In addition, applying the established detection protocol enabled for the selection of the best binders of the remaining CD40 VHH and CLEC9a VHH clones in the MutuDC1940 cell line (Figure 7.15). As a result, five out of the ten CD40 VHHs, namely the clones 4A6, 4A7, 4E1, 4E2, and 4G5, showed a positive cell gating over 80% (Figure 7.15 A), with three out of the five exceeding the MFI of the α -CD40-PE IgG control antibody (Figure 7.15 B). Contrary, the CLEC9A VHH incubation showed very weak binding for each clone compared to the α -CLEC9A-PE IgG control antibody (Figure 7.15 C and D).

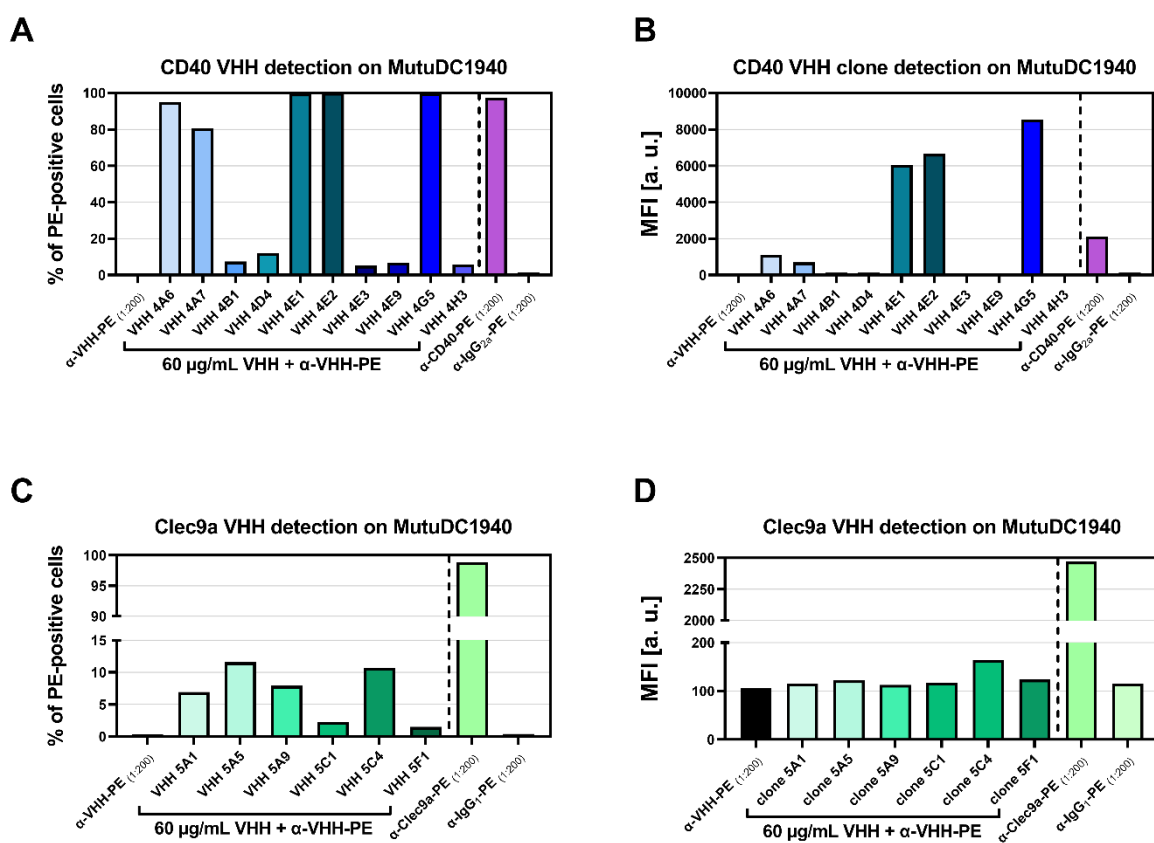


Figure 7.15: CD40 and CLEC9A VHH clone binding on MutuDC1940. The VHH clone binding in MutuDC1940 cells is analyzed by flow cytometry. CD40 VHH (A and B) and CLEC9A VHH clones (C and D) are indicated in the images. As targeting controls, the rat α -mouse CD40-PE, the α -rat IgG_{2a}-PE, the rat α -mouse CLEC9A-PE, and the α -rat IgG₁ were applied (all 1:200). For the experiment, 1×10^5 cells were transferred in 100 μ L PBS and incubated with the FcR antibody (5 μ g/mL) for 15 min at 4 °C. Then, the cells were treated with the VHH clones (60 μ g/mL), followed by the incubation with the α -VHH-PE (1:200). Each incubation was performed for 30 min at 4 °C with 2 – 3 centrifugations (500 g for 5 min) in between each step to wash off unbound molecules. In the control group, no VHH was applied. The flow cytometry data is represented as MFI [a.u.] = median fluorescence intensity [arbitrary units] or as the percentage of positive cells. Values are given as single measurements (raw data by Dr. Michael Fichter).

Therefore, changing the CLEC9A VHH binding protocol by first reacting the VHH with the α -VHH-PE followed by the incubation with the F_c receptor blocked MutuDC1940 cells examined the CLEC9A VHH binding under these settings (Figure 7.16). Unfortunately, this strategy also showed a weak binding, where the CLEC9A VHH clone 5A9 bound the best with around 15 – 30 % positive cells (Figure 7.16 A), and a slightly increased MFI (Figure 7.16 B).

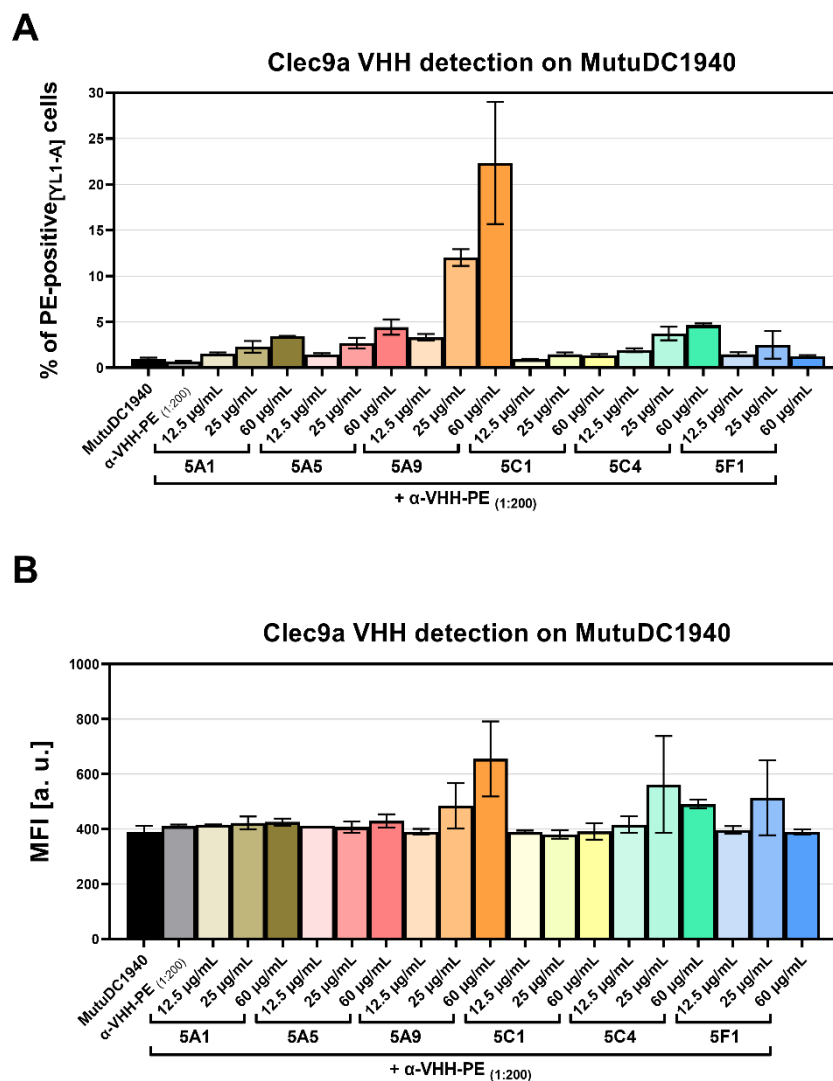


Figure 7.16: CLEC9A VHH clone to α -VHH-PE binding before MutuDC1940 cell incubation. CLEC9A binding of six VHH clones (5A1, 5A5, 5A9, 5C1, 5C4, and 5F1) in MutuDC1940 cells is analyzed by flow cytometry. For the experiment, 1×10^5 cells were transferred in 100 μ L PBS and incubated with the F_cR antibody (5 μ g/mL) for 15 min at 4 $^{\circ}$ C. Then, the cells were treated with three concentrations (12.5, 25, and 60 μ g/mL) of the VHHs, followed by the incubation with the α -VHH-PE (1:200). Each incubation was performed for 30 min at 4 $^{\circ}$ C with 2 – 3 centrifugations (500 g for 5 min) in between each step to wash off unbound molecules. In the control group, no VHH was applied. The flow cytometry data is represented as MFI [a.u.] = median fluorescence intensity [arbitrary units] (A) or as the percentage of positive cells (B). Values are given as mean \pm SD (n = 3).

Based on the investigation on the VHH antigen-binding ability, the results enabled a selection of one to three clones for each antigen (CD11c, CD40, and CLEC9A). Those include the clones 1A9, 1C2, and 1H1 for CD11c, the clones 4E1, 4E2, and 4G5 for CD40, and the clone 5A9 for CLEC9A.

In general, the selection of the VHH clones aimed to reproduce these clones with an additional C-terminal cysteine tag (Cys-tag) for their covalent-attachment onto the nanocarrier surface.

Preparation of VHHs for their covalent immobilization onto the nanocarrier surface

In the next attempt, VHHs required a testing for their covalent nanocarrier surface-immobilization. For this purpose, two additional VHHs carrying the Cys-tag (DC-SIGN VHH and HIV VHH) enabled the examination of their covalent attachment onto the mgHES surface. Namely, the conjugation between maleimide-functionalized mgHES nanocarriers and the thiol group of the VHHs' Cys-tag.

For this purpose, in the first investigation, SDS-PAGE and silver staining visualized the molecular weight of the two VHHs (α -DC-SIGN and α -HIV) (Figure 7.17).

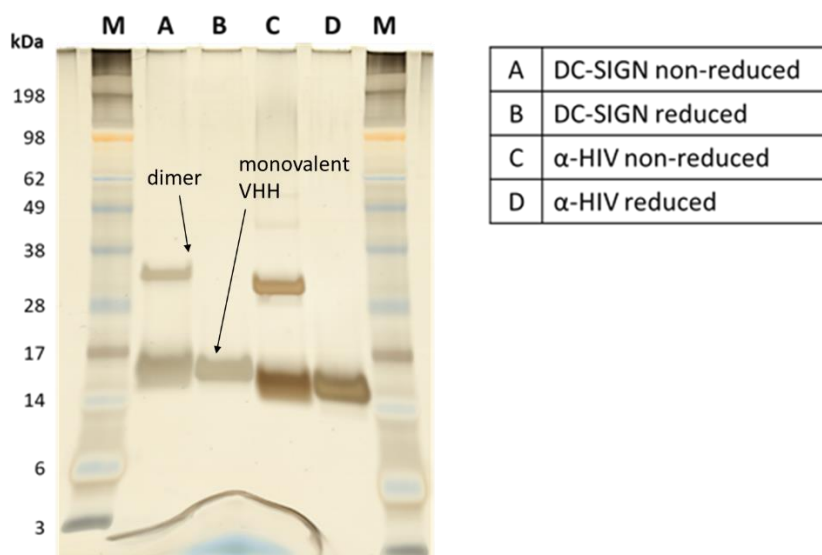


Figure 7.17: Recombinantly expressed nanobodies with Cys-tags form dimers. For the detection of the α -DC-SIGN and α -HIV VHHs, 2 μ g of sample were used for the SDS-PAGE (with or without DTT) and run for 1 h at 120 V. Silver staining was used according to the manufacturer's protocol to visualize the protein bands.

Without a reduction agent, both recombinantly expressed VHHs appeared either as dimers at around 30 kDa that formed via their free Cys-tags or as monomers at around 14 to 17 kDa. Only the native VHH monomers appeared when using a reduction agent. This visualization demonstrated the importance of preventing the formation of disulfide bridges via the free thiol

groups between two VHH monomers when considering their covalent attachment onto the nanocarrier surface. Preferably, all Cys-tags should be freely accessible during the conjugation step. Therefore, validation studies with TCEP as a mild reduction agent and a 5 kDa PEG linker with a maleimide reactive chemistry for the reaction with the free Cys-tag revealed the time and amount for a sufficient VHH thiol-maleimide conjugation (Figure 7.18).

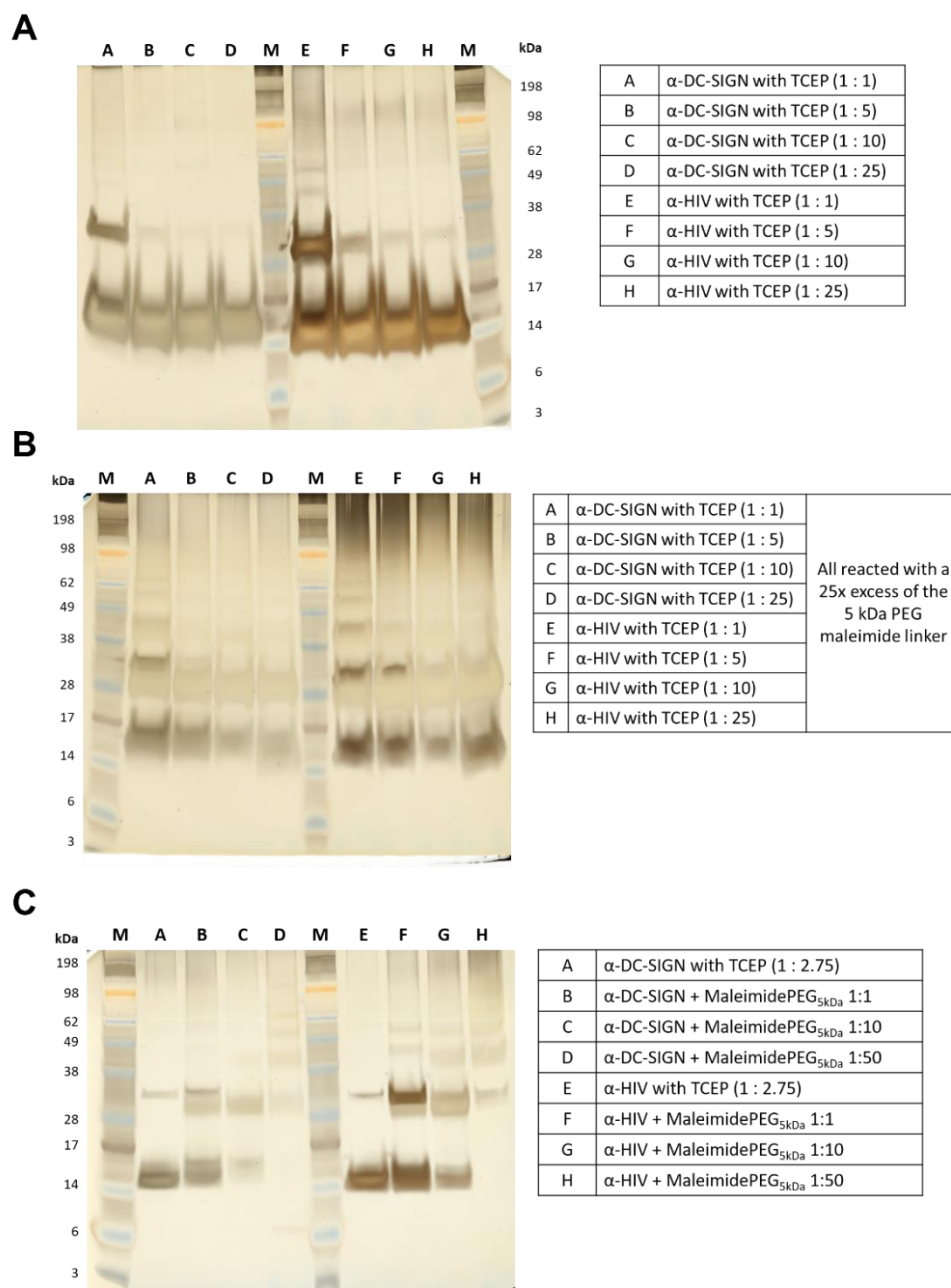


Figure 7.18: TCEP and PEG-maleimide reactions with VHHs. Visualization of VHHs treated with TCEP for the reaction with a 5 kDa PEG-maleimide linker. VHHs reacted with different amounts of TCEP for 1 h (A). VHHs reacted with different amounts of TCEP for 1 h and their subsequent reaction with a 25-molar excess of a 5 kDa PEG-maleimide linker overnight (B). VHHs reacted with a 2.75-molar excess TCEP for 3 h and subsequent reaction with different molar-excess ratios of a 5 kDa PEG-maleimide linker overnight (C). For the SDS-PAGE, 2 μ g of sample were used and run for 1 h at 120 V. Silver staining was used according to the manufacturer's protocol to visualize the protein bands. M = marker.

As a result, low amounts of TCEP to VHH interfered in the dimer formation, where ratios higher than a 10-fold molar excess of TCEP fully prevented the disulfide linkage without any visual traces at 30 kDa on the SDS-PAGE (Figure 7.18 A). In combination with a 5 kDa PEG-maleimide linker, the thiol-maleimide reaction worked with different TCEP and linker ratios (Figure 7.18 B and C).

TCEP has shown to be more compatible in maleimide conjugations compared to, for example, DTT because it does not contain sulfhydryl groups and, therefore, does not necessarily needs removal before the protein thiol-conjugation²⁹⁷. However, certain conditions, like high TCEP concentrations, do interfere with the thiol-maleimide conjugation²⁹⁸.

For this reason, applying a desalting column with a molecular weight cut-off (7 kDa) for TCEP removal before the thiol-maleimide conjugation led to the appearance of an additional lane that formed below the typical 30 kDa VHH dimer band, which potentially represented a VHH-PEG conjugate (Figure 7.19).

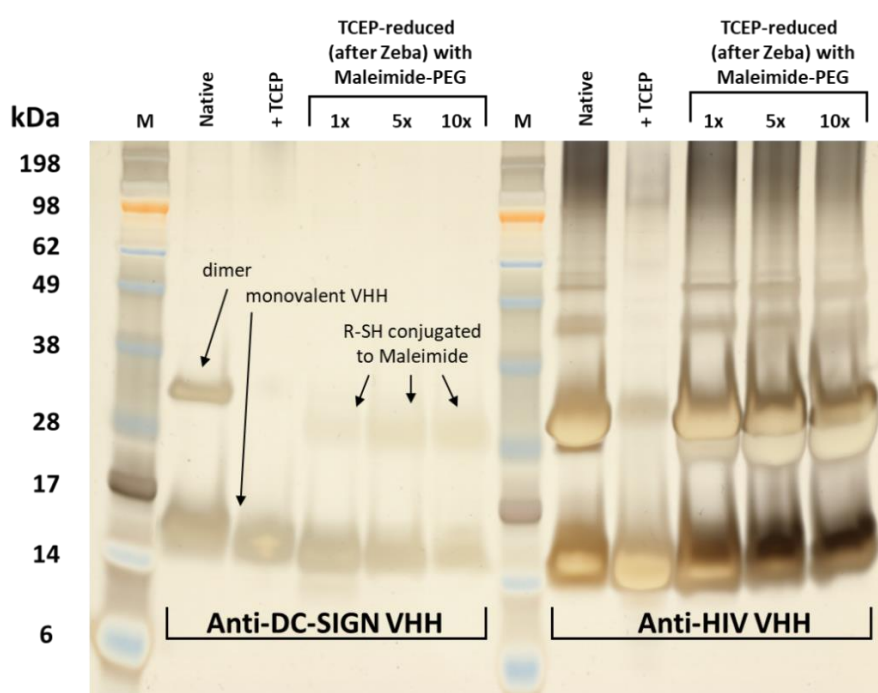


Figure 7.19: Monovalent VHHs conjugate to maleimide-PEG after TCEP removal. Visualization of VHHs reacted with a maleimide-PEG linker. After the 1 h TCEP treatment of the VHHs (100x molar-excess of TCEP) and removal of excess TCEP by a desalting column (7K MWCO Zeba™), the VHHs reacted with three molar-excess ratios (1x, 5x, and 10x) of a 5 kDa PEG-maleimide linker overnight at room temperature. For the SDS-PAGE, 2 µg of sample were used (no use of DTT) and run for 1 h at 120 V. Silver staining was used according to the manufacturer’s protocol to visualize the protein bands. The “Native” bands represent the VHHs without any reduction agent and the “+ TCEP” bands the respective VHH treated with TCEP as described above. R-SH = VHH-thiol, M = marker.

This thiol-maleimide DC-SIGN VHH-PEG conjugate appeared at around 28 kDa and increased in band intensity with higher linker excess, whereas the monovalent DC-SIGN VHH band at

around 15 kDa steadily decreased. The HIV VHH labeling worked less efficiently with a strong background signal and aggregation bands found above 38 kDa.

Despite the labeling-efficiency of the DC-SIGN VHH, antigen-binding experiments in bone marrow-derived dendritic cells (BMDCs) revealed the influence of the TCEP amount on the bioactivity of the VHHs (Figure 7.20).

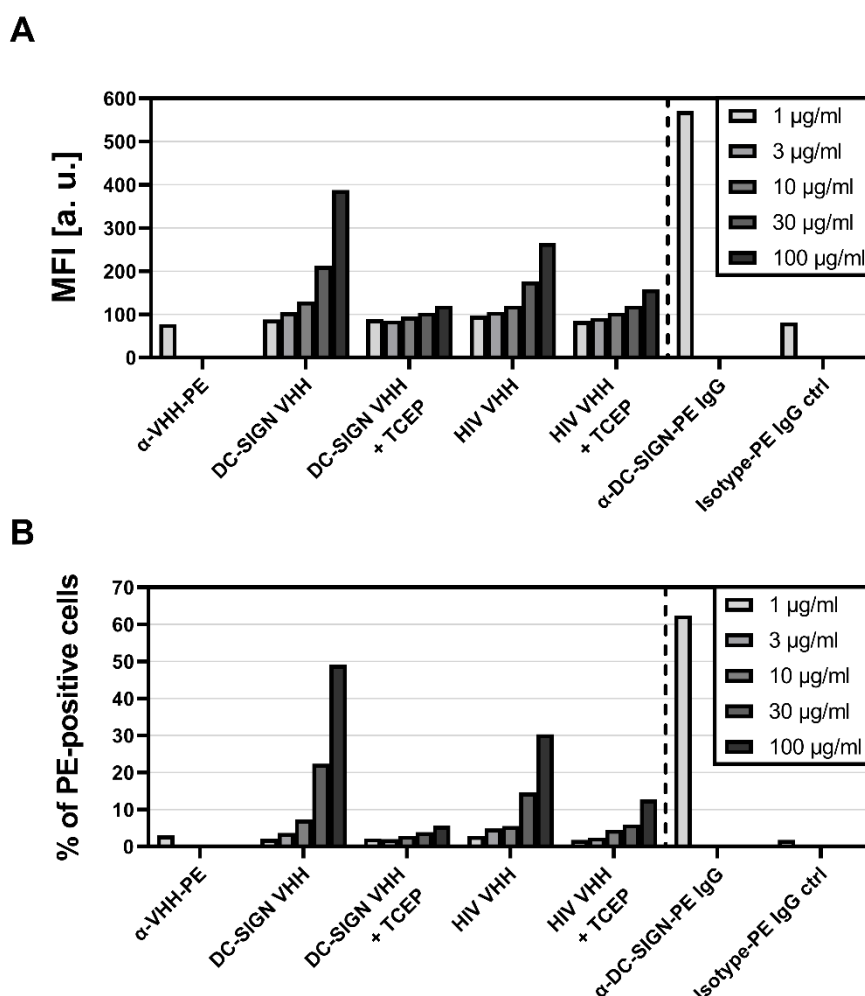


Figure 7.20: TCEP influences the antigen binding ability of VHHs in BMDCs. The BMDC cell uptake analyzed by flow cytometry and represented as MFI [a.u.] = median fluorescence intensity [arbitrary units] (A) or as the percentage of positive cells (B) is shown. BMDCs incubated with different amounts (1, 3, 10, 30, and 100 µg/mL) of native, or TCEP-treated (100-fold molar excess of TCEP to VHH for 1 h) and buffer exchanged DC-SIGN VHHs and HIV VHHs for 30 min at 4 °C. The VHH binding was detected with the α-VHH-PE. The regular α-DC-SIGN-PE IgG and Isotype-PE IgG ctrl (control) were used as a positive control (1 µg/mL). Data sets represent single measurements (raw data by Dr. Michael Fichter).

Both, the MFI (Figure 7.20 A) and the percentage of positive cells (Figure 7.20 B) highlighted that the applied TCEP amount (100-fold molecular excess of TCEP to VHH) drastically abolished the antigen-binding ability of the VHHs compared to the untreated control. Interestingly, Bolli *et al.* used the same amount of TCEP without any influence on their VHHs'

targeting-ability²⁹⁹. These differences in the sensitivity towards TCEP observed in VHHs might correlate to the presence of a second disulfide bond. Next to the canonical disulfide bond, which connects the FR1 and FR3, some VHHs contain a second disulfide bond connecting the CDR3 with the CDR1 (camels), or the CDR2 (llamas)³⁰⁰. This additional disulfide bond provides the VHH with conformational stability required for a proper binding affinity, and a reduced VHH aggregation²⁸⁸. Therefore, a proper amount of reduction agent for the prevention of disulfide dimer-formation must consider a precise testing for each VHH clone without impairing the binding ability of the VHH. For the first conjugation test onto the nanocarrier surface, VHHs treated with a 10-fold molecular excess of TCEP (1 h at RT), followed by removal of excess TCEP, reacted with the previously maleimide-functionalized (150-fold excess of the Sulfo-SMCC) nanocarriers. As a result, validation by flow cytometry using the goat IgG α -VHH-PE proved the presence of the attached VHHs on the nanocarrier surface (Figure 7.21).

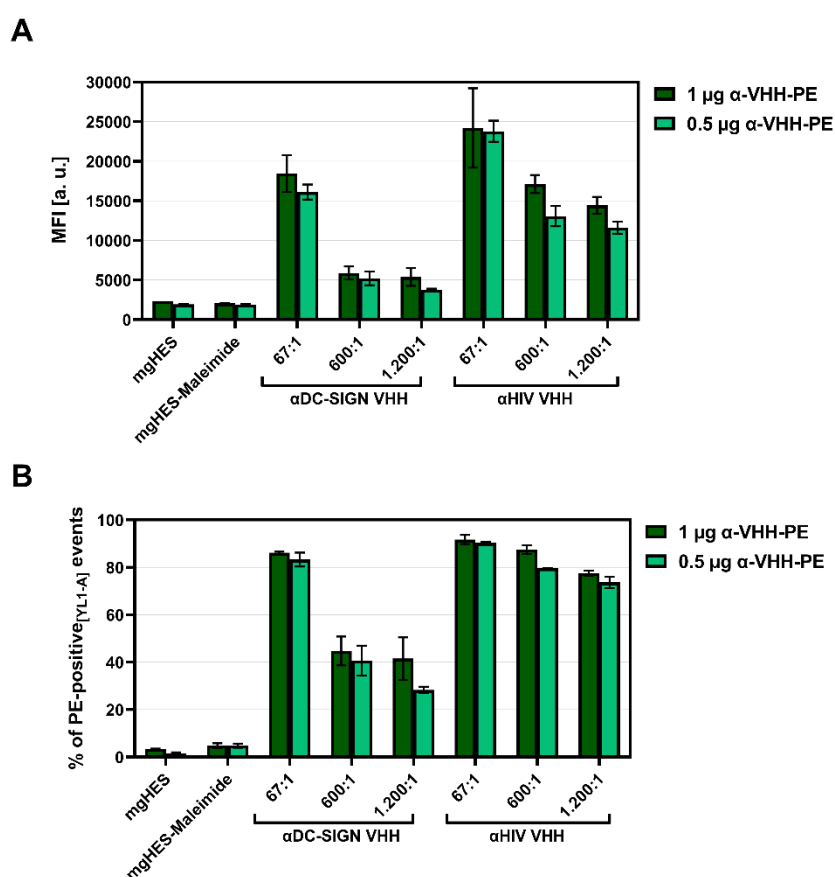


Figure 7.21: Surface-detection of covalently bound VHHs. For the detection, 2 μ g of sample were reacted with 1 μ g and 0.5 μ g of the α -VHH-PE in a total volume of 20 μ L PBS for 30 min at 4 $^{\circ}$ C. After adding 1 mL of PBS, all samples were analyzed by flow cytometry. For each VHH clone, different nanocarrier to VHH ratios were investigated (67:1, 600:1, 1,200:1). The data is represented as MFI [a. u.] = median fluorescence intensity [arbitrary units] (A) or as the percentage of positive cells (B). Values are given as mean \pm SD (n = 2).

Based on the different VHH amounts used for the conjugation (67:1 with 9.60 μg VHH, 600:1 with 1.10 μg of VHH and 1200:1 with 0.54 μg VHH), the α -VHH-PE detected the DC-SIGN VHH and HIV VHH in a concentration dependent manner highlighting different VHH conjugation densities for each group (Figure 7.21 A and B). Furthermore, the two α -VHH-PE amounts (0.5 μg and 1.0 μg) showed almost the same detection values, which lowers the amount necessary for a VHH surface-detection by flow cytometry. Regarding the detection of covalently bound antibodies on the nanocarrier surface, fluorescence correlation spectroscopy (FCS) demonstrates a quantitative approach to analyze the exact number of targeting ligands. For example, FCS determined the average numbers of antibodies on polysarcosine-based peptobrushes³⁰¹, amphiphilic block copolymers³⁰², and polyplexes³⁰³. After the validation of the VHH presence on the nanocarrier surface, the nanocarrier-VHH conjugates incubated with BMDCs at different concentrations to examine the antigen-binding ability (Figure 7.22).

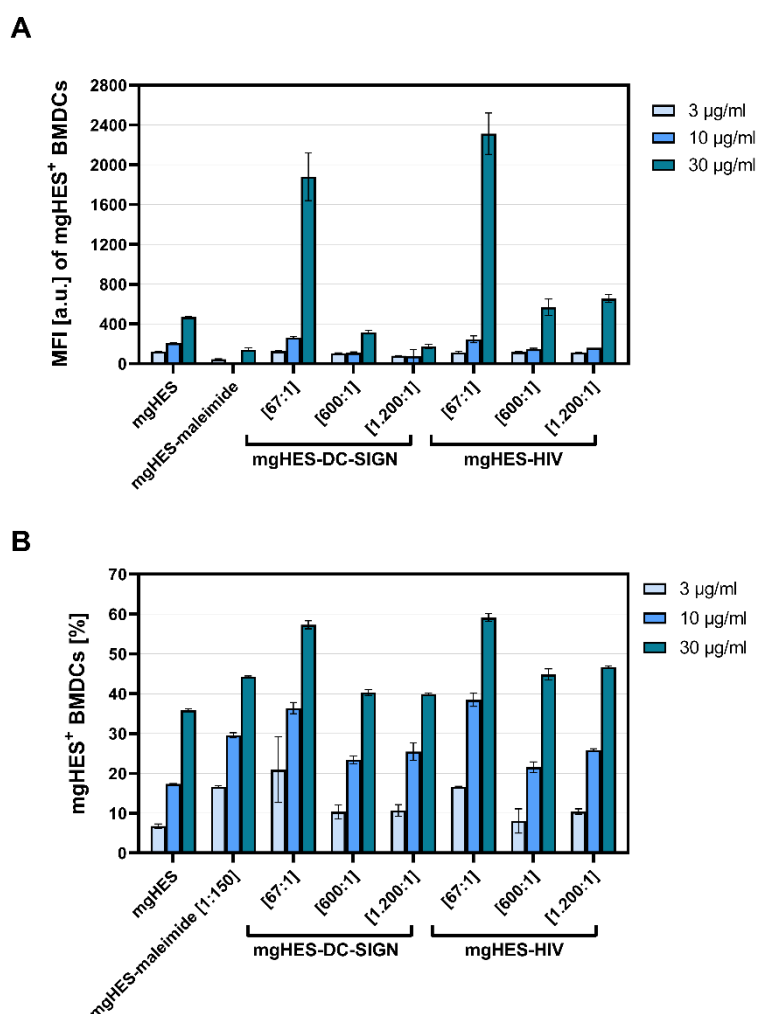


Figure 7.22: Targeting ability of VHH-modified nanocarriers. BMDC uptake of VHH-modified nanocarriers analyzed by flow cytometry and represented as MFI [a.u.] = median fluorescence intensity [arbitrary units] (A) or as the percentage of positive cells (B) is shown. The samples incubated with different amounts (3, 10, and 30 $\mu\text{g/mL}$) for 20 h at 37 $^{\circ}\text{C}$ with the cells. Values are given as mean \pm SD (n = 2) (raw data by Dr. Michael Fichter).

Conjugating the nanocarriers with different amounts of VHHs on the surface showed to influence the binding ability towards the DC-SIGN receptor on BMDCs. The different amounts of VHHs correlated to three nanocarrier to VHH ratios (67:1 with 9.60 μg VHH, 600:1 with 1.10 μg VHH, and 1200:1 with 0.54 μg VHH). In the uptake experiment, only the highest amount of VHH on the mgHES surface (67:1) showed a different uptake compared to the pristine and maleimide-functionalized nanocarrier control groups (Figure 7.22 A and B). This increased uptake demonstrated a strong detection in the MFI (Figure 7.22 A) at a concentration of 30 $\mu\text{g}/\text{mL}$. Therefore, the first examination of VHH-modified nanocarriers with different VHH surface densities highlighted the importance of an exact quantity of VHHs present on the surface to target the cell surface receptor of interest.

Similarly, Van de Broek *et al.* also investigated an optimal concentration to couple their α -HER2 VHHs to branched gold nanoparticles³⁰⁴. They show optimal conjugation conditions between the C-terminal cysteine of the VHHs and the maleimide-functionalized nanoparticles between 1 and 10 μg of VHH/mL. Higher α -HER2 VHH concentrations led to nanoparticle aggregation, although this aggregation depended on the specific VHH, whereby their control VHH (α -PSA) showed a higher concentration tolerance in coupling. In our case, the nanocarrier to VHH ratio 67:1 with 13.71 μg VHH/mL (9.60 μg in 0,7 mL total volume) demonstrated the best nanocarrier uptake in BMDCs, regarding the other two ratios of 600:1 with 1.57 μg VHH/mL and 1200:1 with 0.77 μg VHH/mL.

In another conjugation strategy, Yong *et al.* demonstrate a precise orientation of their VHH onto nanocrystals using a biorthogonal click reaction with a strained cyclooctyne³⁰⁵. For this attempt, they precisely incorporated one azido synthetic amino acid into the VHH structure and clicked it to a DBCO-biotin linker followed by the reaction with the streptavidin-modified nanocrystals. As a result, they present a controlled VHH orientation on the nanoparticle surface, which enables an improved targeting efficiency compared to the controlled immobilization via the C-terminus.

Conclusion and outlook

Despite the beneficial properties that nanotechnology has to offer, clinically-approved applications in the biomedical field of cancer immunotherapy are limited or, in regard to antibody-decoration, completely missing. Accordingly, the current understanding of nanotechnology in the interdisciplinary fields of chemistry, cancer biology, and medicine impairs a successful translation into the market. For this reason, the presented work focuses on antibody-modified nanocarriers and their ability to maintain a desired dendritic cell targeting-functionality under physiological conditions and in a living organism.

In general, the present study addresses three major topics concerned about the use of nanotechnology applied as transport vehicles in the biomedical field of cancer immunotherapy. In this regard, unbiased preliminary studies on the interaction of nanocarriers and blood proteins forming the biomolecular corona are of great importance to reflect physiological conditions to enable a proper *in vitro* to *in vivo* translation (**chapter A**). Furthermore, improving the targeting property of nanocarriers with antibodies requires a sophisticated conjugation strategy to ensure an oriented immobilization of the antibody molecule on the surface. A proper antibody orientation results in an addressed cargo delivery to the desired cells of interest without an undesired uptake both *in vitro* and *in vivo* (**chapter B**). In addition, the prospective development of such nanocarriers as transport vehicles with antibody derivatives that exhibit lower structural complexity is necessary to improve the targeted and controlled cellular interactions (**chapter C**).

In **chapter A**, we demonstrate that the choice of washing media has a direct impact on the hard protein corona composition of several nanocarrier systems as shown by SDS-PAGE and LC-MS. Additionally, via the nanoDSF we found that the washing media has a significant impact on the protein stability and thus on the interaction with the nanocarrier. In our cell uptake experiments, we verified a strong effect of the chosen media, especially, pure H₂O when used as the washing media. This selection of a particular washing media influences the interaction with HeLa and RAW 264.7 cells. In summary, our data highlights that the choice of media is a crucial factor, which needs consideration in the evaluation of the possible key players in the protein corona that might be involved in recognition or shielding from targeted cells. Moreover, the washing diversity underlines the urgent need for standardized protein corona protocols. For this reason, we want to take a first step and recommend a washing media that covers the physiological conditions of a biological fluid as far as possible to not interfere with the native structure and functionality of the adsorbed proteins. Therefore, we suggest using the buffer solution PBS⁻, which enables protein handling at a constant pH with an osmotic pressure comparable to that found inside the human body³⁰⁶.

In **chapter B**, subchapter 4 shows that copper-free click chemistry generated nanocarrier conjugates surpass the efficacy of thiol-maleimide chemistry produced conjugates. This comparison proves that the enzymatic modification of CD11c antibodies is specific with modified antibodies carrying up to four azido groups. In contrast, the Traut's modification is highly unspecific and modifies unwanted antibody regions, such as the light chain or N-terminus. Evaluating the targeting specificity of nanocarriers with different amounts of conjugated CD11c antibodies *in vitro* highlighted a limit up to which a specific uptake by dendritic cells is evoked. Especially, blocking experiments have emphasized the importance of a site-directed conjugation chemistry, which considers the spatial orientation of the attached antibody on the nanocarriers' surface. Additionally, targeting experiments with mouse plasma prove that the biomolecular corona does not impair the binding efficiency of antibody-modified nanocarriers towards dendritic cells. These properties underline the great potential of the here presented copper-free click generated antibody nanocarriers, which need a further validation of their targeting functionality under *in vivo* conditions.

In addition to subchapter 4, the follow-up study in subchapter 5 demonstrates to extent the targeting from CD11c to other dendritic cell-targeting antibodies. Each antibody successfully conjugates to magnetic nanocarriers in a site-specific and orientated manner. The biomolecular corona that formed onto the nanocarriers after intravenous injection did not prevent binding of the antibodies towards the cell surface receptors on CD11c⁺ dendritic cells *in vitro* and *in vivo*. CD11c and CLEC9A antibodies proved to be excellent candidates for dendritic cell targeting, while anti-CLEC9A exhibited a specific targeting towards cDC1 and plasmacytoid DCs, representing the cells of interest for vaccination approaches. The proteomic analysis revealed major differences in the composition of the protein corona formed during *in vitro* incubation and *in vivo* circulation explaining the great discrepancies of successful *in vitro* and failing *in vivo* studies in terms of antibody-mediated nanocarrier targeting. To overcome this problem, we developed an *ex vivo* approach using whole blood, which allowed us to mimic the protein corona formed *in vivo*. In conclusion, this study demonstrates how to prove the targeting specificity *in vivo*, which can be transferred to a broad range of nanocarriers and antibodies. Thereby, this novel conjugation technique paves the way for the development of antibody-functionalized nanocarriers for dendritic cell-based vaccination approaches in the field of cancer immunotherapy.

In the final investigation of chapter B, the subchapter 6 provides additional investigations on the developed antibody-nanocarrier conjugation strategy by comparing different molecular weight heterobifunctional PEG linkers for the spacing of the antibody to the nanocarrier surface. This spacing determines the flexibility of the attached antibody and directly influences the targeting ability of the nanocarrier. Accordingly, our findings highlighted differences

between a dendritic cell line and primary dendritic cell subsets with regard to the influence of PEG linker lengths upon the antibody-based targeting ability of nanocarriers. In particular, the CD11c-based DC2.4 targeting proved to be most efficient when using the shortest linker (0.65 kDa PEG), whereas a distinct subset-specific cDC1 targeting in primary cells required a longer linker (5 kDa PEG). This discrepancy most likely gives an explanation to the misinterpretation of *in vitro* data generated with dendritic cell lines and subsequently leading to unexpected *in vivo* findings. Thereby, the herein presented study demonstrates that a successful targeting strategy, especially for DC-based subset targeting, requires a coordinated interplay of the nanocarrier, the targeting ligand, and the spacer molecule.

Ultimately, the subchapter 7 in **chapter C** sheds light on antibody derivatives as alternatives to whole antibodies investigated in the previous chapters. In particular, the work presents the generation of antibody fragments from whole antibodies using an enzymatic approach combined with the reduction of disulfide bonds by cysteamine. Thereby, we specifically provide a fragmentation protocol for the rat IgG₁ isotype into the F_{(ab)₂} and F_{ab'} fragments. Nevertheless, experiments on additional purification methods, such as size-exclusion chromatography, need to ensure a full separation from the desired fragment and the undesired F_c region. Once purified, the F_{(ab)₂} and F_{ab'} fragments require a special focus on their covalent-conjugation onto the nanocarrier surface, namely the mild reduction of disulfide bonds forming free thiols for the subsequent reaction with the maleimide-functionalized nanocarriers. In addition, our study on nanobodies demonstrates how to validate a proper nanobody binding to the target of interest enabling a sufficient clone selection. Furthermore, we provide a conjugation strategy to immobilize nanobodies onto the nanocarrier surface and highlight the influence on the reduction agent (TCEP) influencing the biological nanobody activity. In our first testing, we proofed the presence of covalently bound nanobodies on the nanocarrier surface and observed an influence on the nanobody amount leading to an increased uptake in BMDCs for the highest nanobody quantity. In conclusion, a comparative study needs to demonstrate which antibody format and quantity on the nanocarrier surface shows the best targeting ability. This targeting ability of the chosen ligand must be highly specific towards the cell surface-receptor of interest without an undesired uptake in off-target cells and must withstand the influence of the biomolecular corona, especially under the *in vivo* situation.

Future work in the field of surface-modification of nanocarriers with antibodies and derivatives needs to focus on the creation of a multifunctional and biocompatible system. Accordingly, an effective nanocarrier system must protect its cargo until the delivery and release to the cells of interest without an accumulation in off-target compartments. Therefore, the nanocarrier-decoration requires a proper amount of targeting ligands and stealth polymers or dysopsonin proteins enabling a dendritic cell subset-specific targeting and disguising at the same time.

References

1. J. A. Shadish and C. A. DeForest, *Matter*, 2020, 2, 50-77.
2. D. A. Richards, A. Maruani and V. Chudasama, *Chemical Science*, 2017, 8, 63-77.
3. A. Juan, F. J. Cimas, I. Bravo, A. Pandiella, A. Ocaña and C. Alonso-Moreno, *Pharmaceutics*, 2020, 12, 802.
4. M. Arruebo, M. Valladares and Á. González-Fernández, *Journal of Nanomaterials*, 2009, 2009.
5. Z. Yang, Y. Ma, H. Zhao, Y. Yuan and B. Y. Kim, *Wiley Interdisciplinary Reviews: Nanomedicine and Nanobiotechnology*, 2020, 12, e1590.
6. M. S. Singh and S. Bhaskar, *Immunotargets Ther*, 2014, 3, 121-134.
7. X. Feng, W. Xu, Z. Li, W. Song, J. Ding and X. Chen, *Advanced science*, 2019, 6, 1900101.
8. A. Rotte, *Journal of Experimental & Clinical Cancer Research*, 2019, 38, 1-12.
9. C. Fitzmaurice, C. Allen, R. M. Barber, L. Barregard, Z. A. Bhutta, H. Brenner, D. J. Dicker, O. Chimed-Orchir, R. Dandona and L. Dandona, *JAMA oncology*, 2017, 3, 524-548.
10. G. D'Errico, H. L. Machado and B. Sainz, *Clinical and translational medicine*, 2017, 6, 1-10.
11. Z. Jiang, J. Guan, J. Qian and C. Zhan, *Biomaterials science*, 2019, 7, 461-471.
12. T. Boon, J.-C. Cerottini, B. Van den Eynde, P. van der Bruggen and A. Van Pel, *Annual review of immunology*, 1994, 12, 337-365.
13. N. Thakur, S. Thakur, S. Chatterjee, J. Das and P. C. Sil, *Frontiers in Chemistry*, 2020, 8, 1217.
14. T. Tian, S. Olson, J. M. Whitacre and A. Harding, *Integrative Biology*, 2011, 3, 17-30.
15. S. Musetti and L. Huang, *ACS nano*, 2018, 12, 11740-11755.
16. C. L. Ventola, *Pharmacy and therapeutics*, 2017, 42, 375.
17. F. S. Hodi, S. J. O'Day, D. F. McDermott, R. W. Weber, J. A. Sosman, J. B. Haanen, R. Gonzalez, C. Robert, D. Schadendorf, J. C. Hassel, W. Akerley, A. J. van den Eertwegh, J. Lutzky, P. Lorigan, J. M. Vaubel, G. P. Linette, D. Hogg, C. H. Ottensmeier, C. Lebbé, C. Peschel, I. Quirt, J. I. Clark, J. D. Wolchok, J. S. Weber, J. Tian, M. J. Yellin, G. M. Nichol, A. Hoos and W. J. Urba, *N Engl J Med*, 2010, 363, 711-723.
18. G. Kroemer and L. Zitvogel, *Nature Reviews Immunology*, 2018, 18, 87-88.
19. G. Q. Phan, J. C. Yang, R. M. Sherry, P. Hwu, S. L. Topalian, D. J. Schwartzentruber, N. P. Restifo, L. R. Haworth, C. A. Seipp and L. J. Freezer, *Proceedings of the National Academy of Sciences*, 2003, 100, 8372-8377.
20. D. H. Munn and V. Bronte, *Current opinion in immunology*, 2016, 39, 1-6.
21. M. A. Buabeid, E.-S. A. Arafa and G. Murtaza, *Journal of immunology research*, 2020, 2020.
22. S. Logothetidis, in *Nanomedicine and Nanobiotechnology*, Springer, 2012, pp. 1-26.
23. R. Bayford, T. Rademacher, I. Roitt and S. X. Wang, *Physiological measurement*, 2017, 38, R183.

References

24. S. Behzadi, V. Serpooshan, W. Tao, M. A. Hamaly, M. Y. Alkawareek, E. C. Dreaden, D. Brown, A. M. Alkilany, O. C. Farokhzad and M. Mahmoudi, *Chemical Society Reviews*, 2017, 46, 4218-4244.
25. A. N. Papadopoulos, D. N. Bikiaris, A. C. Mitropoulos and G. Z. Kyzas, *Nanomaterials*, 2019, 9, 607.
26. M. J. Mitchell, M. M. Billingsley, R. M. Haley, M. E. Wechsler, N. A. Peppas and R. Langer, *Nature Reviews Drug Discovery*, 2021, 20, 101-124.
27. L. Y. Rizzo, B. Theek, G. Storm, F. Kiessling and T. Lammers, *Current opinion in biotechnology*, 2013, 24, 1159-1166.
28. Y. Matsumura and H. Maeda, *Cancer research*, 1986, 46, 6387-6392.
29. M. A. Subhan, S. S. K. Yalamarty, N. Filipczak, F. Parveen and V. P. Torchilin, *Journal of Personalized Medicine*, 2021, 11, 571.
30. S. Wilhelm, A. J. Tavares, Q. Dai, S. Ohta, J. Audet, H. F. Dvorak and W. C. Chan, *Nature reviews materials*, 2016, 1, 1-12.
31. H. Ledford, *Nature News*, 2016, 533, 304.
32. M. Mahmoudi, *Trends in biotechnology*, 2018, 36, 755-769.
33. A. Salvati, A. S. Pitek, M. P. Monopoli, K. Prapainop, F. B. Bombelli, D. R. Hristov, P. M. Kelly, C. Åberg, E. Mahon and K. A. Dawson, *Nature nanotechnology*, 2013, 8, 137-143.
34. A. Cifuentes-Rius, H. de Puig, J. C. Y. Kah, S. Borros and K. Hamad-Schifferli, *ACS nano*, 2013, 7, 10066-10074.
35. M. P. Monopoli, C. Åberg, A. Salvati and K. A. Dawson, *Nature nanotechnology*, 2012, 7, 779-786.
36. Z. J. Deng, M. Liang, M. Monteiro, I. Toth and R. F. Minchin, *Nature nanotechnology*, 2011, 6, 39-44.
37. M. Mahmoudi, S. E. Lohse, C. J. Murphy, A. Fathizadeh, A. Montazeri and K. S. Suslick, *Nano letters*, 2014, 14, 6-12.
38. M. Hadjidemetriou and K. Kostarelos, *Nature nanotechnology*, 2017, 12, 288-290.
39. Q. Dai, Y. Yan, J. Guo, M. Björnmalm, J. Cui, H. Sun and F. Caruso, *ACS Macro Letters*, 2015, 4, 1259-1263.
40. G. Berrecoso, J. Crecente-Campo and M. J. Alonso, *Drug delivery and translational research*, 2020, 10, 730-750.
41. L. Vroman, A. Adams, G. Fischer and P. Munoz, 1980.
42. E. Casals, T. Pfaller, A. Duschl, G. J. Oostingh and V. Puntès, *ACS nano*, 2010, 4, 3623-3632.
43. S. Tenzer, D. Docter, J. Kuharev, A. Musyanovych, V. Fetz, R. Hecht, F. Schlenk, D. Fischer, K. Kiouptsi and C. Reinhardt, in *Nano-Enabled Medical Applications*, Jenny Stanford Publishing, 2020, pp. 251-278.
44. S. Tenzer, D. Docter, J. Kuharev, A. Musyanovych, V. Fetz, R. Hecht, F. Schlenk, D. Fischer, K. Kiouptsi and C. Reinhardt, *Nature nanotechnology*, 2013, 8, 772-781.

References

45. O. Vilanova, J. J. Mittag, P. M. Kelly, S. Milani, K. A. Dawson, J. O. Rädler and G. Franzese, *ACS nano*, 2016, 10, 10842-10850.
46. H. Wang, Y. Lin, K. Nienhaus and G. U. Nienhaus, *Wiley Interdisciplinary Reviews: Nanomedicine and Nanobiotechnology*, 2018, 10, e1500.
47. C. von Roemeling, W. Jiang, C. K. Chan, I. L. Weissman and B. Y. Kim, *Trends in biotechnology*, 2017, 35, 159-171.
48. Z. J. Deng, M. Liang, I. Toth, M. J. Monteiro and R. F. Minchin, *ACS nano*, 2012, 6, 8962-8969.
49. B. Halamoda-Kenzaoui and S. Bremer-Hoffmann, *International journal of nanomedicine*, 2018, 13, 5419.
50. M. M. Frank and L. F. Fries, *Immunology today*, 1991, 12, 322-326.
51. E. Papini, R. Tavano and F. Mancin, *Frontiers in Immunology*, 2020, 11, 2343.
52. R. Cai and C. Chen, *Advanced Materials*, 2019, 31, 1805740.
53. L. K. Müller, J. Simon, C. Rosenauer, V. Mailänder, S. Morsbach and K. Landfester, *Biomacromolecules*, 2018, 19, 374-385.
54. S. Schöttler, K. Klein, K. Landfester and V. Mailänder, *Nanoscale*, 2016, 8, 5526-5536.
55. M. Kokkinopoulou, J. Simon, K. Landfester, V. Mailänder and I. Lieberwirth, *Nanoscale*, 2017, 9, 8858-8870.
56. C. Weber, S. Morsbach and K. Landfester, *Angewandte Chemie International Edition*, 2019, 58, 12787-12794.
57. Z. Hu, L. Zhao, H. Zhang, Y. Zhang, R. a. Wu and H. Zou, *Journal of Chromatography A*, 2014, 1334, 55-63.
58. Y. V. Karpievitch, A. D. Polpitiya, G. A. Anderson, R. D. Smith and A. R. Dabney, *The annals of applied statistics*, 2010, 4, 1797.
59. H. R. Kim, K. Andrieux, C. Delomenie, H. Chacun, M. Appel, D. Desmaële, F. Taran, D. Georgin, P. Couvreur and M. Taverna, *Electrophoresis*, 2007, 28, 2252-2261.
60. O. Vilanova, J. J. Mittag, P. M. Kelly, S. Milani, K. A. Dawson, J. O. Radler and G. Franzese, *ACS Nano*, 2016, 10, 10842-10850.
61. S. Zanganeh, R. Spitler, M. Erfanzadeh, A. M. Alkilany and M. Mahmoudi, *Int J Biochem Cell Biol*, 2016, 75, 143-147.
62. P. Foroozandeh and A. A. Aziz, *Nanoscale Res Lett*, 2015, 10, 221.
63. J. Wolfram, Y. Yang, J. Shen, A. Moten, C. Chen, H. Shen, M. Ferrari and Y. Zhao, *Colloids Surf B Biointerfaces*, 2014, 124, 17-24.
64. C. D. Walkey, J. B. Olsen, H. Guo, A. Emili and W. C. Chan, *J Am Chem Soc*, 2012, 134, 2139-2147.
65. Q. Feng, Y. Liu, J. Huang, K. Chen, J. Huang and K. Xiao, *Sci Rep*, 2018, 8, 2082.
66. S. Schöttler, K. Klein, K. Landfester and V. Mailänder, *Nanoscale*, 2016, 8, 5526-5536.
67. J. Simon, J. Muller, A. Ghazaryan, S. Morsbach, V. Mailänder and K. Landfester, *Nanoscale*, 2018, 10, 21096-21105.

References

68. K. Strojan, A. Leonardi, V. B. Bregar, I. Krizaj, J. Svete and M. Pavlin, *PLoS One*, 2017, 12, e0169552.
69. C. Weber, J. Simon, V. Mailänder, S. Morsbach and K. Landfester, *Acta biomaterialia*, 2018, 76, 217-224.
70. D. Walczyk, F. B. Bombelli, M. P. Monopoli, I. Lynch and K. A. Dawson, *Journal of the American Chemical Society*, 2010, 132, 5761-5768.
71. M. Lundqvist, J. Stigler, T. Cedervall, T. Berggard, M. B. Flanagan, I. Lynch, G. Elia and K. Dawson, *ACS Nano*, 2011, 5, 7503-7509.
72. M. Lundqvist, C. Augustsson, M. Lilja, K. Lundqvist, B. Dahlback, S. Linse and T. Cedervall, *PLoS One*, 2017, 12, e0175871.
73. G. Caracciolo, S. Palchetti, V. Colapicchioni, L. Digiaco, D. Pozzi, A. L. Capriotti, G. La Barbera and A. Lagana, *Langmuir*, 2015, 31, 10764-10773.
74. M. Hadjidemetriou, Z. Al-Ahmady, M. Mazza, R. F. Collins, K. Dawson and K. Kostarelos, *ACS Nano*, 2015, 9, 8142-8156.
75. J. Saikia, M. Yazdimamaghani, S. P. Hadipour Moghaddam and H. Ghandehari, *ACS Appl Mater Interfaces*, 2016, 8, 34820-34832.
76. L. Treuel, S. Brandholt, P. Maffre, S. Wiegele, L. Shang and G. U. Nienhaus, *ACS Nano*, 2014, 8, 503-513.
77. S. Palchetti, L. Digiaco, D. Pozzi, G. Peruzzi, E. Micarelli, M. Mahmoudi and G. Caracciolo, *Nanoscale*, 2016, 8, 12755-12763.
78. A. S. Pitek, A. M. Wen, S. Shukla and N. F. Steinmetz, *Small*, 2016, 12, 1758-1769.
79. N. V. Konduru, R. M. Molina, A. Swami, F. Damiani, G. Pyrgiotakis, P. Lin, P. Andreozzi, T. C. Donaghey, P. Demokritou, S. Krol, W. Kreyling and J. D. Brain, *Part Fibre Toxicol*, 2017, 14, 42.
80. A. Abdelkhalik, M. van der Zande, A. Punt, R. Helsdingen, S. Boeren, J. J. M. Vervoort, I. Rietjens and H. Bouwmeester, *J Nanobiotechnology*, 2018, 16, 70.
81. K. Landfester, *Annu. Rev. Mater. Res.*, 2006, 36, 231-279.
82. I. García-Moreno, A. Costela, L. Campo, R. Sastre, F. Amat-Guerri, M. Liras, F. López Arbeloa, J. Bañuelos Prieto and I. López Arbeloa, *The Journal of Physical Chemistry A*, 2004, 108, 3315-3323.
83. S. Jiang, L. Lv, Q. Li, J. Wang, K. Landfester and D. Crespy, *Nanoscale*, 2016, 8, 11511-11517.
84. S. Tenzer, D. Docter, S. Rosfa, A. Wlodarski, J. r. Kuharev, A. Rekić, S. K. Knauer, C. Bantz, T. Nawroth and C. Bier, *ACS nano*, 2011, 5, 7155-7167.
85. D. Hofmann, S. Tenzer, M. B. Bannwarth, C. Messerschmidt, S.-F. Glaser, H. r. Schild, K. Landfester and V. Mailänder, *Acs Nano*, 2014, 8, 10077-10088.
86. R. A. Bradshaw, A. L. Burlingame, S. Carr and R. Aebersold, *Molecular & Cellular Proteomics*, 2006, 5, 787-788.
87. J. C. Silva, M. V. Gorenstein, G.-Z. Li, J. P. Vissers and S. J. Geromanos, *Molecular & Cellular Proteomics*, 2006, 5, 144-156.
88. K. Hodge, S. T. Have, L. Hutton and A. I. Lamond, *J Proteomics*, 2013, 88, 92-103.

References

89. Z. J. Deng, G. Mortimer, T. Schiller, A. Musumeci, D. Martin and R. F. Minchin, *Nanotechnology*, 2009, 20, 455101.
90. K. Oikonomopoulou, D. Ricklin, P. A. Ward and J. D. Lambris, *Semin Immunopathol*, 2012, 34, 151-165.
91. H. Brunel, R. Massanet, A. Martinez-Perez, A. Ziyatdinov, L. Martin-Fernandez, J. C. Souto, A. Perera and J. M. Soria, *PLoS One*, 2016, 11, e0167187.
92. U. Sakulkhu, M. Mahmoudi, L. Maurizi, J. Salaklang and H. Hofmann, *Sci Rep*, 2014, 4, 5020.
93. J. Xu, J. Fang, Z. Cheng, L. Fan, W. Hu, F. Zhou and H. Shen, *Journal of Experimental & Clinical Cancer Research*, 2018, 37, 180.
94. F. Chen, G. Wang, J. I. Griffin, B. Brenneman, N. K. Banda, V. M. Holers, D. S. Backos, L. Wu, S. M. Moghimi and D. Simberg, *Nat Nanotechnol*, 2017, 12, 387-393.
95. M. Kokkinopoulou, J. Simon, K. Landfester, V. Mailander and I. Lieberwirth, *Nanoscale*, 2017, 9, 8858-8870.
96. S. Schottler, K. Landfester and V. Mailander, *Angew Chem Int Ed Engl*, 2016, 55, 8806-8815.
97. F. Rosso, G. Marino, A. Grimaldi, G. Cafiero, E. Chiellini, F. Chiellini, M. Barbarisi and A. Barbarisi, *Biomed Res Int*, 2013, 2013, 539348.
98. C. Fedeli, D. Segat, R. Tavano, L. Bubacco, G. De Franceschi, P. P. de Laureto, E. Lubian, F. Selvestrel, F. Mancin and E. Papini, *Nanoscale*, 2015, 7, 17710-17728.
99. S. B. Gunnarsson, K. Bernfur, U. Englund-Johansson, F. Johansson and T. Cedervall, *PLoS One*, 2019, 14, e0218211.
100. S. B. Gunnarsson, K. Bernfur, A. Mikkelsen and T. Cedervall, *Nanoscale*, 2018, 10, 4246-4257.
101. A. Gonzalez-Quintela, R. Alende, F. Gude, J. Campos, J. Rey, L. M. Meijide, C. Fernandez-Merino and C. Vidal, *Clin Exp Immunol*, 2008, 151, 42-50.
102. M. Leeman, J. Choi, S. Hansson, M. U. Storm and L. Nilsson, *Anal Bioanal Chem*, 2018, 410, 4867-4873.
103. R. Chaudhuri, Y. Cheng, C. R. Middaugh and D. B. Volkin, *AAPS J*, 2014, 16, 48-64.
104. W. Strutz, *Exploring Protein Stability by NanoDSF*, 2016.
105. A. Gardner, Á. de Mingo Pulido and B. Ruffell, *Frontiers in Immunology*, 2020, 11, 924.
106. D. S. Chen and I. Mellman, *immunity*, 2013, 39, 1-10.
107. L. E. Paulis, S. Mandal, M. Kreutz and C. G. Figdor, *Current opinion in immunology*, 2013, 25, 389-395.
108. J. Banchereau and R. M. Steinman, *Nature*, 1998, 392, 245-252.
109. I. Mellman and R. M. Steinman, *Cell*, 2001, 106, 255-258.
110. T. H. Tran, T. T. P. Tran, H. T. Nguyen, C. Dai Phung, J.-H. Jeong, M. H. Stenzel, S. G. Jin, C. S. Yong, D. H. Truong and J. O. Kim, *International journal of pharmaceuticals*, 2018, 542, 253-265.
111. K. Palucka and J. Banchereau, *Nature Reviews Cancer*, 2012, 12, 265-277.

References

112. R. Bastola and S. Lee, *Journal of Pharmaceutical Investigation*, 2019, 49, 279-285.
113. V. Manolova, A. Flace, M. Bauer, K. Schwarz, P. Saudan and M. F. Bachmann, *European journal of immunology*, 2008, 38, 1404-1413.
114. I. Mellman, *Cancer immunology research*, 2013, 1, 145-149.
115. K. Lundberg, F. Rydnert, L. Greiff and M. Lindstedt, *Immunology*, 2014, 142, 279-288.
116. A. M. Dudek, S. Martin, A. D. Garg and P. Agostinis, *Frontiers in immunology*, 2013, 4, 438.
117. A. Cifuentes-Rius, A. Desai, D. Yuen, A. P. Johnston and N. H. Voelcker, *Nature Nanotechnology*, 2021, 16, 37-46.
118. S. Eisenbarth, *Nature Reviews Immunology*, 2019, 19, 89-103.
119. F. Veglia and D. I. Gabrilovich, *Current opinion in immunology*, 2017, 45, 43-51.
120. Y. Jung, J. Y. Jeong and B. H. Chung, *Analyst*, 2008, 133, 697-701.
121. A. Kausaite-Minkstimiene, A. Ramanaviciene, J. Kirlyte and A. Ramanavicius, *Analytical chemistry*, 2010, 82, 6401-6408.
122. A. D Friedman, S. E Claypool and R. Liu, *Current pharmaceutical design*, 2013, 19, 6315-6329.
123. M. E. Wiseman and C. W. Frank, *Langmuir*, 2012, 28, 1765-1774.
124. D. Bartczak and A. G. Kanaras, *Langmuir*, 2011, 27, 10119-10123.
125. Q. Zhang, L. Rui-Xue, C. Xin, H. Xing-Xing, H. Ai-Ling, F. Guo-Zhen, L. Ji-Feng and W. Shuo, *Chinese Journal of Analytical Chemistry*, 2017, 45, 662-667.
126. C. Parolo, A. de la Escosura-Muñiz, E. Polo, V. Grazú, J. M. De La Fuente and A. Merkoçi, *ACS applied materials & interfaces*, 2013, 5, 10753-10759.
127. S. Panowski, S. Bhakta, H. Raab, P. Polakis and J. R. Junutula, 2014.
128. S.-W. Chou, Y.-H. Shau, P.-C. Wu, Y.-S. Yang, D.-B. Shieh and C.-C. Chen, *Journal of the American Chemical Society*, 2010, 132, 13270-13278.
129. T. T.-H. Pham and S. J. Sim, *Journal of Nanoparticle Research*, 2010, 12, 227-235.
130. J.-M. Montenegro, V. Grazu, A. Sukhanova, S. Agarwal, M. Jesus, I. Nabiev, A. Greiner and W. J. Parak, *Advanced drug delivery reviews*, 2013, 65, 677-688.
131. R. Rezaeipoor, R. John, S. G. Adie, E. J. Chaney, M. Marjanovic, A. L. Oldenburg, S. A. Rinne and S. A. Boppart, *Journal of innovative optical health sciences*, 2009, 2, 387-396.
132. E. Polo, S. Puertas, M. Moros, P. Batalla, J. M. Guisán, M. Jesús and V. Grazú, in *Immobilization of Enzymes and Cells*, Springer, 2013, pp. 149-163.
133. X. Lin, A. O. R. Beringhs and X. Lu, *The AAPS Journal*, 2021, 23, 1-16.
134. A. M. Scott, J. D. Wolchok and L. J. Old, *Nature reviews cancer*, 2012, 12, 278-287.
135. M. L. Chiu, D. R. Goulet, A. Teplyakov and G. L. Gilliland, *Antibodies*, 2019, 8, 55.
136. H. W. Schroeder Jr and L. Cavacini, *Journal of Allergy and Clinical Immunology*, 2010, 125, S41-S52.

References

137. J. Xue, L.-P. Zhu and Q. Wei, *Glycoconjugate journal*, 2013, 30, 735-745.
138. M. Daëron, in *Fc Receptors*, eds. M. Daëron and F. Nimmerjahn, Springer International Publishing, Cham, 2014, DOI: 10.1007/978-3-319-07911-0_7, pp. 131-164.
139. A. Sadiki, S. R. Vaidya, M. Abdollahi, G. Bhardwaj, M. E. Dolan, H. Turna, V. Arora, A. Sanjeev, T. D. Robinson and A. Koid, *Antibody therapeutics*, 2020, 3, 271-284.
140. Q. Luo, H. H. Chung, C. Borths, M. Janson, J. Wen, M. K. Joubert and J. Wypych, *Analytical chemistry*, 2016, 88, 695-702.
141. N. K. Lee, C.-P. J. Wang, J. Lim, W. Park, H.-K. Kwon, S.-N. Kim, T.-H. Kim and C. G. Park, *Nano convergence*, 2021, 8, 1-11.
142. A. Sadiki, E. M. Kercher, H. Lu, R. T. Lang, B. Q. Spring and Z. S. Zhou, *Photochemistry and photobiology*, 2020, 96, 596-603.
143. C. Pellegrino, N. Favalli, M. Sandholzer, L. Volta, G. Bassi, J. Millul, S. Cazzamalli, M. Matasci, A. Villa and R. Myburgh, *Bioconjugate Chemistry*, 2020, 31, 1775-1783.
144. A. Juan, F. J. Cimas, I. Bravo, A. Pandiella, A. Ocaña and C. Alonso-Moreno, *International Journal of Molecular Sciences*, 2020, 21, 6018.
145. H. C. Kolb, M. Finn and K. B. Sharpless, *Angewandte Chemie International Edition*, 2001, 40, 2004-2021.
146. C. D. Hein, X.-M. Liu and D. Wang, *Pharmaceutical research*, 2008, 25, 2216-2230.
147. A. Marques, P. Costa, S. Velho and M. Amaral, *Journal of Controlled Release*, 2020, 320, 180-200.
148. Z. Cheng, A. Al Zaki, J. Z. Hui, V. R. Muzykantov and A. Tsourkas, *Science*, 2012, 338, 903-910.
149. J. M. Montenegro, V. Grazu, A. Sukhanova, S. Agarwal, J. M. de la Fuente, I. Nabiev, A. Greiner and W. J. Parak, *Adv Drug Deliv Rev*, 2013, 65, 677-688.
150. E. Polo, S. Puertas, M. Moros, P. Batalla, J. M. Guisan, J. M. de la Fuente and V. Grazu, *Methods Mol Biol*, 2013, 1051, 149-163.
151. A. J. Sivaram, A. Wardiana, C. B. Howard, S. M. Mahler and K. J. Thurecht, *Advanced healthcare materials*, 2018, 7, 1700607.
152. S. Puertas, M. Moros, R. Pacheco, M. R Ibarra, V. Grazu and J. Fuente, *J. Phys. D: Appl. Phys.*, 2010, *J. Phys. D: Appl. Phys.*, 474012.
153. J. M. Silva, M. Videira, R. Gaspar, V. Preat and H. F. Florindo, *J Control Release*, 2013, 168, 179-199.
154. M. Diwan, P. Elamanchili, H. Lane, A. Gainer and J. Samuel, *Journal of Drug Targeting*, 2003, 11, 495-507.
155. R. V. Chari, *Acc Chem Res*, 2008, 41, 98-107.
156. K. Tsuchikama and Z. An, *Protein & cell*, 2018, 9, 33-46.
157. J. Xue, L. P. Zhu and Q. Wei, *Glycoconj J*, 2013, 30, 735-745.
158. F. Higel, A. Seidl, F. Sörgel and W. Friess, *European Journal of Pharmaceutics and Biopharmaceutics*, 2016, 100, 94-100.

References

159. E. Boeggeman, B. Ramakrishnan, M. Pasek, M. Manzoni, A. Puri, K. H. Loomis, T. J. Waybright and P. K. Qasba, *Bioconjugate chemistry*, 2009, 20, 1228-1236.
160. B. Ramakrishnan and P. K. Qasba, *Journal of Biological Chemistry*, 2002, 277, 20833-20839.
161. G. Chaubet, F. Thoreau and A. Wagner, *Drug Discovery Today: Technologies*, 2018, 30, 21-26.
162. J. Wu, H. Wu, J. An, C. M. Ballantyne and J. G. Cyster, *Proceedings of the National Academy of Sciences*, 2018, 115, 6786-6791.
163. H. Matsuo, M. Somiya, M. Iijima, T. Arakawa and S. i. Kuroda, *Journal of Nanobiotechnology*, 2018, 16, 59.
164. M. P. Monopoli, C. Aberg, A. Salvati and K. A. Dawson, *Nat Nanotechnol*, 2012, 7, 779-786.
165. M. Colombo, L. Fiandra, G. Alessio, S. Mazzucchelli, M. Nebuloni, C. De Palma, K. Kantner, B. Pelaz, R. Rotem and F. Corsi, *Nature communications*, 2016, 7, 1-14.
166. B. Saha, T. H. Evers and M. W. Prins, *Analytical chemistry*, 2014, 86, 8158-8166.
167. N. A. Byzova, I. V. Safenkova, E. S. Slutskaya, A. V. Zherdev and B. B. Dzantiev, *Bioconjugate chemistry*, 2017, 28, 2737-2746.
168. D. Pozzi, G. Caracciolo, A. L. Capriotti, C. Cavaliere, G. La Barbera, T. J. Anchordoquy and A. Lagana, *J Proteomics*, 2015, 119, 209-217.
169. H. de Puig, I. Bosch, M. Carré-Camps and K. Hamad-Schifferli, *Bioconjugate chemistry*, 2017, 28, 230-238.
170. M. Tonigold, J. Simon, D. Estupiñán, M. Kokkinopoulou, J. Reinholz, U. Kintzel, A. Kaltbeitzel, P. Renz, M. P. Domogalla, K. Steinbrink, I. Lieberwirth, D. Crespy, K. Landfester and V. Mailänder, *Nature Nanotechnology*, 2018, 13, 862-869.
171. B. D. Chithrani, A. A. Ghazani and W. C. Chan, *Nano Lett*, 2006, 6, 662-668.
172. M. P. Desai, V. Labhasetwar, E. Walter, R. J. Levy and G. L. Amidon, *Pharm Res*, 1997, 14, 1568-1573.
173. D. Guarnieri, A. Guaccio, S. Fusco and P. A. Netti, *Journal of Nanoparticle Research*, 2011, 13, 4295.
174. A. Solorio-Rodriguez, V. Escamilla-Rivera, M. Uribe-Ramirez, A. Chagolla, R. Winkler, C. M. Garcia-Cuellar and A. De Vizcaya-Ruiz, *Nanoscale*, 2017, 9, 13651-13660.
175. L. Shen, S. Tenzer, W. Storck, D. Hobernik, V. K. Raker, K. Fischer, S. Decker, A. Dzionek, S. Krauthauser, M. Diken, A. Nikolaev, J. Maxeiner, P. Schuster, C. Kappel, A. Verschoor, H. Schild, S. Grabbe and M. Bros, *J Allergy Clin Immunol*, 2018, 142, 1558-1570.
176. D. Rosenblum, N. Joshi, W. Tao, J. M. Karp and D. Peer, *Nature communications*, 2018, 9, 1-12.
177. U. Sahin, A. Muik, E. Derhovanessian, I. Vogler, L. M. Kranz, M. Vormehr, A. Baum, K. Pascal, J. Quandt, D. Maurus, S. Brachtendorf, V. Lorks, J. Sikorski, R. Hilker, D. Becker, A. K. Eller, J. Grutzner, C. Boesler, C. Rosenbaum, M. C. Kuhnle, U. Luxemburger, A. Kemmer-Bruck, D. Langer, M. Bexon, S. Bolte, K. Kariko, T. Palanche, B. Fischer, A. Schultz, P. Y. Shi, C. Fontes-Garfias, J. L. Perez, K. A. Swanson, J. Loschko, I. L. Scully, M. Cutler, W. Kalina, C. A. Kyratsous, D. Cooper, P. R. Dormitzer, K. U. Jansen and O. Tureci, *Nature*, 2020, 586, 594-599.
178. Y. H. Chung, V. Beiss, S. N. Fiering and N. F. Steinmetz, *Acs Nano*, 2020, 14, 12522-12537.

References

179. L. A. Jackson, E. J. Anderson, N. G. Rouphael, P. C. Roberts, M. Makhene, R. N. Coler, M. P. McCullough, J. D. Chappell, M. R. Denison, L. J. Stevens, A. J. Pruijssers, A. McDermott, B. Flach, N. A. Doria-Rose, K. S. Corbett, K. M. Morabito, S. O'Dell, S. D. Schmidt, P. A. Swanson, 2nd, M. Padilla, J. R. Mascola, K. M. Neuzil, H. Bennett, W. Sun, E. Peters, M. Makowski, J. Albert, K. Cross, W. Buchanan, R. Pikaart-Tautges, J. E. Ledgerwood, B. S. Graham, J. H. Beigel and R. N. A. S. G. m, *N Engl J Med*, 2020, 383, 1920-1931.
180. E. J. Anderson, N. G. Rouphael, A. T. Widge, L. A. Jackson, P. C. Roberts, M. Makhene, J. D. Chappell, M. R. Denison, L. J. Stevens, A. J. Pruijssers, A. B. McDermott, B. Flach, B. C. Lin, N. A. Doria-Rose, S. O'Dell, S. D. Schmidt, K. S. Corbett, P. A. Swanson, M. Padilla, K. M. Neuzil, H. Bennett, B. Leav, M. Makowski, J. Albert, K. Cross, V. V. Edara, K. Floyd, M. S. Suthar, D. R. Martinez, R. Baric, W. Buchanan, C. J. Luke, V. K. Phadke, C. A. Rostad, J. E. Ledgerwood, B. S. Graham, J. H. Beigel and m.-S. Grp, *New Engl J Med*, 2020, 383, 2427-2438.
181. R. V. Chari, *Accounts of chemical research*, 2008, 41, 98-107.
182. E. L. Sievers and P. D. Senter, *Annual review of medicine*, 2013, 64, 15-29.
183. M. M Cardoso, I. N Peca and A. CA Roque, *Current medicinal chemistry*, 2012, 19, 3103-3127.
184. Y. Barenholz, *Handb. Harnessing Biomater. Nanomed*, 2012, 335-398.
185. Y. C. Barenholz, *Journal of controlled release*, 2012, 160, 117-134.
186. M. K. Yu, J. Park and S. Jon, *Theranostics*, 2012, 2, 3.
187. V. J. Yao, S. D'Angelo, K. S. Butler, C. Theron, T. L. Smith, S. Marchiò, J. G. Gelovani, R. L. Sidman, A. S. Dobroff and C. J. Brinker, *Journal of Controlled Release*, 2016, 240, 267-286.
188. I. Caminschi, A. I. Proietto, F. Ahmet, S. Kitsoulis, J. Shin Teh, J. C. Lo, A. Rizzitelli, L. Wu, D. Vremec, S. L. van Dommelen, I. K. Campbell, E. Maraskovsky, H. Braley, G. M. Davey, P. Mottram, N. van de Velde, K. Jensen, A. M. Lew, M. D. Wright, W. R. Heath, K. Shortman and M. H. Lahoud, *Blood*, 2008, 112, 3264-3273.
189. L. J. Cruz, P. J. Tacke, R. Fokkink, B. Joosten, M. C. Stuart, F. Albericio, R. Torensma and C. G. Figdor, *J Control Release*, 2010, 144, 118-126.
190. P. J. Tacke, I. J. M. de Vries, K. Gijzen, B. Joosten, D. Y. Wu, R. P. Rother, S. J. Faas, C. J. A. Punt, R. Torensma, G. J. Adema and C. G. Figdor, *Blood*, 2005, 106, 1278-1285.
191. A. Kretz-Rommel, F. Qin, N. Dakappagari, R. Torensma, S. Faas, D. Wu and K. S. Bowdish, *J Immunother*, 2007, 30, 715-726.
192. D. V. Haute and J. M. Berlin, *Therapeutic delivery*, 2017, 8, 763-774.
193. V. J. Venditto and F. C. Szoka Jr, *Advanced drug delivery reviews*, 2013, 65, 80-88.
194. A. Pietrzak-Nguyen, M. Fichter, M. Dedters, L. Pretsch, S. H. Gregory, C. Meyer, A. Doganci, M. Diken, K. Landfester, G. Baier and S. Gehring, *Biomacromolecules*, 2014, 15, 2378-2388.
195. Y. J. Kwon, E. James, N. Shastri and J. M. J. Frechet, *P Natl Acad Sci USA*, 2005, 102, 18264-18268.
196. S. O. Stead, S. Kireta, S. J. P. McInnes, F. D. Kette, K. N. Sivanathan, J. Kim, E. J. Cueto-Diaz, F. Cunin, J. O. Durand, C. J. Drogemuller, R. P. Carroll, N. H. Voelcker and P. T. Coates, *Acs Nano*, 2018, 12, 6637-6647.
197. Q. Dai, N. Bertleff-Zieschang, J. A. Braunger, M. Björnmalm, C. Cortez-Jugo and F. Caruso, *Adv. Healthc. Mater.*, 2017.

References

198. A. Salvati, A. S. Pitek, M. P. Monopoli, K. Prapainop, F. B. Bombelli, D. R. Hristov, P. M. Kelly, C. Åberg, E. Mahon and K. A. Dawson, *Nature nanotechnology*, 2013, 8, 137.
199. M. Bros, L. Nuhn, J. Simon, L. Moll, V. Mailänder, K. Landfester and S. Grabbe, *Frontiers in immunology*, 2018, 9, 1760.
200. M. Brückner, J. Simon, K. Landfester and V. Mailänder, *Nanoscale*, 2021, 13, 9816-9824.
201. K. Immig, M. Gericke, F. Menzel, F. Merz, M. Krueger, F. Schiefenhövel, A. Lösche, K. Jäger, U. K. Hanisch and K. Biber, *Glia*, 2015, 63, 611-625.
202. S. A. Shu, Z. X. Lian, Y. H. Chuang, G. X. Yang, Y. Moritoki, S. Comstock, R. Q. Zhong, A. Ansari, Y. J. Liu and M. E. Gershwin, *Clinical & Experimental Immunology*, 2007, 149, 335-343.
203. M. B. Dong, M. J. Rahman and K. V. Tarbell, *Journal of immunological methods*, 2016, 432, 4-12.
204. C. M. Le Gall, J. Weiden, L. J. Eggermont and C. G. Figdor, *Nature materials*, 2018, 17, 474-475.
205. K. F. Bol, G. Schreibelt, K. Rabold, S. K. Wculek, J. K. Schwarze, A. Dzionek, A. Teijeira, L. E. Kandalaf, P. Romero and G. Coukos, *Journal for immunotherapy of cancer*, 2019, 7, 109.
206. A. B. Zaneti, M. M. Yamamoto, F. B. Sulczewski, B. d. S. Almeida, H. F. S. Souza, N. S. Ferreira, D. L. N. F. Maeda, N. S. Sales, D. S. Rosa and L. C. d. S. Ferreira, *Frontiers in immunology*, 2019, 10, 59.
207. C. Grüttner, K. Müller, J. Teller, F. Westphal, A. Foreman and R. Ivkov, *Journal of Magnetism and Magnetic Materials*, 2007, 311, 181-186.
208. A. Natarajan, C. Gruettner, R. Ivkov, G. DeNardo, G. Mirick, A. Yuan, A. Foreman and S. DeNardo, *Bioconjugate chemistry*, 2008, 19, 1211-1218.
209. D. Paßlick, K. Piradashvili, D. Bamberger, M. Li, S. Jiang, D. Strand, P. R. Wich, K. Landfester, M. Bros and S. Grabbe, *Journal of Controlled Release*, 2018, 289, 23-34.
210. S. Gehring, E. M. Dickson, M. E. San Martin, N. Van Rooijen, E. F. Papa, M. W. Harty, T. F. Tracy JR and S. H. Gregory, *Gastroenterology*, 2006, 130, 810-822.
211. M. Fichter, G. Baier, M. Dedters, L. Pretsch, A. Pietrzak-Nguyen, K. Landfester and S. Gehring, *Nanomedicine: Nanotechnology, Biology and Medicine*, 2013, 9, 1223-1234.
212. D. Hofmann, S. Tenzer, M. B. Bannwarth, C. Messerschmidt, S.-F. Glaser, H. Schild, K. Landfester and V. Mailänder, *ACS Nano*, 2014, 8, 10077-10088.
213. S. Tenzer, *ACS Nano*, 2011, 5, 7155-7167.
214. A. Bernardin, A. Cazet, L. Guyon, P. Delannoy, F. Vinet, D. Bonnaffé and I. Texier, *Bioconjugate chemistry*, 2010, 21, 583-588.
215. N. J. Agard, J. A. Prescher and C. R. Bertozzi, *Journal of the American Chemical Society*, 2004, 126, 15046-15047.
216. L. Li and Z. Zhang, *Molecules*, 2016, 21, 1393.
217. S. K. Wculek, F. J. Cueto, A. M. Mujal, I. Melero, M. F. Krummel and D. Sancho, *Nat Rev Immunol*, 2020, 20, 7-24.

References

218. M. Tonigold, J. Simon, D. Estupiñán, M. Kokkinopoulou, J. Reinholz, U. Kintzel, A. Kaltbeitzel, P. Renz, M. P. Domogalla, K. Steinbrink, I. Lieberwirth, D. Crespy, K. Landfester and V. Mailänder, *Nature Nanotechnology*, 2018, DOI: 10.1038/s41565-018-0171-6, 1.
219. Q. Dai, N. Bertleff-Zieschang, J. A. Braunger, M. Björnmalm, C. Cortez-Jugo and F. Caruso, *Advanced healthcare materials*, 2017.
220. J. Simon, G. Kuhn, M. Fichter, S. Gehring, K. Landfester and V. Mailander, *Cells-Basel*, 2021, 10.
221. U. Sakulkhu, L. Maurizi, M. Mahmoudi, M. Motazacker, M. Vries, A. Gramoun, M. G. O. Beuzelin, J. P. Vallee, F. Rezaee and H. Hofmann, *Nanoscale*, 2014, 6, 11439-11450.
222. N. Singh, C. Marets, J. Boudon, N. Millot, L. Saviot and L. Maurizi, *Nanoscale Adv.*, 2021, DOI: 10.1039/d0na00863j, 1209.
223. L. G. Rico, J. Juncà, M. D. Ward, J. A. Bradford, J. Bardina and J. Petriz, *Scientific reports*, 2018, 8, 1-8.
224. I. I. Slowing, C. W. Wu, J. L. Vivero-Escoto and V. S. Y. Lin, *Small*, 2009, 5, 57-62.
225. L. Q. Chen, L. Fang, J. Ling, C. Z. Ding, B. Kang and C. Z. Huang, *Chemical research in toxicology*, 2015, 28, 501-509.
226. C. Sunderkötter, T. Nikolic, M. J. Dillon, N. Van Rooijen, M. Stehling, D. A. Drevets and P. J. Leenen, *The Journal of Immunology*, 2004, 172, 4410-4417.
227. M. Fichter, K. Piradashvili, A. Pietrzak-Nguyen, L. Pretsch, G. Kuhn, S. Strand, M. Knuf, F. Zepp, F. R. Wurm, V. Mailander, K. Landfester and S. Gehring, *Biomaterials*, 2016, 108, 1-12.
228. S. Jiang, D. Prozeller, J. Pereira, J. Simon, S. Han, S. Wirsching, M. Fichter, M. Mottola, I. Lieberwirth, S. Morsbach, V. Mailander, S. Gehring, D. Crespy and K. Landfester, *Nanoscale*, 2020, 12, 2626-2637.
229. Y.-N. Zhang, W. Poon, A. J. Tavares, I. D. McGilvray and W. C. Chan, *Journal of controlled release*, 2016, 240, 332-348.
230. S. M. Moghimi, A. C. Hunter and J. C. Murray, *Pharmacological reviews*, 2001, 53, 283-318.
231. F. Veglia and D. I. Gabrilovich, *Curr Opin Immunol*, 2017, 45, 43-51.
232. L. Shen, S. Krauthauser, K. Fischer, D. Hobernik, Y. Abassi, A. Dzionek, A. Nikolaev, N. Voltz, M. Diken, M. Krummen, E. Montermann, I. Tubbe, S. Lorenz, D. Strand, H. Schild, S. Grabbe and M. Bros, *Nanomedicine (Lond)*, 2016, 11, 2647-2662.
233. J. A. Katakowski, G. Mukherjee, S. E. Wilner, K. E. Maier, M. T. Harrison, T. P. DiLorenzo, M. Levy and D. Palliser, *Mol Ther*, 2016, 24, 146-155.
234. E. Fossum, D. Y. Tesfaye, S. Bobic, A. Gudjonsson, R. Braathen, M. H. Lahoud, I. Caminschi and B. Bogen, *J Immunol*, 2020, 205, 661-673.
235. R. Ghinnagow, J. De Meester, L. J. Cruz, C. Aspord, S. Cognac, E. Macho-Fernandez, D. Souldard, J. Fontaine, L. Chaperot, J. Charles, F. Soncin, F. Mami-Chouaib, J. Plumas, C. Faveeuw and F. Trottein, *Oncoimmunology*, 2017, 6, e1339855.
236. P. Y. Lam, T. Kobayashi, M. Soon, B. Zeng, R. Dolcetti, G. Leggatt, R. Thomas and S. R. Mattarollo, *Cancer Immunol Res*, 2019, 7, 952-962.
237. H. Parra-Sanchez, L. Puebla-Clark, M. Resendiz, O. Valenzuela and J. Hernandez, *Mol Immunol*, 2018, 96, 1-7.

References

238. H. Parra-Sanchez, L. Bustamante-Cordova, M. Resendiz, V. Mata-Haro, A. Pinelli-Saavedra and J. Hernandez, *Viruses*, 2019, 11.
239. H. He, L. Liu, E. E. Morin, M. Liu and A. Schwendeman, *Accounts of chemical research*, 2019, 52, 2445-2461.
240. C. Horejs, *Nature Reviews Materials*, 2021, 6, 1075-1076.
241. A. N. Ilinskaya and M. A. Dobrovolskaia, *Toxicology and applied pharmacology*, 2016, 299, 70-77.
242. A. Vonarbourg, C. Passirani, P. Saulnier and J.-P. Benoit, *Biomaterials*, 2006, 27, 4356-4373.
243. S. Y. Fam, C. F. Chee, C. Y. Yong, K. L. Ho, A. R. Mariatulqabtiah and W. S. Tan, *Nanomaterials*, 2020, 10, 787.
244. J. S. Suk, Q. Xu, N. Kim, J. Hanes and L. M. Ensign, *Advanced drug delivery reviews*, 2016, 99, 28-51.
245. S. Schöttler, G. Becker, S. Winzen, T. Steinbach, K. Mohr, K. Landfester, V. Mailänder and F. R. Wurm, *Nature nanotechnology*, 2016, 11, 372-377.
246. G. Kozma, T. Shimizu, T. Ishida and J. Szebeni, *Advanced Drug Delivery Reviews*, 2020.
247. A. C. Anselmo and S. Mitragotri, *Bioengineering & translational medicine*, 2019, 4, e10143.
248. R. Dolcetti, A. López-Soto and J. Dal Col, *Frontiers in immunology*, 2020, 11, 507.
249. J. Calmeiro, M. A. Carrascal, A. R. Tavares, D. A. Ferreira, C. Gomes, A. Falcão, M. T. Cruz and B. M. Neves, *Pharmaceutics*, 2020, 12, 158.
250. M. Collin and V. Bigley, *Immunology*, 2018, 154, 3-20.
251. J. Simon, M. Fichter, G. Kuhn, M. Brückner, C. Kappel, J. Schunke, T. Klaus, S. Grabbe, K. Landfester and V. Mailänder, *Nano Today*, 2022, 43, 101375.
252. M. C. Johnston and C. J. Scott, *Drug Discovery Today: Technologies*, 2018, 30, 63-69.
253. J. F. Stefanick, J. D. Ashley, T. Kiziltepe and B. Bilgicer, *ACS nano*, 2013, 7, 2935-2947.
254. H. S. Jeong, K. Sook Na, H. Hwang, P. S. Oh, D. Hyun Kim, S. Tae Lim, M. H. Sohn and H. J. Jeong, *Journal of biomedical materials research Part A*, 2014, 102, 4545-4553.
255. L. J. Cruz, P. J. Tacke, R. Fokink and C. G. Figdor, *Biomaterials*, 2011, 32, 6791-6803.
256. C. H. Kapadia, S. Tian, J. L. Perry, J. C. Luft and J. M. DeSimone, *ACS omega*, 2019, 4, 5547-5555.
257. S. Tenzer, D. Docter, S. Rosfa, A. Wlodarski, J. Kuharev, A. Rekić, S. K. Knauer, C. Bantz, T. Nawroth, C. Bier, J. Sirirattanapan, W. Mann, L. Treuel, R. Zellner, M. Maskos, H. Schild and R. H. Stauber, *ACS Nano*, 2011, 5, 7155-7167.
258. R. A. Bradshaw, A. L. Burlingame, S. Carr and R. Aebersold, *Molecular & Cellular Proteomics*, 2006, 5, 787-788.
259. M. Bros, E. Montermann, A. Cholaszczyńska and A. B. Reske-Kunz, *International immunopharmacology*, 2016, 35, 174-184.
260. D. Passlick, K. Piradashvili, D. Bamberger, M. Li, S. Jiang, D. Strand, R. W. P. K. Landfester, M. Bros, S. Grabbe and V. Mailänder, *J Control Release*, 2018, 289, 23-34.

References

261. G. Caracciolo, S. Palchetti, V. Colapicchioni, L. Digiaco, D. Pozzi, A. L. Capriotti, G. La Barbera and A. Laganà, *Langmuir*, 2015, 31, 10764-10773.
262. M. Li, S. Jiang, J. Simon, D. Paßlick, M.-L. Frey, M. Wagner, V. Mailänder, D. Crespy and K. Landfester, *Nano letters*, 2021, 21, 1591-1598.
263. S.-D. Li and L. Huang, *Journal of controlled release: official journal of the Controlled Release Society*, 2010, 145, 178.
264. D. E. Owens III and N. A. Peppas, *International journal of pharmaceutics*, 2006, 307, 93-102.
265. S. Salmaso and P. Caliceti, *Journal of drug delivery*, 2013, 2013.
266. D. Ricklin, G. Hajishengallis, K. Yang and J. D. Lambris, *Nature immunology*, 2010, 11, 785-797.
267. S. M. Moghimi and J. Szebeni, *Progress in lipid research*, 2003, 42, 463-478.
268. C. D. Walkey, J. B. Olsen, H. Guo, A. Emili and W. C. Chan, *Journal of the American Chemical Society*, 2012, 134, 2139-2147.
269. L. J. Cruz, R. A. Rosalia, J. W. Kleinovink, F. Rueda, C. W. Löwik and F. Ossendorp, *Journal of Controlled Release*, 2014, 192, 209-218.
270. C. Ammon, S. Meyer, L. Schwarzfischer, S. Krause, R. Andreesen and M. Kreutz, *Immunology*, 2000, 100, 364-369.
271. J. D. Berry, A. Licea, M. Popkov, X. Cortez, R. Fuller, M. Elia, L. Kerwin, D. Kubitz and C. F. Barbas Iii, *Hybridoma and hybridomics*, 2003, 22, 23-31.
272. J. Banchereau, F. Briere, C. Caux, J. Davoust, S. Lebecque, Y.-J. Liu, B. Pulendran and K. Palucka, *Annual review of immunology*, 2000, 18, 767-811.
273. W. Wang, E. Wang and J. Balthasar, *Clinical Pharmacology & Therapeutics*, 2008, 84, 548-558.
274. R. E. Kontermann, *Current opinion in molecular therapeutics*, 2006, 8, 39.
275. J. Vlasak and R. Ionescu, 2011.
276. V. Crivianu-Gaita and M. Thompson, *Biosensors and Bioelectronics*, 2016, 85, 32-45.
277. A. W. Kinman and R. R. Pompano, *Bioconjugate chemistry*, 2019, 30, 800-807.
278. H. Ma and R. O'kenedy, *Methods*, 2017, 116, 23-33.
279. A. C. Grodzki and E. Berenstein, in *Immunocytochemical methods and protocols*, Springer, 2010, pp. 15-26.
280. Y. Asaadi, F. F. Jouneghani, S. Janani and F. Rahbarizadeh, *Biomarker Research*, 2021, 9, 1-20.
281. L. S. Mitchell and L. J. Colwell, *Proteins: Structure, Function, and Bioinformatics*, 2018, 86, 697-706.
282. G. Robinson, C. Hamers and E. B. Songa, *Nature*, 1993, 363, 3.
283. M. Chiu, D. Goulet, A. Teplyakov and G. Gilliland, *Journal*.
284. A. Bates and C. A. Power, *Antibodies*, 2019, 8, 28.

References

285. E. Y. Yang and K. Shah, *Frontiers in oncology*, 2020, 10, 1182.
286. E. De Genst, K. Silence, K. Decanniere, K. Conrath, R. Loris, J. Kinne, S. Muyldermans and L. Wyns, *Proceedings of the National Academy of Sciences*, 2006, 103, 4586-4591.
287. K. A. Henry and C. R. MacKenzie, 2018.
288. P. Kunz, K. Zinner, N. Mücke, T. Bartoschik, S. Muyldermans and J. D. Hoheisel, *Scientific reports*, 2018, 8, 1-10.
289. M. Johnson, *Mater Methods*, 2012, 2, 120.
290. M. Mariani, M. Camagna, L. Tarditi and E. Seccamani, *Molecular Immunology*, 1991, 28, 69-77.
291. H.-N. Song, D.-H. Kim, S.-G. Park, M. K. Lee, S.-H. Paek and E.-J. Woo, *Bioscience, Biotechnology, and Biochemistry*, 2015, 79, 718-724.
292. H. Ma and R. O'Kennedy, in *Peptide Antibodies*, Springer, 2015, pp. 153-165.
293. J. Rousseaux, M. Picque, H. Bazin and G. Biserte, *Molecular Immunology*, 1981, 18, 639-645.
294. W. Choe, T. A. Durgannavar and S. J. Chung, *Materials*, 2016, 9, 994.
295. B. Choi, H. J. Gye, M.-J. Oh and T. Nishizawa, *Journal of aquatic animal health*, 2014, 26, 168-172.
296. S. A. Fernando and G. S. Wilson, *Journal of immunological methods*, 1992, 151, 47-66.
297. E. B. Getz, M. Xiao, T. Chakrabarty, R. Cooke and P. R. Selvin, *Analytical biochemistry*, 1999, 273, 73-80.
298. K. Tyagarajan, E. Pretzer and J. E. Wiktorowicz, *Electrophoresis*, 2003, 24, 2348-2358.
299. E. Bolli, M. Scherger, S. M. Arnouk, A. R. Pombo Antunes, D. Straßburger, M. Urschbach, J. Stickdorn, K. De Vlaminck, K. Movahedi and H. J. Räder, *Advanced Science*, 2021, 2004574.
300. J. Wesolowski, V. Alzogaray, J. Reyelt, M. Unger, K. Juarez, M. Urrutia, A. Cauerhff, W. Danquah, B. Rissiek and F. Scheuplein, *Medical microbiology and immunology*, 2009, 198, 157-174.
301. C. Kappel, C. Seidl, C. Medina-Montano, M. Schinnerer, I. Alberg, C. Leps, J. Sohl, A.-K. Hartmann, M. Fichter and M. Kuske, *ACS nano*, 2021, 15, 15191-15209.
302. S. Kramer, D. Svatunek, I. Alberg, B. Gräfen, S. Schmitt, L. Braun, A. H. van Onzen, R. Rossin, K. Koynov and H. Mikula, *Biomacromolecules*, 2019, 20, 3786-3797.
303. S. Beck, J. Schultze, H.-J. Räder, R. Holm, M. Schinnerer, M. Barz, K. Koynov and R. Zentel, *Polymers*, 2018, 10, 141.
304. B. Van de Broek, N. Devoogdt, A. D'Hollander, H.-L. Gijs, K. Jans, L. Lagae, S. Muyldermans, G. Maes and G. Borghs, *ACS nano*, 2011, 5, 4319-4328.
305. K. W. Yong, D. Yuen, M. Z. Chen, C. J. Porter and A. P. Johnston, *Nano Letters*, 2019, 19, 1827-1831.
306. M. A. Mendoza Garcia, M. Izadifar and X. Chen, *J Funct Biomater*, 2017, 8.

Curriculum Vitae

Personal Information

Name: Maximilian Bernhard Brückner

Birth: 17.04.1992 in Mainz

Nationality: German

Education

12.2018 – 04.2022: Doctoral candidate in Biology at the Max-Planck-Institute for Polymer Research in Mainz, Germany

10.2016 – 10.2018: Master program in Physical Cell Biology and Cell Interactions at the Goethe University in Frankfurt, Germany

10.2012 – 10.2016: Bachelor program in Biotechnology in Darmstadt, Germany

Work Experience

2017: Student trainee, supervisor of the human genetics practical course

2010 – 2018: Interviewer at Forum GmbH/TeleMatrix

Acknowledgements

After more than four years of working together, especially during the tragic pandemic, which brought us even closer together, I would like to thank Prof. Katharina Landfester and Prof. Volker Mailänder, without whom my Ph.D. would not have been possible. I am especially grateful to both of you for having allowed me to work on this interesting topic with such wonderful people at the Max-Planck-Institute for Polymer Research (MPIP) and in collaboration with the Paul-Klein-Zentrum für Immunintervention (PKZI) at the University Clinic in Mainz. Thank you very much for the supervision during the years.

Another thank you goes to the Johannes-Gutenberg-University in Mainz and the department of biology by giving me the opportunity to get the Ph.D. in natural sciences. Here, also a special thanks to Prof. Harald Paulsen as my second expert, as well as to Dr. Anne Régnier-Vigouroux as a referee.

Within Katharina Landfester's department of physical chemistry of polymers, in the group of Volker Mailänder, I would like to express my gratitude to all former students, in particular Dr. Johanna Simon who additionally supervised me during my internship, master thesis, and the beginning phase of my Ph.D., thank you for all the advises and papers that we were able to publish. In addition, I would like to thank the polymer analysis group (Christine Rosenauer, Elke Muth, and Beate Müller) for their measurements and support. Moreover, I want to thank all technicians who additionally supported me in any possible way (Christoph Siebert, Kathrin Kirchoff, Katja Klein) and Stefan Schuhmacher who was a great help in the digital visualization of scientific concepts.

In addition, I would like to express my sincere thanks to the bio-group. Thank you for the great time, the social activities and fun, as well as the scientific discussions and pleasant working atmosphere. Thanks to all of you!

Finally, I would like to thank my family and friends, as well as Fabrizio for their continued support throughout my doctoral work and beyond. A profound thanks to you.